Delft University of Technology

Advanced Nano Telescope

A cornerstone solution in Earth observation

DSE Group 09 - 2011

Earth image courtesy: ESA/Hubble

Delft University of Technology

Advanced Nano Telescope

A cornerstone solution for Earth observation

Group:
DSE Group 09 - 2011

Authors:
M.F. van de Bos (1305859)
R.J.F. Bijster (1506706)
D. Dolkens (1305921)
C. Mathis (1398032)
R.B.M Peters (1357018)
L.B.M. Rotthier (1399233)
R.F.M Schoemaker (1507699)
L.N.C. Sikkel (1507745)
R. van de Wetering (1314742)

Principal Tutor:
Ir. J.M. Kuiper

Coaches:
Dr. ir. P.N.A.M. Visser
Dr. X. Wu

June 28, 2011

Preface

This report aims to present the results of the Design Synthesis Exercise (DSE) Group 9 investigating the possibility to develop a multiple synthetic aperture system for Earth observation. The DSE is the final project of the Bachelor's study of Aerospace Engineering at Delft University of Technology conducted in small groups each assigned a specific project. This report summarizes the development undergone and the results achieved.

We would like to express our gratitude to Hans Kuiper, Pieter Visser and Jason Wu for their assistance and guidance during this project.

Summary

Recent developments in satellite industry gaining strong attention are so called nanosatellites. These small satellites, with sizes of about a milk carton, are easy to build and much more affordable, promising great advantages for future space missions. Up until today no reliable mid-resolution Earth observation instrument has been build that can be operated on such a small, low cost satellite. In light of these events this years Design Synthesis Exercise group 9 developed such a camera system which is called the Advanced Nano Telescope (ANT) providing a novel instrument that can be carried as payload by nanosatellites. The novelty lies in the applied principles of miniaturization and intelligent distribution in order to compete with a single large scale instrument.

The strength of the instrument developed lies in the fact that it can take images with 7.5 meter resolution, requiring a volume of only 10 x 10 x 15 cm at an estimated cost about €100,000. The small dimensions allow it to fit into half a standard 3 unit CubeSat such as the Delfi-n3Xt. The resolution is achieved by limiting the system to sense a narrow band around a single color, making use of a well designed combination of lenses and mirrors folding the light path enabling a long focal length. The thermo-mechanical design is designed such that the instrument functions in the hostile space environment from altitudes of 540 to 1440 km altitude. ANT has a smart modular structure that allows a mission designer to simply purchase the instrument and plug it into a satellite. Since all required electronic components are already present in the instrument the host satellite only needs to provide power and pointing capability to be able to achieve a fully functional system. One ANT by itself can take mid-resolution mono-chromatic images, but its real value will show when it is launched in a constellation, something which the low cost per unit allows. Multiple constellations of ANT's can outperform single satellites systems with similar ground resolutions in terms of development time, construction costs, operating costs and revisit time, enabling color composite imagery and promising improved availability at a lower price per image. Furthermore dedicated relay satellites can be added to achieve higher data rates. Overall catastrophic failures are eliminated as multiple satellites performing independent tasks are present offering redundancy and the possibility of replacement.

The conclusion is that the system developed holds a promising future with a wide range of possible applications. The instrument itself is striking due to its apparently simple but intelligent and robust design enabling Earth observation without the need of expensive large scale satellites. For future work it is recommended to further develop the concept in order to prototype and test the actual performance of the ANT instrument.

List of symbols

Symbol	Description	Unit
a	Fraction of reflected solar radiation	$[-]$
a	Semi-major axis	$[m]$
a_e	Mean Earth radius	$[m]$
c	Specific heat capacity	$[\frac{J}{kg \cdot K}]$
d	Projectile diameter	$[m]$
d_p	Characteristic length penumbra	$[m]$
d_u	Characteristic length umbra	$[m]$
e	Eccentricity	$[-]$
f	Frequency electromagnetic radiation	$[Hz]$
i	Inclination	$[rad]$
k	Material conductivity	$[\frac{W}{m \cdot K}]$
k	Structural stiffness	$[\frac{N}{m}]$
k_b	Boltzmann constant	$[\frac{J}{K}]$
m	Mass	$[kg]$
$\vec{q}$	Local heat flux	$[\frac{W}{m^2}]$
r	Position vector magnitude	$[m]$
$\vec{r}_{cartesian}$	Position vector	$[m]$
t	Time	$[s]$
A_{albedo}	Area exposed to the albedo radiation	$[m^2]$
A_a	Area of absorber	$[m^2]$
A_e	Area of emitter	$[m^2]$
A_i	Contact area i	$[m^2]$
A_i	Energy leaving surface	$[m^2]$
A_j	Contact area j	$[m^2]$
A_j	Energy intercepting area	$[m^2]$
A_j	Field of view	$[m^2]$
A_{planet}	Area exposed to planetary IR radiation	$[m^2]$
A_{solar}	Area exposed to solar radiation	$[m^2]$
$A_{surface}$	Total emitting area	$[m^2]$
C	Speed of sound	$[\frac{m}{s}]$
C	Thermal capacity	$[\frac{J}{K}]$
C_{i-j}	Conductive coupling between node i and j	$[\frac{W}{K}]$
D	Aperture diameter	$[m]$
E	Eccentric anomaly	$[rad]$
E	Total energy	$[J]$
E	Young's modulus	$[Pa]$
E_j	Etendue	$[sr \cdot m^2]$
F	Visibility factor	$[-]$
F_0	Fluence	$[\frac{kg}{m^2}]$
F_a	Half field of view	$[m]$
F_{e-a}	View factor for emitter and absorber	$[-]$
F_{fill}	Quantum efficiency	$[-]$
F_{i-j}	View factor	$[-]$
H	Brinnel hardness	$[HB]$
H	Distance pixel to ground	$[m]$
H	Height above the ground	$[m]$
J_2	Gravitational harmonic coefficient for the Earth obliquity	$[-]$
J_a	Albedo radiation flux	$[\frac{W}{m^2}]$
J_p	Planetary IR radiation	$[\frac{W}{m^2}]$
J_s	Solar radiation flux	$[\frac{W}{m^2}]$
L_i	Conductive path length i	$[m]$
		Continued on next page

Symbol	Description	Unit
L_j	Conductive path length j	$[m]$
M	Mean anomaly	$[rad]$
P	Power	$[W]$
P_inf	Penetration depth	$[m]$
P_0	Orbital period	$[s]$
P_n	Orbital period	$[s]$
$P_{n,th}$	Thermal noise power	$[W]$
Q	Heat added	$[J]$
$\dot{Q}_{emitted}$	Emitted heat flux	$[\frac{W}{m^2}]$
$\dot{Q}_{heatloss}$	Heat loss flux	$[\frac{W}{m^2}]$
$\dot{Q}_{received}$	Received heat flux	$[\frac{W}{m^2}]$
R_{i-j}	Radiative coupling between node i and j	$[\frac{W}{K}]$
R_E	Radius of the Earth	$[m]$
R_S	Radius of the Sun	$[m]$
R_ω	Rodrigues Rotation Matrix	$[-]$
S	Signal current	$[\frac{C}{s}]$
SR	Spectral radiance	$[\frac{photons}{s \cdot m^2 \cdot nm \cdot sr}]$
T	Blackbody temperature	$[K]$
T	Time in orbit	$[s]$
T_e	Emitter temperature	$[K]$
T_i	Integration time	$[s]$
T_i	Temperature of node i	$[K]$
T_j	Temperature of node j	$[K]$
T_j	Transmission	$[-]$
V	Velocity	$[\frac{m}{s}]$
V	Volume	$[m^3]$
V_n	Reference speed	$[\frac{m}{s}]$
W	Work done	$[J]$
∇T	Temperature gradient	$[\frac{K}{m}]$
α	Coefficient of thermal expansion	$[K^{-1}]$
α	Number of synodic days	$[-]$
α	Solar absorptance	$[-]$
α_a	Absorbtance of absorber	$[-]$
α_p	Penumbra angle	$[rad]$
α_u	Umbra angle	$[rad]$
β	Number of orbits	$[-]$
$\vec{\delta}$	Perpendicular distance from the center of the umbra to the satellite	$[m]$
$\delta\lambda$	Wavelength bandwith pixel	$[nm]$
ϵ	IR emissivity/absorptance	$[-]$
ϵ_e	Emittance of the emitter	$[-]$
θ	Half field angle	$[°]$
θ	True anomaly	$[rad]$
κ	Instantaneous width of the penumbra	$[m]$
λ	Wavelength	$[m]$
λ	Thermal conductivity	$[\frac{W}{m \cdot K}]$
μ	Gravitational constant Earth	$[\frac{m^3}{s^2}]$
ξ	Instantaneous width of the umbra	$[m]$
ρ_N	Density	$[\frac{kg}{m^3}]$
ρ_p	Projectile density	$[\frac{kg}{m^3}]$
ρ_t	Target density	$[\frac{kg}{m^3}]$
σ	Stefan-Boltzmann constant	$[\frac{W}{m^2 \cdot K^4}]$
ω	Eigenfrequency	$[Hz]$
ω	Solid angle	$[sr]$
ω_p	Precession of the argument of perigee	$[\frac{rad}{s}]$
Ω_p	Precession of the ascending node	$[\frac{rad}{s}]$

List of acronyms

Acronym	Description
AIT	Assembly, Integration & Testing
ANT	Advanced Nano Telescope
AO	Atomic Oxygen
ASIC	Application-Specific Integrated Circuits
BIB	Box-In-Box
CAD	Computer-Aided-Design
CBS	Cost Breakdown Structure
CCD	Charged Coupled Device
CMOS	Complementary Metal Oxide Semiconductor
COTS	Commercial Off-The-Shelf
CTE	Coefficient of Thermal Expansion
DSP	Digital Signal Processors
ESA	European Space Agency
FEA	Finite-Element-Analysis
FEM	Finite-Element-Method
FOV	Field-Of-View
FPGA	Field Programable Gate Arrays
FFD	Functional Flow Diagram
IAA	Instantaneous Access Area
IR	Infrared
LEO	Low Earth Orbit
LMN	Lumped Network Model
MLI	Multi-Layered Insulation
MSIS	Mass Spectrometer Incoherent Scatter
MTF	Modular Transfer Function
NASA	National Aeronautics and Space Administration
NIR	Near-infrared
PCB	Printed Circuit Board
SAA	South Atlantic Anomaly
SDOF	Single-Degree-Of-Freedom
SF	Safety Factor
SNR	Signal-to-Noise Ratio
SPE	Solar Particle Events
SPENVIS	Space Environment Information System
SRS	Shock Response Spectrum
SWOT	Strength Weaknesses Opportunities Threats
TCS	Thermal Control System
TML	Total Mass Load
TPM	Technical Parameter Measurement
UV	Ultraviolet
VIS	Visible

Table 2: List of acronyms

Contents

Chapter 1

Introduction

The tsunami hitting Japan and the earthquake in Haiti are just the most recent examples of natural disasters changing the face of the Earth within the blink of an eye. Such disasters require a precise organization of aid in order to save lives, prevent lasting damages and return to normal life. To provide better and less expensive imagery for applications such as disaster response, a mid-resolution Earth observation instrument operating on very small satellites (nanosatellites) holds a promising future.

Satellite images have become an essential part of our every day life. However Earth observation instruments are usually very large in size, extremely complex and expensive driving up the prices for satellite imagery. Recent developments in satellite industry gaining strong attention are so called nanosatellites. These small satellites, with sizes of about a milk carton, are easy to build and much more affordable, promising great advantages for future space missions. Up until today no reliable mid-resolution Earth observation instrument has been build that can be operated on such a small, low cost satellite.

In light of these developments the purpose of this report is to present the design of a multiple aperture Earth observation system. Design Synthesis Exercise group 9 developed a camera system called the Advanced Nano Telescope (ANT) providing a novel instrument applicable to nanosatellites. The novelty lies in the applied principles of miniaturization and intelligent distribution of tasks in order to compete with single large scale instrument. Specifically the system should fit into a box of 10 x 10 x 15 cm, provide a focal length of about 40 cm and achieve a ground resolution of 7.5 m per pixel.

The main structure of the report starts with an introduction 1 which is followed by the strategy analysis in chapter 2 which lays out the requirements to be met. In chapter 3 the space environment the system is operating in is investigated. Chapter 4 includes the summary of the concepts considered, the trade off used to select the best performing and the detailed optical design of the chosen concept. The structural design in chapter 5 including the iterative design process, the material selection and the thermo-mechanical analysis presents the housing for the electrical subsystem explained in detail in chapter 6. The thermal control of the design is discussed in chapter 7 closely related to the following chapter 8 on the protection from the hostile space environment. A detailed production plan in chapter 9 finalizes the design, which is then assessed in chapter 10. The actual purpose of application of the single system developed is outlined in chapter 11, highlighting the outstanding opportunities. Finally the report will be concluded in chapter 12 by summarizing the outcome of the project and stating recommendations for further research and development.

Chapter 2

Strategy analysis

Before starting the project the goals of the project and the means by which these goals are to be achieved will have to be determined. These issues are addressed by asking why to do the project at all, which can be explained using a market analysis and in order to detect sufficient demand. To then serve these markets the functions involved to produce a system meeting the market demands are laid out. Therefore this chapter starts with a market analysis followed by a functional analysis for the system to be developed. From the market analysis and the functional analysis a list of specific requirements for the design are derived. After this the operations and logistics involved are discussed as well as the sustainable approach considerations.

2.1 Market analysis

In order to design a successful product, first a thorough market analysis must be conducted. It must be analyzed if there is a market for the product, if there are any market segments that are potential targets and what requirements must be met for the product to be successful.

The market analysis will be conducted in multiple steps. First of all, the size of the current market will be analyzed. After that, the various market segments and their specific requirements will be analyzed. The growth of the market will also be looked at, as well as the competitiveness of the market using Porter's five forces model. All the data will then be combined in a SWOT analysis and success factors of the market will be analyzed. Finally, a marketing strategy will be chosen.

2.1.1 Market size analysis

Due to the enormous number of applications of satellite images and the ever increasing quality of the images, the market for satellite imagery has grown significantly over the past few years. In figure 2.1, the revenues over the last few years can be seen, peaking in 2009 at one billion dollars. Even though the revenue is modest compared to the 93 billion total revenue in the satellite sector, the field does attract serious investments. The European Space Agency, for instance, allocates 21.1% of its billion dollar budget to remote sensing missions [1].

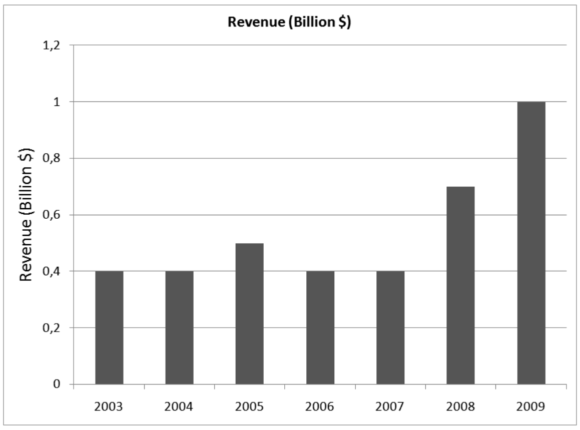

Figure 2.1: Cumulative revenue in the remote sensing industry (Satellite Industry Association, 2010) [2]

2.1.2 Market segmentation

In this section the market for satellite images will be segmented according to the applications of the images, since image requirements depend on the application. A quick overview of the sectors and their requirements can be found in table 2.1.

Agriculture Satellite images can for example be applied to predict the yield and monitor the soil and crop conditions [3]. A resolution of 10 to 30 meters is needed such that information from individual agricultural parcels can be retrieved. The most useful wavelength range is near infrared, which can be combined with visual light to determine the vegetation index. Because the quality of crops may vary from week to week, information needs to be updated frequently.

Archeology Remote sensing can be used for detecting, acquiring inventory and prioritizing surface in a rapid, accurate, and quantified manner [4]. High resolution images of visual light may give an indication of present and past land use. Infrared images may reveal buried stones or ancient irrigation ditches. The image data does not need to be up to date, therefore buying archive material may be a more economical approach than acquiring new material [5].

Cartography and regional planning The process of creating detailed maps these days largely depends on satellite data. Map types vary from road and infrastructure to cadastral maps and city models. The required resolution depends on the population density. The market in this field is mature, yet the market potential remains high. Large areas of the Earth remain unmapped even at medium resolutions and mapped areas require regular updates [3]. The wavelengths that are useful are mainly visible light.

Disaster response and prevention By continuously monitoring the Earth some disasters may be prevented. Or when a disaster has already taken place, satellite imagery can help to assess the damage and prioritize the actions which must be taken. Images that can be used for disaster response need to have a decent resolution, but most of all, they need to be up to date and, after the disaster, they need to be updated continuously. Useful wavelengths include visual light and infrared.

Environmental protection Observations in this field are mainly related to land cover and use, water management and impact assessment [3]. Examples of environmental issues are for example deforestation, destruction of natural habitats and the growth of the desert. The required resolution ranges from just half a meter to 20 meters. [6]. Capturing visual light is very useful for examining land use and near infrared is particularly useful for detecting vegetation. Since environmental research focuses on the analysis of changes, data needs to be updated frequently for such changes to be detected.

Geology and mining The wavebands that are mainly of interest in this sector are near-, short wave- and thermal infrared. Multi-spectral images using this data allows geologists to interpret the surface properties to identify clays, oxides and soils [7]. Data can be relatively old to be useful for these purposes.

Humanitarian aid Satellite images can be used to detect humanitarian disasters at an early stage or it can be used to pinpoint regions which need urgent humanitarian attention. An example of a recent project in the field of humanitarian aid is the Satellite Sentinel Project. This project combines satellite imagery analysis and field reports to monitor recent developments in politically unstable regions of Sudan. Results of the project focus world attention on the situation and it generates rapid response by the international community to deter further violence [8].

Intelligence and warfare Earth observation data has become indispensable in modern intelligence and warfare. Satellite imagery is used for surveillance, reconnaissance, identifying enemy ground, naval and air forces. Furthermore, weapon development and testing by other nations can be detected [9]. Satellite imagery needs to be highly detailed and up to date. Useful wavelengths are visual light as well as infrared.

Marine and coastal The field of Marine and Coastal has a lot of market potential, since a lot of valuable economic activities are located in marine environments, such as shipping and fishing [3]. Applications in the fishing sector are mainly focused on the detection of fish, which is indirectly possible with satellite imagery [10]. Low to medium resolutions will be sufficient for this, but the coverage should be high. In the shipping sector satellite images can be used to track ships, for this medium resolutions are sufficient. For both application the data needs to be updated frequently and the wavelength range should be visible light with the addition of infrared for fishing.

2.1.3 Summary

In table 2.1, the market segments mentioned in the section and their requirements in terms of ground resolution, wavelength range and temporal resolution are summarized. These values are based on general direction and/or explicit value references uncovered during the market analysis. In the table VIS is used to designate three band color images (blue: 440 nm, visual: 550 nm, red: 660 nm). Monochromatic images are rarely used in the industry, whereas panchromatic or multi-spectral images have become the norm.

Table 2.1: Market segments and their spectral information use

Market Segment	Information Type	Ground Resolution $[m]$	Wavelength Range	Temporal Resolution
Agriculture	Vegetation index	1 - 30	VIS, NIR	10-15 days
Archeology	Site search	1 - 10	VIS, IR	years
Cartography / Regional Planning	Cadastral / City Planning	<1 - 5	VIS	weeks
	Cartography	1-30	VIS	weeks
	Regional Mapping	10-30	VIS	weeks
Disaster Response	Damage monitoring	1-30	VIS	daily
Environmental Protection	Land cover / Land use	30	VIS, NIR	weeks
	Detailed Flora and Fauna	0.5	VIS, NIR	weeks
Geology / Mining	Exploration	30	VIS, NIR, IR	years
Humanitarian aid	Social Control and Monitoring	1 - 20	VIS, IR	days
	Urban Development	1 - 20	VIS	years
Intelligence / Warfare	Ground Forces	1 - 5	VIS, IR	real time
	Reconnaissance / Surveillance	1 - 20	VIS, IR	days
Marine and Coastal	Locating fish populations	>20	VIS, IR	days-weeks
	Shipping	10-20	VIS	days-weeks

It is evident that not all segments can be served by a CubeSat. It is very hard to produce a system that can capture infrared light and it is impossible to reach the resolution required for some purposes. Also some fields do not require up to date data or need data for extensive periods of time. Given the short mission duration of a CubeSat mission, it is not profitable to target such markets. The fields of regional mapping, environmental protection, humanitarian aid and marine and coastal could be served well by a CubeSat system.

2.1.4 Market growth analysis

It is important to analyze the growth of a market and find out which particular segments are likely to grow. Finding a niche in an upcoming market can be the key to great scientific and commercial success.

Northern Sky Research expects the cumulative revenue in the sector to grow to a massive 6.2 billion dollars compared to a revenue of 1 billion in 2009. It also expects the most promising applications to be in the fields of environmental monitoring, land management, natural disaster response, insurance and real estate and tourism [11]. The fastest growth is expected in the medium resolution, low-cost market. This would be beneficial for CubeSat based systems. The field of environmental monitoring was also found to be a promising segment in the previous section. A reason for the expected growth is that environmental awareness in societies all over the world has grown over the years and this sentiment has increased the demand for environmental research. Additionally, a widespread anxiety over the potentially harmful effects of climate change, as well as mounting evidence pointing to permanent damage of fragile ecosystems, have fueled the demand for better environmental monitoring.

According to Eurimage [3] the consumer market has a very high potential. A reason for this is that satellite data is slowly becoming embedded in modern society. Targeting the consumer market directly may be lucrative because of its size. According to Eurimage, the key to success is to bridge the gap existing between Earth observation data and these users, through actions that must rely mainly on the "pictorial" aspect of the data. [3]. The widespread access that the global community now has to satellite imagery based mapping software has also opened up new possibilities in the field of humanitarian aid. As the satellite data for these purposes should be updated frequently, demand for satellite imagery will continue to soar.

2.1.5 Porter's five forces

The Five Forces model consists of five competitive forces which can be used to shape the strategy of a company or influence the design of product. In the next paragraphs the forces will be described in general and applied to our project. This section is based on the work of Micheal E. Porter [12].

The intensity of competitive rivalry One of the forces in Porters model is the intensity of competitive rivalry. This threat comes from direct competitors that all want a share of the same market. The Earth

Observation market is dominated by a few very big corporations and several relatively new systems. Given the low number of competitors and the fact that the competitors each have a slightly different focus, the competitive rivalry in the market remains limited (except for very high resolutions, where competitors try to beat each others resolution). The degree of competition from CubeSats is low given the fact that none of the CubeSats so far have succeeded in creating a product with any commercial value.

The threat of entry of new competitors Another force influencing the competitiveness of a certain market is the threat of new entrants. This threat exists because the revenue in the market is high and the market is likely to grow substantially over the time to come. There are however barriers that deter companies from entering the market. Traditionally the development and launch costs for satellites are quite high and there is a long development period during which no profit is made. This barrier can be mitigated somewhat in the case of a CubeSat system, since launch development costs as well as time are a lot lower. Other barriers are the possibility of launch failure and loyalty of customers to existing solutions.

The threat of substitute products or services When analyzing a market, one should not only look at direct competitors, but also at companies offering products that can serve as a substitute. Possible substitutes to space imaging are airborne imaging, for instance by a plane or a balloon, and in-situ imaging. Both these options offer ground resolutions that cannot be matched by satellite images. However, their spatial coverage is much lower and in the long run airborne observation is more expensive, especially when a high temporal resolution is required.

The bargaining power of customers For many of the buyers the costs of satellite images are a significant part of their total budget. This means that they are willing to look for other suppliers that are cheaper or offer better service for the same price. This gives the customer a large bargaining power, since they can go to a competitor unless you satisfy their needs (pricing, service, availability, etc.). From this it can be concluded that the customer has a large bargaining power. Although the volume does not give bargaining power, both the importance of the images to the final product of the buyer and the price sensitivity of the buyer do.

The bargaining power of suppliers One example of a supplier which has substantial power on the market of satellite imagery is the company offering launch services. CubeSats usually hitch-hike along with bigger commercial or scientific satellite missions. There are multiple launchers available from different countries, but still there are not that many launches each year. This puts the supplier in a good position, but development of cheap launching solutions tailored for CubeSats will mitigate this power to some extend. Another example of a supplier is the supplier of the parts used in the design of CubeSats have very little power. In the design, mainly commercially off the shelf products will be used, which are available from a wide variety of vendors. Supplier power may be further reduced by producing more parts in-house.

2.1.6 Summary

From the analysis of the Five Forces it follows that the market for satellite imagery is quite competitive. This is mainly caused by the fact that there are several very large corporations active in the market as well as some companies that have entered the market more recently. They offer a diverse range of products ranging from high to medium resolutions at a variety of prices. However, all options that are currently available are quite expensive, especially if a user needs data that is updated frequently. The bargaining power of customers is also very high in the market, due to the fact that high quality images are available from several competing providers. On the other hand the threat of new competitors in the market is quite low due to high development and launch costs, but these costs can be reduced by using CubeSats. Suppliers in the market do not have a lot of bargaining power although an exception to that would be the launch agencies. Finally, substitutes in the market such as in-situ observations as well as aerial photography do not increase the competitiveness in the market.

2.1.7 SWOT analysis

In order to pick a good marketing strategy, an analysis of the strengths, weaknesses, opportunities and threats (SWOT) should be performed. Information from the previous sections and the general characteristics and technical analysis of a CubeSat based system has been distilled and put in the SWOT format as shown in table 2.2.

2.1.8 Success factors and marketing strategy

In order to be successful in the market of satellite imagery the following factors have to be taken into account:

Table 2.2: SWOT analysis

Strengths	**Weaknesses**
• Low development cost and time • Ability to achieve a high temporal resolution • Autonomous operation • Use of COTS parts • Low cost per image • In-house production of parts	• Trade-off between FOV and ground resolution • Highest resolutions in the market can never be matched • Short mission duration • Limited power and link budget • Higher risk due to short development cycle
Opportunities	**Threats**
• Constellation operation • Anticipated growth in medium resolution, low cost market segment • Cooperation with space agencies • Bridging the gap between the image provider and the consumer	• Intense competitive rivalry • Risk of market saturation • Competition from substitutes (airborne and in-situ measurements) • Loyalty of customers to existing technology

- **Ground resolution:** The ground resolution is a good measure of the amount of detail that can be sensed by an optical system and has a direct influence on the market segments that can be served.
- **Wavelength range/spectral region:** Systems with large wavelength ranges may be suited for a wider variety of purposes, but optimizing for a narrow band is possible too.
- **Field of View:** The field of view, or swath width, will determine how wide a region can be captured at a certain time.
- **Temporal Resolution:** High temporal resolutions will allow the customer to get updated information frequently.
- **Cost per Image:** All customers prefer to get the data they require for the lowest possible cost. Keeping the cost per image low will allow a system to be very competitive.

It is impossible for a system to score well on all success factors, since high performance in one field often compromises the performance in another. This holds true especially for a CubeSat based system with its limited resources, thus a trade-off must be made. To determine which factors are the most important, a marketing strategy should be chosen.

In his book "Competitive Strategy: Techniques for Analyzing Industries and Competitors" [13] Michael E. Porter has defined three generic marketing strategies that can be adopted. These strategies are:

- **Differentiation strategy:** The differentiation strategy focuses heavily on the quality of a product.
- **Cost leadership:** Using the cost leadership strategy the company focuses on offering services or products at a lower price than the competition.
- **Segmentation strategy:** A company following the segmentation strategy has a narrow focus on a certain market segment.

Looking at the results of the SWOT analysis, it is a logical conclusion to go for a combination of a low cost and segmentation strategy. The CubeSat optical system should focus on market segments that require medium ground resolutions and a high temporal resolution and serve them at a low cost.

2.1.9 Conclusion

Over the years, the Earth observation market has grown significantly. Cumulative revenue has risen to a value of 1 billion dollars in 2009 and the sector attracts major investments from large corporations and space agencies. Also, a significant part of the launches every year is devoted to Earth observation missions.

The number of applications for satellite images is immense. Satellite images are now used in a lot of market segments. Each market segment has different requirements for the data that is used in terms of spatial resolution, the wavelength range that is captured and the rate with which data is updated. A CubeSat based system has a couple of limitations, for instance its difficulty to capture infra red light, its short mission duration and its inability to reach very high resolutions. As such, market segments requiring images capturing visual light, at a moderate resolution but at a high temporal resolution, are potential targets. These segments include the fields of regional mapping, environmental protection, humanitarian aid, disaster response and prevention, and marine and coastal.

The Earth observation market is still growing rapidly; it is expected that cumulative revenue will rise to 6.2 billion dollars by 2018. Especially the demand for low cost, moderate resolution imagery is likely to increase. Of the segments mentioned above, the fields of environmental protection and disaster response and prevention have the biggest potential. Additionally, targeting the consumer market directly also has a lot of market potential.

An analysis using Porter's Five Forces model showed that the market for satellite imagery is very competitive. Particularly in the field of very high resolution images, the competition is tough, and the products already available will be impossible to match with a CubeSat based system. However, if the data a user requires needs to be updated frequently and the user does not require very high resolutions, the options currently available are very expensive. Additional factors that raise the competitiveness in the market and make it more difficult for a new entrant to gain a foothold in the market are the high launch cost and limited launcher availability, customer loyalty to existing technology and the high development costs. A CubeSat can overcome some of the barriers, because they are cheaper to develop and launch.

Based on the SWOT analysis that has been derived from the characteristics of CubeSats and the rest of the market analysis, it was determined that a suitable marketing strategy would be to go for cost leadership in specific market segments. It can be concluded that for the system to be successful in the current and future market, it must comply to the following requirements:

- **Spatial resolution:** Reach a resolution of at least 10 meters per pixel
- **Wavelength range:** Multi-spectral images of visual light
- **Temporal resolution:** Ability to be able to update results on a daily to weekly basis
- **Costs per image:** Deliver results for a cost per image far below current market standards

In conclusion, if the system to be designed can match the requirements stated above, it will have a lot of market potential.

2.1.10 Requirements

From the market analysis and the functional analysis several requirements and sub requirements can be distilled. Together with the top-level requirements, which were given at the start of this project, they form all the requirements of the optical system. All the requirements and their unique identifiers can be found in table 2.3.

Table 2.3: Requirements breakdown

ID Level 0	ID Level 1	ID Level 2	ID Level 3	ID Level 4	Description	Source
1.0					Perform mission technically	
	1.1				Provide sufficient image quality	
		1.1.1			Ground resolution of 7.5 m at 540 km altitude	Top-level
		1.1.2			Field-of-view of 10 x 10 km	Top-level
		1.1.3			Provide sufficient optical image quality	

Continued on next page

ID Level 0	ID Level 1	ID Level 2	ID Level 3	ID Level 4	Description	Source
			1.1.3.1		Mirror surface reflection > 90%	[14]
			1.1.3.2		Lens transmissivity > 95%	[14]
			1.1.3.3		Provide opto-mechanical-thermal stability	Top-level
			1.1.3.4		Provide a maximum focal ratio of 1/10	[15]
			1.1.3.5		Provide a low aberration optical track	[14]
		1.1.4			Sense the relevant wavelength (VIS 0.3-0.7 μm)	2.1
	1.2				Provide sufficient image quantity	
		1.2.1			Link budget	
			1.2.1.1		Bitrate > 9600 bit/s	6
			1.2.1.2		Time between pictures < 2 seconds	6.5.2
	1.3				Required power < 1 Watt	6
2.0					Perform mission with constraints	
	2.1				Reliability	
		2.1.1			Provide no single point of failure	Top-level
	2.2				Operational lifetime of 2 years	Top-level
	2.3				Sustainability > 80%	Top-level
	2.4				Integrate-able in the CubeSat standard	[16]
	2.5				Design within available resources and budgets	
		2.5.1			Mass budget of 2 kg	Top-level
		2.5.2			Volume budget of 10 x 10 x 15 cm	Top-level
		2.5.3			Cost < 50.000 €	Top-level
	2.6				System tolerances	
		2.6.1			Launch constraints	Top-level
			2.6.1.1		Acoustic loads of max. 2000 Hz with Safety Factor (SF)=1.41	[17]
			2.6.1.2		Vibration levels of 31 Hz with SF=1.25	[17]
			2.6.1.3		Quasi-static loads of max. 6.0 g	[17]
				2.6.1.3.1	Static load factors of max. 4.55 g with SF=1.25	[17]
				2.6.1.3.2	Dynamic load factors of max. 1.45 g with SF=1.25	[17]
			2.6.1.4		Shock loads of max. 2000 g	[17]
		2.6.2			Space environment constraints	
			2.6.2.1		Withstand radiation levels	
			2.6.2.2		Provide low outgassing values for all materials	

2.2 Operations and logistics concept description

2.2.1 Operations

The operations part of the optical system consists of the functions of the system during the operational phase. Thus the "perform scientific mission" part of the functional flow diagram (FFD) of the optical system gives a good indication of the operations. It has to be noted that the FFD only shows operations of the optical system, while the ground operations should be included as well.

The ground operations consist of (amongst others) data reception, image processing, distribution, marketing, updating software. For the data reception there has to be a ground station or another way of receiving the image data (such as radio amateurs). The data has to be received for the entire lifetime of the satellite. When the data has been received it has to be processed, since in the current shape it is unlikely to be of sufficient value for customers. When the data from the optical system is processed into a useful form it has to find its way to the customer. It will become apparent when reading the next section on logistics that there is a link between operations and logistics. This does not come as a surprise as logistics support all operations. Further operations consist of marketing the final product and updating software of either ground stations or the optical system when necessary.

2.2.2 Logistics

According to the Van Dale dictionary logistics is the control of product flow and personnel and data traffic needed to make a company function [18]. In the case of our project the product flow and data traffic are closely related as the product consist of digital image data. The product flow consists of more than only digital data and the data flow consist of more than only the final product, but they will be discussed together because of the before mentioned similarity. The personnel traffic will be in a separate paragraph.

The product flow will be discussed first. There are products coming in from suppliers and there are products going out to customers. Logistics has to make sure that the products that are needed from suppliers arrive on time in order not to delay the production process and keep storage capacity small. Also expensive parts have to be ordered as late as possible to decrease investment costs, but they do have to arrive in time. For this project the mirrors or lenses that are needed are very important and expensive parts. The planning has to be such that these parts do not have to be stored for a long time before assembly and also they should not arrive too late, delaying the production process.

Next the combination of product flow and data traffic will be treated. The optical system produces an image of the Earth, which consist of digital data. This data is only useful when it arrives at the customer (e.g. the farmer when considering agriculture). First the image inside the memory of the processor on-board of the optical system first has to be downlinked to Earth. This will be done by transmitting radio waves. The waves have to be received on Earth by for example a dedicated ground station or by radio amateurs. In the case of radio amateurs the logistics department has to set up a (digital) infrastructure in order to get all data together. After this the data has to be processed into a form which is useful for the customer (the final product). Finally the final product has to be distributed to these customers. Thus there is a data traffic which has to be properly routed and this data has to be processed to form a product. After this the product has to be distributed. These are all logistics tasks.

The personnel traffic will be discussed now. The personnel can be divided into several groups such as design, production, operation and maintenance. In order to be efficient the amount of personnel movement should be reduced as much as possible. This means that it is the task of the logistics department to plan this movement well. In order to have a successful optical system all previously named personnel groups are needed, but for this concept the focus will be on design. The movement of designers can be reduced by making sure that all necessary resources they need are in one place. Also the designers should be able to communicate with each other, meaning that they themselves need to be close together as well. Thus logistics has to plan movement of personnel in order to improve efficiency (less time wasted on movement).

2.3 Sustainable development approach

This chapter will highlight the sustainable approach used in the project in the broadest sense, i.e. with respect to management, resource usage and design. To obtain funding and social acceptance for a project it is very important to express the sustainability and "greenness" of the final product. Also for the project team itself it is important to have a sustainable working environment, in order to improve task efficiency.

The sustainability of the design depends mainly on the material that is used, the function it fulfills and the way of disposal. Recycling which was already mentioned is not an option, but there are other options that improve the sustainability of the satellite in which the optical system is integrated. One option is that the satellite will be disposed of in the atmosphere to make room for a new satellite. Not disposing of the satellite would harm the sustainable development, since it is not possible to keep increasing the number of satellites in a certain orbit for ever.

Furthermore the amount of resources that are used during product development and operation should be minimized or they should be renewed at a sustainable rate. Options that can be used to minimize resource usage during project development are for example minimizing the amount of prototypes and tests, but also printing less paper and decreasing the amount of transportation. A very strong point of a nanosatellite hosting the Advanced Nano Telescope is that it can be launched with the 'piggy-back option, so no dedicated launch is required. Looking at this paragraph might give the idea that sustainable development is only amount minimizing, but luckily this is not the case. It is also possible to improve processes such that they become more sustainable without having to decrease the usage. A good example of this is for electricity generation using solar cells. The satellite that carries the optical system that will be designed during this project is most likely to incorporate solar cells, which gives a boost to the sustainability.
It was already mentioned in the beginning that it is important to have a sustainable working environment during the project. This has also to do with resources, but it is mentioned here separately since it concerns human resources. Also this resource should not be exhausted as this will degrade the efficiency of the people involved. Good project management, i.e. good planning and control, will reduce the pressure due to upcoming deadlines and will also reduce conflicts that arise due to a lack of knowledge of the schedule.

It can be concluded that it is important to have a good overall sustainable system. This can be obtained by looking at for example the materials that are used, the way in which the system is launched and disposed of, use of human resources, facilities etc. Also it is important to note that sustainable development is not only about minimizing, but also about looking for smart alternatives.

Chapter 3

Requirements and constraints induced by the space environment

Already the conditions on Earth can be stringent and burdensome to an optical system, but the space environment is much more hostile. An instrument does not only experience a different atmosphere, it will also have to survive, the chemical composition of the atmosphere, high levels of radiation, micro asteroids and high temperature differences. In this chapter the space environment and the requirements and constraints it yields for the optical instrument are discussed. The influence of the highly reactive atomic oxygen is discussed in section 3.2, whereas the radiation environment is given in section 3.3. Finally a discussion of the particle debris found in LEO is presented in section 3.4.

3.1 Orbit selection

As for every space mission the orbital parameters have to be determined. Because the design considers an instrument and not a specific mission, the analysis in this section will be study of orbits that a mission designer is likely to choose if the instrument is installed in the satellite. In section 3.1.1 the influence of the altitude on the design will be discussed after which limits are set on the altitude in section 3.1.2. In section 3.1.3 several orbit types are excluded from the analysis. A rationale for doing so is included. The remaining interesting orbits are discussed in section 3.1.4. The discussion includes a study of the revisit times encountered in specific orbits and the combinations of altitude and inclination associated to a temporal resolution. The access rate and the field of view are described in sections 3.1.5 and 3.1.6 respectively.

3.1.1 The influence of orbits on the design

The orbital parameters influence the end product in several ways. First of all is the resolution and field-of-view (FOV) determined by the altitude. If the configuration of the instrument does not change it can be said that increasing the altitude also leads to an increasing field of view and a decrease in resolution. A change in altitude and inclination also leads to a change in temporal and spatial resolution. The altitude determines the number of orbits per day and combined with the inclination it determines the coverage and spatial resolution.

With the orbit also the space environment encountered by the instrument changes. For example the thermal fluxes are dependent on altitude, but also the concentrations of constituents in the atmosphere and radiations levels are dependent on the orbital parameters.

3.1.2 Limits on altitude

Before the characteristics of the interesting orbits can be considered the bounds on the altitude need to be set. From the mission need statement a minimum ground resolution of 7.5m at an altitude of 540km was required. The maximum altitude allowable can be derived from the market analysis. This stipulates that a resolution of 20 m/pixel is still sufficient to have commercial value. To achieve this ground resolution the altitude can be found by equating the ratios as shown in the equation below:

$$\frac{7.5\,[m]}{540\,[km]} = \frac{10\,[m]}{Altitude_{\max}\,[km]} \rightarrow Altitude_{\max} = 1440\,[km] \tag{3.1}$$

This way also the field of view (FOV) at the maximum altitude can be calculated. The FOV at 540 km was found to be 15 km wide during the conceptual design phase. Using this information equation 3.2 can be used to find the FOV that corresponds to an altitude of 1440 km.

$$\frac{15\,[km]}{540\,[km]} = \frac{FOV_{\max Altitude}\,[km]}{1440\,[km]} \rightarrow FOV_{\max Altitude} = 40\,[km] \tag{3.2}$$

Based on the bounds on the altitude and a given or derived inclination the spatial and temporal resolution can be derived. It is possible to go lower in altitude, but this will have an effect on the lifetime of the satellite. This causes either loss of mission lifetime, or inclusion of extra propellant for orbit maintenance. Without going into detail an estimation of the ballistic coefficient of a 3-cube nanosatellite can be given by comparing it to the Oscar-1 satellite in table 8-3 in [19]. The ballistic coefficient will be between 42.8 and 16.7 $\frac{kg}{m^2}$. From [19] can be derived that if the ballistic coefficient is 20 $\frac{kg}{m^2}$ the instrument can still be used at 450 km during a solar minimum. In that case the lifetime will still be approximately 2 years. However, during a solar maximum the lifetime will be reduced to approximately 2 months.

Using the ratio in equation 3.1 the resolution obtained at the 450 km altitude is 6.25 $\frac{m}{pixel}$. Therefore a trade-off will be necessary between gain in resolution and loss of mission lifetime. Because the gain in resolution is considered minor, the reference altitude is set at the benchmark altitude of 540 km.

3.1.3 Exclusion of typical orbits

In principle Earth observation can be performed from (almost) any orbit. However only some orbits are reasonable for the specific design constrains of the optical system developed during this project. As mentioned in the section 3.1.2 the orbit aimed for should range between 540 km and 1440 km altitude for acceptable to good performance, but ground resolution and field of view are not the only design parameters. Also the spatial resolution and temporal resolution are important. These parameters are assessed in more detail in the following section. By benchmarking the performance that can be reached in a certain orbit (type) against the performance measures above, the number of possible orbits the instrument is likely to be used in can be reduced.

- Geostationary Orbit:

  A geostationary orbit has the unique and interesting feature of an orbital period equal to one sidereal day. This causes the subsatellite point to be (almost) invariant, which means that this point can be observed continuously by one satellite. It also means that on-board storage of the images would not be necessary, because a continuous downlink with a ground station would be possible. However, as mentioned before, the altitude has to be 1440 km at most for acceptable performance of the optical system. For a geostationary orbit the altitude is approximately 36000 km. For this reason the geostationary orbit is not a viable option for the instrument.

- Molniya orbit:

  The very distinct Molniya orbit, originally designed for long coverage times over Russia, is like the Tundra orbit a highly eccentric orbit with its apogee over the area of interest. It has the feature that the precession of perigee is equal to zero. Because the apogee is over the area of interest the satellite has a long coverage time for that area, which might be very interesting if pictures have to be taken of a specific area of the Earth. The orbital parameters of the Molniya orbit, however, make it a not commercially viable option. The Molniya orbit is limited to inclinations of 63.4° or 116.6° and with an apogee height of 540 - 1440 km not a big increase in coverage time with respect to other Low Earth Orbits can be achieved.

- Polar orbit:

  A polar orbit with its inclination of 90 degrees has the interesting feature of not having a polar gap. Every orbit with any other inclination will not go over the poles, creating a gap in the coverage. When global coverage is required this is an interesting option. Many Earth observation missions use (near) polar orbits and it is therefore also a proven commercially viable option.

- Sun-synchronous:

  For a sun-synchronous orbit the precession of the orbit around the Earth's rotation axis is equal to the rotation of the Earth around the Sun. This allows for constant lighting conditions on the subsatellite point every time the satellite passes. Special cases of the sun-synchronous orbit are the dawn-dusk orbit and the noon-midnight orbit. In the dawn-dusk orbit the satellite rides the terminator and has continuous lighting conditions on its solar panels. The advantages of this orbit for the power budget are strongly counteracted by the difficulties that arise in the thermal environment. A further analysis of this problem can be found in 7.7.8. In a noon-midnight orbit the satellite passes over every point around noon or midnight. This means that the lighting conditions at the sub satellite point are constant, it is either in full sunlight or in total darkness when the instrument passes over.

3.1.4 Discussion of interesting orbits

In continuation of section 3.1.3 the polar, sun-synchronous and an arbitrary Low Earth Orbit (LEO) and their distinctive features will be discussed here. All orbits given are likely options a mission designer will choose.

Constants and relations used

For the analysis performed in this chapter several constants are used. The first of these constants, the gravitational constant of the Earth GM, is used in orbit calculations and in Kepler's laws. This constant is given by equation 3.3:

$$GM = \mu = 3.98600434 \cdot 10^{14} \left[\frac{m^3}{s^2}\right] \tag{3.3}$$

The Earth is not spherical and its radius is a function of geometric latitude and longitude. To simplify the calculations it is assumed constant and set to the Mean Earth radius as given by [20]. The Mean Earth Radius is given by equation 3.4.

$$a_e = 6378135\,[m] \tag{3.4}$$

Because the Earth is not spherical, its gravity field is also not homogeneous. The gravity field can be modelled using spherical harmonics as explained in [20]. The most noticeable effect, the oblateness of the Earth, can be described by the J_2 coefficient. This coefficient is given by equation 3.5.

$$J_2 = 0.00108263 \tag{3.5}$$

The oblateness of the Earth has several effects on the orbit. The two most noticeable and sometimes most useful effects are the precession of nodes. When a satellite approaches the equator it is slightly pulled towards it, changing its inclination slightly. If the satellite a few moments later distances itself from the equator again the same happens but in opposite direction. This causes the longitude of ascending node to precess either west or east, depending on the original inclination of the orbit. This effect is given by equation 3.6.

$$\Omega_p = -\frac{3J_2\sqrt{\mu}a_e^2 a^{-\frac{7}{2}}\cos(i)}{2(1-e^2)^2} \tag{3.6}$$

In this equation Ω_p is the rate of change of the longitude of the ascending node $\left[\frac{rad}{s}\right]$, a_e is the radius of the Earth $[m]$, a is the semi-major axis of the orbit (radius of Earth plus altitude for a circular orbit) $[m]$, i is the inclination $[rad]$ and e is the eccentricity (equal to zero for circular orbits). The second effect is the change in argument of perigee. This effect however can be ignored for circular orbits, for no perigee exists in a circular orbit. The orbital period for a satellite around a celestial body is derived from Kepler's third law. In its original form it is given by equation 3.7.

$$P_0 = 2\pi\sqrt{\frac{a^3}{\mu}} \tag{3.7}$$

If however also the inclination of the orbit and the obliquity of the Earth are taken into account this expression is extended to the form in equation 3.8:

$$P_n = 2\pi\sqrt{\frac{a^3}{\mu}}\left(1 + \frac{3J_2\sqrt{\mu}a_e^2}{4a^2}\left\{1 - 3\cos^2(i) + \frac{1-5\cos^2(i)}{(1-e^2)^2}\right\}\right) \tag{3.8}$$

Better approximation of repeat orbits

Using equation 3.7 or 3.8 the period of an orbit can be found. If this is combined with equation 3.6 a first order approximation of the revisit period can be found. This method is improved by [21]. In this method the following expression for exact repeat orbits can be used.

$$n' = \frac{\beta}{\alpha}\dot{S} - \frac{3}{4}J_2 n'\left(\frac{R}{a'}\right)^2\left[5\cos^2 i - 2\frac{\beta}{\alpha}\cos i - 1\right] \tag{3.9}$$

In which β is the number of orbits, α is the number of synodic days, n' is the mean mean motion in $\frac{rad}{s}$, a' is the mean semi-major axis and R is the mean Earth radius. This equation cannot be solved analytically. By relating the mean mean motion n' and the mean semi-major axis a' using Kepler's third law:

$$n'^2 a'^3 = \mu \tag{3.10}$$

and assume the initial value of $n_0^{'} = \frac{\beta}{\alpha}\dot{S}$ then the altitude, inclination combination for a certain repeat orbit can be found. $\dot{S}$ is the average rotational speed of the Earth $\left[\frac{rad}{s}\right]$ and is given by equation 3.11.

$$\dot{S} = \frac{2\pi}{365,25 \cdot 24 \cdot 3600} = 1.991021278 \cdot 10^{-7}\left[\frac{rad}{s}\right] \tag{3.11}$$

The polar orbit

The polar orbit is characterised by its 90 degree inclination. This inclination renders the polar orbit an advantage over other orbits by giving it full coverage of all latitudes, including the poles. In other orbits the poles are not (fully) covered by the subsatellite point.

The possible repeat orbits between these altitudes can easily be found using the method described by equations 3.9 and 3.10. To find the limits for the iterative process required for these equations, an approximation of the maximum revisit time is required. The maximum revisit time is obtained if one instrument gives coverage of all longitudes. At 540 km altitude the FOV was found to be 15 km wide. Assuming the Earth is spherical with a mean radius of 6378.135 km the circumference is equal to 40075 km. This means approximately 2672 adjacent orbits are needed for full coverage of all longitudes with one instrument. The orbital period corresponding to a polar orbit at 540 km altitude is found to be approximately 5727 s or 95 minutes and 27 seconds using equation3.7. If the orbital period is combined with the amount of adjacent planes it can be derived that a 2672/177 repeat orbit will give full Earth coverage.

Similarly, for 1440 km altitude the orbital period equals approximately 6880 s or 114 minutes and 40 seconds. With a ground track width of 40 km 1002 orbital adjacent orbital planes will be required. With one satellite this will take approximately 80 days. This gives a 1002/80 repeat orbit. However, this orbit equals 501/40 repeat orbit which means only half of the Earth will be covered. A mission designer would already need two similar orbital planes to cover all longitudes. By changing the altitude slightly for example a 1003/80 orbit would give global coverage with one orbital plane. In figure 3.1 all repeat orbits for a polar orbit with an altitude between 540 and 1440 km and a revisit time of at most half a year can be found. As can be seen from the graph, the revisit time can be tweaked to the requirements of the mission designer by simply choosing a different altitude. The designer will have to do a trade-off however between resolution and field of view on one hand and revisit time on the other. If only one instrument is used, however, the lighting conditions will

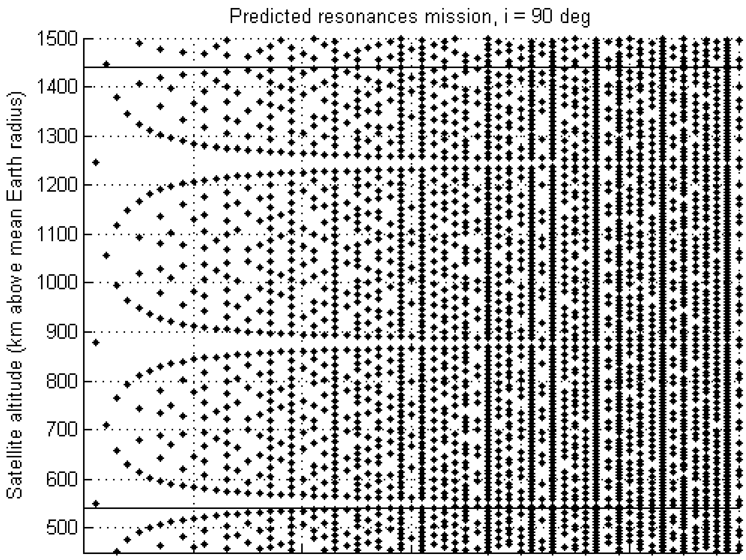

Figure 3.1: Predicted resonance orbits for inclinations for a polar orbit between 540 and 1440 km altitude.

be different for every location. Therefore either a sunsynchronous orbit has to be selected or the constellation has to be composed in such a way that every location is at least covered once when the lighting conditions are sufficient to take pictures. The designer also has to take into account that if an altitude of 800 km or higher is chosen, the Van Allen belts will pose limitations to the instrument lifetime due to radiation degrading the electronics.

The sunsynchronous orbit

The sunsynchronous orbit has the distinct feature that the precession of the longitude of the ascending node is equal to the rotation of the Earth around the sun. This causes the orbital plane to always have (approximately) the same orientation with respect to the sun. Depending on the exact orientation of the orbital plane this can have several advantages. The main advantage for the instrument is that every time the instrument passes over an arbitrary point, the local time is constant. For example in a noon-night orbit, the instrument passes over a

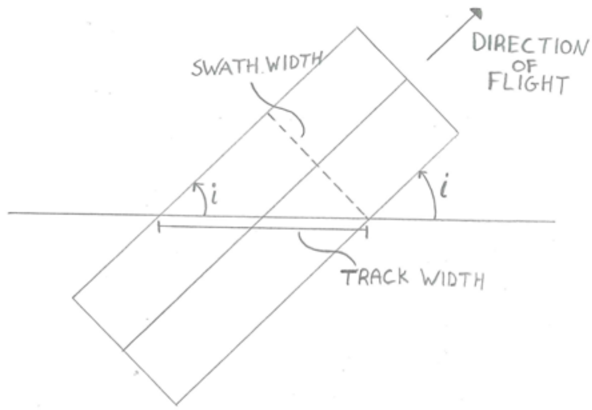

Figure 3.2: Schematic representation of the relation between track width and swath width.

location on Earth when the local time is approximately 12:00 am or 12:00 pm. This renders the images to have the same lighting conditions.

By setting equation 3.6 equal to 3.11 and solving for the inclination, the value corresponding to a sun-synchronous orbit at a specific altitude can be found. For an altitude of 540 km the inclination has to be approximately 97.55 degree. For 1440 km altitude, the inclination changes to 101.6 degree.

When considering the revisit times for these orbits, full Earth coverage will be used again. For a first order approximation on the global coverage, it is assumed that the swath width of the nadir looking instrument is 15 km at 540 km altitude and 40 km at 1440 km altitude. The track width (the width of a track with respect to the equator) is not equal to the swath width by definition. From the figure 3.2 it can be derived to be equal to equation 3.12.

$$trackwidth = \frac{swathwidth}{\sin i} \tag{3.12}$$

From equation 3.12 and the inclinations given above then follows that the track width is equal to 15.1 km for the orbit at 540 km and it is equal to 40.8 km for an orbit at 1440 km. Similar to the estimations performed for the polar orbit the revisit times can be estimated. For a sun-synchronous orbit at 540 km the orbital period equals 5734 s or 95 minutes and 34 seconds and are 2654 orbits needed for coverage of all longitudes. For the 1440 km altitude sun-sunchronous orbit, the period equals 6886 s or 114 minutes and 46 seconds. The orbital periods are obtained from equation 3.8. From this data can be derived that for a sun-synchronous orbit at 540 km a 1327/88 repeat orbit can be used, whilst for the 1440 km equivalent a 491/39 repeat orbit will give coverage of half of the longitudes.

An arbitrary Low-Earth orbit

If none of the distinct features or advantages of the polar or sun-synchronous orbit is required, another arbitrary Low-Earth Orbit (LEO) that fits the coverage requirements can be chosen. By choosing an inclination, the mission designer limits the maximum and minimum latitudes that can be pictures by the nadir looking instrument. Although global coverage is lost this way, extra coverage is gained in specific latitudes as can be seen in figure 3.3. Due to the inclination that can be chosen freely, it is possible to get streets of double or triple coverage over areas of interest, while still having a long revisit time per satellite from the repeat orbit. This can be useful if higher coverage is required for specific parts of the world.

Effect of orbits on the constellation size

As already touched upon in the discussion on orbit types, the constellation size depends on the temporal resolution needed. From the market analysis, section 2.1, can be concluded that a repeat period of approximately 30 days would be commercially viable. In combination with the discussion or orbit types this leads to conclusion that approximately 5 or 6 orbital planes are necessary.

3.1.5 Footprint area

The footprint area or also known as the Field Of View (FOV) is defined as "Area that a specific instrument or antenna can see at any instant" [19]. It is the area on the Earth that the instrument observes at a given instant.

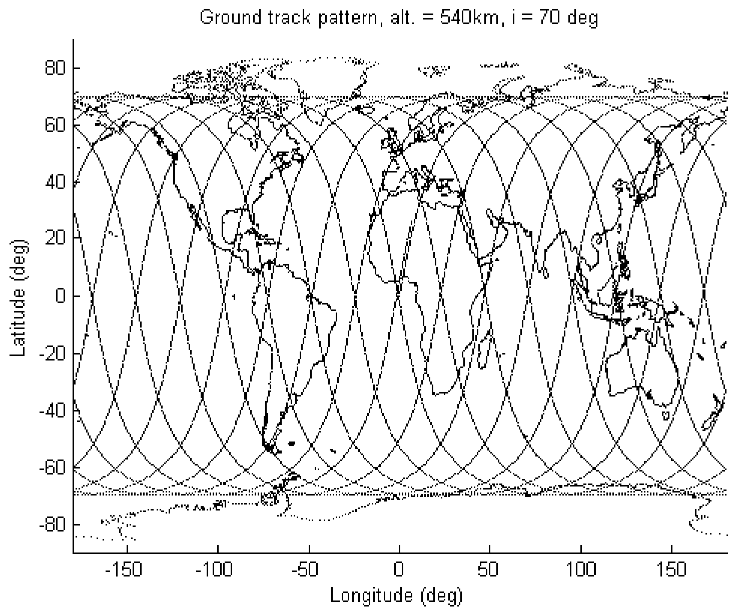

Figure 3.3: Ground track for a LEO orbit at 540 km and 60° inclination.

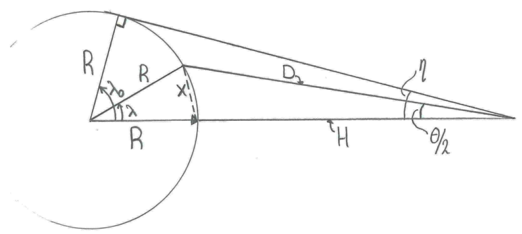

Figure 3.4: Geometrical relations for the field of view.

Using figure 3.4, equation 3.13 can be derived from simple geometrical relations.

$$x = 2R^2 - 2R^2 \cos\lambda = H^2 + D^2 - 2HD\cos\frac{\theta}{2} \tag{3.13}$$

Looking again at figure 3.4 a relationship between the slant range D and the Earth's radius R can be derived as shown in equation 3.14.

$$\frac{D}{\sin\lambda} = \frac{R}{\sin\frac{\theta}{2}} \tag{3.14}$$

Isolating equation 3.14 for D and substituting this in equation 3.13 results in equation 3.15.

$$2R^2 - 2R^2\cos\lambda = H^2 + R^2\frac{\sin^2\lambda}{\sin^2\frac{\theta}{2}} - 2HR\frac{\sin\lambda\cos\frac{\theta}{2}}{\sin\frac{\theta}{2}} \tag{3.15}$$

Using small angle approximations an equation for the Earth central angle is derived.

$$\lambda = \frac{1}{2}\frac{H}{R}\theta \tag{3.16}$$

After inserting the determined half field angle θ (1.2 °) found in the conceptual design phase and orbit height H (540 km) in equation 3.17 a half field view of about 7.5 km is calculated. For an altitude of 1440 km a half field view of 20 km is calculated.

$$F_A = H\theta \tag{3.17}$$

3.1.6 Instantaneous access area

The Instantaneous Access Area (IAA) is defined as: "All the area that the instrument could potentially see at any instant if it were scanned through its normal range of orientations" [19]. Depending on the pointing mode of the satellite, the IAA changes. For an always nadir pointing satellite the IAA is equal to the FOV. Thus for a pointable satellite the IAA has to be calculated. A relation between the orbit height H, Earth radius R and Earth central angle λ can be derived from figure 3.4. This relation is expressed in equation 3.18.

$$\cos\lambda = \frac{R}{R+H} \tag{3.18}$$

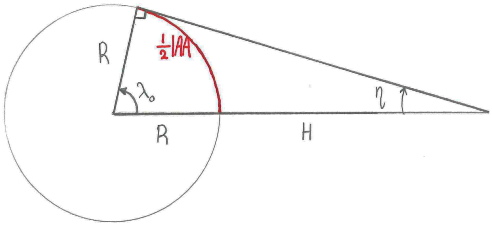

Figure 3.5: Geometrical relations for the instantaneous access area.

From figure 3.5 and again using small angle approximations it is derived the IAA can be calculated with equation 3.19.

$$IAA_{max} = 2\pi\lambda R^2 \tag{3.19}$$

Isolating equation 3.18 for λ and substituting in equation 3.19 results in equation 3.20. After inserting the known values for the Earth radius R and orbit height H in equation 3.20 an IAA of 102 x 10^6 km^2 is calculated for an altitude of 540 km and 158 x 10^6 km^2 for an altitude of 1440 km.

$$IAA_{max} = 2\pi R^2 \arccos\frac{R}{R+H} \tag{3.20}$$

3.1.7 Subsatellite point velocity

Because the satellite moves with a relatively large velocity with respect to a certain point on the ground, the exposure time of the CMOS sensor must not exceed a certain value. Since light from several points will be captured on the same pixel and therefore image blur can arise. To get an indication what the exposure time of the CMOS sensor can maximally be before the image will blur the subsatellite point velocity has to be calculated. Before this velocity can be calculated the nodal period has to be calculated first. Equation 3.21 can be used as a first order approximation for the nodal period. In where a is the semi-major axis and μ the Earth gravitational constant. At an altitude of 540 km the semi major axis is 6918 km and at 720 km the semi major axis is 7818 km. The Earth's gravitational constant μ equals 3.986x10^{14} m $\frac{m^3}{s^2}$. Inserting these values in equation 3.21 gives a nodal period of 95.4 minutes for an altitude of 540 km and 114.7 minutes for an altitude of 1440 km.

$$P_0 = 2\pi\sqrt{\frac{a^3}{\mu}} \tag{3.21}$$

Now the nodal period is known the subsatellite point velocity can be calculated. By using equation 3.22 the velocity is calculated to be 7.0 km/s at an altitude of 540 km and 5.8 km/s at an altitude of 1440 km.

$$\bar{v} = \frac{2\pi R_E}{P_n} \tag{3.22}$$

If the system aims for a ground resolution of 7.5 m the exposure time to be 0.075/7.0 = 1.1 ms for an altitude of 540 km and 0.075/5.8 = 1.3 ms for an altitude of 1440 km. If the exposure time is longer than these values there is a chance the image will blur. Because the Earth is curved in reality this calculation method can only be used for relatively small distances as a first order approximation.

3.2 The atmosphere

The optical instrument will operate on board of a satellite in a Low Earth Orbit (LEO) at 540 km. At these altitudes a noticeable atmosphere is still present, although the density is much lower than at sea level. As the altitude increases not only the density but also the composition of the atmosphere changes.

At LEO altitudes, atomic oxygen is the most notorious constituent. It reacts aggressively with many materials and degrades their mechanical and optical properties. In these LEO orbits not only the atmosphere influences the system, also the ionosphere and the magnetosphere influence the system. Highly energetic protons and electrons can damage or disrupt the electrical system. To quantify the requirements for the system related to the above mentioned effects, several empirical models are utilized. This chapter discusses the model that is used to describe the atmosphere the instrument will be facing.

3.2.1 Types of models

For the composition of the atmosphere both physical models and empirical models exist. The accuracy of the physical models is limited by the accuracy of their inputs, their scope and computational constraints. They require expert knowledge and are often more computational intensive than empirical models [22]. Because of the limited scope of the requirements discovery and the limited amount of time given an empirical model is chosen to quantify the requirements and constraints.

The model of choice is the often used Mass Spectrometer Incoherent Scatter (MSIS) model. The first version was developed by A.E. Hedin and his colleagues in 1977 and describes the neutral densities and temperatures in the upper atmosphere. The model is based on measurements with Mass Spectrometers, as the name does suggest. However, in 2001 a more advanced model was developed which includes data based on drag and accelerometer data. [23],[24],[25],[26],[27]

In figure 3.6 the composition of the atmosphere in a range of 400 to 1000 km altitude above the mean Earth surface is shown. The input parameters to NRL-MSIS-E-00 are given in the caption. Although the concentrations do decline rapidly with altitude, it can be deduced that at the reference altitude of 540 km the number concentration of atomic oxygen (O) is still in the order of 10^8 particles per cubic centimeter. The effects of these levels of atomic oxygen at relatively low temperatures (up to 500 K) will not be of direct consequence but will add up over time and can result in considerable corrosion of the system.

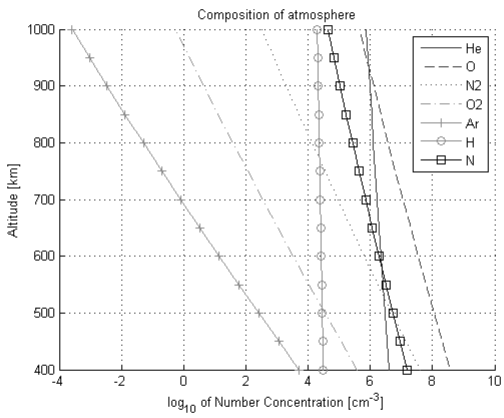

Figure 3.6: Composition of the Earth's atmosphere at 400 to 1000 km above Delft. Reference date: 127th day of the year, at 08.33 AM Universal Time (UT), F10.7 = 240 [sfu] at a 81 day average centered at day of reference date, Earth magnetic index Ap = 15 [-] (Corresponding to a period of solar maximum)

3.2.2 Accuracy of the MSIS model and safety factors

The accuracy of these models is 15-30% [28] during a normal solar cycle. During a solar storm the values may vary 100% [22].

Depending on whether the risk of compromising the mission or complete mission failure due to a solar storm is allowed, a safety factor of 1.3-2.0 has to be applied. Figure 3.6 however, does not provide sufficient information on the maximum concentrations that have to be taken into account. The local composition of the atmosphere is highly variable with time. Therefore the simulation has been extended to include a global distribution of the constituents of the atmosphere. These results are shown in figure 3.7. Because the variation over the year was found to be marginal (<2%) only the predictions for 1 January, 2001 are shown. It appears that the maximum concentration during solar maximum conditions drops slightly over the year, but this can be attributed to modeling errors. As can be seen from figure 3.7, a distinct region of high concentration just below the equator can be found. This peak region does not change much in shape and rotates with the position of the sun relative to the Earth. Although this maximum appears to be relatively local, a satellite carrying the optical instrument will pass through it multiple times a day.

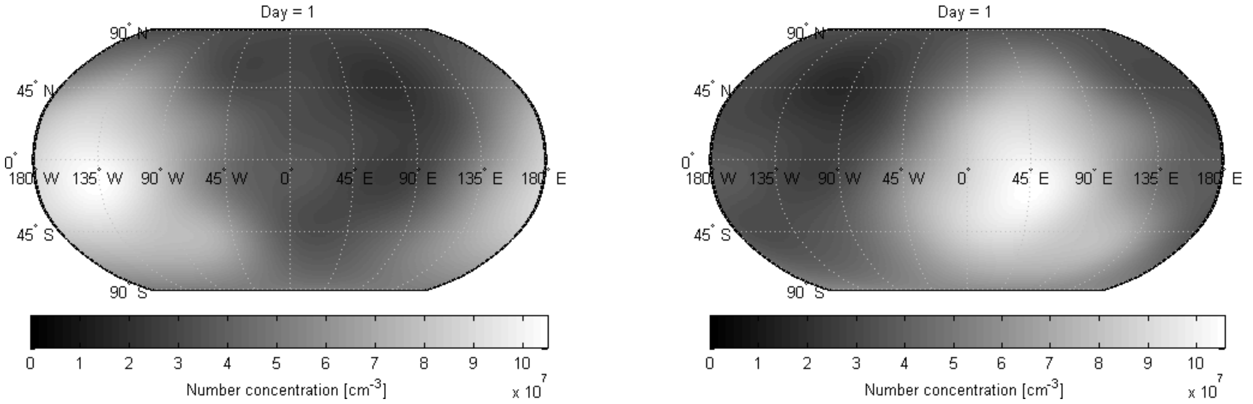

Figure 3.7: Number concentrations of atomic oxygen at the first day of the year at 43000 s UT and 86000 s UT. Ap = 15, F10.7 = 240 [sfu], the left figure is at noon, the right figure at night

The effects of the levels of atomic oxygen will be low to moderate on short term, due to the relatively low temperatures involved. In re-entry vehicles, for which the temperatures are much higher, the effect is much more pronounced. The effects on the optical instrument will be noticeable over longer timespans as the effect accumulates. A more detailed study on chemical stability of the materials used can be performed in a later stage of the design as more information on the structure is available.

Based on the current analysis the concentrations stated in table 3.1 have to be considered in material selection and the protection of sensitive components.

Table 3.1: Number concentrations Atomic Oxygen during solar maximum

Number concentration $[1/cm^3]$	1.048e+008
Including safety factor 1.3 $[1/cm^3]$	1.362e+008
Including safety factor 2.0 $[1/cm^3]$	2.097e+008

In the upcoming design phase a more detailed analysis can be carried out that includes a sample orbit and the integrated dose of atomic oxygen the instrument will have to sustain over its two year lifetime. From that more detailed figures for corrosion and degradation can be given.

Although the levels of atomic oxygen are now estimated, more work is still to be performed. As mentioned earlier the space environment is composed of much more than just the Earths atmosphere. For example also the levels of particle radiation will have to be considered, just as the Van Allen Belts and temperature differences over the instrument. Using appropriate models other requirements and constraints can also be quantified with an admissible level of accuracy.

3.3 Radiation environment for differential altitude considerations

Next to the thermal protection of an arbitrary system, one will need to consider another source that makes the space environment so hostile to occupy, namely the various radiation sources present. With the determination of a valid range of orbits for which the market desires are satisfied, a detailed analysis of the altitude variation with respect to the cumulative radiation dose can be performed. This cumulative dose will degrade certain components within the optical and electrical subsystems.

3.3.1 Structural limiting radiation sources

A distinct number of radiation sources need to be considered, whose contributions to the radiation environment are significant and pose restriction onto the instrument. Following these criteria, the following radiation sources are being evaluated:

- **Trapped proton and electron fluxes:** The magnetic field that protects the Earth from harmful radiation also captures charged particles in the so-called Van Allen radiation belts. Within this torus of energetic parts one can identify an inner ($\approx$ 1 Re - 1.5 Re) and outer radiation belt ($\approx$ 3 Re - 10 Re), for which the composition changes. The inner belt consists of a combination of charged protons and electrons, whereas the outer belt only carries highly charged electrons. The absence of protons in the outer belt is most likely to be caused by the fact that the magnetic fields near the inner belt is much stronger than

those near the outer belt.
The most characteristic occurrence of the Van Allen belts is the South Atlantic Anomaly (SAA), which is a highly energetic region at a relatively low altitude. This occurrence is caused by the misalignment of the Earth's rotational axis and the center line composing the locus of the Earths magnetic field by at least 11°. This inevitably causes the center of the geomagnetic field to shift by more than 500 km and the particles in one of the rings within the inner region to be present at very low altitudes as is shown in figure 3.8.

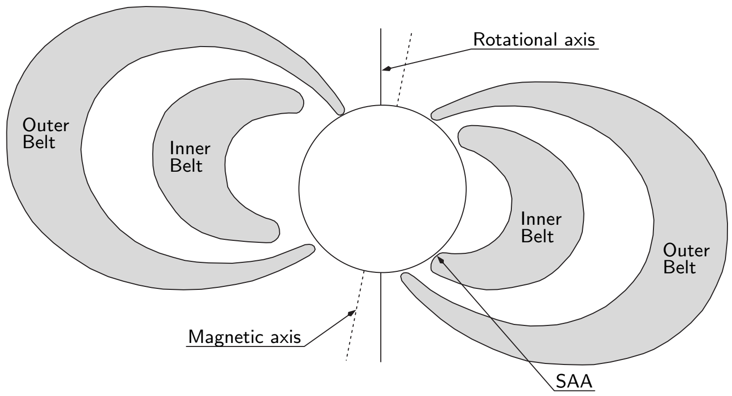

Figure 3.8: The Earth's radiation belts and the South Atlantic Anomaly (SAA) [29]

- **Bremsstrahlung:** The next radiation source that needs to be considered is the Bremsstrahlung, which is the shielding induced radiation. Bremsstrahlung describes the law of conservation of energy [19] when an electron impacts on the shielding applied to the instruments. As the particles decelerate, by either a collision with one of the atoms of the shielding material or by a particle's Lorentz force (F_L) induced deceleration, a photon has to be released in order to satisfy the condition of energy equivalence. For high-energy particles and high-density shielding this photon will be in the X-ray spectrum, thus introducing another degradation source as provided by [30].

- **Solar energetic proton events:** As described in [19]: "Solar particle events (SPEs) occur in association with solar flares". This indicates that during a solar flare, high increases in flux of energetic particles are observed within the range of approximately 1 MeV to above 1 GeV. Proton and electron particle events are most common, however as only particles with high (relativistic) energies are capable of penetrating shielding shortly after such an solar event, proton particle events will be considered. Lower energy particles are considered to be slowed down by the diffusion within the corona of the sun or even reflected. Diffusion within the interplanetary medium is being neglected. The time evolution of such an event is given in figure 3.9 and is dominated by the actual energy levels of the particles at hand.

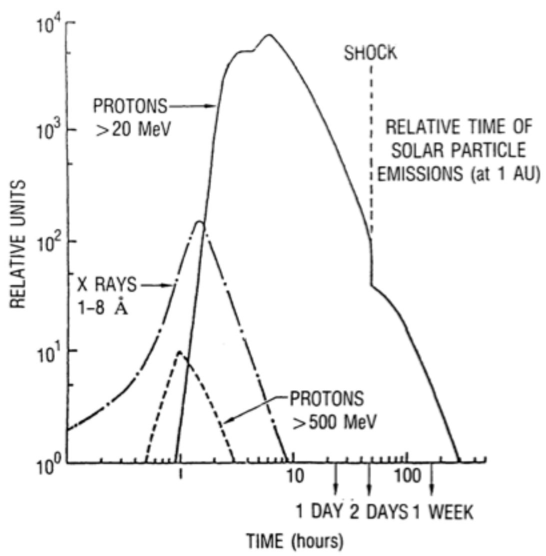

Figure 3.9: Time evolution of a solar energetic proton event [19]

The sun follows a certain cycle with respect to the external activity, also known as the cycle between sunspot maximum and sunspot minimum. As the sun enters a period of four years around solar maximum, a peak in the frequency of proton events may be observed. During this instantaneous increase in frequency a corresponding increase in the number of protons impacting on the outer surface of the satellite's bus and the additional shielding accompanying the instrument will be noticed.

3.3.2 Models of the particles flux distribution within the outer atmosphere

The environment under consideration needs to be defined in order to choose an appropriate model to describe that environment. From the market analysis and optical design it becomes apparent that the (circular) orbits vary from 540 km above the Earth's surface up until 1440 km. The discussion of the Van Allen Belts (3.3.1) reveals that the altitude range under consideration only occupies the inner Van Allen radiation belt. Because of the low altitude of this particular belt and the shielding by the outer belt, the inner belt is hardly affected by the solar wind, resulting in a very stable region.

The trapped proton and electron flux distribution through the inner radiation belt is modeled by the AP8 and AE8 radiation models respectively, which are well-accepted radiation environment models developed by NASA and widely used within the industry. The models as described in [31] offer an empirically obtained dataset as a function of the particle energy and the corresponding orbital McIlwain coordinates. The McIlwain coordinates describe a location in space based on the radial distance L and the magnetic field strength B. The radial distance may be described as the distance in Earth radii at which a magnetic field intersects with the geomagnetic equator when the Earth magnetic field is assumed to be a perfect dipole, whereas the B describes the location along the magnetic field line itself. This coordinate system still allows for an improved location determination within the geomagnetic field if the magnetic field is not considered to be a perfect dipole.

The radiation models as presented by NASA are available for both solar minimum and solar maximum conditions with an epoch of 1964 and 1970 respectively. This allows for a comparison of both models and will reveal limiting conditions with respect to radiation doses as experienced by the system. Because of the empirical nature of the four datasets (AP8MAX, AP8MIN, AE8MAX, AE8MIN), one will need to interpolate between the McIlwain coordinates as presented within the data. This will introduce interpolation errors, especially at the outer boundaries ($\leq L \approx 1.1$ and $\geq L \approx 10$) of the available information and near the SAA. Knowing this, ESA developed an improved model for the proton flux distribution for low altitude orbits, called the PSB97 model. This particular model uses data retrieved from both the SEMPEX and PET satellites such that it is primarily applicable to satellites with an orbital altitude lower than 600 km.

The results obtained from the AP8 and AE8 models for the 1440 km altitude orbit, as well as the results following from the combination of the SEMPEX/PSB97 radiation model and the AE8 model for the 540 km orbital boundary, describing the trapped proton and electron flux (per unit energy) in solar maximum are shown in the electronic supplement.

As already discussed, the solar proton fluence (flux integrated over a period of time) should also be observed, since the highly charged protons emerging from solar flares are capable of penetrating radiation shields, thus posing severe design restrictions. The solar proton model that is being used in order to compute the total proton fluence is the so-called ESP (worst case) model, which is capable of modeling a range of years with a significantly high solar activity, thus introducing a limiting case with respect to the proton flux or fluence. The fluence of solar protons for both the 1440 and 540 km altitude orbits is also shown in the electronic supplement.

3.4 Protection against space debris

Not only functioning satellites orbit the Earth. Most satellites are not operational anymore after a few years but their remains can stay in orbit for hundreds of years. After a while they start losing small components. There are also naturally occurring objects in space that are too small to detect. These tiny objects could severely damage the satellite. The representative velocity at low Earth orbits is about 10 km/s. This means that even very small objects have a lot of energy. Shielding from these objects can only be done up to a certain extent. It will be cheaper to replace satellites destroyed by collisions, especially given the nature of the satellite. Also because the spacecraft is so small there is a very small chance of a significant hit. [32] [33]

3.4.1 Risk of collision with space debris

The LDEF experiment gives an indication about the severity of the problem [34]. The number of impacts with an object diameter of more than 1 millimeter in 2 years is small. A SPENVIS extrapolation for 2016 at 500 km (see figure 3.10) with sun synchronous inclination estimates the number to be about $8 \cdot 10^{-3} impacts \cdot m^{-2} \cdot yr^{-1}$.

The chance of such a hit during a 2 year lifetime is very small because of the cross section of the reference satellite. Atmospheric drag will reduce the amount of objects at lower altitudes. Hence the satellite will have less chance of collisions if it is below 500 km altitude. It does not really matter if the orbit is above 500 km. The amount of debris between 500 km and 1440 km remains the same regardless of the orbit.

Figure 3.10: SPENVIS: Nasa-90 model: expectation value of number of encounters per square meter

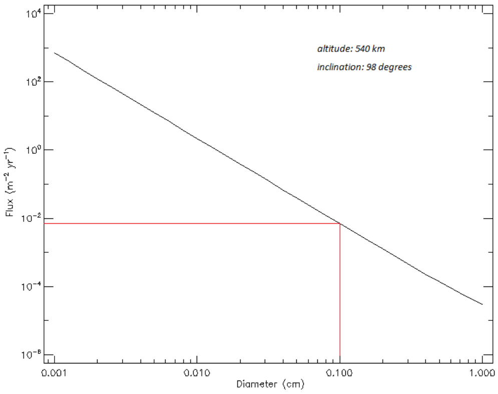

3.4.2 Vulnerability to space debris

Something that also can be seen from figure 3.10 is that the chance of a hit by a particle of around one hundreds of a millimeter is much larger. This particle size cannot penetrate the shell of the instrument, but the average number of hits during the lifetime is about 30 and therefore significant. This will damage the surface of the satellite. If an aluminum particle hits the satellite with 10 km/s relative velocity and has a diameter of 0.025 mm it will not penetrate the outer shell. This is given by equation 3.23 and 3.24. [35]

$$P_\infty = 5.24 \cdot d^{19/18} \cdot H^{-0.25} \cdot \left(\frac{\rho_p}{\rho_t}\right)^{0.5} \cdot \left(\frac{V_n}{C}\right)^{2/3} \tag{3.23}$$

$$t = 2.2 \cdot P_\infty \tag{3.24}$$

In 3.23 H is the Brinnel Hardness which is 150 for aluminum [36], C is the speed of sound in the target, V_n is the reference speed, d is the projectile diameter in cm, ρ_p is the projectile density where ρ_t is the target density and P_∞ is the penetration depth into a semi infinite block of target material. Equations 3.24 and 3.23 are for a single layer shield. The first equation which relates the penetration depth of debris into a target of semi infinite depth. The shell has no infinite depth, the second equation corrects for that. By combining these two equations one gets an approximation how the shield reacts to the incoming debris. Looking back at figure 3.10 the chance of this happening is low. The chance of this happening in the lifetime of one satellite is about 1 %. This means that when 100 ANT's are launched most likely only one or two will have their outer shell penetrated. A shell penetration does not necessarily lead to mission failure. If the instrument is hit by an object that can penetrate the shell but is still small it will vaporize due to the concentration. The products of this vaporization are not likely to damage the mountings and they cannot reach the sensitive components directly. In case protection is deemed insufficient the inner Super Invar® wall can be made completely closed creating a very effective 2 layer shielding. In the current design the inner walls are cut open to save mass without taking into account protection because the chance of a fatal hit is very small during a 2 year lifespan. This should change if the lifetime of the instrument needs to be significantly longer.

Although the chance for a shell penetration is low, if an object does not penetrate the outer wall it still causes damage. The cavity resulting from the impact in the material will increase vulnerability to atomic oxygen and the reflective properties of the material will change, with consequences for the thermal stability of the instrument. This vulnerability means that the cavity created by the debris will erode faster than the rest of the surface. For aluminum this is not a problem because atomic oxygen will form an oxide layer on the aluminum and erosion will stop.

Chapter 4

Optical design

When designing an optical system for a nanosatellite, one of the most difficult challenges that needs to be faced is to fit a long focal length within the small volume available. To tackle this problem, three concepts were developed to determine the optimal way to bend the light path. Since the concept study was aimed at choosing a light path, the sensor and the focal length that each system would be designed for were determined separately.

In this chapter, the complete design process of the optical system will be described, starting from the sensor selection and the concept trade-off and ending with the final optical design and an analysis of the optical performance. To provide the reader with necessary background knowledge to fully understand the design process, several sections have been included to provide some background knowledge on optics. Additionally, the thermal optical stability of the design as well as the effects of production tolerances on the optical performance have been analyzed.

4.1 Sensor choice

One of the most important elements needed to capture an image is the sensor. In this section this subsystem will be analyzed. First of all, two different sensor types will be looked at, namely CMOS and CCD. After that the requirements a sensor must comply with in order to be useful in the design are determined and finally the sensors currently available in the market will be looked at.

4.1.1 CCD vs CMOS

There are two different types of image sensors available, namely CMOS (complementary metal oxide semiconductor) and CCD (charge coupled device). The main difference between the two sensor types lies in the way in which the sensor is read out and the data is processed. In a CCD sensor every pixel charge is transferred through a limited number of output nodes, where it is converted to a voltage. This voltage is led into the circuit board of the camera, where most imaging functions take place, such as the amplification of the signal as well as the analog to digital conversion. In a CMOS sensor on the other hand, these imaging functions take place on the sensor chip itself. Every individual pixel has its own charge to voltage conversion [37].

Traditionally CCD sensors used to offer a much higher image quality than CMOS, but they were more expensive and used more power. CMOS sensors, on the other hand, were mainly used in low cost, low power applications. Due to changes in the manufacturing processes, though, the difference between the two sensor types became smaller. CMOS sensors can now match the image quality of CCD sensors and are used in for many high performance cameras, such as several professional digital SLR cameras. The power requirements and production costs of CCD sensors, on the other hand, have decreased to the point where they can now be found in low-cost, low-power cell phone cameras.

However, all other things being equal, CMOS sensors have kept their edge with respect to the power consumption [38]. Since the power budget is limited due to the fact that the entire satellite must be powered using solar panels and a large portion of the available power must be reserved for the downlink, a low power sensor should be chosen. Therefore, a CMOS sensor will be selected.

4.1.2 Sensor requirements

In this subsection, the various requirements that a sensor must fulfill in order to be a viable option will be analyzed. Amongst other things, the pixel pitch, the amount of pixels and the radiation hardness will be discussed.

4.1.3 Pixel pitch

The pixel pitch is the distance between two adjacent pixels. When the focal length and optical quality of a lens remains equal, one can say that the closer the pixels are spaced, the more detail can be picked up. Since long effective focal lengths are hard to obtain given the volume restrictions, close pixel pitches are required to make sure that the ground resolution of 7.5 meters per pixel can be reached.

A downside of a small pixel pitch, however, is that when pixels are placed closer to one another they also become smaller. This results in more noise and a loss of dynamic range [39]. Hence, the pixel pitch must be chosen in such a way that the ground resolution can be reached, without compromising the image quality.

In figure 4.1 it can be seen how the maximum signal to noise ratio drops as the pixel pitch becomes smaller. The same happens to the pixel full-well capacity. This value gives an indication for the maximum brightness level that a pixel can register before it is saturated and it is therefore one of the most important things determining the dynamic range of the sensor. The figure shows that the performance start to degrade rapidly when pixel pitches get smaller than 3.5 micrometer.

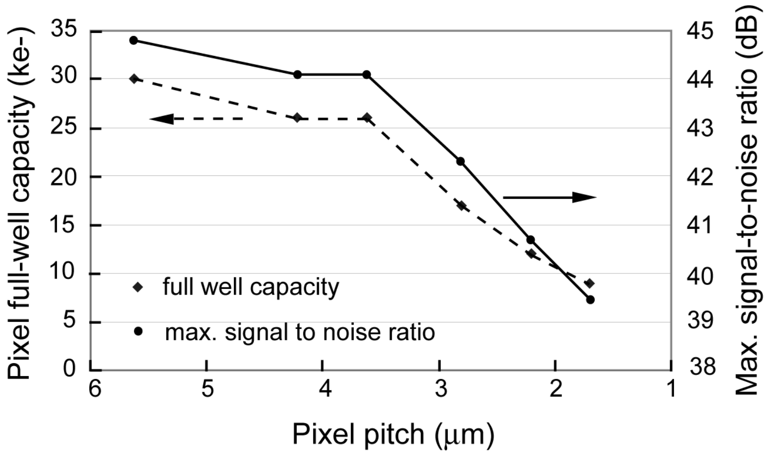

Figure 4.1: The effect of smaller pixel pitches on the full-well capacity and maximum signal to noise ratio

An alternative to finding a sensor with an optimal pixel pitch is to pick one that has a pixel pitch that is significantly smaller. A technique called pixel binning can then be used to reach an acceptable image quality. With this technique, the data captured by a group of adjacent pixels is merged, which leads to a higher signal to noise ratio at the cost of resolution. An advantage of this technique is that the sensor has more pixels than required, which means that there is a degree of redundancy that may, for instance, be useful when pixels are damaged by radiation.

Amount of pixels

By dividing the required 10 km field of view by the 7.5 m ground resolution per pixel the minimal amount of pixels necessary to achieve the ground resolution is found to be 1334 by 1334 pixels. A sensor should have at least this amount of pixels to provide the required field of view. More pixels will allow for larger fields of view, but it may become more difficult to develop an optical system that can deliver sharp results in the corners of the frame.

Monochrome vs color

Designing an optical system to capture the complete spectrum of visible light is very challenging, particularly on such a small scale. Therefore, it was decided that the system would be designed and optimized for a small range of wavelengths, which would be selected by using a filter. If a color sensor would be used in this case, the Bayer filter (the filter that directs light of different wavelengths to different pixels) will result in only a portion of the pixels being actually used. Therefore, primarily monochrome sensors will be looked at. An additional advantage is that such sensors do not suffer from the loss of light that is generally associated with Bayer filters.

Radiation hardening

While a sensor is in orbit, it is exposed to a significant amount of radiation. This can cause damage to the sensor as well as a loss of performance. The damage caused by radiation that can occur in orbit can typically be attributed to two main sources, namely the total ionizing dose effects and the single event effects. The latter are effects caused by high energy particles, that range from slight errors in the readout of the sensor to the destruction of a pixel. Beyond shielding the sensor, few measures can be taken to protect the sensor from this effect.

The total ionizing dose effects constitute the total damage caused by ionizing radiation. When a CMOS sensor is exposed to radiation, mobile electrons are created in the insulating silicon oxide layers present in the device. These electrons leave electron holes in this layer, which causes electrical charges to be trapped in the oxide layer. This raises the dark current of the sensor - the signal that is present even when no light is captured - and, in the long run, may cause failure of individual pixels or even the sensor itself [40].

This effect is particularly pronounced when the silicon oxide layer is thick. The thicker the layer, the more holes can be trapped and thus the larger the radiation induced charge will become. The effect of the total ionizing dose can thus be mitigated significantly by reducing the thickness of the silicon oxide layer [41].

However, reducing the oxide layer thickness, can cause several problems. Leakage currents may increase dramatically and the quantum efficiency of the sensor may be reduced [42]. Therefore, state of the art production processes are needed to reduce the oxide layer thickness without compromising the image quality, which raises the price of a sensor substantially.
One may wonder whether such sensors are worth the costs. NASA has performed radiation tests on several commercial consumer grade sensors, such as the Aptina MT9D131 [43]. In the test, the sensor showed an excellent imaging performance following an exposure to radiation of 10 $krad$. The radiation did cause malfunction of several pixels as well as a significant increase in the noise levels, but images remained usable. However, the same report mentions that the sensor is less useful for scientific purposes or in situations where the radiation exceeds the level of 10 $krad$. Thus, it would be best to invest in sensors that are build according to production processes that increase the radiation hardness of the sensor, provided that the cost of the sensors remains acceptable.

4.1.4 Available sensors

In this subsection, sensors that are currently commercially available are looked at. In table 4.1 several monochrome CMOS sensors are listed. To keep the table concise, for each manufacturer, only the most interesting sensors given the mission constraints are listed. The data has been obtained using data sheets, pricing information at various online stores and extensive e-mail correspondence with the manufacturers and/or their distributors.

Table 4.1: CMOS sensors currently available

Manufacturer	Type	Pixel Pitch [μm]	Resolution [pixels]	Radiation Hardened	Price
Aptina	MT9P031	2.2	2592 x 1944	No	€15,40
CMOSIS	CMV4000	5.5	2048 x 2048	Yes	€300
Cypress	CYII4SM6600	3.5	2210 x 3002	No	€321
Cypress	VITA 5000	4.8	2592 x 2048	No	?
Cypress	Star-1000	15	1024 x 1024	Space Grade	€38,028
E2V	EV76C560BB	5.3	1280 x 1024	No	?
E2V	CIS101	14.81	1415 x 1430	Space Grade	?
Fairchild Imaging	Scientific CMOS	6.5	2560 x 2160	Yes	TBA
Omnivision	OV10131	4.2	1280 x 800	No	€20
Photonfocus	A2080-160	8	2080 x 2080	Yes	?
Viimagic	9215	5	1968 x 1108	No	<€800

Two space grade sensors are included in the table, namely the STAR 1000 by Cypress and the CIS101 by E2V. Although the performance of these sensors would be affected the least by radiation, the two sensors do not offer the pixel pitch needed to reach the required ground resolution. Additionally, the price of the STAR 1000 is much too high compared to the total budget of this project. Although the price of the E2V sensor is currently unknown, its price is expected to be in the same order of magnitude.

Photonfocus and CMOSIS produce their sensors using a state of the art process in which the oxide thickness is kept at a minimum. As said in the previous subsection, this improves the radiation hardness of their sensors while retaining a high quantum efficiency. Neither sensor is marketed as being space grade or even radiation hardened, but both manufacturers expect their sensors to perform well when exposed to radiation. On the Photonfocus sensor several radiation test have been performed by customers. It was found that the sensor could not be damaged by radiation. There was, however, an increase in the dark current, but this occurs with any CMOS sensor, even space grade ones such as those by Cypress [44].

The CMOSIS sensor has been tested for radiation hardness by the department of electrical engineering at Delft University of Technology [45]. According to the test results the sensor can be used when the radiation dose stays below 100 $krad$. However, with increasing radiation, the readout speed of the sensor has to be

increased to limit the amount of noise and dark current.
The CMOS sensor by Fairchild Imaging also has a high radiation tolerance [46]. However, as was learned from an e-mail correspondence with the manufacturer, this sensor will not be sold separately until March 2012.

The other sensors are not build using technologies improving the radiation hardness or no information could be found that suggests otherwise. Given the price point of the other two Cypress sensors, it can be suspected that the sensors may be quite radiation tolerant. However, the company has up till now not responded to any inquiries regarding this subject, possibly because the image sensor division of Cypress has just been sold to ON Semiconductors.

Several sensors in the list do not meet the resolution requirements that were stated earlier. Removing these from the list, as well as the sensors that are too expensive, a new table can be created. In table 4.2 possible candidates that were selected from the table 4.1 have been listed and more characteristics of the sensors have been added.

Table 4.2: CMOS sensors currently available

Manufacturer	Type	QE x FF	Sensitivitity $[V/lux.s]$	Dynamic Range $[dB]$	Power $[mW]$
Aptina	MT9P031	?	1.4	70.1	381
CMOSIS	CMV4000	60%	5.56	60	600
Cypress	CYII4SM6600	25%	2.01	?	190
Cypress	VITA 5000	52%	60	No	600
Photonfocus	A2080-160	>30 %	?	60	TBD
Viimagic	9215	<55 %	6	60	1100

In the table, the product of the Quantum Efficiency and the Fill Factor (with microlenses) is given. These figures give a good indication of the portion of the incoming light that is actually registered by the sensor [47]. The power consumption given is only applicable if the sensor is used at its maximum performance, which occurs when the maximum read out speed is used.

Note that the data is not complete. This has several reasons. First of all, not all manufacturers have included the data required in their datasheet. Secondly, some companies will only provide datasheets after a non disclosure agreement has been signed (after which publishing the data in this report is out of the question). Finally some companies express sensor characteristics such as sensitivity using vastly different methods, which makes comparison between manufacturers rather hard.

Looking at the data in the table, it can be concluded that the CMV4000 sensor by CMOSIS, which is shown in figure 4.2 is currently the best choice for the system. It has the pixel pitch that is required and the resolution is more than large enough. Furthermore, the sensor has a high sensitivity and it easily fits the budget. The sensor is also radiation tolerant due to the production process that has been used. The power consumption may be on the high side, although it is not nearly as high as that of the Viimagic sensor. However, according to the datasheet of the sensor, the power consumption is significantly lower if slower readout speeds are used. Finally, the shape of the sensor array is a square, which means that optimal use can be made of the image circle created by the optical system. For the sensor to perform optimally the electronic subsystem should be breadboarded to ensure good interoperability and correct calibration is essential for operation with sufficient quality.

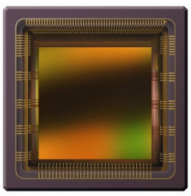

Figure 4.2: The CMOSIS CMV4000

4.2 Focal length and field of view

Now that a sensor has been chosen, the necessary focal length that the system needs to be designed for can be computed. To do so, paraxial lens equations can be used. When such equations are used, it is assumed that all angles are considered to be negligibly small, which is considered to be valid for the altitude at which most

Earth observation satellites are located.

An equation with which the required focal length can be computed using the altitude of the satellite and the pixel pitch of the sensor can be derived from the first-order lens equation as shown in equation 4.1.

$$\frac{1}{f} = \frac{1}{s} + \frac{1}{s"} \tag{4.1}$$

Where f is the focal length needed for a certain object distance s and image distance $s"$.

As the image distance is yet unknown, the concept of *magnification* is introduced. Magnification can be seen as the creation of an imaginary image in order to support the focal length of the system. The magnification is described by the following relation:

$$m = \frac{s"}{s} = \frac{h"}{h} \tag{4.2}$$

Where $h"$ is the height of the image and h the altitude of the satellite. The way magnification can be used to shorten the focal distance can be seen when substituting equation 4.1 into 4.2. The result can be seen in equation 4.3.

$$f = s'(m+1) \tag{4.3}$$

The focal length can now be found by applying another substitution of equation 4.2 into equation 4.1. The resulting expression is found in equation 4.4.

$$\frac{1}{f} = \left(1 + \frac{h}{h"}\right)\frac{1}{s} \tag{4.4}$$

Using s = 540 km, h = 7.5 m and h" = 5.5 μm the focal length f is determined to be f = 0.4032 m, or approximately 400 mm. Thus, concepts will be developed that support a focal length of 400 mm.

Since the selected sensor has a resolution of 2048 by 2048 pixels, it follows that the field of view that is covered by the system is approximately 15 by 15 kilometer. This field of view is larger than the required 10 by 10 kilometers, which is a good thing. A larger field of view means that a lot less satellites are needed to obtain the coverage and temporal resolution required for the product to be competitive in the market. Additionally, a larger field of view means that requirements for the pointing accuracy of the satellite carrying the optical system may be less strict, since the odds that the target to be photographed is missed are reduced substantially when the satellite covers a larger region.

Even though it is possible to only use the center part of the sensor, all optical concepts will be designed to support the full field of view for the reasons stated above.

4.3 Evaluation of optical performance

When designing an optical system for an Earth observation satellite, the most important goal to strive for is to make a system that can deliver the sharpest images possible. Therefore, it is very important to have an understanding of how such a high level of sharpness may be achieved.

In this section several optical phenomena that can degrade the image quality, also known as aberrations, will be described. Secondly, several useful tools are described which may be used to evaluate the optical performance of a system. These tools are very helpful in the process of improving and optimizing the optical system.

4.3.1 Aberrations

When light originating from a single point source in the object plain would pass trough a perfect lens, all light would be focused onto a single point on the image plain. Perfect lenses, however, do not exist. Optical phenomena known as aberrations cause light originating from a single point to be spread out over a larger region, which induces blur in the image. The key to a successful optical design is to make sure that these aberrations remain within bounds so that the image remains sharp.

There are several types of optical aberrations, that each have different causes and different effects on the final image. The following aberrations will be discussed in this section: Spherical aberrations, Coma, Astigmatism, Chromatic aberrations, Field Curvature and Diffraction.

Spherical aberrations

Spherical aberrations occur when light passing through the center of a lens is not focused on the same location as the rays passing through the edge of the lens [48]. This phenomenon is illustrated in figure 4.3. The exaggerated figure shows that light passing through the edge of the lens is focused on a location in front of the theoretical (or paraxial) focal point, which induces blurriness in the image.

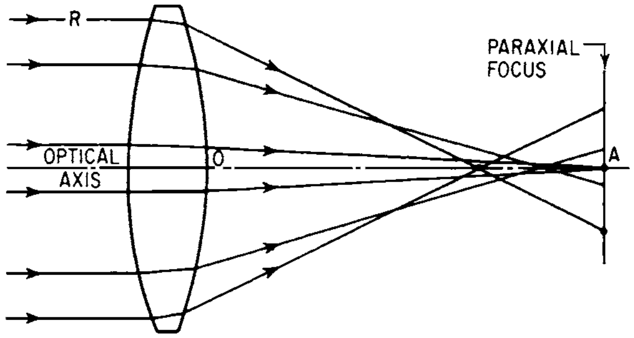

Figure 4.3: Spherical Aberration (image source: [49])

The lens shown in figure 4.3 is a positive lens; a lens for which parallel light rays passing through the lens will converge. For such lenses, light passing through the edge of the lens will be focused on a position in front of the paraxial focal point. This is called undercorrected spherical aberration. For negative lenses, on the other hand, light passing through the edge of the lens is focused behind the paraxial focal point, which results in overcorrected spherical aberration.

The amount of spherical aberration which is present in an image is a function of the lens shape and the object distance. In general, it can be said that lenses with larger curvatures are more prone to spherical aberrations. Additionally, when focusing on an object at infinity, meniscus lenses have much more spherical aberrations than plano-convex lenses [49]

There are several ways to reduce spherical aberrations. First of all, a lens shape should be chosen such that aberrations remain limited. Secondly, combinations of positive and negative lenses can be used in such a way that the undercorrected spherical aberration resulting from the use of a positive lens is corrected by the negative lens. Finally, spherical aberrations can be reduced by using a field stop to block light passing through the edges of the lens is blocked.

Coma

Another type of optical aberration is coma. Coma occurs when light rays originating from a source away from the optical axis are focused on a different heights on the image plane. Light going through the center of the lens is focused on a single point, but light going through the edges of the lens is spread out over circular patterns either towards or away from the optical axis, as is illustrated in figure 4.4. As a result, imaging a single point source will result in a point with a comet-like tail, which is what gave this type of aberration its name [49]. The effect generally does not occur in the center of the image, but it becomes more pronounced towards the edge of the frame.

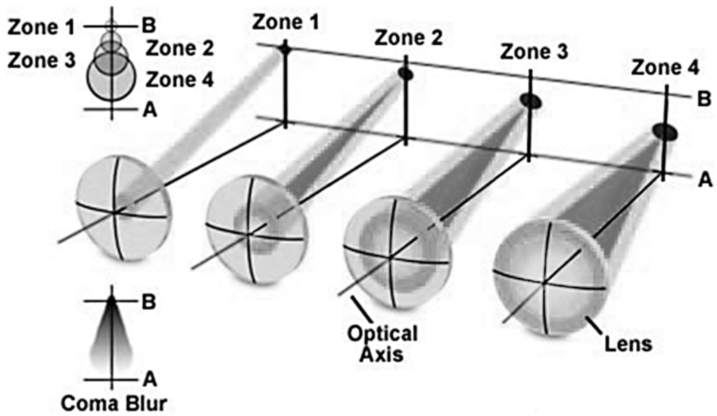

Figure 4.4: Coma (image source: [48])

Coma is often considered to be one of the most problematic aberrations, because it causes asymmetric blur in an image. It should therefore be corrected as much as possible. Like spherical aberration, coma can be reduced by using multiple elements or by using a field stop in such a way that light passing through the edge of the lens is blocked.

Astigmatism

Before discussing the concept of astigmatism, first the difference between the tangential and the sagittal plane must be discussed. A tangential plane is a plane which includes the optical axis, the centerline of a lens, and the point on the object plane from which the light rays originate. A sagittal plane, on the other hand, is perpendicular to the tangential plane.

Astigmatism occurs whenever light rays in the tangential plane are focused on a different location than light rays in the sagittal plane. This phenomenon is illustrated in figure 4.5. In the figure, light rays in the tangential plane are focused on a location in front of the light rays in the sagittal plane.

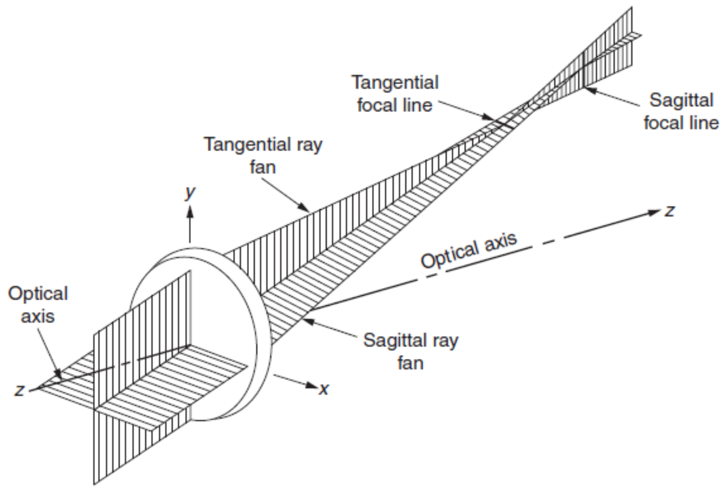

Figure 4.5: Astigmatism (image source: [49])

Astigmatism generally does not occur in the center of the image, but the effect gets worse towards the edge of the frame, where the aberration generally result in elliptical blur patterns.

Field curvature

In a well corrected optical system, light rays from any point in the object plain is brought into focus on the image plane. When field curvature occurs, this is no longer the case as off axis light is brought into focus in front or behind the image plane. This type of aberration is an inherent property of lens systems and is called field curvature.

Field curvature can occur in two directions. If light originating from off axis points is focused in front of the image plane, the field curvature is inward curving, while if the points are focused behind the image plane, the field curvature is said to be backward curving. Inward curving field curvature is often caused by positive lenses, while backward curving field curvature is caused by negative lenses. The aberration can therefore be corrected by using combinations of these lens types.

Chromatic aberration

Chromatic aberrations are a result of the fact that the index of refraction of optical materials varies with the wavelength of light. In general the index of refraction becomes higher for shorter wavelengths. The result of this is that blue light is brought into focus closer to the lens than red light. The distance along the axis between the focus points for the two colors of light is the longitudinal axial chromatic aberration as is illustrated in figure 4.6

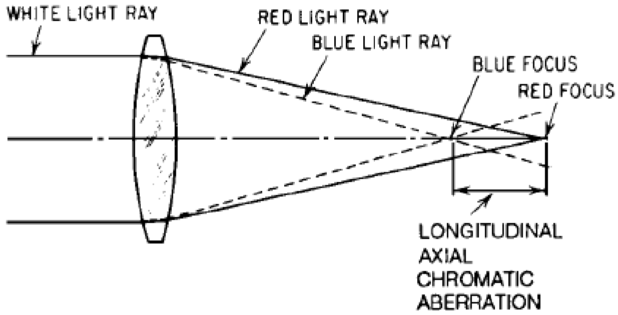

Figure 4.6: Longitudinal chromatic aberration (image source: [49])

In full-color images, longitudinal chromatic aberration generally shows up as a purple-ish halo around edges, when the image plane is located on the focus point of green light. This is caused by the blurry images which are created by the blue and red light. When light is captured using a monochrome sensor, chromatic aberrations induce additional blur to the image.

Moving away from the center of the image, an additional chromatic aberration, known as lateral chromatic aberration, may be present. This is caused by the fact that different colors of light originating from an off axis point are projected onto the image plane at different heights. Like longitudinal chromatic aberrations, lateral chromatic aberrations will cause colored halos around edges.

Chromatic aberrations can be corrected by combining positive and negative lenses made from different optical materials. A common combination of lenses that is often used to correct chromatic aberration is an achromatic doublet. This combination is made from a positive lens made from a crown glass and a negative lens made from flint glass. A crown glass has a low refractive index, while a flint glass has a high refractive index. The combination of the two types of glass, as well as the fact that one lens is positive and the other negative, means that chromatic aberrations resulting from the first lens are canceled out by those resulting from the other lens.

Diffraction

The phenomenon of diffraction can be described as the spreading out of light waves as they enter a small opening, which induces a blur in the image. Diffraction ultimately limits the detail that can be resolved by an optical system [49]. While the aberration described before in principle can be corrected, this is not the case for diffraction. The only way in which the effect of diffraction can be reduced, is by enlarging the size of the aperture of the system or increasing the size of the field stop. Since aberrations like spherical aberration and coma may be mitigated by using smaller field stop sizes, a trade-off needs to be made to determine the optimal stop size. Generally, the image quality at the edges of the frame, where many aberrations are more prominent, will improve when smaller stop sizes are used. The image quality in the center of the frame will often drop as small stop sizes are used.

A system is said to be diffraction limited if all aberrations have been corrected to such an extend that the spatial resolution that can be accomplished is limited only by the effect of diffraction. For such systems, the best ground resolution that can be obtained is given by formula 4.5.

$$d = 1.22\frac{\lambda H}{D} \tag{4.5}$$

In this equation, which is called Rayleigh's Criterion, λ is equal to the wavelength, H is the height above the ground, D is the diameter of the aperture of the lens and d is the smallest distance on the ground that can be observed.

4.3.2 Evaluation of optical performance

Throughout the process of designing an optical system, it is essential to be able to evaluate the optical performance of the system. Only then can it be verified if changes that are made to the design have the desired effect. One of the best ways to do this job is to model the system in a raytracing program. Most of these programs produce graphs which give values for the optical aberrations present in the optical system under consideration. This section will explain the way in which the graphs should be interpreted.The graphs have been made in a professional raytracing program called Code V. The example lens is a simple 100 mm doublet as shown in figure 4.7.

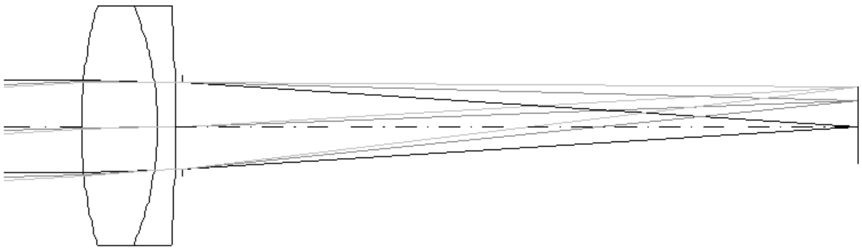

Figure 4.7: The achromatic doublet that will be used in the examples.

Ray intercept curves

The ray intercept or H'-TAN(U') curve is shown in figure 4.8. The curve is a plot of the height (H') at which the rays hit the image plane vs their slope with the optical axis (TAN(U')) as they leave the last lens. According to [49] (pag. 94) *The shape of the intercept curve not only indicates the amount of spreading or blurring of the image directly, but also can serve as a diagnostic to indicate which aberrations are present.* Why this is the case will be discussed briefly in the remainder of this section.

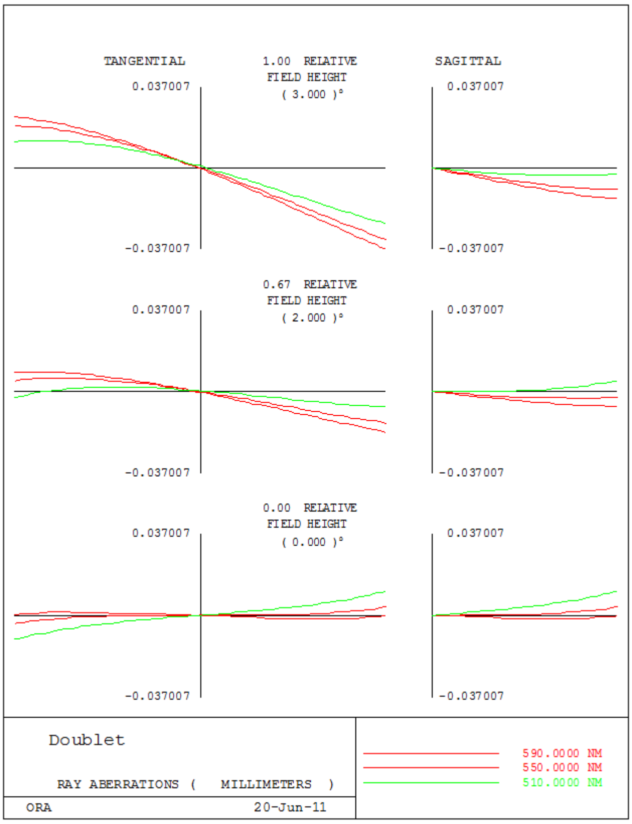

Figure 4.8: The ray intercept curve is a plot of the height on the image plane where a ray hits versus the slope of that ray with the optical axis. (left) Tangential ray intercept plots for (top) full field, (middle) 0.67 field and (bottom) on-axis. (right) Sagittal ray intercept plots for (top) full field, (middle) 0.67 field and (bottom) on-axis.

The left curves shown in figure 4.8 are for the tangential rays with full field at the top, 0.7 field at the middle and on axis at the bottom. The right curves are for the sagittal rays. The sagittal rays only need a half graph due to point symmetry that exists in rotationally symmetric optical tracks. The convention is such that only the positive image heights are plotted and the topmost ray that passes the lens is plotted on the right of the figure. With compound lens systems the ray with the most negative slope is plotted right. From the plot it can be directly seen whether the image is focused correctly, since $\delta = H'/TAN(U')$ with δ the distance of the focal point to the image plane. Therefore a sloping line indicates a distance between the focus and the image plane, while a horizontal line constitutes the focus and image plane coinciding.

Aberrations can be identified using standard shapes. Example ray intercept curve shapes from [49] are given in figure 4.9. Looking at the example lens ray intercept plots the focus seems good, while there is under corrected spherical aberration present.

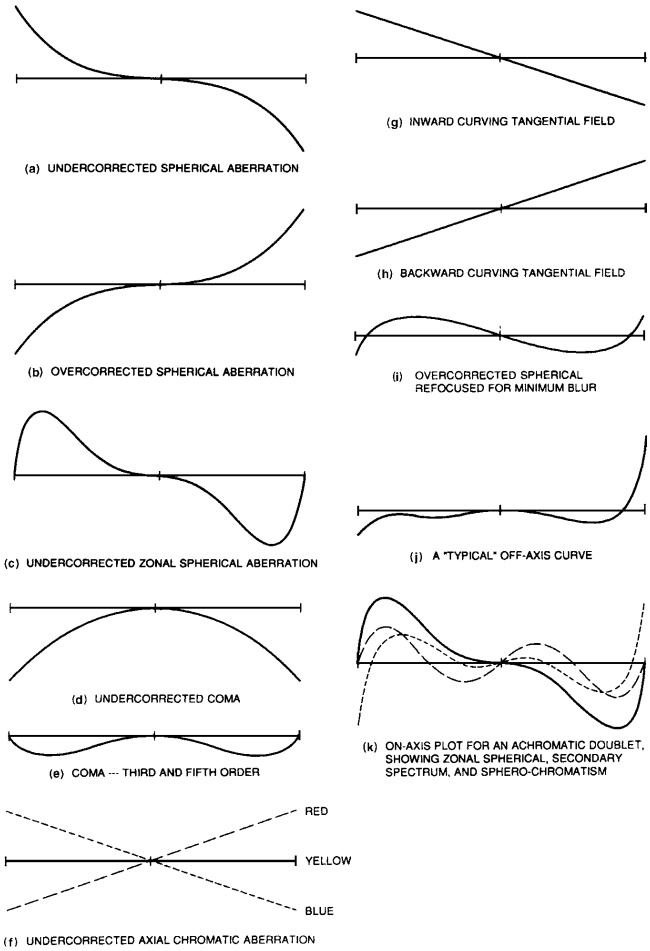

Figure 4.9: Ray intercept curve shapes [49].

Spot diagram

The spot diagram is shown in figure 4.10 and shows the ray positions on intersection of the image plane of light rays emitted from a point source. Due to aberrations in the optical system the focal distance for sets of rays will be different and the rays which have a focus away from the image plane (i.e. out of focus) will form two separate points instead of one. The figure only shows a section of the spot diagram information that is generated by the raytracer, which consists of spot diagrams for the on axis (shown), 0.67 field and full field cases.

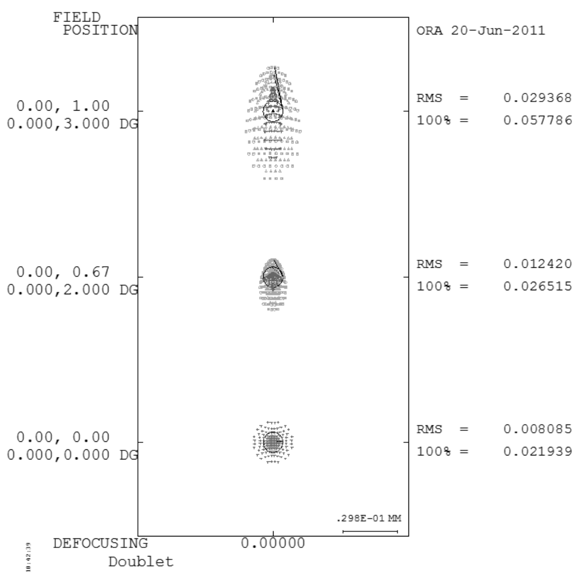

Figure 4.10: Spot diagrams of the example doublet lens indicating the intersection of rays with the image plane of a single point source. Out of focus rays will hit the image plane at a different location than where the on focus point would have been, creating a spot.

Spot diagrams are a good way to determine if a system is afflicted with aberrations like coma or astigmatism. Coma will show up as dotted circular patterns that grow in diameter and seems to move along an axis away from the image center (forming a sort of comet with tail shape). It is important to note that the spot diagram is generated using geometric optics without considering diffraction effects. The inclusion of the diffraction effects is incorporated by showing the Rayleigh criterion as a black circle superimposed on the spot diagram, as can be seen in the figure. Getting the spot size to fall within the Rayleigh criterion is the aim as this will make the optical system diffraction limited. This essentially means that the optical performance of the designed system is limited by the natural achievable boundary, and as such no changes to the optical system, other than changing the parameters affecting the Rayleigh criterion, will improve image quality. In the case of the doublet: the lens is not diffraction limited, as the spot is a lot larger than the circle indicting the diffraction limit.

Encircled energy

Another very useful tool to evaluate the performance of an optical system is a graph of the encircled energy. Like the spot diagram, an encircled energy graph describes the way in which a point source in the object plane is projected on the image plane. However, instead of looking at where light rays originating from a point intersect the image plane, the graph shows how the energy from the point is distributed over the image plane. In figure 4.11, the encircled energy has been plotted for the full field, 0.67 field and the center of the frame.

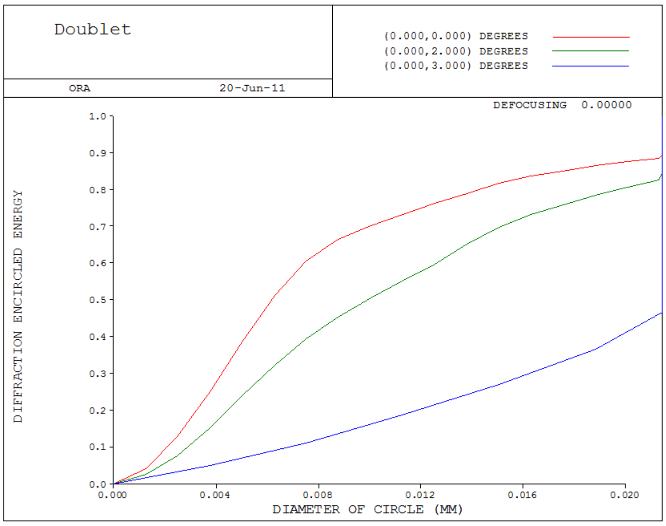

Figure 4.11: Graph of the encircled energy for the example doublet.

In a good optical design, a system is optimized in such a way that as much energy as possible falls within the area of a pixel, because if large amounts of energy end up outside the pixel area, the image will appear blurry.

Modulation transfer function

The Modulation Transfer Function, abbreviated as MTF, is a useful tool for evaluating the sharpness and contrast of a lens. In the camera industry, the tool has become the industry standard for judging the performance of a lens. The MTF looks at how a lens can resolve line patterns of black and white lines. Generally, line patterns in two directions are looked at, namely the saggital and meridional directions. The modulation is then given by the following equation [49]:

$$Modulation = \frac{max - min}{max + min} \tag{4.6}$$

Max and min in this function are respectively the maximum and minimum light levels that are observed in the image of the line pattern.

When the MTF is plotted versus the image position, the chart gives a good indication of the level of sharpness throughout the picture. Generally, the modulation of line patterns with various spatial frequencies are shown in such a chart. The left side of figure 4.12 shows an MTF versus field chart of the doublet used as an example in this section. The line patterns with a low frequency show how a lens can render small scale contrast, while higher frequency patterns are used to evaluate how well a lens can resolve fine detail. The modulation of line patterns with a frequency of 10, 30 and 60 lines per millimeter have been plotted. As can be seen, the performance in the center of the frame is quite good, while the image quality degrades rapidly towards the edges. Another thing that can be seen in the graph is that the modulation transfer functions for the saggital and meridional planes start do diverge toward the edge of the frame. This indicates that the blur in different directions is not equal, which means that astigmatism occurs on the edge of the frame [50].

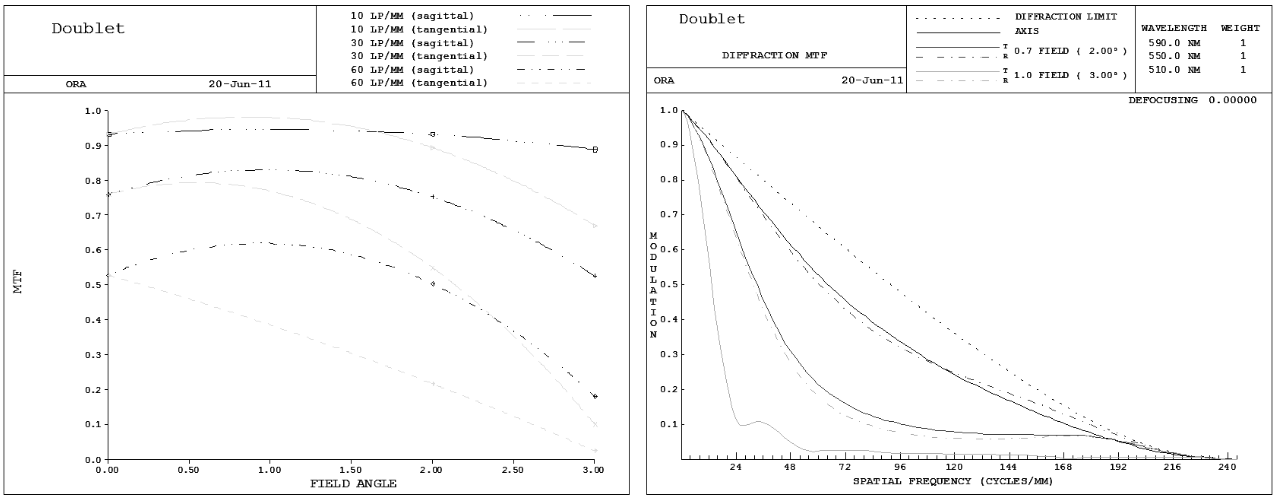

Figure 4.12: Modulation Transfer Function versus the image position (on the left) and versus the frequency (on the right)

The modulation can also be plotted as a function of the frequency of the line pattern. This is shown in the chart on the right side of figure 4.12. The modulation is plotted for various image positions: for the center, halfway and at the edge. One very useful value which can be retrieved from this graph is the spatial frequency for which the MTF is 50 percent. This frequency, which is often refered to as MTF50, provides an excellent measure of perceived image sharpness, because detail is diminished but still visible [51].

The MTF50 value that follows from the graph is given in cycles per millimeter. Multiplying this by the sensor height will give the number of cycles that can be resolved at a modulation of 50 percent. This value can be converted to the effective instantaneous field of view (EIFOV) [52]. This is the ground resolution for which the MTF of the system is 50 percent, which can be seen as the effective ground resolution which can be attained by the system.

Note that the EIFOV is often larger than the instantaneous field of view (IFOV), which is equal to the size of an individual pixel projected on the ground surface. For many commercial systems, the IFOV is stated as being the ground resolution, while in fact, the EIFOV is significantly larger. The IKONOS system, for instance, boasts a panchromatic ground resolution of 80 *cm*, while the panchromatic EIFOV is equal to 3.6 *m* [53].

Throughout the rest of the report, the effective ground resolution is used as one of the prime indicators used to measure the performance of the optical system as well as the effects manufacturing tolerances and temperature changes may have on the system.

4.4 Evaluating the signal-to-noise ratio

The Signal-to-Noise Ratio (SNR) indicates the amount of useful signal received by a photodetector over the amount of noise. This ratio can be used to quantify the performance of the system. In order to determine the SNR one will need to evaluate the signal and noise separately as is shown in section 4.4.1 and section 4.4.2 respectively.

4.4.1 Signal characteristics

The signal that is being considered consists of both an electromagnetic and a photo-voltaic part. The electromagnetic radiation in the form of photons coming from the target area, including diffusive source contributions, is to be converted to electrons within a photo-voltaic cell. This photo-voltaic cell is considered to be a single independent pixel on the sensor. The signal propagation equation as proposed by [54], provides a straightforward method in order to compute the amount of photons arriving at the sensor.

The amount of particles that are culminated during the total exposure time is dependent upon the aperture of the system, i.e. the area of the solid angle that is enclosed by the *etendue* of the external optical path. The *etendue* describes the total spread out of the light coming from the target area with respect to the aperture of the system, as is described by equation 4.7

$$E_j = A_j\Omega \tag{4.7}$$

where E_j gives the *etendue* at the entrance pupil for a distinct channel j. The field-of-view (A_j) seen by an individual pixel is given by the ground resolution characteristic for the optical system. The solid angle (Ω) enclosed by the light spread, as already has been discussed, is proportional to the altitude and aperture diameter according to the definition of the solid angle (in steradian). Using this definition, equation 4.8 can be defined

$$\Omega = \frac{D^2\pi}{4H^2} \tag{4.8}$$

where D indicates the diameter of the aperture, whereas H represents the distance (altitude) between the area being observed by an individual pixel and the aperture of the system.

The signal as given by [54] can now be analytically modeled by equation 4.9

$$S = SR \cdot (A_j\Omega) \cdot \overline{T}_j \cdot \Delta\lambda \cdot (\eta \cdot F_{fill}) \cdot T_i \tag{4.9}$$

with: S = The signal current in C/s, SR - Scene spectral radiance given in photons/(s $\cdot$ m^2 $\cdot$ nm $\cdot$ sr), $\overline{T}_j$ = Dimensionless transmission of the optical track, $\Delta\lambda$ = Wavelength bandwidth for an individual pixel, $QE_j = \eta_j(\lambda, T) \cdot F_{fill}$ = Quantum efficiency of the sensor describing the number of electrons freed by the incident photons, T_i = Integration time of the system. The scene spectral radiance needs to be defined with respect to the number of photons leaving the observed area or to the number of photons arriving at the aperture, thus the spectral radiance will be directly proportional to the wavelength (bandwidth) and the total target area. As the reflections and emissions characteristic to the area are omni-directional, one will also need to define the radiance as a function of the solid angle. From [55] figure 4.13 the Top-Of-Atmosphere (TOA) radiance against wavelength is taken. It is assumed that if one wants to incorporate a band of wavelengths an average value for the spectral radiance should be chosen and that when the amount of energy is being converted to the amount of photons an average photon energy should be used.

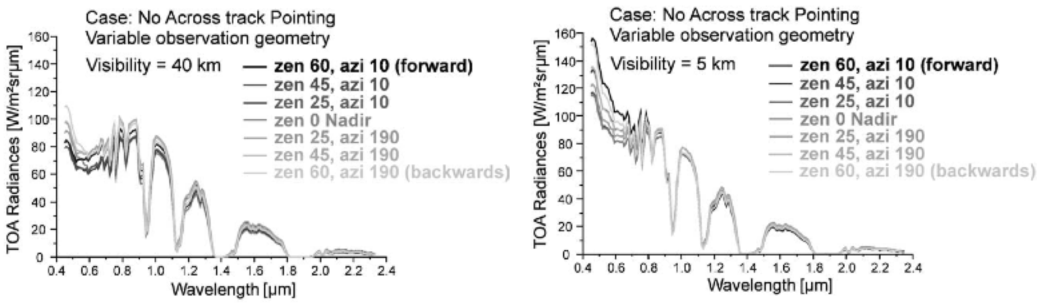

Figure 4.13: Top-Of-Atmosphere (TOA) scene spectral radiance adopted from [55]

As can be seen from 4.13, there are two conditions being considered, namely a condition assuming a clear sky and a condition assuming a visibility of only 5 km. As clouds are highly reflective a higher spectral radiance may be assumed, however the amount of detail of the area being considered decreases.

4.4.2 Photodetector noise characteristics

The noise within an optical system can be differentiated with respect to a distinct number of sources, which are derived from [56]. The noise sources are: signal shot noise, dark shot noise, Johnson-Nyquist noise and read-out noise. Shot noise can be considered to be caused by the quantum behavior of the signal, i.e. the quantum-mechanical probabilistic nature of photons. If the Earth's surface reflects a distinct number of photons, then those photons will not be distributed uniformly in time. They will therefore arrive at the detector randomly in time. Assuming that the random fluctuations of photons can be described by a Poisson distribution, one then can determine the average values at which photons hit the surface of the detector. The probability of receiving S photons within a time-interval T_i (integration time) can be given by the probability distribution as presented in equation 4.10.

$$p(S) = \frac{\overline{S}^S e^{-\overline{S}}}{S!} \tag{4.10}$$

The mean square signal noise can then be evaluates as being the variance and is given by equation 4.11.

$$\overline{S_n^2} = \sigma_n^2 = \sum_S p(S)(S - \overline{S})^2 = \overline{S} \tag{4.11}$$

The photons that hit the surface of the detector create a quantum event that generates an electrical current, i.e. a flow of electrons. The conversion factor used in order to describe this event is called the *Quantum Efficiency* (QE / μ_q), which describes the number of electrons that are freed by a certain quantity of photons. The probability distribution of the charge carriers can now be given by rewriting expression 4.11 in terms of the charge carriers, using $N = \mu_q S$, where N describes the number of electrons and μ_q represents the quantum efficiency

$$p(N) = \frac{\overline{N}^N e^{-\overline{N}}}{N!} \tag{4.12}$$

Such that the mean square noise, as for the total signal, can be given by:

$$\overline{N_n^2} = \sigma_N^2 = \overline{N} \tag{4.13}$$

For a detector without any internal gain, as is being assumed, one is able to determine the noise current as is caused by the quantum fluctuations during the conversion of photons in a flow of charge carriers, i.e. a stream of electrons. The shot noise current is given in equation 4.14, where B describes the electrical bandwidth (as follows from the Nyquist criterion) and q is the elementary charge.

$$\overline{i_{n,sh}^2} = 4q^2B^2\overline{N_n^2} = 4q^2B^2\overline{N} = 2qB\overline{i_s} \tag{4.14}$$

As already noted, B, describes the electrical bandwidth that follows from the Nyquist sampling criterion. As the sampling frequency is directly related to the number of images that are taken along the orbit, it should be clear that the integration time should be as small as possible such that the sampling frequency is as high as possible. The signal-to-noise ratio is thus proportional to integration time and this value value should be chosen accordingly.

By applying the following statistical equation: $\overline{s^2} = \overline{s}^2 + \sigma_s^2$ one can then rewrite the mean squared signal as follows:

$$\overline{i_s^2} = \overline{i_s}^2 + 2qB\overline{i_s} \tag{4.15}$$

Next to the noise induced by the signal itself, one could also incorporate other sources of shot noise, such as dark current and background noise. Dark current can best be described as the current generated by the photodetector when it is not illuminated. If one considers additional noise sources, though neglecting background noise, the signal variance can then be described as:

$$\overline{i_{n,sh}^2} = 2qB\overline{i} = 2qB(\overline{i_s} + \overline{i_d}) \tag{4.16}$$

The next noise factor that needs to describe is the Johnson-Nyquist noise, which is caused by thermal motions of the freed electrons within the element. The Johnson-Nyquist noise is thus equivalent to the noise generated by the resistive components within the sensor circuit. Because of this relation, the Nyquist noise can be modeled by the law of blackbody radiation as follows:

$$P_{n,th}(f)df = \frac{4hf}{e^{hf/k_bT} - 1}df \tag{4.17}$$

Where $P_{n,th}$ describes the Nyquist noise power, f the frequency of the electromagnetic radiation and the parameter k_b is equal to the Boltzman constant. For normal operation of a photodetector it holds that $f << k_bT/h$, such that the noise power may be written as:

$$P_{n,th}(f)df = 4k_BTdf \tag{4.18}$$

Integration of a prescribed bandwidth yields:

$$P_{n,th} = 4k_BTB \tag{4.19}$$

The Johnson-Nyquist noise current can than be evaluated by using Ohms law:

$$\overline{i_{n,th}^2} = \frac{4k_BTB}{R} \tag{4.20}$$

The final noise source one needs to discuss is the read-out noise, which is caused by fluctuation within the sensors read-out modules and by random interference. Since for many sensors the read-out noise fluctuations are not normally distributed, one will have to estimate this noise source when one is to model the signal-to-noise ratio. As is noted in [57], the dynamic range may be represented by the ratio between the number of saturation electrons and the number of read-out noise electrons as is given in equation 4.21

$$DR = 20 \cdot log_{10}\left(\frac{N_{sat}}{N_{n,r}}\right) = 10 \cdot log_{10}\left(\frac{N_{sat}^2}{N_{n,r}^2}\right) \tag{4.21}$$

and by rewriting this expression, one is able to determine an expression for the read-out current:

$$\overline{i_{n,r}^2} = 2qB\left(\frac{N_{sat}}{10^{\frac{DR}{10}}}\right) \tag{4.22}$$

4.4.3 Analog-to-Digital Converter (ADC) noise characteristic

As the analog signal is to be converted in a digital image, an additional noise source need to be taken into account caused by the ADC on the sensor. This particular noise source is directly proportional to the full well charge (or saturation value) and inversely proportional to the quantization bits (n) used in the ADC per color channel. As this section only contains a preliminary SNR computation, only a single channel is assumed.

From [19] the following relation regarding the quantization noise can be derived:

$$\overline{i_{n,q}^2} = \left(2qB\frac{N_{sat}}{\sqrt{12} \cdot 2^n}\right)^2 \tag{4.23}$$

4.4.4 Signal-to-noise ratio

The total noise current may now be considered to be the addition of all the various noise sources as is given below:

$$\overline{i_n^2} = \overline{i_{n,sh}^2} + \overline{i_{n,th}^2} + \overline{i_{n,r}^2} + \overline{i_{n,q}^2} \tag{4.24}$$

The Signal-to-Noise Ratio (SNR) for a photodetector without internal gain can be approximated by evaluating the ratio between the incoming signal current with respect to the root mean squared of the total detector noise current. The resulting expression is shown in equation 4.25.

$$SNR = \frac{\overline{i_s}}{\sqrt{\overline{i_n^2}}} = \frac{\overline{i_s^2}}{\sqrt{\overline{i_{sh}^2} + \overline{i_{n,th}^2} + \overline{i_{n,r}^2} + \overline{i_{n,q}^2}}} \tag{4.25}$$

The question remains of what value for the integration time and quantization step should be taken in order to satisfy the signal-to-noise requirements. The following figures show how the signal-to-noise ratio varies if the value for the integration time or quantization step would vary:

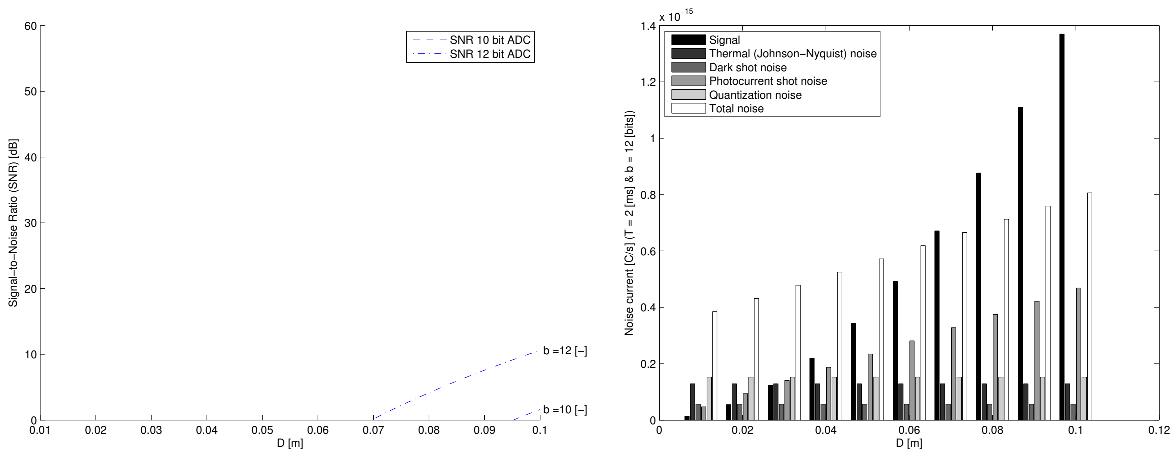

(a) Signal-to-noise ratio in dB

(b) Signal and noise histogram

Figure 4.14: Signal-to-noise characteristics for a 1 ms integration time

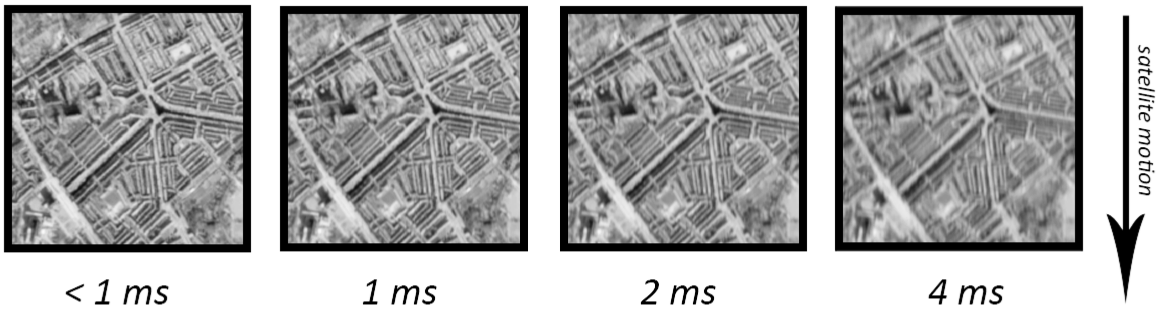

Figure 4.16: Motion blur induced by a range of integration times

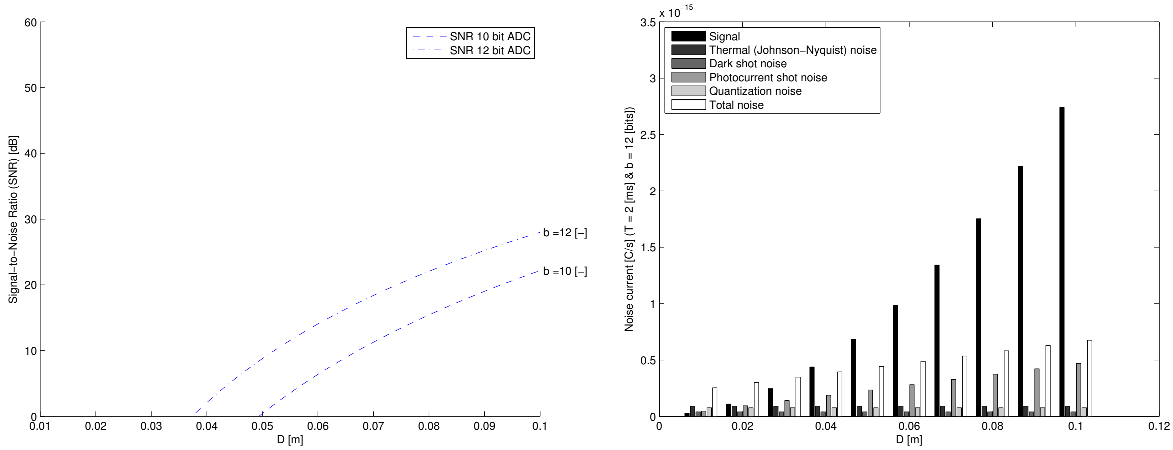

(a) Signal-to-noise ratio in dB

(b) Signal and noise histogram

Figure 4.15: Signal-to-noise characteristics for a 2 ms integration time

From figure 4.14 and figure 4.15 it can be concluded that a 12-bit analog-to-digital converter (ADC) is needed, such that the quantization error is limited and in either case that the signal-to-noise ratio attains a high enough value. It however restricts the video capabilities of the system. It can also be concluded from both figures, that at least a 2 ms integration time is needed in order to allow for a proper signal-to-noise ratio independent of altitude. The *etendue* scales proportional to the altitude, as the FOV goes up. This particular value is in direct contrast with the integration time found in section 3.1.7. As already noted, this will in both cases introduce motion blur as is shown in figure 4.16. From figure 4.16 it can be seen that using sharpening techniques the motion blur may be corrected for. A 4 ms integration time is considered to be too degrading for image processing techniques to still provide an image interesting for the market. If the instrument is operated in a constellation, the value of the SNR is allowed to be smaller because of the multiple aperture benefit allowing an increased combined SNR, and therefore a smaller integration time could be used.

4.5 Concept descriptions

4.5.1 Cassegrain concept

The Cassegrain Concept layout is given in figure 4.17. Light entering the system from the left is reflected by the large concave primary mirror and subsequently reflected by the smaller convex secondary mirror onto the image sensor.

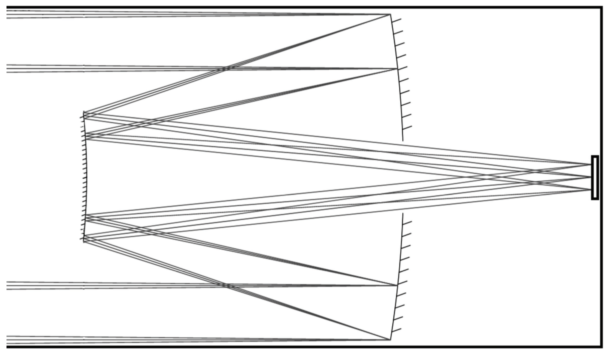

Figure 4.17: Cassegrain configuration (own image)

4.5.2 Double off-axis parabolic mirror system

An impression of the concept utilizing a single achromatic doublet lens as focusing element is shown in figure 4.18. Light enters the system from the left. After the mirrors are traversed, the parallel beam needs to be imaged with the sensor. Two possibilities for focusing the beam have been explored: a doublet lens or a Petzval lens set.

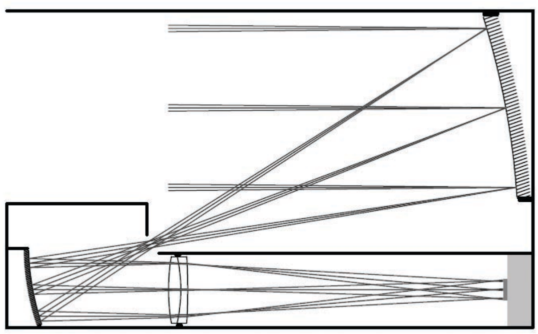

Figure 4.18: Double off-axis parabolic mirror configuration (own image)

4.5.3 Doublet lens-mirror concept

This concept approached the problem of fitting the focal length by folding the light path using planar mirrors. Several options of mirror placements where investigated as are shown in figure 4.19. Note that the fourth option proved the most beneficial of all concepts as will be shown in section 4.6.

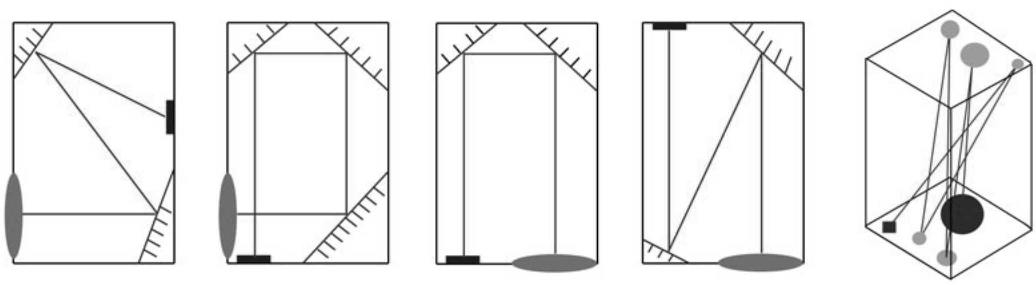

Figure 4.19: From left to right optical configuration number 1 to 5 are shown respectively.

4.6 Trade off

In this section a trade-off was performed to determine the most beneficial concept to be further developed in the preliminary design phase is discussed. First the weighting system is elaborated upon after which the actual trade-off figures will be presented.

4.6.1 Criteria and scoring system

The scoring system consists of a cardinal scale in which the trade-off criteria receive weights corresponding to their importance. A fixed amount of 50 points were divided amongst the criterion. Using a fixed amount of points forced careful consideration in their distribution. Next subscores from 1 to 5 where given to 3 to 5 choices for each criteria. After construction of the trade-off system several reference 'designs' were inserted in the system to see if the results matched expectation i.e. calibrating the system. An example test would be to take a bad camera in a very heavy structure and see if this design would win from a very fragile structure with a good camera. According to the authors the latter design should win so the scoring system was calibrated to arrive at such conclusions. After the correct calibration was found the actual conceptual design could be inserted. A discussion on each criteria will follow next after which the trade-off criterion table is shown in table 4.3.

The **optical performance** of the system is weighted most heavily as is to be expected with an optical instrument design. The performance was measured via ray trace analyses done on the different conceptual designs. For comparison of the optical systems performance of the concepts the FOV was taken to be constant at 1.2° half field angle.This half field was chosen partially because it would supply a light cone that would illuminate the selected sensor and partially because the market analysis indicated a high temporal resolution was important. A high temporal resolution would be difficult to achieve if the half field angle would have been taken lower. As was just mentioned the sensor was preselected which had as reason that the selected sensor was far beyond the competition in terms of suiting the design requirements.

The **thermal stability** is an indication of the ability of making the structure cope with changes in the thermal environment. Some first estimation computations on mirror and lens deformations supplied objective information for this criteria. Due to the objective determination and the mission criticality, catastrophic if thermally unstable, the thermal stability has received a high weighting in the trade-off.

Mechanical stability is the ability of the structure to cope with the launch loads. A more qualitative approach was utilized in which larger and curved mirrors, any rod suspended masses or the amount of lens elements would be classed as a worse performing system.

Volume indicates the scoring of the amount of CubeSat cubes the system would occupy. More being less.

Cost indicates the manufacture and material cost of the system. This consisted mainly of cost estimates of of actual COTS component price sums. Furthermore an estimated relative labor effort was added to determine this qualitative value.

The **mass** shows the estimated mass of the system. The mass has been determined using first order approximations of the geometrical shapes, with which the mass is determined using the volume times the density of the material.

The **SNR** criteria gives an indication of the SNR performance of the system. The detail of the conceptual design did not allow an accurate enough SNR value to be determined. Therefore a rudimentary SNR computation was devised on the basis of the aperture size of the system. It appeared that the value of the Signal-to-Noise ratio was approximately similar for all concepts, since that scales with $\sqrt{Signal}$ $\sqrt{Aperture_{area}} = Aperture_{diameter}$ and the aperture diameters were very similar. Therefore only a qualitative assessment was performed.

Power indicates the amount of power the system consumes. For the camera system extendable or internally actively driven components were termed as unwanted. Therefore basically only the sensor would tax the power budget. This criteria was taken along within the trade-off in case certain concepts could not operate without internally moving parts (e.g. for focusing) but in the end this criteria proved superfluous.

Table 4.3: Trade-off criterion table

(a)

Trade-off criterion - Weight	Score
Optical performance - Weight: 15	
Low	1
Medium	3
High	5
Thermal stability - Weight: 8	
Low	1
Low / Medium	2
Medium	3
Medium / High	4
High	5
Mechanical stability - Weight: 6	
Low	1
Low / Medium	2
Medium	3
Medium / High	4
High	5
Volume - Weight: 6	
>2 Cubes	1
1.5 - 2 Cubes	3
1 - 1.5 Cubes	5

(b)

Trade-off criterion - Weight	Score
Cost - Weight: 5	
High	1
Medium	3
Low	5
Mass [kg] - Weight: 5	
>2	1
1.5 - 2	2
1 - 1.5	3
0.5 - 1	4
<0.5	5
SNR [dB] - Weight: 4	
<30	1
30 - 35	2
35 - 40	3
40-45	4
>45	5
Power - Weight: 1	
High	1
Medium	3
Low	5

4.6.2 Concept trade-off

The trade-off is executed by selecting a score for each criteria of each concept. The score of each criterion is then multiplied by the weight of that criterion to determine the weighted score. Thereafter all the weighted scores are summed up to form the total score for the concept. This is done for all the concepts, so in the end the best overall concept will have the highest score.

4.6.3 Concept scores

Cassegrain system

The scores for the Cassegrain System are shown in table 4.4.

Table 4.4: Scoring table for the Cassegrain System

(Weight) Criterion	Value	Score	Weighted Score
(15) Optical performance	Low	1	15
(8) Thermal stability	Low / Medium	2	16
(6) Mechanical stability	Medium	3	18
(6) Volume	1.5 Cube	5	30
(5) Cost	High	1	5
(5) Mass [kg]	<0.5	5	25
(4) SNR [dB]	45	5	20
(1) Power	Medium	3	3
Total Score			**132**

The Cassegrain System scores low on optical performance. Simulations made with optical design software showed that the off-axis aberrations of the system grow rapidly towards the image edge. This results in much smaller usable imaged areas relative to the other systems reducing the image market potential. Furthermore the system has very tight tolerances regarding the relative mirror positioning resulting in difficulties creating a thermally stable system. The cost is not known exactly because the hyperbolic mirrors require custom solutions and are difficult to create. At this point the specifics of these components (e.g. the mirrors) are not known, so the price could not be determined. In the end the concept scored 132 out of 250 points.

Double off-axis parabolic mirror system

The scores for the Double Off-axis Parabolic Mirror System are shown in table 4.5.

Table 4.5: Scoring table for the Double Off-axis Parabolic Mirror System

(Weight) Criterion	**Value**	**Score**	**Weighted Score**
(15) Optical performance	Low / Medium	2	30
(8) Thermal stability	Medium	3	24
(6) Mechanical stability	Medium	3	18
(6) Volume	1.5 Cube	5	30
(5) Cost	Medium	3	15
(5) Mass [kg]	<0.5	5	25
(4) SNR [dB]	39	3	12
(1) Power	Low	5	5
Total Score			**159**

The Double Off-Axis Parabolic Mirror System scores low / medium on optical performance. Simulations made with optical design software showed that the optical performance was under par. This is mainly caused by the magnification of the mirrors that also effects the angle between the incident rays and the optical axis. Rays from the image edge exit the secondary mirror at an angle which is four times bigger, causing much more severe aberrations to occur after the doublet lens is traversed. The thermal and mechanical stabilities are moderate because the parabolic mirrors are small but still susceptible to deformation. The total score of this system is 159 out of 250.

Doublet lens-mirror system

The scores for the Doublet Lens-Mirror System are shown in table 4.6.

Table 4.6: Scoring table for the Doublet Lens-Mirror System

(Weight) Criterion	**Value**	**Score**	**Weighted Score**
(15) Optical performance	Medium / High	4	60
(8) Thermal stability	High	5	40
(6) Mechanical stability	Medium / High	4	24
(6) Volume	1.5 Cube	5	30
(5) Cost	Low	5	25
(5) Mass [kg]	<0.5	5	25
(4) SNR [dB]	39	3	12
(1) Power	Low	5	5
Total Score			**221**

The Doublet Lens-Mirror system scores high points for almost all the trade-off criteria. The doublet lens basically gives the same performance as the Double Off-axis Parabolic Mirror System without the problematic field angle magnification. Furthermore tolerances are more relaxed compared to the Cassegrain system. Simulations made with optical design software showed that image quality remained higher towards the edge of the image compared to both other concepts, but still degraded near the image edge. Because the system is simple, it has a low cost and good thermal-mechanical properties. Therefore the system scores quite high with a score of 221 out of 250.

4.6.4 Selected concept

The selected concept is the Doublet Lens-Mirror System, with a score of 221, because it clearly outperforms the other concepts (having 132 and 159 points) in almost all of the trade-off criteria. Although some image degradation occurred near the edge of the image the image quality generally showed the best performance over the complete field. The entire trade-off table with all the scores and weights combined can be found in figure 4.20

Criterion	Weight	Score Parabolic mirror	Weighted score	Score Cassegrain	Weighted score	Score Doublet system	Weighted score
Optical Performance	15	**2**	30	**1**	15	**4**	60
Thermal control	8	**3**	24	**2**	16	**5**	40
Mechanical stability	6	**3**	18	**3**	18	**4**	24
Volume	6	**5**	30	**5**	30	**5**	30
Cost	5	**3**	15	**1**	5	**5**	25
Mass	5	**5**	25	**5**	25	**5**	25
SNR	4	**3**	12	**5**	20	**3**	12
Power	1	**5**	5	**3**	3	**5**	5
Total score	50		159		132		221

Figure 4.20: Trade-off table

4.7 Detailed optical design

Now that the doublet mirror system has been chosen as the winning concept, it must be further analyzed to see if and how the design can be optimized to achieve a better optical performance. In section 4.3.2 it was shown that while the system is able to get sharp results in the center of the image, the performance drops considerably towards the edges of the frame, which is caused primarily by field curvature and an increase in astigmatism towards the edge of the frame. Thus, solving these issues will be the main focus when optimizing the optical design.

In this section, the process that has been followed will be described, after which the final optical design will be presented. Finally, the optical performance of the optimized design will be further evaluated.

4.7.1 Design process

To correct the flaws of the single doublet, several methods can be used. First of all, a smaller field stop can be used and secondly an extra lens element may be introduced to correct for optical flaws. Both options will be discussed here.

Field stop

When a field stop is used, the light which goes through the edges of the lens is blocked and only the light through the center of the lens can pass through. Some aberrations, such as coma and spherical aberration are caused by a difference in the location where light going through the edge of the lens and light going through the center is focused. By blocking the light going through the edges of the glass, these aberrations can therefore be reduced significantly - especially near the edges of the frame.

However, using a smaller field stop has several disadvantages as well. First of all, blocking a part of the light means that less light will reach the sensor. which makes it significantly harder for the system to produce well exposed pictures that are free of unacceptable noise levels. Furthermore, using a small field stop will also reduce the effective pupil diameter. From Rayleigh's criterion, which was given in section 4.3.1, it then follows that the maximum resolution that can be obtained will be reduced significantly. Particularly in the center of the frame, where the performance is close to the diffraction limit, using a smaller stop size is highly likely to cause a reduction in optical quality.

To determine what stop size would be best, several stop sizes have been tried. The stop sizes that were tried were f/8.5, f/11 and f/16. Note that stop sizes in optics are not expressed as their physical size, but rather as the focal ratio, since this measure also gives a good indication of the amount of light that can enter the system. In figure 4.21, the result of using several stop sizes can be seen in the MTF versus field charts.

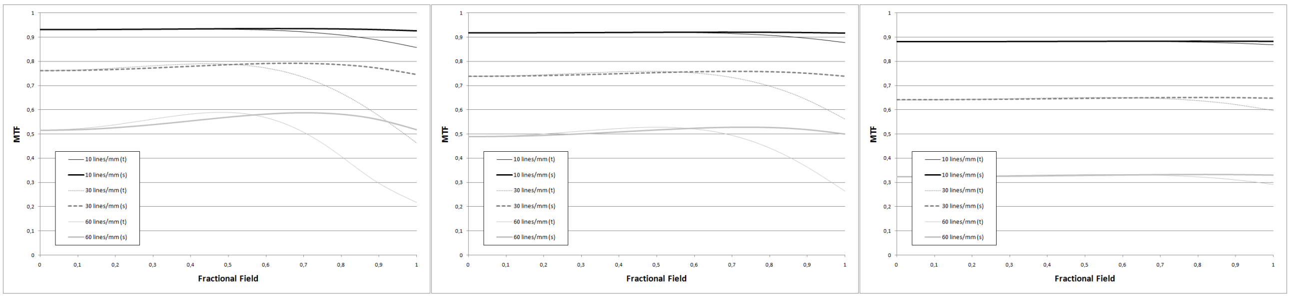

Figure 4.21: The effect of using smaller stop sizes: (left) MTF versus field chart of the original lens (f/8.5), (center) a smaller stop size is used (f/11), (right) an even smaller stop size is used (f/16)

As can be seen, reducing the stop size for this system has very few benefits. While the performance in the corner improves slightly when a focal ratio of f/11 is used, this ratio is offset by the drop in performance in the center of the image due to diffraction. The performance is more constant throughout the image, but the improvement is not worth the drop in light which can enter the system. When using an even smaller stop size, the performance throughout the entire image drops considerably.

Changing the position of the field stop has very little effect on the optical performance of the system. While for some optical systems, moving the stop size can have major effects on the optical performance [49], this is not the case here. This is due to the fact that the field of view is small and the light enters the system with only small angles with respect to the optical axis. Therefore, changing the position of the field stop has only marginal effects on the section of the lens that light will travel through.

To conclude, using a smaller field stop does not lead to significant improvements in image quality. Therefore, to fix the errors of the optical system, clearly one ore more optical elements must be added.

Doublet and meniscus

One of the methods to correct the spherical aberration of a single doublet is to combine it with a meniscus lens [58]. Placing a meniscus lens close to the achromatic doublet, shortens the focal length of the system. Therefore, a doublet with a longer focal length than necessary should be chosen to make sure that the system has the effective focal length required. The main downside of the combination is that some of the achromatic properties of the system are lost, and thus chromatic aberrations will increase.

The performance of the doublet meniscus combination looked promising, when assuming that a narrow waveband will be used. The performance near the edges of the frame improves, although the differences are not groundbreaking. However, the difference could probably be increased with further development and optimization.
On the left side of figure 4.22 the performance of the system when observing a narrow waveband (10 nm) can be seen. The chart on the left shows the MTF versus field chart for a wider waveband (80 nm) is shown. As can be seen, the performance plummets when long wavebands are used.

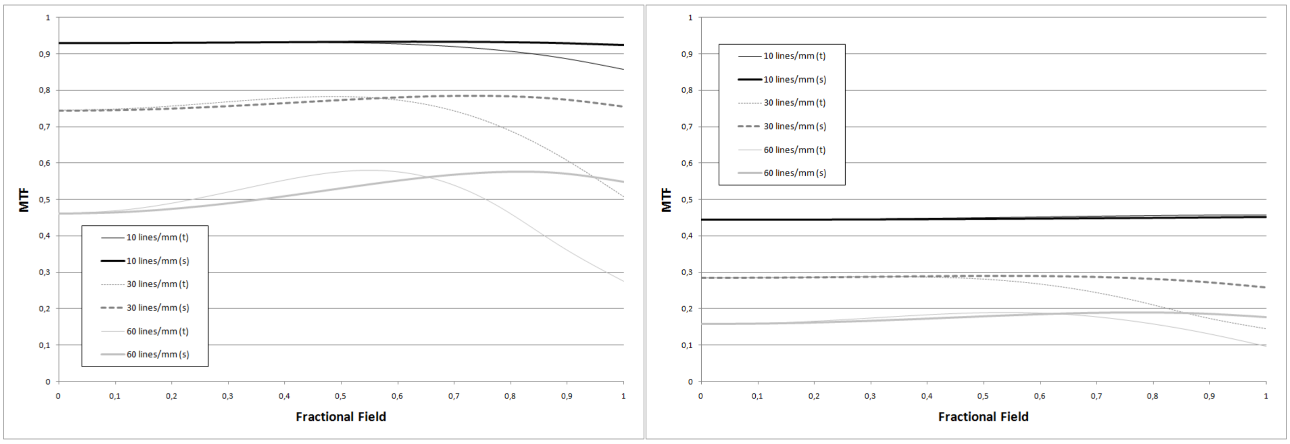

Figure 4.22: MTF vs Field: on the left for a narrow waveband (10 nm) and on the right for a wider waveband (80 nm)

Using a narrow waveband means that less light will reach the sensor. This will severely limit the signal-to-noise ratio that can be achieved. During the design of this concept it was determined that using a narrow waveband is not realistic and therefore, the idea was dropped.

Telephoto design

As was mentioned in section 4.3, positive lens elements generally suffer from undercorrected spherical aberration and an inward curving focus plane, while negative lenses suffer from overcorrected spherical aberration and a backward curving focus plane. Thus, by combining the effects of the two lens types, both flaws may be corrected and a significantly better performance may be achieved.

A common optical design that uses a positive and negative optical elements is the telephoto design. A telephoto design consists of a positive front element, followed by a negative rear element. The combination of the two elements results in a shorter physical length than the effective focal length, as is illustrated in figure 4.23. This is very convenient, since it allows for more space for the optical mountings.

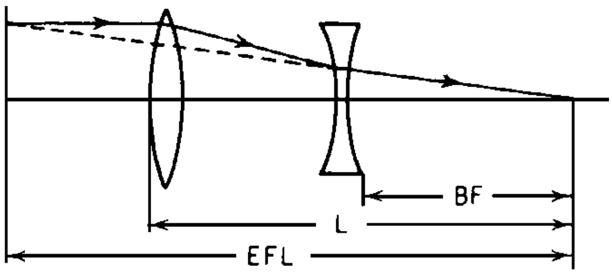

Figure 4.23: A simple telephoto design. The focal ratio is equal to the effective focal length (EFL) divided by the length (L) [49]

The ratio of the physical length and the effective focal length is called the telephoto ratio, which is smaller than 100% for telephoto lenses. Combining stronger lenses (with a shorter focal length) allows for small telephoto ratios of 60% or even less. While some aberrations are corrected when a combination of positive and negative lenses are used, using extreme telephoto ratios will enlarge other flaws of the optical system. Additionally, using extreme telephoto ratios may result in a strong inclination to a backward curving field of focus [14]. Therefore, using moderate telephoto ratios of 80% or more are preferred.

To make sure that the lens possesses good achromatic properties, so that the image quality does not degrade too much when a wider waveband is used, it was chosen to use a positive and a negative achromatic doublet as the lens elements. In theory, an infinite number of combinations of achromatic doublets is possible to reach the required effective focal length. However, since one of the requirements of the project was to use COTS components, the number of possibilities is limited by the number of doublet lenses that is available.

In the design process, several combinations of positive and negative doublets out of the catalog of Edmund Optics have been evaluated. Edmund Optics was chosen because they have a wide variety of doublet lenses available, including negative doublets, unlike some of the competing companies. In the end, it was determined that a 350 mm achromatic doublet combined with a -100 mm negative achromatic doublet provides the best results throughout the frame. In figure 4.24 an indication of the performance of the system is given.

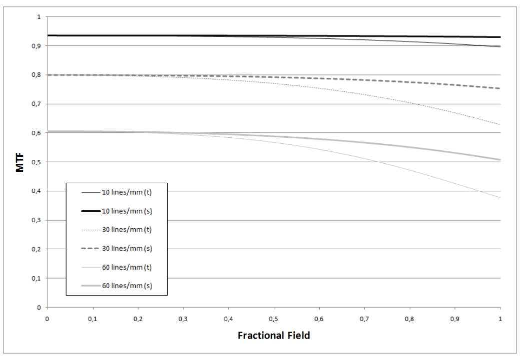

Figure 4.24: MTF vs field

As can be seen in figure 4.24, the telephoto system performs considerably better than the single doublet. The degradation in performance towards the edge of the image is far less severe and the degree of astigmatism is considerably smaller. The improvement in quality towards the edges of the frame did not come at the expense of the image quality in the center; in fact, also in the center a slight increase in image quality may be observed.

Since the telephoto design performs considerably better than the other options that have been evaluated, it was chosen as the final design. Although the addition of the second element adds complexity and mass towards the system, these downsides are heavily outweighed by a vast improvement in optical performance. In the next section the final design will be described in more detail and it's performance will be evaluated.

4.7.2 Final Design

As was described in the previous section, a telephoto design was chosen as the final design. In figure 4.25 the light path of the design can be seen. In this section, the design will be described and evaluated in more detail. First of all, the selected components will be described, after which the optical performance will be described in more detail.

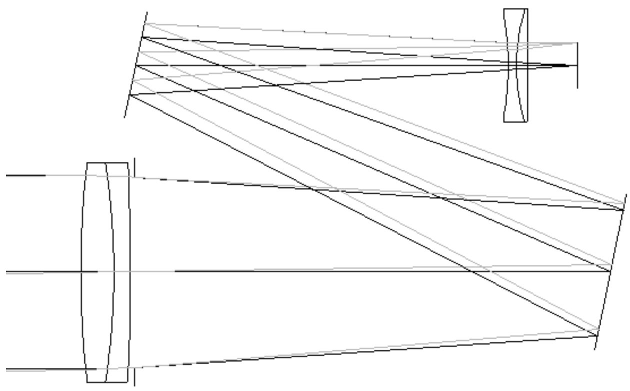

Figure 4.25: Lightpath of the final optical design

Selected components

Even though the addition of a second element has added complexity to the design, the design remains quite simple. The number of components remains limited. Arguably the two most important components used in the system are the two doublets. The first doublet is a 350 mm doublet made by Edmund Optics (type NT45-354), which can be bought for 110 dollars. The second doublet has a focal length of -100 mm (type NT45-222) and is sold by the same company for 75 dollars.

The glass types used for the doublets are N-BAK4 and N-SF10 for the first doublet and N-BAF10 and N-SF10 for the negative doublet. For both lenses, the two elements have been cemented using Norland Optical Adhesive NOA61. This type of optical glue can withstand a wide range of temperatures; from -150 up to 125 degrees Celsius and can be used in situations where low outgassing are required [59].

As for the mirrors: di-electric mirrors have been selected because this type of mirror offers a very high reflectivity, which means that the loss of light is minimized. The mirrors have a zerodur substrate, which offers very low thermal expansion, which means that deformation of the mirror remain minimal.
One final component that will be added to the optical track is a bandpass filter to select the bandwidth that will be captured. The selection of this item will be discussed in section 4.8.

4.7.3 Optical performance

In this section, the optical performance of the telephoto design will be discussed in more detail, using graphs that have been created using Code V. The waveband for which the plots are shown ranges from 510 to 590 nanometers, which corresponds to the green band-pass filter that was chosen. The final design has been optimized for green light, but by shifting the focus, it can be made to work with other wavelengths. More on this topic can be read in the coming sections about filter selection and full color imaging.

The MTF versus field chart of the telephoto system was already shown in figure 4.26. In that graph it can be seen that the performance of the system is very good throughout the entire image. The performance degrades somewhat towards the edges and there is an increase in astigmatism, but the modulation for fine line patterns remains well above 40%, even near the edge of the frame, which is excellent.

Figure 4.26 shows the MTF versus the spatial frequency. The diffraction limit has also been plotted in the figure. As can be seen in the graph, the performance in the center of the frame is very close to the diffraction limit. The performance drops a bit towards the edge of the frame, as indicated by the lower, light gray curves, but the curve still converges to the diffraction limit as the spatial frequency grows.

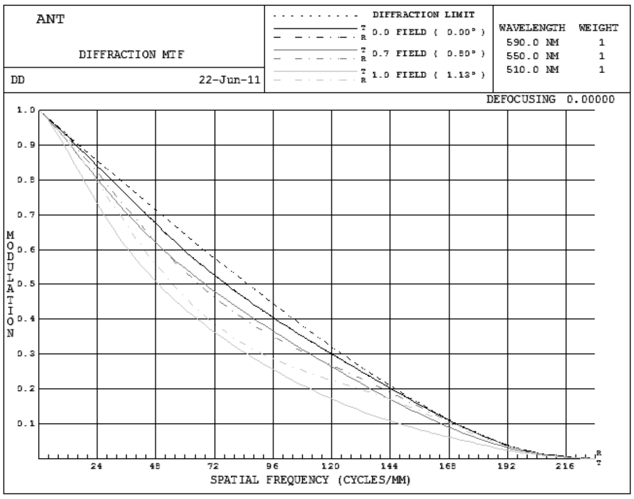

Figure 4.26: MTF versus Spatial Frequency

From the graphs, the MTF50 values can be read out (an average of the tangential and sagittal modulation curves is taken here). For this system, the MTF50 frequency is 77 cycles/mm for the center, 68 cycles/mm for the edge, and 47 cycles/mm for the corner of the image. As described in section 4.3.2, these values can be converted to the effective geometric instantaneous field of view, which can also be called the effective ground resolution. For the center, edge and corner of the image, the effective ground resolutions that can be obtained are respectively 8.7, 9.8 and 14.5 meters. These values deviate from the target resolution of 7.5 meters per pixel, but as described before, the deviation is also present with other commercial systems, such as IKONOS.The deviations which are found for the telephoto seem relatively small compared to those that are given for the IKONOS system [53].

The spot diagram for the system is given in figure 4.27. In the diagram, both the airy dis, (the circle) and the detector size (the square) have been included. The airy disk is the smallest possible spot size for a system that is limited by diffraction. As can be seen in the figure, in the center of image, all light rays that have been traced end up within the airy disk, which confirms that the performance in the center is diffraction limited. Towards the edge of the frame, some rays that are traced end up outside the disk. The shape of the spot indicates that some coma is present. However, the fast majority of the rays ends up within the airy disk, which indicates a near diffraction limited performance for the entire field of view.

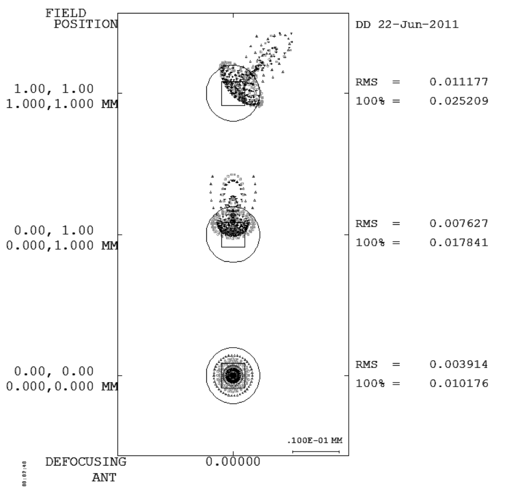

Figure 4.27: Spot Diagram

A graph for the encircled energy is shown in figure 4.28. In the figure it can be seen that for the center of the frame, as well as for edge, well over 50 percent of the received energy falls within the circle bounding a 5.5 micrometer pixel, which is a diameter of about 7.7 micrometer. This is an excellent result, because it indicates that the light that the majority of the light captured by a pixel was supposed to be focused there. Using a bounding circle instead of computing the energy that falls within a square of 5.5 by 5.5 micrometer is a fair approximation in this case since only a relatively small section of each pixel is actually sensitive to light. In the corner of the image, only 40 percent of the energy ends up within the bounding circle, which means that the corners of the image will appear more blurry.

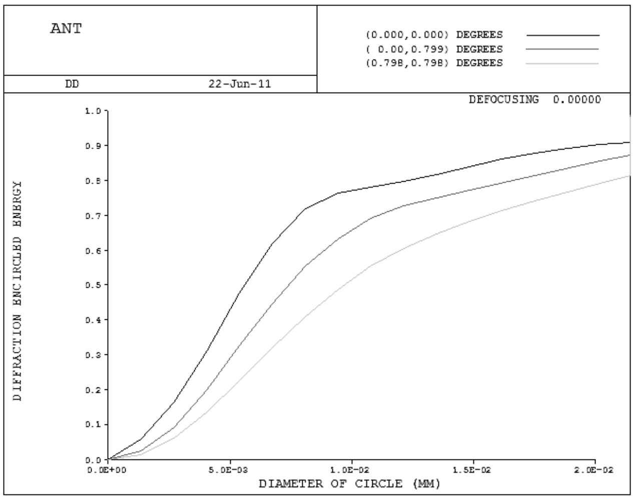

Figure 4.28: Encircled Energy

To get a feeling of how well an optical system performs, Code V is not only capable of producing graphs. The software also includes a powerful image simulation feature. Using a high resolution source image as the object, the program can simulate what the image would look like when it is photographed using the optical system. The simulation takes into account the effects of diffraction, aberrations and the pixel size. To test the performance of the telephoto system, the image shown in figure 4.29 has been used.

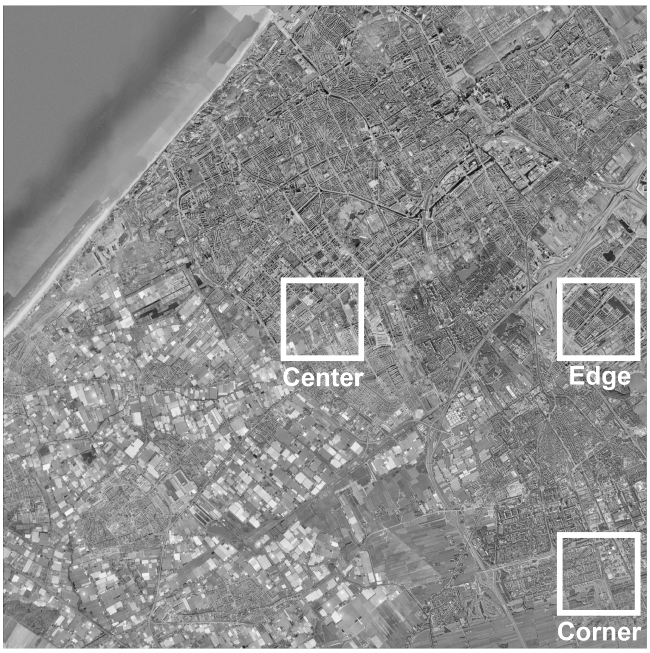

Figure 4.29: Scene showing the area around Rotterdam and Delft used for the Image Simulation

In figure 4.30 some enlarged sections of the rendered image are shown. As can be seen, the optical performance is very good from the center until the corner of the image. The optimal result (i.e. the source image) is also included for the corner, the softest section of the image. While there is definitely a difference between the rendered image and the optimal result, the performance of the system remains good. Using sharpening techniques, such as an unsharp mask or high pass sharpening, the difference between the two results would diminish.

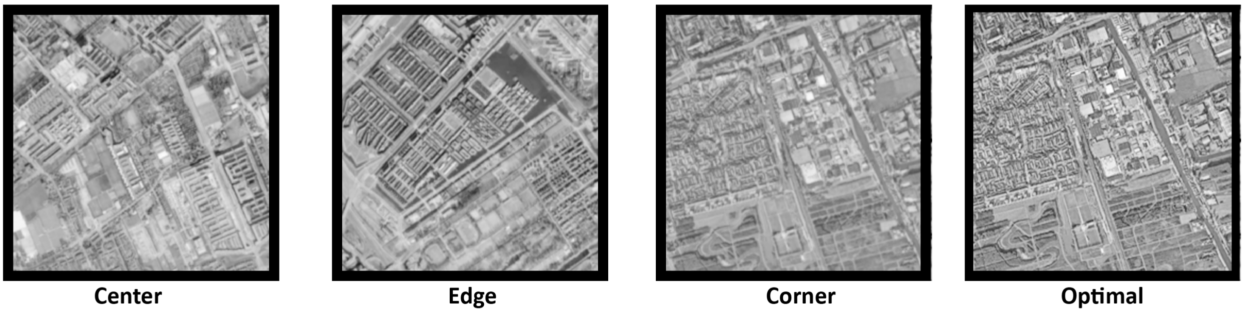

Figure 4.30: Images rendered using Image Simulation in Code V

Since it is very hard to judge the difference in performance between the various sections of the image are very hard to judge when comparing different scenes, also a commonly used test chart (USAF 1951) has been rendered using code V. The results for the various parts of the image are shown in figure 4.31. As can be seen in the figure, the performance in the center and edge of the frame is almost identical, with the corner being slightly softer.

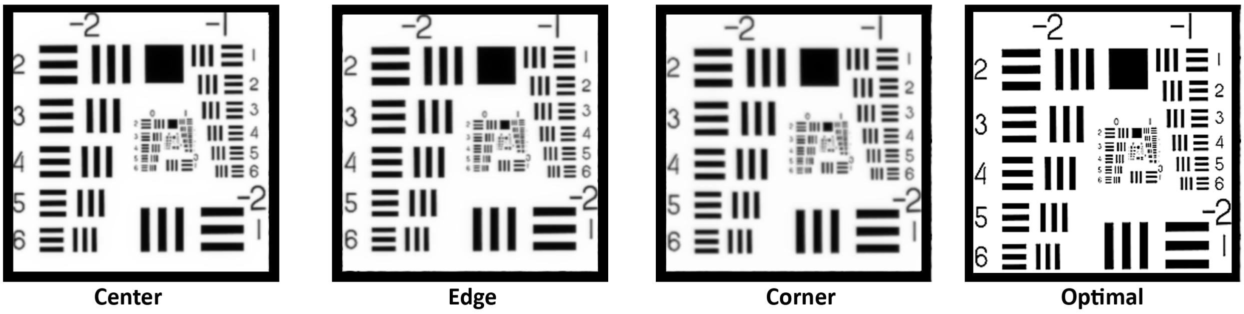

Figure 4.31: Images of the USAF 1951 test chart rendered using Image Simulation in Code V

All in all, the optical performance of telephoto system is very good. The MTF and spot diagram show that the optical performance is close to the diffraction limit throughout most of the image frame and image simulation results provide another confirmation of the optical performance. However, up until now it has been assumed that temperatures remain constant and that the system can be build exactly as specified. In reality, both production and temperature shifts can have a huge impact on the optical performance. These effects will be analyzed further on in this chapter.

4.8 Filters

In this section the filter choice will be described. The text focuses on the red, green and blue filter, but also hints to to other filters that might be added. First the criteria for the filter selection are discussed, then a choice is made for the filter bandwidth taking into account the SNR and the resolution. Finally a list of COTS components is given.

Selection of Filters

In order to select a certain wavelength for the camera the best technology to use is dichoric multiple cavity filters [60]. Dichoric filters can be applied to almost any optical surface as long as it is not curved, hence the filter cannot be incorporated in the lenses. The problem is finding the right filter.

In order to meet as many markets as possible 3 to 5 color filters must be chosen. A red-pass filter, a blue-pass filter, a green-pass filter, a UV-pass filter, and a NIR-pass filter. By doing this the customer can choose the wavelengths he wants to view. By reviewing the glass properties of the lens materials it is clear that UV sensing is no longer an option. A NIR wavelength is feasible however the resolution will decrease. In order to eliminate chromatic aberrations the bandwidth has to be as narrow as possible. When the bandwidth of the filter is very narrow, for example 10 nm, the chromatic aberrations are small, but beyond that the aberrations increase noticeably with bandwidth. However having a narrow bandwidth reduces the SNR. Most colors have a range of about 70 nm (only 40 nm for blue). [61] To make a true color image it is best to stay close to these wavelengths however some overlap can be allowed of course. The size of the instrument makes it impossible to achieve a signal to noise ratio comparable to for example ENVISAT, however a sufficient SNR can be obtained by choosing the right filters.

It is imperative that all but the desired wavelengths are passed to the sensor. Unfortunately a narrow bandpass filter usually also has a small rejection region, usually ending before 800 nm, which means some infrared light might hit the sensor. As can be seen from 4.32 the sensor is sensitive up to about 1000 nm. In order to block the infrared one mirror could be made a cold mirror, or a hot mirror could be placed in front of the optical path. The infrared blocker is not required for every filter. Some filters have a rejection region large enough to block the unwanted light by themselves. This also mainly depends on the number of cavities in the filter. Although wavelengths larger than 1 μm will not give a signal the hot mirror after may still be added, to protect the sensor from the focused heat from NIR spectrum radiation. The NIR region still has a lot of energy in it. However the use of the hot mirror also reduces the transmission lowering the signal to noise ratio. Preventing the sensor from heating however, will improve the signal to noise ratio. This means that at some point a detailed thermal noise calculation will have to decide upon the use of a hot mirror. In principle the hot mirror is not used in the design. The filter will have to have a bandwidth between 50 and 100 nm wide. The first look at suitable filters comes from the Mars rovers. [62] These filters have shown to be very reliable and good performance, but COTS components are usually not this good.

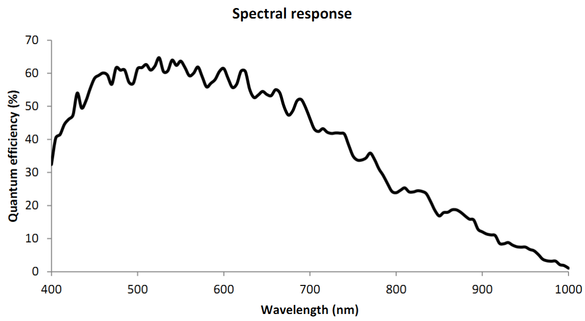

Figure 4.32: response of sensor [63]

Filter problems

Filters are meant to be used with collimated light. If the filters are placed in positions where the light is being focused, there is a small negative effect. The cone of the light is about 10 degrees. Therefore equation 4.26 applies. [64]

$$\lambda_\theta = \lambda_0 \cdot \left(1 - \left(\frac{N_e}{N^*}\right)^2 \cdot \sin^2(\theta)\right)^{\frac{1}{2}} \tag{4.26}$$

Here N_e is the index of refraction for the medium, 1 for vacuum, N^* is the effective index of refraction of the filter. Furthermore θ is then angle of incidence, and λ_θ is the center wavelength and λ_0 the center wavelength for zero degrees angle of incidence. For an effective index of refraction of 2 this will give wavelength shift of 1.5 nm toward the edges. Most filters have an index of refraction of about 1.5 to two. This will not affect the system because the waveband required for the signal to noise ratio will be much larger. More importantly is that when the filter is placed after the lenses, the orientation and position of the filter will affect to the performance of the optical system because it will affect the focal length and increase aberrations unless the filter glass is perfectly aligned and without surface roughness. If the filters are placed in front of the lenses, the light can be assumed to be collimated, however due to the field of view angle there is still an angle which means the light from the edge of the frame will experience a slightly different passband than the on axis light. This effect is negligible however. Another problem is that the narrower the bandwidth, the less the transmittance of the filter reducing the SNR even further.

Placement of the filters

Because of the effect on the focal length the best place to install the filter is in front of the first lens. Although having the filter in front of the sensor results in lower system weight, this is not a good solution because optical performance is more important than the weight. In front of the filter a thin glass window has to be placed to prevent the vulnerable filters from damage, since most filter coatings are extremely vulnerable.

4.8.1 Choice of filter bandwidth

Several possibilities for filters have been mentioned in this section. Now a choice for the bandwidth is made. The filter placement has already been discussed, hence the primary goal is to find the optimum combination of parameters to get both good optical performance and a high signal to noise ratio. As explained before increasing SNR and reducing chromatic aberrations come with completely opposing requirements for the filter. A wide band is good for the SNR, where a narrow band is results in less aberrations.

Bandwidth Green Light

The choice for the bandwidth for green light was driven by the several things but eventually it was decided by the aim for a high resolution. As can be seen from figure 4.34 the resolution drops really quickly once the bandwidth is larger than 80 nm. From figure 4.33(a) At that point the SNR is 15 dB which is sufficient. Therefore the bandwidth is chosen to be 80 nm. In figure 4.33(b) can be seen how the noise develops.

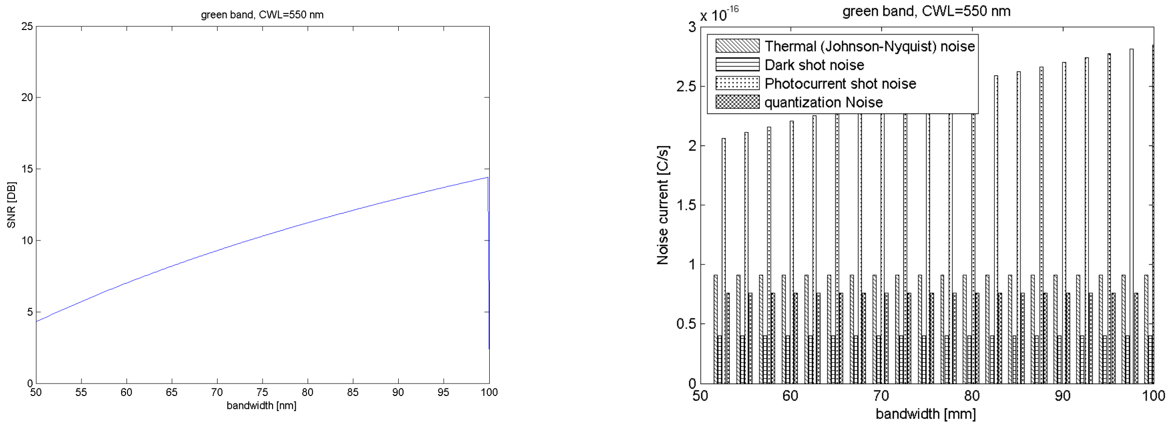

(a) Effect of waveband choice on SNR

(b) Noise as function of waveband

Figure 4.33: Greenband

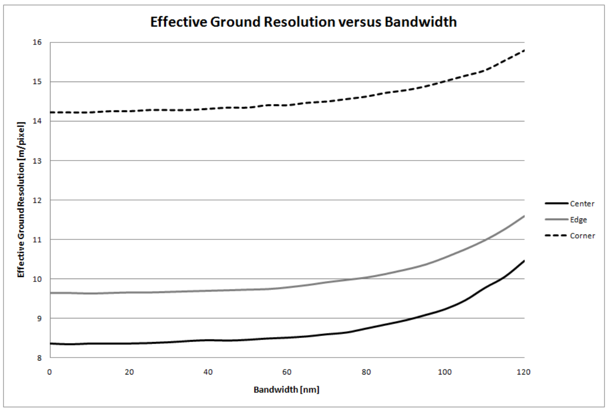

Figure 4.34: effect of waveband choice on resolution

Bandwidth other colors

For the other two wavelengths the story is a bit different. This is caused by the fact that the lenses are optimized for green light. The effect will be explained further in section 4.9. For blue light a large waveband is worse than a large waveband for green. Therefore waveband is chosen to be 60 nm This may mean that the SNR value is lower than the noise floor this is amplified because blue photons have more energy per photon. Since the amount of energy for blue is almost equal the number of photons is less. Unfortunately even with a narrower band the quality of the blue image is less than the green image. For the red band the waveband is chosen to be this case the waveband is also chosen to be 80 nm. With this filter the instrument has a good performance in red light. Plots of the SNR for blue and red light can be found in the electronic supplement.

4.8.2 COTS Filters

From a cost perspective the instrument is preferably constructed from commercial of the shelf products. Edmund optics has a small selection of high performance bandpass mirrors as COTS component. LOT-Oriel has a wide selection of commercial grade filters. It is clear from table 4.7 the performance is better than the ones from LOT-Oriel, however due to the small size of the selection no high performance filter was found for most wavelengths. For green and red the LOT-Oriel filter is chosen, for blue the Edmund filter. This shows that a custom filter component will have better performance more tailored to its use. The performance use of custom filters should therefore be considered. The curve for the green high performance filter can be found in appendix XX!! on the electronic supplement.

Table 4.7: COTS Filters

light color	manufacturer	transmission	thickness [mm]	bandwidth [nm]
green	Edmund	$\geq$ 90 %	3.5	468-552
green	LOT-Oriel	$\geq$70 %	7	510-590
blue	Edmund	$\geq$90 %	3.5	417-477
red	LOT-Oriel	$\geq$70 %	7	610-690

4.9 Full color imaging

As was described in the market analysis, for a system to rival existing technology, it is essential that full color images can be delivered. However, designing a small satellite that can deliver sharp results using the full waveband, was proven to be nearly impossible. Even though both elements used in the system are achromatic doublets, the chromatic aberrations are severe. Figure 4.35 shows that for bandwidths larger than 80 nm (centered around 550 nm) the effective ground resolution drops rapidly; the system clearly cannot take good images using a bandwidth that spans the complete spectrum of visible light.

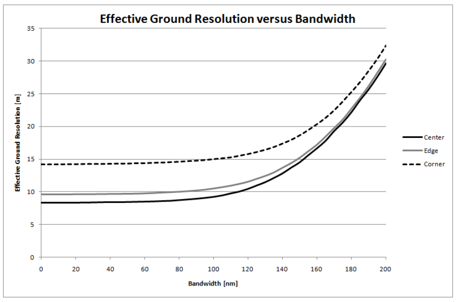

Figure 4.35: The effective ground resolution versus the bandwidth centered around 550 nm

Therefore, using the filters selected in the previous section, the optical system should be optimized for one specific waveband. The different wavebands will then be captured using different satellites and merged after the images have been send back to Earth. During the design process, green light was selected as the waveband to optimize for, but the system can be adapted to match other wavebands by shifting the sensor to correct for the chromatic focus shift. Figure 4.36 it can be seen how large a focus shift is required to optimize the system for a different wavelength.

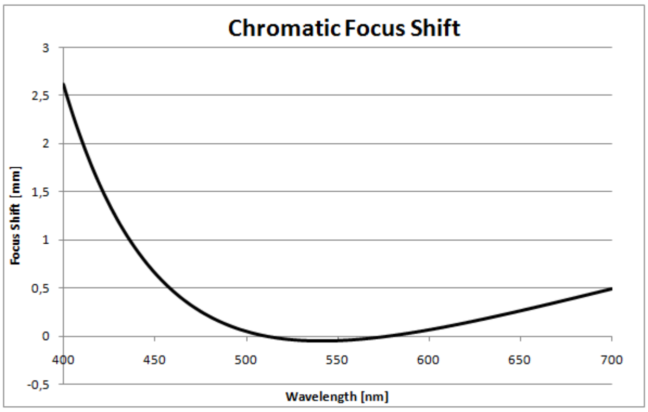

Figure 4.36: The chromatic focus shift versus the wavelength

While using a change in focus will optimize the system for a different waveband, it is obvious that the results will clearly not be as good as for the green waveband. The curve for the chromatic focus shift is relatively level between 510 and 590 nanometer - the waveband of the green filter - which means that the chromatic aberrations within this waveband are small. However, the curve is a lot steeper between 417 and 477 nanometer, which means that chromatic aberrations are much more severe in this section and a loss in spatial resolution can be expected.

When the effective ground resolution for a system capturing the blue waveband is determined using the MTF50 value, it can be found that an effective ground resolution of approximately 60 meters throughout the entire image can be achieved. Thus, there is a severe loss in resolution compared to the nominal case, which boasts an effective ground resolution of 8.7 meters in the center of the image. For the red waveband, there is also a drop in resolution, but it is not nearly as severe. The effective center resolution drops to 17 meters, while the EIFOV in the corner drops to 20 meters.

Figure 4.37 shows image simulation results of the different wavebands. In this figure it can clearly be seen that the performance of the blue system is significantly worse than that of the green and red systems.

Figure 4.37: Image simulation results for the three wavebands

When the images are blended, the good performance of the blue and red wavebands can somewhat compensate for the mediocre performance of the blue system, especially if the blue channel is sharpened aggressively. On the supplied DVD, full color samples can be found where this is illustrated. However, significantly better results could be obtained if the optical design for the blue waveband would be adapted to reduce the chromatic focus shift in this band.

4.10 Effects of production

Up until now, it has been assumed that an optical system can be build exactly according to the specifications. In real life, however, this is often impossible. An optical system is a high precision system, where even the smallest deviations of the specified dimensions will have a measurable effect on the optical performance. This occurs even when the most accurate production processes are used. In this section, the effects that the production can have on the system will be analyzed. First of all, the production tolerances of the achromatic doublets will be discussed. After that, the minimum tolerances that have to be taken into account during the assembly of the system will be determined. Finally, the determined tolerances have been used with the tolerancing module of Code V to analyze the effects of the production on the optical performance will be discussed.

4.10.1 Tolerances of the achromatic doublets

The achromatic doublets that are used in the optical system are mass produced to meet an accuracy that is typical for commercial optics. In table 4.8 the production tolerances that have been specified for the doublets has been listed. Most of the data has been retrieved from the datasheets of the doublets [65], but not all tolerances required to accurately model the effects of production were included in the datasheet. Tolerance values that were missing have been retrieved from the book Handbook of Optics, in which reasonable starting points for tolerance a lens system are given [66].

Table 4.8: Manufacturing tolerances of the achromatic doublet

Parameter	Tolerance
Glass thickness	± 0.2 mm
Radius of curvature	± 1 % of the radius
Tilt/Decenter	5 arc min
Surface roughness	± 1 fringe
Refractive index	± 0.0010
V-number	± 1 %

The tilt/decenter tolerance, also called the wedge tolerance, is the angular deviation from the optical axis that a beam going through the center of the lens will have after passing through the doublet. It can be modeled in Code V by tilting the first and last surface of the lens. The tolerances on the refractive index and the V-number may cause slight changes in focal length and the achromatic properties of the doublet and have therefore also been included. The tolerance was not included in the datasheet, but instead found in Handbook of Optics. The tolerance on the radius of curvature has also been retrieved from that book. While in principle, tolerances of the radius of curvature could be computed by using the focal length tolerance of 2% (as specified by Edmund Optics), instead the value that is typical for commercial production processes is used. The reason for this is that other parameters influencing the focal length have already been given tolerances. Therefore, setting tolerances for the radius of curvature in such a way that it can account for a 2% shift in focal length, will give an overly pessimistic view of the final performance.

4.10.2 Assembly tolerances

As can be seen in the last part, the specifications of the doublets can differ from the expected values. These are not the only tolerances that have to be taken into account, though. Inaccuracies in the placement of the lenses during production may also degrade the performance considerably. To find to what level of accuracy the lenses must be positioned, an inverse tolerancing process is used. Using this process, it can be analyzed how loose tolerances may be in order to guarantee that the decrease in performance does not exceed a certain value.

During the process, it immediately becomes obvious that it should be possible for at least one element to be repositioned in the final stages of the production process to accommodate for the shift in focal length of the doublets. The most obvious surface to select for this purpose is the sensor. By shifting the sensor towards and away from the final lens will correct the focus shifts which may be induced by the lenses. Additionally, allowing the sensor to be tilted slightly in the final states of the assembly can correct for some misalignment of optical elements.

Tolerances that have been taken into account are tolerances for the placement of all optical elements in three directions and tolerances for the way in which each of these elements may be tilted. As a measure of performance, the MTF at 30 cycles/mm is used, which gives a good indication of how the lens resolves detail. The nominal MTF at this frequency is 0.80 for the center, 0.76 for the edge and 0.67 for the edge of the image.

As a part of the inverse tolerancing process, also a sensitivity analysis is performed. In his process, the effect that each tolerance can have on the optical performance is analyzed. From this analysis it follows that even when loose assembly tolerances are used, inaccuracies that have the most effect on the optical performance are related to the two doublets. Especially the surface roughnesses of the optical elements and the wedge tolerances of the doublets have a major effect on the optical performance. When using loose assembly tolerances, the parameter that has most effect on the optical performance is the surface roughness of the rear surface of the doublet. The wedge tolerance of the doublet can, on its own, cause a drop in MTF of 0.08. By contrast, the assembly tolerance that has most effect on the optical performance, the deviation of the mirror angles, will only lead to a drop of 0.002.

Thus, it is clear that very tight assembly tolerances, will only have marginal benefits. To see the effect of using tighter tolerances, three sets of assembly tolerances, each allowing for a different loss in quality, have been determined using Code V. In table 4.9, the effect of these three sets of tolerances can be seen.

Table 4.9: The effect of several assembly tolerances. The table shows the maximum possible deterioration of the MTF at 30 cycles/mm for 97.7 percent of the cases

	Loose	Medium	Tight
Center	-0.09	-0.09	-0.09
Edge	-0.11	-0.10	-0.10
Corner	-0.20	-0.18	-0.17
Angular Tolerance [arc min]	17	8	1
Position Tolerance [mm]	0.5	0.2	0.05

As can be seen in the table, the center and edge performance are hardly improved by using tighter tolerances. The edge performance, however, does improve a bit. The medium tolerances that are used, are still achievable without highly specialized tools and there are no cost benefits for using tighter tolerances [67]. Using tight tolerances, however, will require precision equipment, which will increase the cost considerably. There is only a marginal improvement in image quality for the edge of the frame, though, which does not warrant the additional effort.

4.10.3 Effects on the optical performance

Assuming that the system will be manufactured according to the medium tolerances, the effect of production errors on the effective ground resolution can be evaluated. This is done with a Monte Carlo analysis. In this type of analysis, many combinations of deviations from the nominal specifications are tried to see how they influences the optical performance. Typically, many trials are needed to find a good estimate. In this case, 6000 trials were performed.

For every trial, the MTF50 value was determined, with which the effective ground resolution (EIFOV) can be determined. The results are shown in figure 4.38. The vertical lines in the figure display the nominal performance.

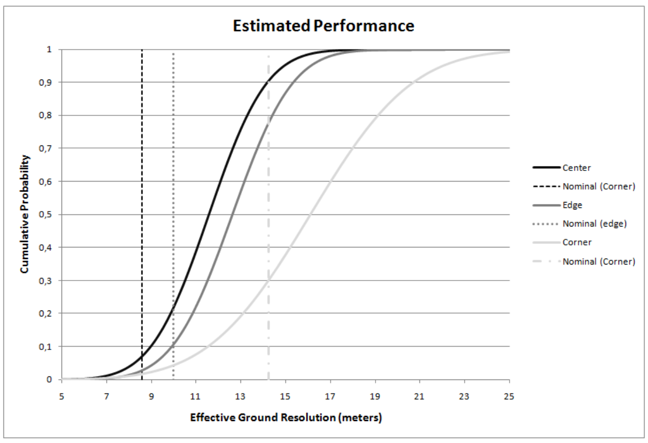

Figure 4.38: The effect of manufacturing on the effective ground resolution

As can be seen, there is a high likelihood that the system will not reach the nominal performance. Only in about 7 percent of the cases, the performance in the center will match the nominal performance or perform slightly better. The chance that the performance in the corner is better than nominal is larger, approximately 30 percent. It has to be noted, however, that a better than nominal performance in one corner is generally offset by a worse performance in another.

Even though the effective ground resolution drops considerably, performance remains acceptable. It is highly unlikely that the effective ground resolution near the the center and edge of the frame exceeds 15 meters. Performance in corner of the frame is likely to deteriorate a bit more, but, in 90 percent of the cases, the resolution will not exceed 20 meters, which means that even in the corner, the system is highly likely to provide a better ground resolution than the disaster monitoring constellation.

Figure 4.39 shows image simulation results of the nominal case and the worst case performance. As can be seen, while performance is visibly affected by the manufacturing inaccuracies, image quality remains reasonable and may be further increased using sharpening techniques.

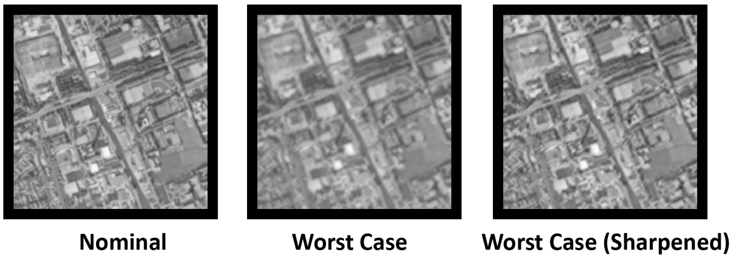

Figure 4.39: Simulation of manufacturing effects

To conclude, while the manufacturing process will visibly reduce the optical performance, the image quality will remain high. To reduce the effect of manufacturing, tightening the assembly tolerances is unlikely to have the desired effect. Custom build doublet lenses that are built with a higher accuracy should be used, but inquiries with several manufacturers of optical elements revealed that this is only done when large quantities of lenses are ordered.

4.11 Thermal optical stability

When the temperature of the optical system changes, several effects occur that will alter the optical performance. First of all, expansion of the mounting structure will mean that the distance between the optical components will change. Secondly, thermal expansion of the glass will result in changing glass thicknesses and, more importantly, a change in the radius of curvature. Finally, the index of refraction of the optical materials will change.

All these effects can result in a focus shift. Depending on the severity of this shift, the optical performance may drop considerably. This section will analyze the effect of temperature changes and propose several methods which can be used to compensate for these effects.

4.11.1 Effects of temperatures on the optical performance

When an aluminum allow with an expansion coefficient of 21.4 $\mu m/m$ is used as a supporting structure, the thermal expansion will lead to a major loss in ground resolution when the temperature changes. When temperatures are outside the range of 10 to 30 degrees Celsius, the effective ground resolution in the corner of the image will be worse than 20 meters. This loss of performance is unacceptable, particularly if the effect is combined with the degradation of performance due to manufacturing tolerances. It is therefore obvious that a material with a low expansion coefficient should be chosen as the mounting structure.

If SuperInvar is chosen as the supporting structure, the loss in performance is a lot more acceptable, as is illustrated in figure 4.40

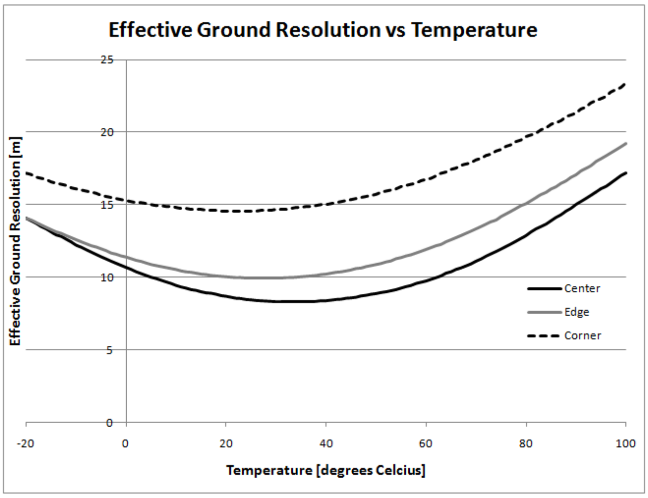

Figure 4.40: Thermal optical stability when using Superinvar

As can be seen, when SuperInvar is used, the effective ground resolution remains well below the 20 meters for the operating range of the sensor (-20 up to -70 degrees Celsius), which is a considerable improvement compared to aluminum. However, especially for colder temperatures, which may occur frequently during the orbit, the performance does drop quite a bit, which may become problematic if the effect is combined with that of the manufacturing tolerances. Therefore, it is desirable to include a means to compensate for the focus shift that results from temperature changes.

4.11.2 Focus shift compensation

To compensate for the temperature induced focus shifts, two methods are possible. The first method is to use an active compensation system. By placing the sensor on an actuator, focus shifts can be corrected and the performance will remain constant for the full temperature range. Disadvantages of such a system is that an actuator is a moving part, which, in case of failure could render the entire system useless. Thus, an actuator should be carefully selected and tested, should this option be selected

Alternatively, a passive system could be used. By using a polymer with a high expansion coefficient as the backing structure of the sensor, the sensor would move towards the last lens as the temperature increases. This will compensate the focus shift and make sure that the optical performance remains fairly constant for the whole temperature range, as is illustrated in figure 4.41. As a compensator, Nylon-11 (Polyamide-11) could be used. This material has a high coefficient of thermal expansion [68] and is not prone to outgassing [69].

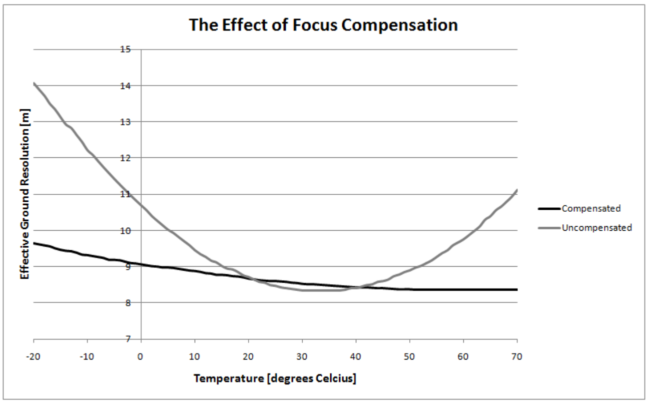

Figure 4.41: The effect of manufacturing on the effective ground resolution

4.12 Conclusion final optical design

To solve the problem of fitting a long focal length in a small nanosatellite, three concepts were developed: a cassegrain system, a system consisting of two parabolic mirrors and a focusing lens and a doublet-mirror system. During the trade-off, it was decided that the doublet-mirror system offered the most potential. The strengths lay in the optical performance and the overall thermo-mechanical stability due to the simple design.

Optimization of the optical system led to the inclusion of a second negative doublet to correct spherical aberrations and field curvature. The final design offers an excellent optical performance. The requirements regarding the resolution and field of view were met and even exceeded. The performance is sustained throughout a wide range of temperatures, and even though inaccuracies in manufacturing may affect the optical performance, the loss of performance remains acceptable. However, to provide full color images and to increase the signal to noise ratio, constellation options should be explored.

Chapter 5

Structural design

5.1 Structural design iterations

The structure of the camera system needs to meet two primary criteria. On one hand the structure needs to be stiff enough to carry the optical elements and sensor systems while surviving the launch environment. On the other hand the structure must be able to endure temperature changes that occur in orbit while maintaining its shape to a very high degree of accuracy. During the structural design several iterations have been made to meet both of these demands while keeping a close eye on manufactureability and system mass. After completion of an iteration a launch load evaluation was performed using the FEM analysis functionality available in Dassault Systèmes CATIA® (ver. 5.19) CAD application.

This section will start with an explanation of the box-in-box design principle that is employed. Basically four iterations are made and these will be described subsequently. The section will continue with a discussion on the lens and mirror mountings that are necessary to hold the optical elements, and the way these elements are attached to the rest of the structure. The necessity and purpose of the thermal correcting expanding sensor base is discussed thereafter. The section will conclude with a rendering showing the completely assembled Advanced Nano Telescope (ANT).

5.1.1 Structural design: Box-in-box (BIB) principle

After preliminary investigation of the thermal expansion properties of an aluminum structure, which is commonly used for satellite outer structures, combined with the length of the camera system and the probable thermal environment, it was determined that the performance of the optical system would be negatively affected if a simple structural solution is employed. This is due to the change in the position of the plates (the authors dubbed them *floors*) that carry the optical elements due to expansion of the supporting outer structure. Next to axial elongation even more problematic out of plane tilt of the floors could occur due to one sided heating of the satellite outer structure.

To combat these thermal problems a solution is devised that consists of a separate inner box structure within the deforming outer box structure. This inner box is constructed from material with a low coefficient of thermal expansion (CTE) which would meet the necessary shape retainment within the thermal range that is expected to be encountered. The inner box is rigidly clamped to the outer box at one edge and slider connected over its length. The slider connections allow the outer box to expand axially without affecting the inner box, still allowing for lateral structural support between the two. This setup is dubbed the box-in-box (BIB) design strategy by the authors and is employed in all iterations. See figure 5.1 for a schematic of the principle.

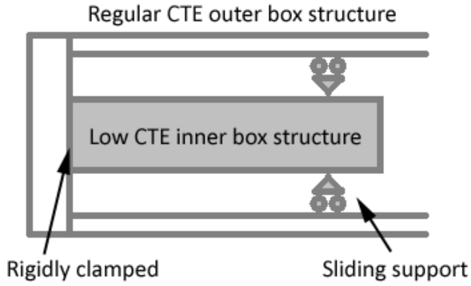

Figure 5.1: Schematic of the box-in-box support structure principle. The low CTE material of the inner box will retain its shape independent of thermal expansion of the outer structure.

5.1.2 Structural design: Iteration 1

Starting the structural design a reference satellite is used to serve as an indicative support structure from which the structural design of the camera system payload can be determined. The reference satellite structure used is that of the Delfi-n3Xt satellite. The empty satellite outer structure into which the camera system under consideration would be installed is shown in figure 5.2(a). The camera structure would fill half of this outer structure. The rods are 3.2 mm in diameter and made of steel and the 1 mm thick cover sheet is made of aluminum. For the first iteration a model is designed within the CAD program of which a rendering is shown in figure 5.2(b).

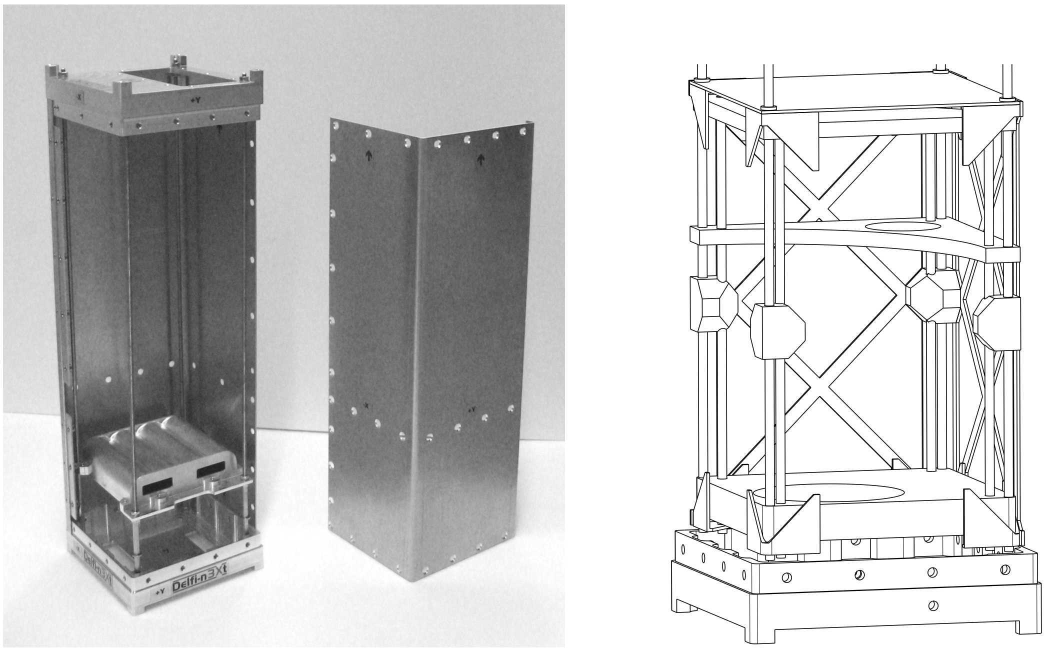

(a) The outer structure of the Delfi-n3Xt satellite. The camera system will take up half of the space shown, where the other space is used for the satellite bus hardware.

(b) First iteration support structure. Note that the crossed side plate structures shown on the back side are present on all sides but are removed to allow an unobstructed view of the interior structure. The camera system will fill about half of the outer structure shown in the left figure.

Figure 5.2: Images of the outer structure and the design of the first iteration.

The base of the outer structure as shown on the left image is also shown at the bottom on the right image. This base will have a hole drilled to allow the primary lens to receive light. For easy viewing of the support structure it has been lifted out of the base that is part of the outer structure. The actual configuration is that the camera structure is sunken into the base, with only a few millimeters of spacing between the lower plate of the inner structure (called *floor*) and the base surface to negate conductive coupling of the inner and outer boxes as much as possible. The lower floor is rigidly connected to the steel rods of the outer structure. The hole in the lower floor in which the primary lens mounting is fitted can be seen on the bottom. The optical elements are not shown. Note that the 1 mm thick crossed side plate structures shown on the back sides are present on all sides but are removed to allow an unobstructed view of the interior structure. Placed at the four corners are a total of eight solid rods of which the inner four are rigidly connected to the three floors that hold the optical elements. The inner rods span only the length of the camera system and are terminated at the top floor (about half the satellite length). The outer rods on the other hand are an integral part of the outer casing of the Delfi-n3Xt satellite, as is shown in figure 5.2(a), and span the entire satellite length connecting both outer endplates. As discussed in section 5.1.1 the inner box, consisting of the floors and inner rods, is made of a low CTE material and is connected using sliders to the outer steel rods that are part of the outer box. Additional blocks are inserted at half height to increase the lateral rigidity between the rods. Note that for this iteration the crossed side plates are made of aluminum and are rigidly attached to the outer box structure at the clamped end. The triangular strips that are displayed at the corners are used to rigidly attach the crossed side plates with the top plate and the outer rods. In effect everything bar the inner rods and floors are part of the outer box structure. This model was analyzed using the CAD program FEM functionality to check if it would survive the launch environment.

5.1.3 Structural design: Iteration 2

The second iteration started from the launch load analysis results of the first iteration. The launch load analysis indicated that the inner rods could not carry the floors and optical mountings due to the axial loading. To solve this problem several changes were made. The floors, lens mountings and mid height blocks are milled to reduce their mass. The inner rods are removed in preference of directly attaching the crossed side plates onto the floors. With the crossed side plates assuming the role of maintaining the spacing between the floors, it is automatically mandated that a low CTE material is used for their manufacture. The triangular strips at the edges that are used to fix the crossed side plates to each other and to the top plate are changed to a low CTE material. This is to avoid thermal strain problems that would otherwise occur between the side plates and the triangle trips. These strips are made such that they now can slide along the outer rods, and the aluminum top plate that was connected to these strips is removed. Furthermore material is added to the crossed side plates to further increase stiffness. The second iteration is shown in figure 5.3(b).

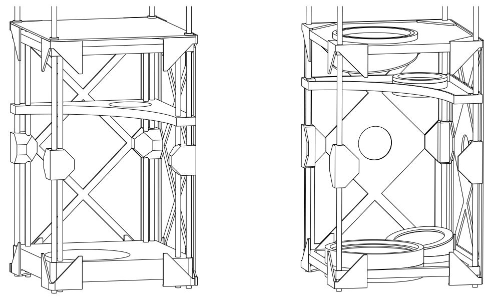

(a) The first iteration repeated here for easy comparison purposes.

(b) The second iteration. On the lowest floor the primary lens and secondary mirror can be seen. At and near the top the primary mirror and the secondary lens are situated.

Figure 5.3: First and second iterations of the structural design.

5.1.4 Structural design: Iteration 3

The launch load analysis of the second iteration indicates that a slight increase in structural stiffness is necessary. Therefore material is added to the crossed side structure and removing the central hole proved to be beneficial for the structural stiffness. Also stringers are added to the floors to increase stiffness. Both an infrared filter and a narrowband filter are incorporated to make sure only an intended small waveband of light incidences on the sensor. These filters are placed around the secondary lens, and are housed together within the elongated lens mounting tube. Furthermore two metal light baffles are added to the primary lens and the secondary lens with the aim of blocking light rays that potentially fall onto the sensor without following the intended light path. These light baffles are sized such that they have the maximal length without interfering with the light rays following the correct route. These tubes are made from the same low CTE material as where the lens mountings are made of to minimize possible fringing effects. The third iteration is shown in figure 5.4(b).

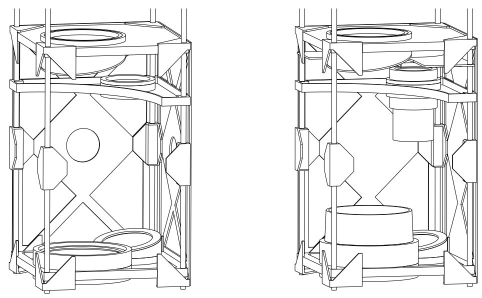

(a) The second iteration repeated here for easy comparison purposes.

(b) The third iteration. The crossed side plates are reinforced. Furthermore optical filter components are added around the secondary lens and light baffles are added.

Figure 5.4: Second and third iterations of the structural design.

5.1.5 Structural design: Final iteration

The main difference between the final iteration and the third iteration is in the placement of the filters. From theory is determined that inserting a square glass (i.e. glass with parallel surfaces perpendicular to the incident beam) into a converging beam would cause a shift in focal length. Ray trace analysis then showed that the image quality degraded regardless of optimization of focal length. Therefore it was decided to move the optical filters in front of the primary lens where the beam was still a collimated (parallel) beam. Furthermore with careful selection of the narrowband filter, i.e. making sure the opaque portion remained opaque until sufficiently long wavelengths, the transmitted longer wavelength light would exceed the wavelength range detected by the sensor. This resulted in elimination of the separate IR filter, bringing the total filter thickness back from 10 mm to 7 mm (reserved) space. The changes resulted in a slimmer secondary lens mounting and an increased primary lens mounting size and proved beneficial both from an optical as well as a structural point of view. An additional glass protection cover was necessary since the filter material is sensitive to the atomic oxygen environment and is the only optical element that is directly exposed to the outside space environment. Also in this final iteration the sensor and circuit board are backed by the focus shift compensating expanding base. This base compensates for the reduction of the focal length that occurs when the temperature of the system changes. The final design is shown in figure 5.5(a) with a diagonal section of the system shown in figure 5.5(b).

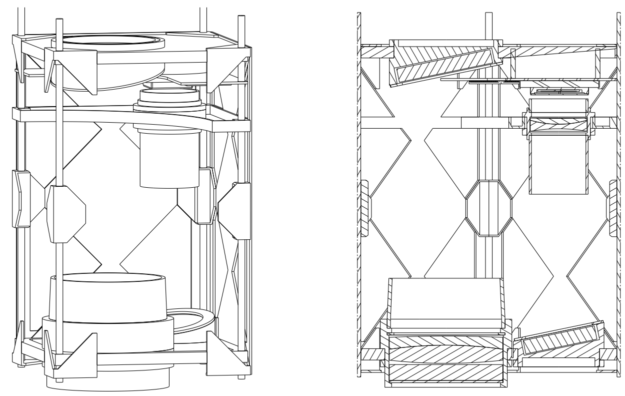

(a) Final iteration of the structural design.

(b) Diagonal cross section of the final structural design

Figure 5.5: Images of the final iteration

5.1.6 Optical mounting design

The optical mount is an important part of the structure that attaches an optical element to the supporting structure. The importance of this element comes from the fact that the alignment of the optical element must adhere to a high degree of accuracy while being exposed to changing thermal conditions. Any fringing of the optical material due to thermal expansion induced stresses could cause severe degradation of the optical performance. A correctly designed optical mounting will allow the optical element to expand due to thermal changes while still restraining the element in its design orientation. With space applications another difficulty arises due to the launch environment. Any optical component must be held within its mounting with enough force such that the usually glass like material will not be damaged during their ascend. This is usually achieved by pretensioning the optical component within its mounting to such a degree, that no axial or lateral force encountered during launch can cause a shift of the optical component. Unfortunately pretensioning oppositely affects the ability of the optical element to deform during temperature changes which appears to result in a stalemate.

Elastomer

The lens mounting design paradigm usually employed for allowing thermal expansion while still applying pretension is using elastomer material. This material has a CTE that according to [70] obeys the general rule as shown in equation 5.1.

$$CTE_{lensmaterial} < CTE_{mountingmaterial} < CTE_{elastomer} \tag{5.1}$$

The lens is placed against the mounting material on one side while on the other side the elastomer material is placed in between the lens and the mounting. Without the elastomer, when the temperature would increase the outer mounting material would expand at a greater rate than the lens, causing the lens to be loosened in its mounting. By adding the elastomer which will expand even more than the lens and the mounting, the tight fitting of the lens will be retained. For the purpose of space operation several space grade elastomers are available.

Flexure mounting

For the lens mounting design one possibility for constraining the lens is using flexure mountings. In this solution use is made of multiple metal strips. One side of such a metal strip is bonded to the lens rim while the other end is connected to the inner mounting surface in a direction along the lens rim. The strips are attached along the lens rim with equal separation and all have the same direction. Once temperature changes occur the strips allow the lens to expand as required due to their lateral flexibility. The flexures themselves also expand longitudinally, but due to the flexure orientation this expansion only rotates the lens around its axis without out of plane rotations. See [70] page 115 for further details. Note that for survival of the launch environment the amount of flexures should be sufficient to negate the possibility of the lens impacting the mounting inner surface.

Applicability to the current design

The material that is used for the mountings was chosen to be Super Invar® (see 5.2 for a further discussion on the chosen materials). This is done to minimize possible fringing problems that could occur when the mounting material would expand more than the Super Invar® floor material, causing possible alignment issues within the optical track. The current design has ZERODUR® as mirror substrate material, which has a lower CTE than Super Invar®. This allows the usage of the elastomer solution for the mirror mountings. Unfortunately the lenses consist of regular lens glass materials such as N-BAK4 and N-SF10 that exceed the mounting material CTE to a large degree. This means that a different solution must be employed for the lens mounting design. For the current design flexure mountings are chosen for the lenses. The flat optical elements that are made from optical glasses like the filter and filter protection glasses are fixed using simple metal clips as the chance of misalignment due to thermal expansion is deemed low.

Primary lens mounting

The primary lens mounting consists of a Super Invar® casing that holds a set of optical elements. An exploded view and a cross section of the optical elements contained within the optical mounting is shown in figure 5.6.

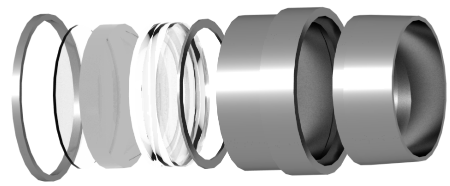

(a) Exploded view rendering of the primary lens assembly.

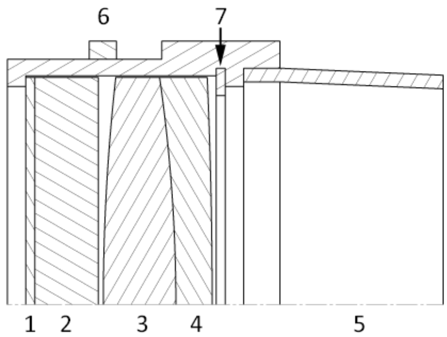

(b) Cross section of the primary lens assembly.

Figure 5.6: The elements within the image are: 1) filter protection glass, 2) optical filter, 3) doublet lens crown glass, 4) doublet lens flint glass, 5) light baffle, 6) fastening ring, 7) aperture stop ring. Note that the metal clips and flexures are not shown. Margin space to allow for the flexures is incorporated in the mounting wall thickness.

The optical elements which light will encounter when it travels into the system (from the left in the image) will be shortly discussed next. The filter protection glass of 1 mm thick is encountered first, and has the function of protecting the filter from harmful atomic oxygen present in LEO orbits. The next element is the up to 7 mm thick narrowband filter that will filter out any other color that the sensor can respond to bar the one color the system is designed for. This filter can directly be put against the glass protective cover without any spacing or even be cemented together. The glass and filter are then prestressed against the narrowing of the circular opening at the edge and will be held using simple metal clips on the other end. The next optical element is the cemented doublet lens. This is attached to the cylindrical inner surface of the mounting using flexure mountings to ensure proper alignment in changing temperature conditions. The optical element that is encountered next is the precision fabricated aperture stop, which forms the intended bottleneck of the system from the perspective of the entrant light. This is held by metal clips on one end and by the light baffle on the other end. The light baffle is threaded as is the inner edge of the lens mounting and can be simply screwed in place.

Secondary lens mounting

The secondary lens mounting consists of a Super Invar® casing that holds the diverging lens. An exploded view and a cross section of the optical elements contained within the optical mounting is shown in figure 5.7.

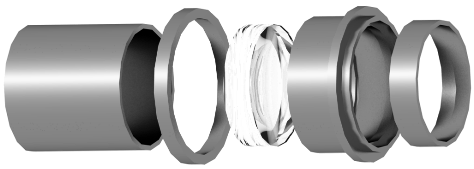

(a) Exploded view rendering of the secondary lens assembly.

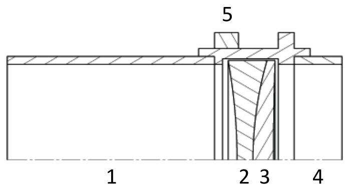

(b) Cross section of the secondary lens assembly.

Figure 5.7: The elements within the image are: 1) front light baffle 2) doublet lens crown glass, 3) doublet lens flint glass, 4) back light baffle, 5) fastening ring. Note that the flexures holding the lens are not shown. Margin space to allow for these flexures is incorporated in the mounting wall thickness.

The secondary lens mounting only contains the diverging (telephoto) doublet lens that is held using flexure mountings. Furthermore baffles are screwed into the mounting on both sides.

Primary and secondary mirror mountings

Both mirror mountings are the same in shape and only differ in their dimensioning. Therefore the remaining elaboration will apply equally well to both mirror mountings. The mirror mounting consist of a Super Invar® casing that holds the mirror. A simple capping ring fixes the mirror within the mounting and is secured using screws. An appropriate space grade elastomer is added to create a thermally stable mount and the complete assembly is prestressed. An exploded view and a cross section of the optical elements contained within the mirror mounting is shown in figure 5.8.

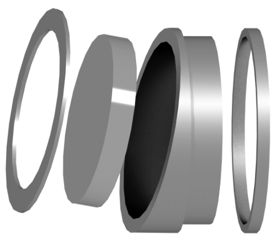

(a) Exploded view rendering of the mirror mounting assembly.

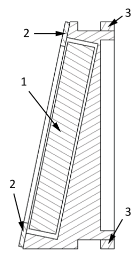

(b) Cross section of the mirror mounting assembly.

Figure 5.8: The elements within the image are: 1) mirror substrate treated with a high reflective coating, 2) capping ring, 3) fastening ring.

Mounting the mountings

Attaching the mountings to the floors is done through their cup like shape that can be placed into a hole that is drilled through the floor. The radius of the upper part of the mounting is 2 mm bigger than the hole resulting in the mounting not falling through. The mounting is then fastened by using a threaded annular fastening ring that is screwed onto the extruding mounting bottom part from the other end. After precision positioning the mounting orientation can be secured from movement using a simple screw drilled through the ring, floor and mounting to ensure no possible rotation of the mounting. This inability to rotate is especially important for the mirror mountings.

Thermal Correcting Expanding Sensor Base

Whenever a temperature change occurs the focal length of an optical system will be affected. This is due to the curvature changes in the lens material as well as its changing index of refraction. As temperature increases the focal length will shorten causing a defocus of the optical system. To mitigate this problem the sensor and circuit board are attached to the floor using a specifically selected thermal expansion material coupled with a certain dimensioning. The materials coefficient of thermal expansion and the dimensions are such that as a certain temperature change occurs, the sensor base will expand or contract exactly the same distance as the focal point moves. This allows the system to keep its focus regardless of the operational temperature conditions. An image of the sensor base is shown in figure 5.9.

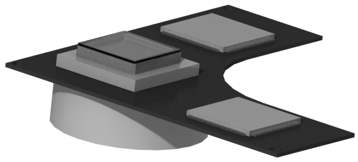

Figure 5.9: The sensor base, made up of a specifically selected material (Polyamide 11) and dimensioning to correct for thermally induced focal shift change.

The expanding sensor base consists of a 13 mm cylinder made of Polyamide (Nylon) 11 (see 5.2 for a further discussion on the chosen materials). The thermal properties of the material and the chosen cylinder length results in the correct amount of expansion to counteract the reduction of the focal point when temperature changes occur. The reduction in focal length with temperature was computed by the optical ray trace software and found to be a linear relation. The dimensioning of the backing material was then made using the simple thermal expansion relation.

An important point to mention is that for the computations of the expansion base dimensions it is assumed that all materials will have the same homogeneous temperature at each point in time. Due to the small satellite size coupled with the box-in-box design principle the assumption of a homogeneous temperature of the inner camera support structure is relatively trustworthy. The remaining uncertainty lies in the fact whether the lens and sensor base material attain a homogeneous temperature and the amount in which their temperatures differ at each point in time. This needs to be examined further before a more adept expansion strategy can be designed. Another point of attention is the low Young's modulus of the sensor base material. This proves difficult, but not impossible, to stabilize within the severe launch environment. Analysis showed that a more detailed design of the backing material is necessary to make the configuration stable enough, but arriving at a stable enough configuration using this material seems feasible.

5.1.7 Structural design: Final design rendering

A rendering of the final design is shown in figure 5.10. Note that in this rendering the materials are shown untreated. The actual internal structure will be coated with a black coating to absorb any stray light that might otherwise be reflected throughout the structure eventually incidenting the sensor surface reducing the image quality.

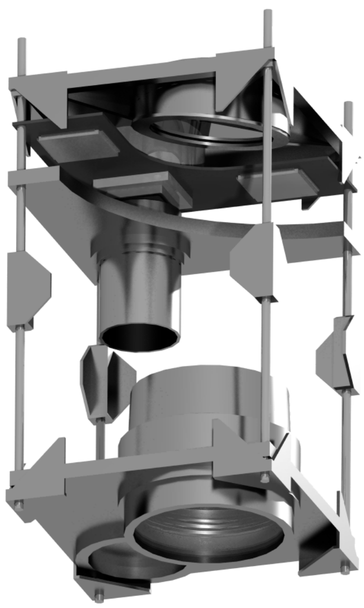

Figure 5.10: A rendering of the final design

5.2 Material selection

Factors considered for the selection of materials which will have to operate in a space environment are different than those used for Earth conditions. Besides using materials which have a relatively low mass it is also important these materials have a good thermal and dimensional stability for high precision optical space systems. The instrument has to resist a lot of heat cycles due to the fact the optical instrument is in a satellite orbiting the Earth. So fatigue of the materials due to the continuous expansion and contraction of the different parts also has to be taken into account.

5.2.1 Support structure

It was determined in section 5.1 the structure should be made from a material which is stiff and has a low coefficient of thermal expansion (CTE). A good way to find the right material for a certain structural design is using the specific stiffness. The specific stiffness can be obtained by dividing the Young's modulus by the density of a material ($E^{1/2}/\rho$) [71] visualized in figure 5.11(a). The Young's modulus is useful because it is a measure of resistance to elastic deformation which is important for vibration control [72]. Thermal effects also need to be taken into account so a measure for this is needed too. Next to thermal expansion also thermal gradients can pose a threat to the optical performance because this may cause a small change in structural shape. Thus a material with a high thermal conductivity can be beneficial to get a uniform expansion and contraction. The chance of optical misalignment can be reduced in this way. To select a material which has both a low CTE (α) and a high thermal conductivity (λ) one can divide these two properties (λ/α), which is imaged in figure 5.11(b) below.

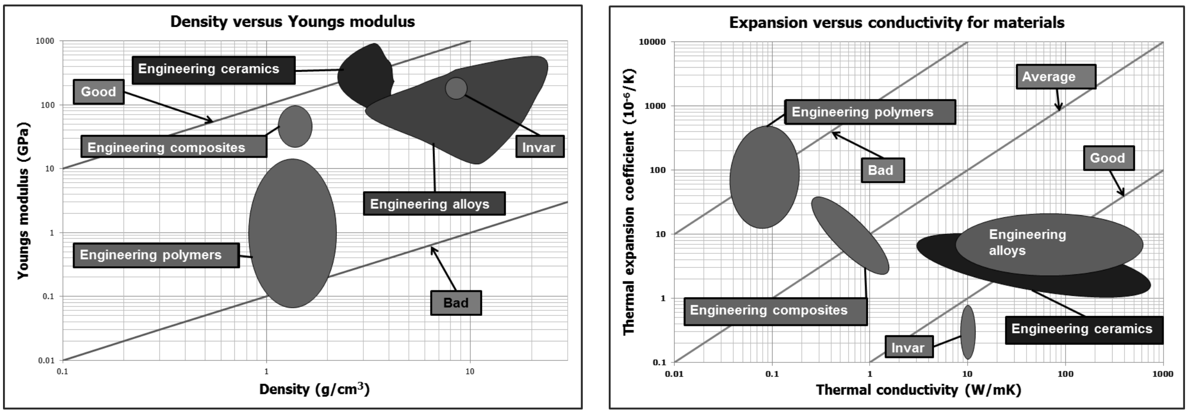

(a) Density versus Young's modulus for different materials. Charts created based on [73].

(b) Linear expansion coefficient versus thermal conductivity for different materials. Charts created based on [73].

Figure 5.11: Materials selection charts.

In figure 5.11(b) one can see a logarithmic plot of the thermal conductivity against the CTE of different material groups. Each dashed line represents a certain ratio which in general means if a number is high a good balance between these properties is found. It can be seen diamond (Engineering ceramics) has the best ratio by far but is very expensive and brittle. Therefore diamond is only suitable for very small precision instruments and not for a bigger supporting structure. One can see some engineering alloys like aluminum and beryllium are on the high ratio line. Beryllium would be a nice material to use if it was not so difficult to handle. Because of its high toxicity it is too dangerous for manufacturing and would involve a lot of additional costs [74]. Aluminum is also on the same high ratio line and could be a good choice. However it is on the higher end of the line and this means the CTE is relatively high. For a small optical space instrument it is better to look at the lower end of the line where one can find Invar. This material still has a medium thermal conductivity but a remarkably small CTE. So Invar seems to be a good material if one solely looks at thermal behavior.

In figure 5.11(a) the density versus the Young's modulus is plotted. In the top left the materials can be found which have a low mass and a high Young's modulus. Of course no known materials are in this region yet. Besides not all applications need a high Young's modulus. Engineering composites have a good Young's modulus to density ratio but a drawback is that their CTE is not as low as Invar.

Literature research showed that so called Super Invar® is often used for space instruments which require a very low coefficient of thermal expansion (0.630 $\mu m/m{-}°$C) [75]. Comparing the CTE of this nickel-iron alloy with the CTE of an aluminum alloy (RSA-443) especially designed for low thermal expansion (13.0 $\mu m/m{-}°$C) [76], it becomes apparent why this material is called invar(iable). Normal Invar was also considered, but as can be seen in figure 5.12 the CTE becomes relatively unstable outside the temperature range of -20 to 40 °C. Since there is a chance certain parts may experience temperatures outside this range, Super Invar® was selected, overcoming the shortcomings.

For the plates supporting the optical mountings honeycomb Invar was considered. These honeycomb panels potentially could be stiff and have a low mass at the same time. From the structural analysis it turned out thin Invar plates are already sufficient to withstand the vibrational loadings. It was decided honeycomb Invar is not necessary.

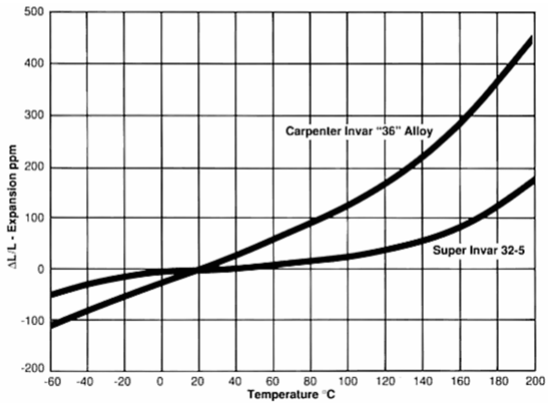

Figure 5.12: Comparison of the thermal expansion curves of Carpenter Super Invar 32-5 and Carpenter Invar 36 alloy. [75]

5.2.2 Optics & optical mountings

Material selection for the optical mountings is a special topic because most of the time different materials are used for specific parts. The use of several materials means that one has to deal with different properties. This can lead to deformation problems for the optical parts in certain cases. In order to avoid higher stresses on the optics than desired, the CTE of the elastomer has to be higher than the CTE of the optical mounting. The optical surface itself needs to have the lowest CTE of all three components [71].

The mirror mountings are made from thermally stable Super Invar® just like the main supporting structure. This is also beneficial to prevent stresses because of differences in the CTE's of the different materials. For the mirror substrates ZERODUR® can be used which is a glass ceramic and has a very low CTE (0.1 $\mu m/m-$°C) [77]. The lens mountings are also made from Super Invar® for the same reasons as for the mirror mountings. However the lenses actually have a higher CTE than the optical mountings which is not desired as stated before. In section 5.1 it is explained how this problem can be solved.

5.2.3 Outgassing

Outgassing is the phenomenon of adsorbed or trapped gases or water vapor which are released from a material. In most cases this happens under vacuum or high temperature conditions so in a space environment this is likely to happen [71]. Since optics and electronics are very sensitive for this disturbing process it is important that the selected materials fulfill certain outgassing requirements. In order to overcome the problem NASA has developed a method for selecting materials for space flight usage. The materials should satisfy two criteria: "A maximum total mass loss (TML) of 1.0 percent and maximum collected volatile condensible material (CVCM) of 0.1 percent." [78]. As a first step in analyzing if a certain material choice is right the NASA outgassing database can be used.

The thermoplastic Polyamide (Nylon) 11 which is used to compensate for the change in focal length has a TML of 0.64 and a CVCM of 0.05. This means that the material satisfies the outgassing criteria as stated by NASA. No outgassing data is available for Super Invar® so it can not be checked if it meets the requirements. However in the structural materials handbook of the European Cooperation for Space Standardization [79] it is stated that outgassing is usually not a problem for metals or ceramics because of their good material stability.

5.3 Launch load evaluation with respect to the structural design

As one is to put the system into the space environment, one will need to comply with the requirements as set by the launch vehicle. From the top-level requirements it became apparent that the space platform (i.e. the Delfi-n3Xt nano-satellite) is piggybacking on a larger satellite and that the combination is to be placed in the Ariane V launch vehicle. In order to supply a compliant system, that is a system that has completed the Ariane verification procedure successfully as provided in [80], one will have to resort to Finite Element Models (FEM) that are capable of predicting the behavior of the system with respect to static loads (5.3.1), vibrations (5.3.2) and shock loads (5.3.3).
The primary importance of such an analysis to this particular instrument, is that one has aimed for independence. The modular structure as proposed in section 5.1 shows that there is only a single mounting interface located at one of the main structural elements of the Delfi-n3Xt satellite. This single interface makes that the structure is cantilevered and relying on its own structural design, thus imposing a separate range of eigenmodes and load limits.

5.3.1 Quasi-static load analysis of the proposed design

During the launch of a respectable space system, it will experience a distinct number of accelerations which induce quasi-static loads on the structure as well as on the payload. The most dominant acceleration is caused by the longitudinal accelerations of each rocket stage by expelling mass as the rocket is burning fuel. When a rocket stage has burned out, an acceleration drop will be noticed because of a pre-defined coasting phase, after which the accelerations increase again when one has initiated a subsequent rocket engine.

From [80] a figure can be derived which shows the acceleration in terms of load factors against the total burning time of the launch vehicle, which according to [81] indicates the acceleration that is limiting for the structure including the Earth's gravitational acceleration and the Earth's rotation. The characteristic figure as discussed above is shown in figure 5.13, whereas the corresponding maximum values of the transient behavior as shown in figure 5.13 are given in table 5.1.

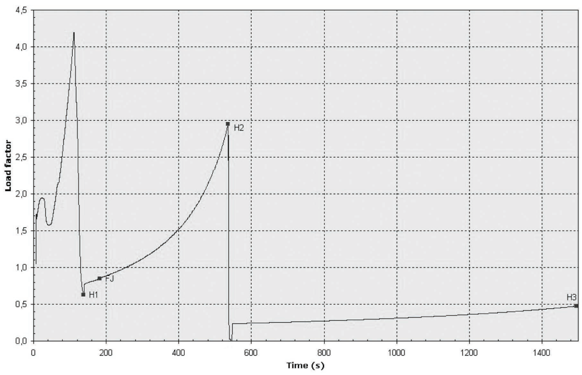

Figure 5.13: Static and dynamic loads as experienced within the launch vehicle (Ariane 5) fairing against time, adopted from [80]

Table 5.1: Limiting load factors within the launch vehicle (Ariane 5) fairing as derived from figure 5.13 as adopted from [80]

Acceleration (g) / Critical flight events	Longitudinal		Lateral	Additional line load (N/mm)
	Static	Dynamic	Static + Dynamic	
Lift-off	- 1.8	± 1.5	± 2	10 (15*)
Maximum dynamic pressure	- 2.7	± 0.5	± 2	14 (21*)
SRB end of flight	- 4.55	± 1.45	± 1	20 (30*)
Main core thrust tail-off	- 0.2	± 1.4	± 0.25	0
Max. tension case: SRB jettisoning	+ 2.5**		± 0.9	0

As can be seen from figure 5.13, there is a clear distinction between static and dynamic longitudinal accelerations. The former caused by the steady-state response of the system to the transient load factor behavior of the launch vehicle, i.e. one assumes that the period of the frequency response function of the instrument is very small in comparison to the period of the transient load factor behavior as shown in figure 5.13, the latter caused by low frequency mechanical oscillations. In order to present the limiting load factor in either the longitudinal or the lateral direction one will need to add both the static as the dynamic load contributions such that the load factor are in fact higher than those shown in table 5.1.

The structure has been modeled to cope with the quasi-static launch loads as such, meaning that all deformations are being considered. As the structure is not allowed to deform plastically, one should take the yield strength of the dominant material into account, i.e. the Super Invar®(≈ 276 MPa) plates that build-up the structure. Performing the already proposed Finite Element Methods (FEM) would present the stresses emerging within the system when subjected to the load factors as presented in table 5.1. As the load factors are essentially acceleration presented in the longitudinal direction with respect to the launch direction (i.e. a minus sign indicates a downward component), a rather low average stress was expected because of the lack of mass of a multiple of structural components. This expectation was confirmed by the FEM analysis, showing a range of stresses from 0 MPa up until 0.452 MPa. This maximum stress components was measured at the smallest taper of the side plates, which is considered to be correct since these side plates were designed in order to carry most of the longitudinal loads.

5.3.2 Evaluation of the natural frequencies of the proposed design

The evaluation of the natural frequency of the structure should present a dominant role in the overall dimensioning of the design. As the natural frequencies and its corresponding modes describe the resonance behavior of the structure, a trade-off has to be performed between the structural mass ($\bar{m}$) and the structural stiffness ($\bar{k}$) according to the general eigenfrequency equation as given in equation 5.2.

$$\omega = \sqrt{\frac{k}{m}} \tag{5.2}$$

The vibrational analysis may be divided into two distinct sections: the mechanical vibrations induced by sinusoidal loading and the loads caused by random vibrations and acoustic loading. The latter should pose restrictions on the actual eigenvalues as possessed by the instrument, thus also on the stiffness.

Sinusoidal loading induced mechanical vibrations

As the satellite is being brought to its insertion altitude by the respective launch vehicle it will experience a wide range of low frequency dynamic loads caused by the dynamic loads of the launch vehicle, i.e. from [80] it can be derived that the system is to withstand a 1.25g (including safety factor) for a frequency sweep up until 100 Hz. The structure of the instrument is because of its size and purpose (designed to be a high performing optical instrument) considered to be rather stiff, and this assumption is being supported by the FEM analysis, thus one is allowed to neglect these low frequency vibrations knowing that the eigenfrequencies are well beyond the low frequency range.

Random vibrations caused by acoustic excitations

There are a distinct number of sources of acoustic disturbances on or along the launch vehicle, e.g. the acoustic loads emerging from the combustion of flammable gas in the combustion chamber, but also the vibrations caused by the expanded gas coming from the nozzle which is being reflected by the launch platform as described in [81]. The spacecraft or in this case the instrument is to be able to withstand these vibrations, that is it should not meet one of its eigenfrequencies throughout the full frequency band.

The characteristic of the acoustic loading however is random, such that there is no predefined frequency at a certain point in time, one however is capable of defining the power of the acoustic load as a function of the frequency band. This type of random loading will propagate through the launch vehicle as mechanical vibrations or the acoustic loading will impact on the sides of the instrument by penetrating the fairing. From [81] it becomes clear that a larger system is more susceptible to the acoustic pressure loading, because of the acoustic energy impacting on the satellite's surfaces which contain a lot more area. For smaller instruments or satellites however it should be noted that the random vibrations are far more significant, because of the low tolerance with respect to displacements.

As the satellite which hosts the ANT is considered to be very small, i.e. far less than 250 kg, one will only have to take the random vibrations into account. As can be seen from table 5.2, a wide range of frequencies has to be taken into account including a predetermined safety factor of 1.41 as given in [80], i.e. one will need to consider to design the system as such that its eigenmodes are not excited assuming that every acoustic frequency has enough energy to excite a corresponding eigenmode.

Table 5.2: Random frequency sweep including acoustic wave field, adopted from [80]

Octave band centre frequency (Hz)	**Qualification Level (dB)**	**Protoflight Level (dB)**	**Acceptance level (flight) (dB)**
	ref: 0 dB = 2 x 10^{-5} Pascal		
31.5	131	131	128
63	134	134	131
125	139	139	136
250	136	136	133
500	132	132	129
1000	126	126	123
2000	119	119	116
Overall level	142.5	142.5	139.5
Test duration	2 minutes	1 minute	1 minute

A finite element analysis performed on the final iteration will yield the values for all eigenfrequencies (and their corresponding eigenmodes). Such an analysis should verify that the structure in its preliminary phase is capable of handling all random vibrations caused by acoustic sources. One considers that with regard to the total potential energy of the system, only the first three eigenmodes are viable to occur in nature. The system is designed as such that its first resonance frequency is above the highest random vibration (including safety factor), but with regard to a finite stiffness. This means that the first eigenmode occurs only at a few hertz higher than the earlier defined random vibration.

The results of the finite element analysis with respect to the frequency response are given in 5.3 for the first 5 eigenmodes. From the table it can be read that the requirements set by the vibration conditions are met.

Table 5.3: Eigenfrequencies computed for a range of eigenmodes using FEM techniques

Number of modes	Frequency (Hz)
1	2925.13
2	3916.37
3	4381.59
4	5143.39
5	5230.14

5.3.3 Single-event shock loads

Shock loads are very common to occur within the time spectrum of the mission of a satellite and thus also within the spectrum of its instruments. As the instrument is launched into space carried by the launch vehicle, it will endure a number very rapid transient shocks that will coalesce with the separation of the different launch stages. Another source of these highly transient loads is the insertion mechanisms used in order to place the parent satellite into the predetermined orbit, since mostly explosive charges are used in order to separate the two objects.

The shock load will, since it is a very rapid transient load, travel through the mounting interfaces to instrument. These loads are characterized by very high accelerations corresponding to equally high transient vibrations, which however are highly damped. Recall the discussion about the eigenfrequencies in section 5.3.2, in which a very high eigenfrequency was selected in order to enhance the modular performance of the instrument, i.e. assuring that the system itself can be considered to be commercial of the shelf (COTS), but also in order to withstand the full range of acoustic vibrations. As the resonance frequencies of the proposed structure are assumed to be very high, this also indicates that high loads due to single-event shocks are expected, however for a very small period of time.

It may thus be assumed that shock loads behave like pulse loads, i.e. it may be assumed that the timespan in which the structure experiences an increased load factor is infinitesimally small. Referring to the second-law-of-mechanics, the total momentum of the load is relatively small. Therefore, one could model for such occurrences. As the timespan of occurrence is infinitesimally small, one assumed that no eigenmodes are excited because of the rapid sweeping through the frequency spectrum.

Knowing that the momentum of the load is very small, and noting that it is impossible to model the highly damped transient behavior of the shock load itself (it is indeed very complex), one will need a tool in order to design the structure accordingly. Such a tool is presented by [80], namely the Shock Response Spectra (SRS) through the interface. The SRS provides a visualization of the severity or damaging behavior of a shock [81], by indicating the maximum response of a Single-Degree-Of-Freedom (SDOF) system with a characteristic eigen-frequency. In other words, the SRS shows the maximum response for an infinite number of SDOF's each with a different resonance frequency.

Referring to table 5.3 and figure 5.14, it can easily be seen that the instrument should be modelled as such that it can withstand a load factor of 2000g for an infinitesimal amount of time (a pulse load). From a Finite Element Analysis (FEA) it became apparent that the maximum stress occurring in the load bearing parts of the structure, which are all of Super Invar® to provide a thermally stable system, is equal to 134 MPa. Comparing it to the yield stress of the material (276 MPa), as the structure is not allowed to plastically deform, yields that the structure is able to withstand the full shock spectrum.

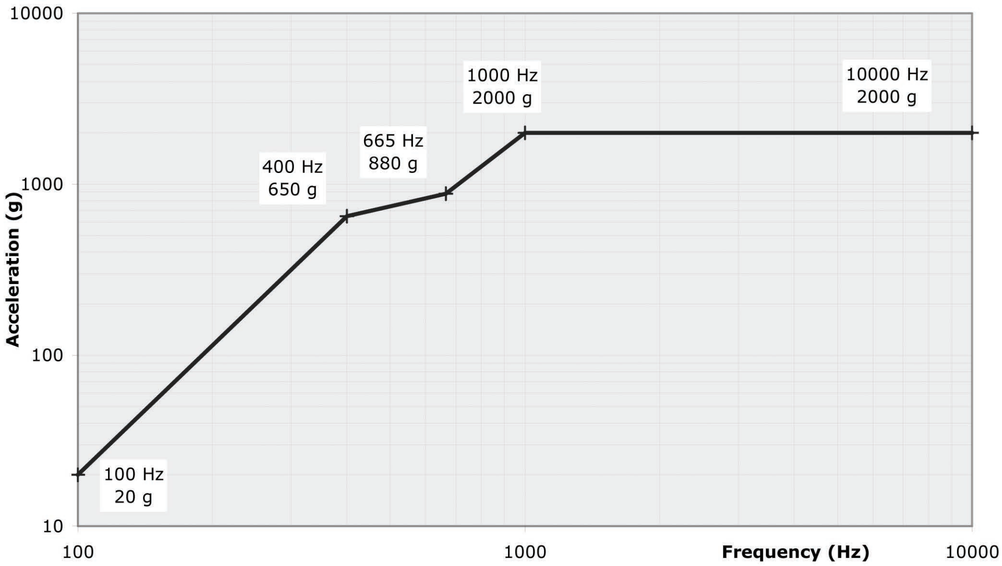

Figure 5.14: Shock Response Spectrum of the satellite interface of the Ariane V launch vehicle

Chapter 6

Electrical system and data handling

Until now the project addressed several major design topics in order to develop the ANT. However a crucial part of the instrument, the electrical subsystem, has not been treated yet. So far the only electronics related section was on the sensor choice in chapter 4. Now the question arises how is this optically suitable sensor actually operating and what electrical system supports it? Using the block diagrams shown in figure 6.1 the electrical subsystem of the ANT is presented, giving an overview of the involved components. The arrows between the blocks indicate interactions between electrical components like data flows or command signals.

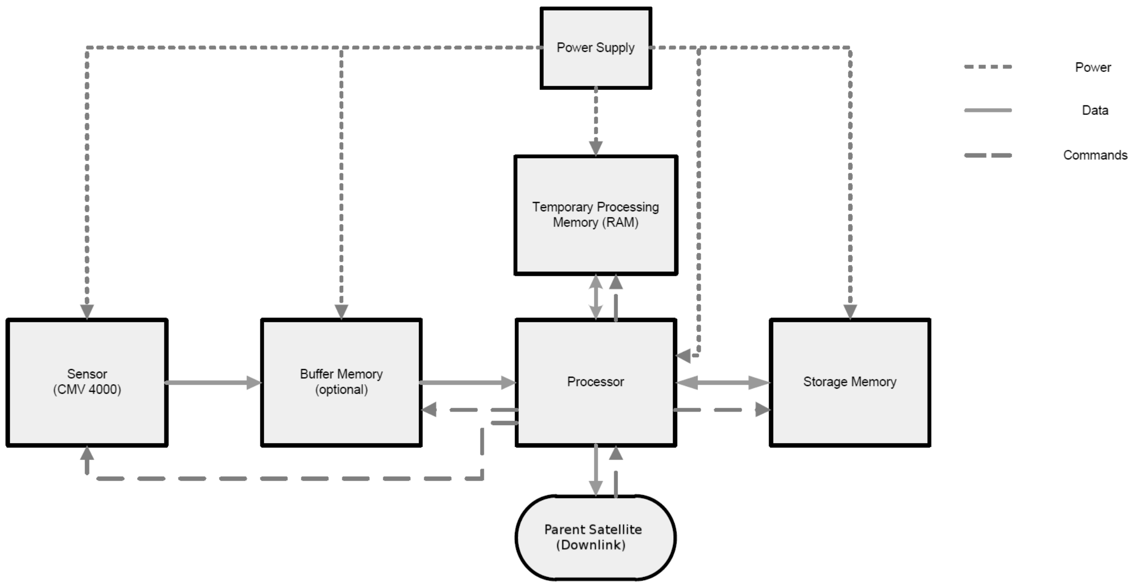

Figure 6.1: Hardware block diagram.

6.1 Diagrams

The very first object of interest in figure 6.1 is the sensor on the very left of the diagram. The choice for the CMV4000 was made earlier in chapter 4 according to requirements imposed on the ANT. The sensor is the unit actually capturing the image projected onto its measurement surface and transforming the image into raw data. Secondly the processor, which can be seen as the brain of the electrical system, is the commanding unit of the entire system. From the processor every other electrical component can be controlled via the commanding channels. The processor therefore controls the sensor, so tells it when to capture an image. Furthermore the processor is, as the name indicates, the unit processing the raw data the sensor produces. Following the raw data from the sensor, one finds a buffer in between the sensor and the processor. This unit is an optional component, which might be needed in case the amount of data coming from the sensor is too much for the processor to handle. The buffer then stores the raw data until the processor is able to process it. Once the raw data reaches the processor, the processor can either immediately start processing or store the data on the available short term memory and retract it once needed. For long term storage there is a separate unit available, which can be seen to the right of the processor. In principle this concludes the duties of the electrical system for the observation unit; however the processed data needs to reach the Earth at some point. For this there is a connection with the parent satellite. General communication between the ANT and the parent satellite can take place over this connection as well as image data transfer to the transmitter (and eventually to Earth). Transferring the images made by the ANT to Earth is important and as such it will be discussed in a separate section.

6.1.1 Power

Most important to the electrical components is the supply of power indicated by the dotted lines in the diagram. All the subsystems in the ANT must be supplied with sufficient power at the right voltage. This means that there has to be some kind of electrical infrastructure in the ANT and an electrical connection between the ANT and the rest of the satellite. The satellite has to regulate power and make sure that it generates enough power with, for example, solar cells.

6.1.2 Data

The solid lines in the diagram indicate the flow of data between each component. As can be seen the arrows coming from the sensor are one sided, so only flowing in one direction. Between the temporary memory and storage memory a two sided arrow indicates the possibility of data flow in both directions.

6.1.3 Command

Looking at figure 6.2 one can see all striped commanding lines originating from the processor. The processor acting as the heart of the ANT controls the different components by sending commands via the command channels as laid out. A description of the block and the flow will now be given. First the processor which is part of the ANT receives data from the satellite to which it is connected.

The first thing that has to be done is to check whether or not the received data represents a valid command. If this is not the case then further processing of the data will not be done. If the message is valid it will be decoded, which means that the message is interpreted as a useful command which is executable. The next step is to execute the command and it can be seen that the execution output is divided into different categories. Firstly there is the "operate sensor" command. This can be used to setup the sensor, i.e. the exposure time, read-out, capture speed and the image resolution can be set. The next command is "initiate processing", with which the processor can be told to start processing. Also the compression and pixel binning ratio can be set with this command. The last command is "handle data", with this command the flow of data can be controlled. It can for example be decided to move data to the storage memory or to the radio frequency transmitter.

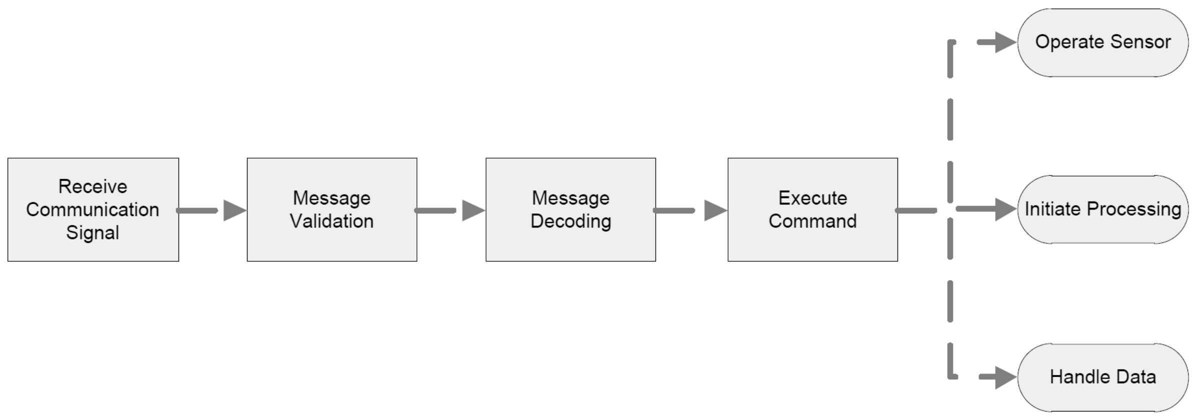

Figure 6.2: Command flow.

6.2 Sensor details

The sensor that has been chosen is the CMV4000 from CMOSIS. In short the reasons for this choice are that the CMV4000 sensor has a high sensitivity, low cost, square imaging area and is tolerant to radiation as laid out in detail in chapter 4. The following paragraphs will deal with the properties of the imaging sensor.

6.2.1 Image data

An important property of the imaging sensor is the amount of data that is generated for one frame. It is given by the product of the amount of bits per pixel (bpp) and the total amount of pixels. The amount of bits per pixel is either 10 or 12 and the total amount of pixels is the product of the amount of horizontal and vertical pixels, i.e. 2048 times 2048 [63]. For 10 bpp this results in a frame size of 5 MiB and 6 MiB for 12 bpp (MiB

= 2^{20} bytes). These numbers are important for buffer sizing. In order to make a choice between reading 10 or 12 bpp it is useful to calculate the SNR due to quantization. This can be done using equation 6.1 [82] [83].

$$SNR_{quantization} = 20log_{10}(2^{bpp})dB \tag{6.1}$$

Table 6.1 shows the number of bits per pixel and the resulting SNR and image data size (without compression). The SNR increases by about 6 dB for every extra bit per pixel. An entry of 8 bpp has been added to the table for comparison, although the sensor cannot be read-out using this value. It might be useful to read 10 bits from the sensor and discard two afterward (which can be done by the processing unit as part of the image compression stage). If it turns out that the noise introduced by the sensor is much higher than the noise due to quantization than it might be a viable option to use less bits per pixel, since this will reduce the downlink rate.

Table 6.1: SNR for different amounts of bits per pixel

bpp	SNR [dB]	Data size [MiB]
8	48	4
10	60	5
12	72	6

6.2.2 Sensor read-out

The minimum read-out speed, the rate at which the sensor reads the data of each of the pixels, should at least be chosen such that the readout period is less than the period between the capture of two frames. For high-speed applications this is an important requirement, since the frame rate is then limited by the read-out speed. For the space camera application this requirement is not present, as will now be shown. When using the slowest clock frequency (5 MHz) and the least amount of data lines (2 lines) the read-out time is approximately 0.42 s, which equals a frame-rate of a little more than 2.3 fps.

6.2.3 Temperature range

Another important sensor property is the temperature operating range. For this sensor the minimum temperature is -30$°C$ and the maximum 70$°C$. The maximum is not a hard limit, but above this temperature the performance of the sensor degrades [63].

6.2.4 Power budget

According to the specifications the imaging sensor has a nominal power consumption of 600 mW [63]. This is a lot considering the amount of power available on a CubeSat, which is in the order of a few Watts. Luckily the nominal conditions refer to continuous imaging, which is not the necessary for our target of at most 1 fps. This means that most of the time the imaging sensor is idle, greatly reducing power consumption. Also, during eclipse the imaging sensor cannot capture useful images and as such it can be shut down. When shut down the power consumption will be negligible, which eases the requirements on energy storage on the satellite to which it is connected.

The power consumption of the imaging sensor during operation depends on the read-out speed. When the speed is reduced the power consumption reduces as well. The read-out speed can be reduced in two ways, by reducing the frequency of the clock signal supplied to the sensor and by using less data lines. The data lines are the physical connections running from the sensor to the processing unit or memory, over which the data from the sensor is conveyed. The sensor clock can be varied between 5 and 48 MHz and this affects the data rate of the data lines. The amount of data lines that are used during read-out is 2, 4, 8 or 16. It has to be noted that when these power reduction measures are used it takes more time to read-out the sensor, such that the amount of energy needed is affected differently. There is no data available on the data reduction due to a lower clock speed, but there is for the amount of data lines. Every disabled data line reduces the power consumption by 17 mW [84]. This means that when using only two data lines at full speed the nominal power consumption is reduced to 238 mW.

If possible no batteries should be used in the electrical system of the ANT. Although batteries have the advantage that they can store a substantial amount of energy they also add weight and complexity (charge/discharge/conditioning circuitry). Short term storage should, when needed, be realized using capacitors. An example calculation of capacitor usage for backup will be used to illustrate this.

Peak power example:

A capacitor discharges from 5 to 3.3 V due to a load consuming 3 W during 10 ms. The amount of energy stored in a capacitor is given by $E = \frac{1}{2}CU^2$. The energy consumed by the load equals $E = Pt$. The value of the capacitance needed to supply the load follows from: $\frac{1}{2}C{U_{begin}}^2 - \frac{1}{2}C{U_{end}}^2 = Pt$, which gives $C = \frac{2Pt}{{U_{begin}}^2 - {U_{end}}^2}$. The capacitance needed is about 4.3 mF, which is in the range of (solid state) tantalum capacitors. In reality calculations will be more difficult due to the need of e.g. power regulation, but a simple calculation does give insight into the order of magnitude.

6.3 Processing

The imaging sensor has to be controlled and the data coming from it needs to be stored. The data might also be compressed if necessary in order to decrease the amount of data to be sent over the downlink. In order to do all this, a processor or programmable hardware in combination with internal or external memory can be used. The following sections will briefly discuss the options and requirements on these parts. Also the possibility of image compression will be discussed.

6.3.1 Hardware

When the processing part of the ANT is to be implemented, a choice should be made for a certain processing part. Initially the following components should be investigated: microprocessors/microcontrollers (e.g. on board computer), Digital Signal Processors (DSP), Field Programmable Gate Arrays (FPGA) and Application-Specific Integrated Circuits (ASIC). Figure 6.3 shows the hardware used for image compression in space. Although it has been mentioned, it is unlikely that an ASIC will be used for a CubeSat based system as the cost of this part will be too high. In large satellites an ASIC is a popular option because it can be made to fulfill a specific function very well.

Furthermore the system needs memory too. First of all a buffer might be incorporated to store one or more images coming from the imaging sensor at high speed. Possible memory types include FIFO and s(d)ram. If long term storage is needed, than a logical choice would be to look at flash memory because of its high data density. Going into the details on processing and memory parts is however not usefull at this point of the design phase and will be left for future research.

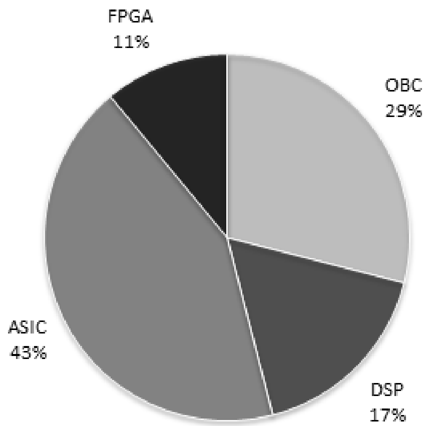

Figure 6.3: "Shares of implementation approaches to compression" [85]

6.3.2 Radiation protection

A radiation risk with a high likelihood of occurrence is a bit-flip, a phenomenon in which the value of a bit in memory changes due to radiation. Changes like these have to be accepted, or counteracted by implementing redundancy data sets with which bit-flips can be detected and corrected. The use of radiation hardened processing hardware and memory parts will not be considered. The reason for this is that the power budget is very limited and the power consumption of equivalent radiation hardened parts is approximately one to two orders of magnitude higher [86]. Also radiation hardened parts have a higher cost compared to generic parts with the same processing capabilities. Finally the use of non radiation hardened parts in space has been proven to work correctly. This can best be illustrated by the example of the Delfi-C3 satellite, which is still operational after three years since its launch although designed for a two year mission. In the satellite 17 non radiation hardened microcontrollers are used and a redundancy data set system to correct for bit flips. During the entire mission duration non of the 17 microcontrolers experienced any signs of failure or malfunction. Furthermore the data received was of good quality indicating the successful operation of the redundancy data system [86].

6.3.3 Temperature range

The temperature range of the processing and memory parts should, if possible, cover the range of the imaging sensor (i.e. -30 to $+70°C$). This must be the case in order to not decrease the operational temperature limits, as this might make the thermal control more complex. It is expected that this will not be a problem and this will be illustrated with an example: the microcontrollers used on the Delfi-C3 are of the Microchip PIC type [87]. These microcontrollers have a temperature range of -55 to $+125°C$ [88]. So these COTS parts have a temperature range that easily extends that of the imaging sensor. It has to be noted that it is not a strictly necessary condition to have a temperature range as high as or higher than the imaging sensor, if it would turn out that the temperature range of the ANT is smaller. For example the temperature of the Delfi-C3 ranges from -5 to $+15°C$ most of the time [86].

6.3.4 Compression

Applying image compression has a considerable influence on the downlink budget and the storage capacity. With the availability of high capacity flash memory devices the storage capacity is not likely to be a bottleneck of the system, but the downlinking of the data will be. A calculation will be performed to illustrate this, using the CMV4000 sensor that has been chosen for this project and a downlink rate of 1 Mbps (a link calculation for this data rate will be given in section 6.5). Please note that no error correction or other overhead has been taken into account in this value.

The sensor will supply, at 10 bpp, $10 \cdot 2048 \cdot 2048$ bits of data. These will be transmitted in $\frac{10 \cdot 2048 \cdot 2048}{1 \cdot 10^6} = 42$ seconds. The amount of data can be reduced by 20% using only 8 bits per pixel. Using lossless (reversible) compression another 50% reduction can be achieved (see reference [85]). When using "lossy" compression (i.e. reversible compression, compression in which some information is lost) the reduction can be higher. Table 6.2 shows the time it takes to transmit an image in the before mentioned situations.

Table 6.2: Image transmit time for different situations at a downlink rate of 1 Mbps. A compression ratio of 2 for lossless and up to 10 for "lossy" compression has been chosen, because this is what for example the RapidEye satellites are capable of [85].

bpp	compression	transmit time [s]
10	none	42
8	none	34
8	lossless (ratio 2)	17
8	"lossy" (ratio 5)	6.7
8	"lossy" (ratio 10)	3.4

From these calculations it follows that image compression can substantially decrease the downlink time for an image. However a trade-off should be done between image quality and data quantity. Using lossless compression, which does not affect the image quality, a compression ratio of about 2 to 5 can be expected [85]. A much higher compression ratio can be achieved using lossy compression, but image quality will degrade. Using this kind of compression a higher compression ratio will result in more loss of data. Furthermore it should be noted that the calculations have been performed in order to gain insight. The numbers used are not necessarily those that will be used in the final design. The use of a different compression ratio, downlink rate or possibly the use of a cloud of (data-relay) satellites all influence the transmit time.

Most image compression algorithms used in space until now depend on the cosine or wavelet transform or pulse code modulation as can be seen in reference [85]. The well known JPEG standard and its successor JPEG2000 are based on the cosine and wavelet transform respectively. The compression algorithm that will be used for the ANT under consideration will not be decided upon now.

When using image compression extra attention should be paid to the reliability of the data transmission to Earth. This is needed because error propagation might occur in the compressed image when the received data is corrupted. Special algorithms are being developed to get as much information as possible out of corrupted compressed images [85]. Also the JPEG2000 standard incorporates error resilience tools [89].

6.3.5 Pixel binning

Another image processing technique that can be performed by the processing unit is pixel binning. Multiple pixels are mapped to a single pixel when using this technique. The advantage of this is that the SNR goes up and the data size goes down. However, a disadvantage is that the resolution will go down as well [90]. If it is desired to use pixel binning it is best to do this on-board the ANT, because this will reduce the amount of data that has to be transmitted. On the other hand when the loss of resolution is not acceptable it should not be used. The method of combining several pixels and treating them as one also allows to correct for pixel failure (which can be caused by radiation). For example when binning four pixels, it will only have a minor effect if one of the four pixel fails since the information collected from the neighboring three pixels will still deliver a considerable amount of image data. It can be concluded that pixel binning, with the current sensor, is not desirable as it negatively influences the resolution. A better solution might be to keep track of damaged pixels, such that further processing can take this into account. If however a certain application does not require the maximum resolution, than pixel binning can be used to increase the SNR and decrease the image data size.

6.3.6 Power Budget

As an initial estimate a maximum power of 1 Watt will be aimed for, including the entire ANT however excluding the downlink power budget. The only fixed component already selected in the earlier optical design phase is the sensor, the CMV4000. From contact with engineers involved in the production of the sensor it was found that using specific configurations the imaging sensor consumes less than 250 mW of power [84]. This leaves about 750 mW for the processing as well as command and data handling to be handled by the power budget available. The TMS320 produced by Texas Instruments was selected as a suitable processor able to meet all imposed requirements [91]. The processor power consumption is completely dependent on the processing performed [92]. Since this consumption is highly variable depending on the amount of processing necessary, which again is dependent on the basic mission objective an average value is set to be 550 mW. This value is generic including all processing as well as command and data handling tasks. However it is important to mention that due to the fast advances in electrical components development it is futile to settle on specific processing and storage components, since improved candidates are continuously being brought forward by the industry. Additionally when power can be saved on the processing equipment more power is left for the transceiver, increasing the downlink bandwidth. From a meeting with an engineer involved in the development of the Delfi nanosatellites it was found that the typical power consumption of the imaging and processing equipment could be kept within 100 mW reference [86]. This means that keeping in mind the sensor, 750 mW should be more than enough remaining power for the processor and optional components.

6.4 Imaging

This section on imaging deals with the steps involved in data acquisition. In order to design a suitable electrical subsystem it is crucial to be aware of the requirements that need to be met by the electronic hardware as well as software components. As explained in section 6.1 the block diagram starts with the sensor and ends with the downlink of the data. However first one needs to know more about what the sensor is going to read in. First the actual field of view (FOV) is calculated in order to determine exactly what area the sensor actually takes an image of, compared to the image area observed by the instrument. As the ANT can experience a diminishing performance over time due to degradation, production errors or orbit mismatch or due to other influencing factors it might be desirable to apply an overlap during the imaging process. Overlap can be used to improve image quality during post processing and is addressed separately below. Then the influences of orbit characteristics such as altitude and inclination are evaluated.

6.4.1 Actual field of view (FOV)

From the image circle observed by the circular FOV one can determine the resulting actual FOV. What happens is that although the optical system images a circular FOV and projects it onto the sensor, the sensor itself has a square surface. This results in the effect of cutting of part of the image circle and only recording the square inside the circle. It is however advantageous since the edges of the image are usually of lower image quality. Losing these edges does in this case not effect the image it solely helps to limit the blurry edges to the corners of the square recorded by the sensor.

Considering the ANT operating in a reference polar orbit with an altitude of 540 km, one can find a maximal half angle θ of 1.131 degrees and resulting image circle diameter of 21.32 km (assuming a FOV 15 km and nadir pointing). However only the rectangle FOV able to fit inside the image circle area is actually recorded by the sensor. The side length of the rectangle corresponding to the FOV is found to be equal to about 15 km.

$$FOV = \frac{ImageCircle_{diameter}}{\sqrt{2}} \tag{6.2}$$

Figure 6.4 shows a graphical representation of the square within the image circle that is actually recorded by the sensor.

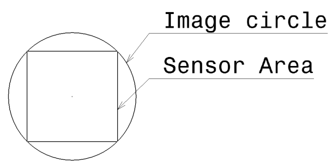

Figure 6.4: Image area vs. sensor area

6.4.2 Overlap

Even though blurriness at the edges is reduced by collecting only data of the unaffected FOV rectangle there might still be need for an overlap of the adjacent images in order to correct for errors. The overlap is simply the unaffected FOV length minus the distance between the two adjacent images. If the distance is less than the unaffected FOV the two adjacent images will overlap. The overlapped area will be imaged twice, once in the first and the second time in the adjacent image overlapping the first one. The data collected can be used to increase the image quality in the overlapped area, usually the edges of the image, which are also the areas mostly affected by degrading. Furthermore the overlapping can be used to correct for inaccuracy in pointing of the satellite.

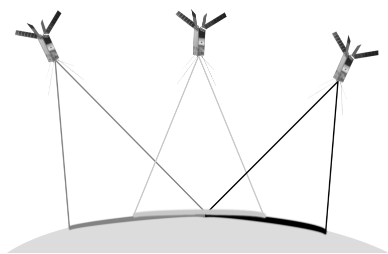

Figure 6.5: Overlap during the imaging process

6.4.3 Inclination

The inclination of the orbital plane has a great influence on the revisit time and the ground coverage pattern. Figure 6.6 illustrates this influence by showing a satellite orbit for an inclination of 70 degrees (top image) and 90 degrees (bottom image). The satellite altitude in the figure is 540 km and the simulated duration is four days. As a logical consequence the coverage of the poles gets less with decreasing inclination. When observation of the poles is of interest to the customer this has to be taken into account. Furthermore one can see from the figure that the change in inclination leads to several cross-overs of the tracks. These cross-overs can be chosen such that they occur over a certain place of the Earth to reduce revisit time.

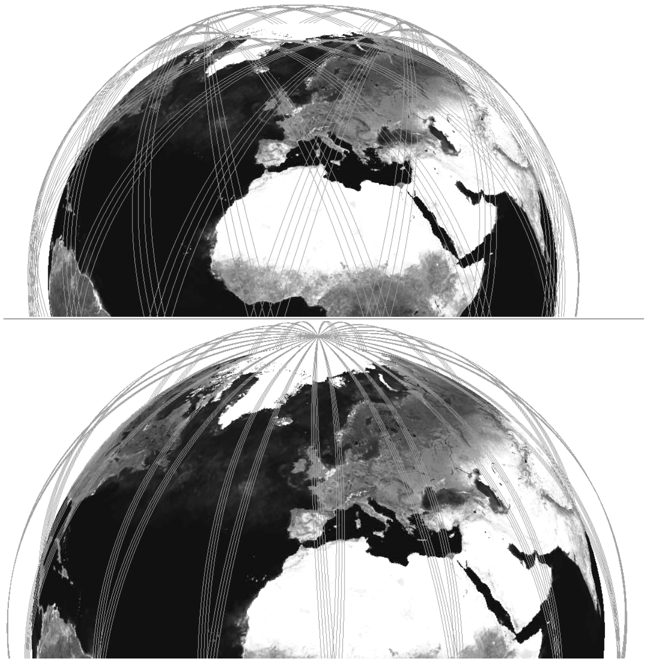

Figure 6.6: Obits at an inclination of 70 degrees (top) and 90 degrees (bottom)

6.4.4 Pointing

Another contributing factor to consider when designing a specific orbit is the pointing ability of the satellite. Considering a certain area of interest it is possible to point the satellite on a this region during each fly over. In this manner even orbits with tracks lying far apart from each other do not prohibit to image a certain area during each fly over.

6.4.5 Altitude

As already discussed in chapter 4 the requirements imposed on the resolution determined a certain altitude range from 540 to 1440 km. With increasing altitude the resolution decreases steadily from 7.5 m at 540 km to 20 m at 1440 km. The FOV also increases with increasing altitude from the 15 km at 540 km to 40 km at 1440 km. Accounting for the reduction in resolution the larger FOV reduces the amount of tracks necessary to image a certain area. The larger FOV also means that the revisit time reduces.

6.5 Downlink

A satellite mission collecting data in space needs to transmit the data to Earth at some point. This action is called downlink and refers to sending data from the satellite to a receiving ground station on Earth. The term "link budget" is an overall term used to discuss not only the transmission of data and commands from the spacecraft to the ground station, but also the other way from the ground station to the satellite. Since the system designed does not require a specific uplink the focus of this section lies on the downlink of the images captured by the ANT. The downlink is not performed by the instrument itself, but by the space platform on which the instrument is operating. The downlink is highly dependent on the amount of data the ANT accumulates during imaging as well as the availability of on-board data handling such as compression techniques. As can be seen in section 6.4 one single image captured results in a very large amount of raw data. In order to reduce the amount of data to be sent to Earth, a processor for on-board compression is incorporated in the electrical subsystem design. This section will discuss the amount of data accumulated by the ANT during operation and how to downlink the compressed image data.

6.5.1 Number of images

In principle the number of images is completely dependent on the customers choice. It is influenced by the orbit chosen, the area of interest as well as the overlap. Therefore the number of images is completely unpredictable without a clear mission objective. Nevertheless it is useful to provide a sample calculation for clarification of the entire process. Making use of the market analysis in chapter 2.1 characteristics about the possible mission objectives of certain market segments and the resulting imaging requirements can be derived. Like in previous sections the orbit considered is circular, with an inclination of 90 degrees set at a reference altitude of 540 km with the period being equal to approximately 95 min [93]. Depending on the area of interest a certain longitudinal distance and latitudinal distance required to cover this area can be found. The amount of images for latitudinal coverage will highly influence the orbit design in order to shift the track by the unaffected FOV width every orbit in order to measure the area of interest within the least amount of orbits necessary.

The longitudinal distance will be the driving factor for the downlink analysis, as the goal is to retrieve the data from the satellite as soon as possible, so if possible during one orbit, in order to avoid a pile up of data after several orbits. The amount of images necessary to image the longitudinal coverage distance during one orbit can be calculated as shown in equation 6.3. The distance per image used in the equation is found in the section 6.4 and is strongly influenced by the overlap. Assuming no overlap one can take the maximum distance between the images being equal to the maximum field of view (FOV) of 15 km. Using this information the number of images required for full coverage of the stripe of the area of interest can be found dividing the longitudinal coverage distance by the distance per image equal to the FOV.

$$\#_{images} = \frac{distance_{longitudinal}}{FOV} \tag{6.3}$$

Assuming as an example that the Delft University of Technology is planning a mission to set up a satellite image aided disaster response system to better monitor floods. Using the previously mentioned orbit configuration and assuming the aim is to monitor the entire country of the Netherlands from Maastricht to the Frisian Islands, roughly 350 km in longitudinal distance, the required number of images is 24 with one image each 15 kilometers.

6.5.2 Capturing time

In order to determine how much time is available for capturing, the ground speed of the satellite needs to be calculated first. Again a reference altitude of 540 km and a reference period of 95 min is considered. Using the radius of the Earth R_E, the semi major axis of the orbit a and the standard gravitational parameter μ one can find the velocity of the satellite on sea level. In equation 6.4 the velocity of the satellite with respect to the Earth's surface is found to be about 7,5 km/s.

$$v_{ground} = \frac{2\pi \cdot R_E}{2\pi \cdot \sqrt{\frac{a^3}{\mu}}} \tag{6.4}$$

When dividing the velocity by the image distance, so the distance between two adjacent images, the time available between each capturing process can be found. In case of no overlap the image distance is simply the FOV since the overlap is equal to zero. The time between each image capturing is then equal to about two seconds.

$$t_{capture} = \frac{FOV - overlap}{v_{ground}} \tag{6.5}$$

Information about this time slot between each image capturing gives a benchmark on how much time it takes to capture a certain amount of images. With information about the integration time and the actual time the sensor needs to record and output the image, the time left before the next image is taken can be found. Thus the design of the electrical components can be performed in such a way that they can use the time slots between the image capturing process, when less power is required by the sensor as it is waiting to take the next image. In this way the available power during the remaining time can be used in other electrical components such as the processor in order to process already taken images. In case of the reference altitude of 540 km and the orbital period of 95 min images would be taken every 2 s using adjacent imaging without any overlap. From the section 6.2.2 on sensor read-out it is known. Using the slowest read-out speed it is possible to take an image every 0.42 s. This shows that principally that 2 s is actually a lot of time and only a small margin of it will be needed to record the image and read it out from the sensor to the processor. All the remaining time until the next image is taken can be used for compressing the images or handling the data, since the power usually needed by the sensor will be available.

6.5.3 Amount of data

In section 6.2.1 the amount of data per image was calculated allowing a precise calculation of how much raw data is actually produced during capturing. In the example of the Netherlands 24 images of each 5 MiB are captured during one orbit, resulting in raw data of 120 MiB. The intermediate electrical components such as the processor and the memory handle the data until the process of downlink is taking place. In order to minimize the time and power needed for downlink, compression will be applied to the raw data. However as can be verified in section 6.3 the amount of compression is limited by the performance of currently developed compression mechanisms and the available computational power.

6.5.4 Downlink options

After having deducted how much data has to be transmitted from the satellite to Earth, the task of the ANT created during this project is actually completed, as the downlink itself is handled by the satellite the ANT is operating on. Nevertheless several ideas regarding the downlink rate and organization have been thought through during the detailed design phase.

Limited downlink - UHF

The most simple way in which a reasonable downlink rate is achieved is by limiting the amount of images captured and therefore the data accumulated ergo to be downlinked. If only little data needs to be transmitted, also small downlink rates suffice to transmit the little data in a short period. Looking at the Delfi-n3Xt mission designed by the Delft University of Technology the available downlink rate provided by the on-board transmitter equals 9600 [bit/s] [94]. This would only suffice for a very limited amount of images to be downlinked during one orbit, also considering the limitation due to the small power budget. The example calculation below illustrates the limited downlink abilities of such a communication system.

Another good example is the PRISM satellite aiming for a similar resolution image as this optical design (it aimed at a ground resolution of 10 m [95]). The PRISM satellite also uses a transmitter providing 9600 bit/s resulting in a very limited link budget for images. In that case only single images were captured by the Earth observation instrument, compressed on board and later on downlinked during contact time with their ground station in Japan. A similar policy was applied to other CubeSat missions like the SwissCube [96] also limiting the amount of images taken. However an interesting option to overcome the limitation on contact time between the satellite and the ground station is to use a large network of ground stations enabling a longer contact time and therefore providing more time for downlink [97]. The foundation for such a network consisting mainly of radio amateur and university ground stations is being developed at the moment. The project is called GENSO and it is aimed specifically at providing communication possibilities for university satellites like Delfi-n3Xt [98]. Instead of the ground network it might also be possible to use a communication network in space. Well known examples are TDRS, Iridium and the soon to come Iridium NEXT [99]. While the use of TDRS is not feasible (pricing, distance), the use of Iridium might be considered. Iridium satellites are in a low Earth orbit (780 km) and provide satellite voice and data services with Earth coverage [99]. When using Iridium it has to be noted that the orbit that is used must be low, preferably at the lowest design altitude of 540 km in order to be within the Earth pointing beam-width of an Iridium satellite. Iridium NEXT will have similar orbital characteristics, but will outperform its predecessor.

Assuming the mission mentioned in the previous paragraph to image the entire country of the Netherlands in total 120 MiB of raw data are accumulated over 48 s. The compression could in principle be done during the time the sensor rests between taking two adjacent images. Assuming a compression ratio of 5, which can be verified in section 6.3 to be a reasonable number, 24 MiB are still to be downlinked during the contact time between the satellite and a ground station. The 24 MiB can be rewritten to equal 201,33 Mbit, which means that at the assumed downlink rate of 9600 bit/s more than 350 min or close to 6 hours of contact time for downlink are required. From this example calculation one can see that the method of limited imaging has very strict limitations on the amount of images, the compression rate and downlink rate.

Another important parameter, besides the amount of data, is the ground station antenna beam-width. It is important because pointing accuracy of the ground station and position determination of the satellite depend on this. This parameter has been calculated and the results can be seen in table 6.3 and table 6.4. Both the input and the output variables are given. The output variables have been calculated for both minimum altitude and maximum altitude, in order to show the dependence on the operating altitude. At the lower end of the operating range of altitudes, 540 km, the antenna diameter is smaller and the beam-width is larger than at the upper end, 1440 km, of the operating range. In order to have a simple ground station, i.e. no pointing, the beam-width should preferably be large. At an altitude of 1440 km the beam-width is only about 11 deg, which might necessitate pointing. The receiver and transmitter parameters were provided by a producing company in Germany named IQ wireless [100].

Table 6.3: Example link calculation for the UHF-band

Input	Quantity	Unit
Frequency	430	$[MHz]$
Transmit Power	22	$[dBm]$
Receive Sensitivity	-104	$[dBm]$
Transmit Antenna Gain	2	$[dBi]$
BER	10^{-5}	$[-]$

Table 6.4: Example link calculation for the UHF-band

Output	540 $[km]$ altitude	1440 $[km]$ altitude	Unit
Path Loss	140	148	$[dB]$
Receive Antenna Gain	15	23	$[dB]$
Receive Antenna Diameter	1.64	4.37	$[m]$
Receive Antenna Beam Width	29.8	11.2	$[deg]$

Increased downlink rate - S-Band

A more interesting method to cope with the large amount of data created during imaging is to increase the downlink rate dramatically. However the rule of thumb that power required for transmission increases proportional to the transmission rate strongly limits this option due to the usually low available power budget on small satellites. Technology advances however have brought forward transmitters using less power and which are available already as COTS components. Delfi-n3Xt is carrying such a high performance transceiver developed by ISIS (www.isis-space.nl) and will test its performance in space environment. The company IQ wireless (www.iq-wireless.com) already offers an entire satellite communication set, including transmitter, receiver and patch antenna for under €15000 allowing speculations on the further improvement of hardware in this technology sector [101]. This specific transmitter provides a downlink rate of 1 Mbit/s at a power consumption of 5 W [100]. With such a transmitter on board the required contact time for the 24 images, required to map a strip of the Netherlands from Maastricht to Groningen, would reduce from roughly 350 min to only 3 min and 22 s. This example calculation shows the dramatic advantages of a increased downlink rate. With these components downlink of the mentioned amount of images within the same orbit becomes a more realistic option. However operating such a transmitter at 5 W continuously introduces a problem, since this amount of power is not available on the reference satellite Delfi n3Xt. However providing sufficient power definitely offers a great option for downlink of large amounts of data requiring very little contact time.

For this scenario the ground station antenna beam-width will be calculated again, but now for the S-band (data from a COTS system are used [100]). The results can be seen in table 6.5 and table 6.6. From this table it becomes clear that the input parameters have changed and in turn the output variables have changed as well. The most important conclusion that can be drawn from this calculation and from the previous one (on the UHF-band) is that at this higher frequency the beam-width is much smaller. The range is now from about 9 down to 3.5 deg. This means that at this frequency pointing of the ground station and determination of the satellite position has to be accurate or else the contact time and reliability will be low.

Indirect downlink - relay satellite

The concept of CubeSats aims for low cost satellites. Also the ANT is aiming for low costs and compliance with the CubeSat standards. As already mentioned in chapter 4 the method of using several satellites holds promising advantages. In case of the color images, three satellites would be required to fly in formation in order to create a color image (i.e. with a dedicated satellite for the red, green and blue color band, as the ANT is only capable of monochromatic images). The idea of indirect downlinking makes use of a relay satellite,

Table 6.5: Example link calculation for the S-band

Input	Quantity	Unit
Frequency	2200	$[MHz]$
Transmit Power	27	$[dBm]$
Receive Sensitivity	-100	$[dBm]$
Transmit Antenna Gain	5	$[dBi]$
BER	10^{-5}	$[-]$

Table 6.6: Example link calculation for the S-band

Output	540 [km] altitude	1440 [km] altitude	Unit
Path Loss	154	162	[dB]
Receive Antenna Gain	25	33	[dB]
Receive Antenna Diameter	1.03	2.76	[m]
Receive Antenna Beam Width	9.24	3.46	[deg]

that could be the fourth one to fly in the formation. Such a satellite would be entirely dedicated to data handling and processing as well as the downlink budget. The advantages include not only the available amount of power due to the absence of the ANT, but also the pointing freedom and available external surfaces for antennas.

Chapter 7

Thermal control system

Almost every spacecraft needs a Thermal Control System (TCS), either passive or active, to maintain an allowable temperature range for its payload and structures during each mission phase. The allowable range of temperatures is limited because electrical components only work in specific temperature ranges, the performance of an optical system changes with temperature and structural stresses can be induced due to thermal expansion. For the instrument, the TCS may be partially provided by the bus. However, since the instrument uses 1.5 full cube according to the CubeSat standard and the temperature range has to be minimized for minimal thermal expansion, it will be assessed as an integral part of the design. In this chapter the thermal control system will be assessed by describing the allowable ranges first. Afterwards a Lumped Network Model (LNM) will be used to find what can be achieved using a passive TCS.

7.1 Typical temperature ranges

As was described earlier, every part of the instrument imposes limits on the thermal environment that the TCS has to provide. The optics (chapter 4 for example indicates a temperature range of 5 to 40°C for good to sufficient image quality (assuming a perfect optical system). In table 7.1 the allowable temperatures for all major subsystems of the instrument are summarized.

Table 7.1: Allowable temperatures for nominal operation and survival

		Allowable temperature ranges	
		Operational temperatures	Survival
Optics subsystems			
	(without moving sensor)	+5 - 40°C	-50 - 70°C
	(incl. polyamide sensor support)	-20 - 100°C	
Structures subsystem			
	Super Invar®(inner box)	-50 - 40°C	-237 - 300°C
	Aluminum 7075 (outer box)		-273 - 110°C
Electrical subsystem		-30 - 70°C	-30 - 70°C

From table 7.1 it can be deduced that for nominal operation the temperature range should be limited to 5 - 40°C when a fixed sensor is used. When a smart moving sensor based on a polyamide 11 support is used the operational temperature range is increased to -20 - 40°C. For system survival, however, the temperature range can be assumed to be -30 - 70°C. Outside this range the materials become too brittle [77] the optical elements can break [64] and the sensor degrades rapidly.

The optical system is allowed to reach survival temperatures when the satellite is in the shade, because no images can be taken due to the low Signal-to-Noise Ratio as explained in section 4.4. The electrical subsystem however will still have to function in this situation, because the images can be processed and down-linked during periods of eclipse. From this and 7.1 can be derived that in direct sunlight the temperature should not exceed 40°C. In eclipse the temperature should not go below -30°C.

7.2 Heat exchange with the space environment

The instrument interacts with its environment. In theory heat can be exchanged with every other body that is either in view or in contact with the instrument via conduction or convection. These sources are schematically drawn in figure 7.1. For the practical study of an instrument in a Low Earth Orbit (LEO) these sources can be limited to the solar radiation from the sun, the albedo radiation (sunlight reflected via the surface of the Earth) and the planetary infrared (IR) radiation. Deep space, with an average blackbody temperature of 2.7 K, can be included as an additional heat source.

The main source of heat input in LEO is the solar radiation. At 1 AU distance from the sun the solar flux is 1371 W/m2 [19]. For some faces of the instrument this flux will be captured directly. For others it might be reflected via the Earth surface first. This reflected radiation, the albedo, can be quantified at 31 - 39% of the total solar radiation flux depending on the reflectivity of the Earth. For example clouds and ice increase the reflectivity.

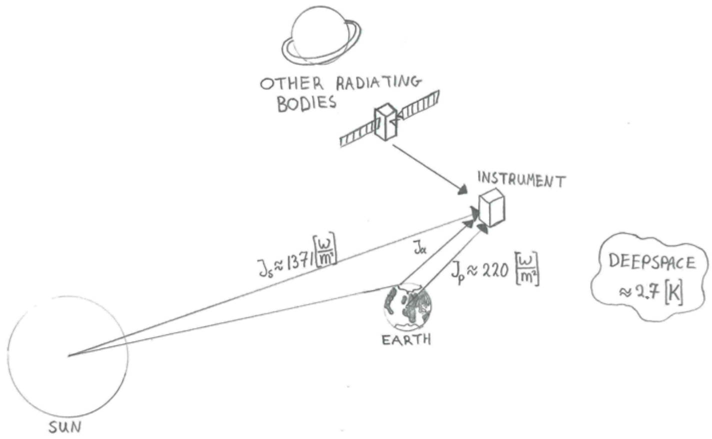

Figure 7.1: The space environment for heat exchange

7.3 Assessment of equilibrium temperature

Before the dynamics of the temperatures in the instrument are considered, the temperatures are initially estimated using a one node model in equilibrium conditions. This one node has a temperature equal to the average temperature of the entire instrument.

For this first assessment of temperature it is assumed that the body has a sufficiently high thermal inertia. This means that the rate at which the temperature changes is low. This is a necessary condition to assume that an equilibrium temperature is reached. It is also assumed that the surface of the body is of the same material for all sides and it is homogeneously radiating. Lastly it is assumed that the body is a gray body. This means the body is neither a perfect absorber nor a perfect emitter, in contrast to a black body.

7.4 Thermal equilibrium

In an equilibrium condition, the heat input is equal to the heat output and the temperature is therefore constant. This condition can be represented in a thermal heat balance as given in equation 7.1:

$$(A_{solar}J_s + A_{albedo}J_a)\alpha + A_{planet}J_p\epsilon + Q - A_{surface}\sigma\epsilon T^4 \tag{7.1}$$

In which A_{solar} is the area exposed to solar radiation [m^2], A_{albedo} is the area exposed to the albedo radiation [m^2], A_{planet} is the area exposed to planetary IR radiation [m^2], $A_{surface}$ is the total emitting area [m^2], J_s is the solar radiation flux [W/m^2], J_a is the albedo radiation flux [W/m^2], J_p is the planetary IR radiation [W/m^2], Q is the internally dissipated heat [W], α is the solar absorptance, ϵ the IR emissivity/absorptance, σ is the Stefan-Boltzmann constant [W/(m$^2K^4$)] and T is the average temperature [K]. In equation 7.1 it is assumed that the temperature of deep space can be neglected compared to the instrument temperature.

The albedo radiation flux Ja can be represented as a fraction of the solar radiation. The albedo radiation flux can then be written as equation 7.2:

$$J_a = J_s a F \tag{7.2}$$

In this equation a is the fraction of reflected solar radiation ($\approx$ 0.31-0.394) and F is the visibility factor. For a small plate in LEO F is equal to approximately 0.85 [30].

7.5 Solar and planetary radiation quantified

At 1 Astronomical Unit (1 AU $\approx$ 149.597.871 km) from the center of the sun, the solar flux is equal to 1361 [W/m2] and can be assumed to be homogeneous in direction and strength near the Earth. It is therefore assumed to be constant with altitude.

The planetary IR radiation can be approximated using equation 7.3 given in [30]:

$$J_p = 237 \left(\frac{R_{Earth}}{R_{orbit}} \right)^2 \tag{7.3}$$

Using that the Earth radius R_{Earth} is approximately equal to 6378 km and the orbital altitude to 540 km and 1440 km the following values for the planetary IR radiation are obtained:

$$J_{p-540km} = 201.4W/m^2 \tag{7.4}$$

$$J_{p-1440km} = 157.7W/m^2 \tag{7.5}$$

7.6 Approximation of the equilibrium temperature

Two scenarios are considered to assess the absolute temperatures the instrument may encounter. The maximum equilibrium temperature is reached when the instrument is exposed to all heat sources that were mentioned in section 7.2. This happens when the satellite on which the instrument is installed is in direct solar radiation. The minimum equilibrium temperature is reached when the instrument is in full shadow. In this case it is only exposed to the planetary IR radiation.

For this calculation the assumed values for the exposed areas are listed in table 7.2. Furthermore it is also assumed that the internally dissipated power can be estimated as 0.7 W. For the maximum equilibrium temperature the albedo fraction α is set to 0.39. The areas correspond to a box of 10x10x15 cm which is nadir pointing in its longitudinal direction. The values are wet-thumb approximations based on geometry and visibility.

Table 7.2: Estimated values for exposed areas

Area	Value $[m^2]$
exposed to Solar radiation	$21 \cdot 10^{-3}$
exposed to Albedo	$15 \cdot 10^{-3}$
exposed to Planetary radiation	$15 \cdot 10^{-3}$
Emitting	$80 \cdot 10^{-3}$

The equilibrium temperatures found for specific covering materials can be found in table 7.3. The values for absorptance and emissivity are adopted from [30]. As can be seen from table 7.3 the temperature differences can be very severe. The thermal control system will be necessary to keep the temperature between the limits required. The listed surface materials will not suffice.

Table 7.3: Equilibrium temperatures for 540 km altitude

Material	$\alpha[-]$	ϵ [-]	T_{max} [°C]	T_{min} [°C]
Polished Beryllium	0.44	0.01	502.3	84.0
Goldized Kapton	0.25	0.02	298.1	29.4
Gold	0.25	0.04	208.0	-13.8
Aluminium Tape	0.21	0.04	189.3	-13.8
Polished Aluminium	0.24	0.08	129.0	-47.4
Aluminized kapton	0.14	0.05	127.4	-25.6
Polished titanium	0.60	0.60	32.9	-98.8
Black paint (epoxy)	0.95	0.85	40.0	-102.5
Black paint (polyurethane)	0.95	0.90	35.9	-103.0
Black paint - Electrically conducting	0.95	0.83	41.8	-102.3
Silver paint	0.37	0.44	22.3	-94.6
White paint (silicone)	0.26	0.83	-33.3	-102.3
White paint (silicone) after 1000 hrs of UV	0.29	0.83	-28.3	-102.3
White paint (silicate)	0.12	0.90	-64.8	-103.0
White paint (silicate) after 1000 hrs of UV	0.14	0.90	-60.1	-103.0

Continued on next page

Material	$\alpha[-]$	ϵ [-]	T_{max} [°C]	T_{min} [°C]
Aluminized Kapton	0.40	0.63	3.9	-99.4
Aluminized FEP	0.16	0.47	-27.1	-95.6
Silver coated FEP (Second Surface Mirror)	0.08	0.78	-71.0	-101.7
Optical Solar Reflector	0.07	0.74	-72.6	-101.2

7.7 Numerical approach to solving the heat balance problem

When the temperature problem is considered a transient problem instead of a problem of equilibrium temperature, equation 7.1 does not longer suffice. To include transient effects and heat exchange between several parts of the instrument, the problem can be solved using differential equations. Unfortunately, these differential equations are hard to solve for an arbitrary orbit and are not suitable for design problems with a lot of design parameters. Therefore a numerical approach was chosen which will be explained further.

7.7.1 The lumped network model and the simulation logic

The method chosen is the Lumped Network Model (LNM). In this model the instrument is discretized to nodes that lump surfaces and masses to discrete points that can easily be evaluated. This is similar to Finite Element Methods used for structural calculations on complex shapes. In the LNM the nodes are assumed to be isothermal. The functional flow diagram for the developed simulation is shown in appendix C in the electronic supplement.

The simulation is broken down into several steps that can be executed independently to allow rapid design changes if the orbital parameters are fixed. Assuming that a discretization of the instrument already exists, the first step is to determine the heat exchange with the environment. To this end the following steps have to be taken:

1. Determine the position of the satellite with respect to the Earth.
2. Determine the position of the Earth with respect to the Sun.
3. Determine whether the instrument is in direct sunlight, penumbra (dusk) or umbra (shadow).
4. Calculate the amount of radiation received by each external surface.
5. Calculate the heat loss to the environment

After the external inputs and outputs have been determined the last steps can be taken to calculate the new temperature.

- Calculate heat exchange between nodes
- Determine new temperature.

In the following subsections the theory behind each of these steps is explained briefly.

7.7.2 Determination of Keplerian elements for satellite and Earth

For the first two steps, the determination of the position of the instrument with respect to the Earth and the determination of the Earth with respect to the sun, the following procedure is used. The results are valid for the position in an Earth Centered Inertial and a Helio Centered Inertial reference frame respectively. The following discussion will cover the procedure for an instrument in orbit around the Earth. For the Earth revolving the sun the procedure is similar. Differences will be indicated where necessary.

Assuming that the Keplerian elements - semi-major axis, eccentricity, longitude of the ascending node, argument of perigee and the inclination - are known, it is possible to determine the position of the revolving body in a Cartesian coordinate system as follows. It is assumed that the satellite passes perigee at the start of the simulation.

First the orbital period is determined using equation 7.6 [20]:

$$P_n = 2\pi\sqrt{\frac{a^3}{GM}}\left(1 + \frac{3J_2a_e^2}{4a^2}\left\{1 - 3\cos^2 i + \frac{1 - 5\cos^2 i}{\left(1 - e^2\right)^2}\right\}\right) \tag{7.6}$$

For the Earth orbiting the Sun only the first part can be used. The J2 effect can be assumed not present in that case.

Secondly, the magnitude of the precession of the nodes is determined using equation 7.7 and 7.8. These precessions are not present for the Earth orbiting the Sun, because the J_2 effect is neglected in that case. The precession of the ascending node in [rad/s] can be calculated as follows [20]:

$$\Omega_p = -\frac{3J_2\sqrt{GM}a_e^2 a^{-7/2}\cos i}{2(1-e^2)^2} \tag{7.7}$$

And the precession of the argument of perigee in [rad/s] can be determined using [20]:

$$\omega_p = -\frac{3J_2\sqrt{GM}a_e^2 a^{-7/2}\left(1-5\cos^2 i\right)}{4(1-e^2)^2} \tag{7.8}$$

If these parameters have been determined one can loop over all time steps of interest. To determine the position of the satellite with respect to the central body the true anomaly θ and the distance to the center of the body r have to be determined. Because the relation between time since perigee and true anomaly is not invertible another approach is needed. Two options are available to solve this problem. The first solution involves an iterative process that relates the mean anomaly M, the eccentric anomaly E and the true anomaly to time [19] . The second solution uses a series expansion of the original equation to approximate the true anomaly in [rad] as a function of time [20]. For simplicity the second method was chosen. The series expansion used can be found in equation 7.9.

$$\theta = \frac{2\pi t}{P_0} + 2e\sin\left(\frac{2\pi t}{P_0}\right) + \frac{5e^2}{4}\sin\left(\frac{4\pi t}{P_0}\right) \tag{7.9}$$

This expansion is limited in its use to small values of eccentricity e. Use of the three terms shown results in an error of $4e^3/3$ radians. For circular orbits equation 7.9 is thus exact.

Using the polar equation of a conic section [19] the magnitude of the position vector r can be found as a function of the true anomaly. This is expressed in equation 7.10.

$$r = \frac{a\left(1-e^2\right)}{1+e\cos\theta} \tag{7.10}$$

Using the equation above the position vector can be defined in polar coordinates in a 2-dimensional reference frame. These coordinates are converted to Cartesian coordinates using equation 7.11:

$$\vec{r}_{cartesian} = M_{rotate}\begin{bmatrix} r\cos\theta \\ r\sin\theta \\ 0 \end{bmatrix} \tag{7.11}$$

Equation 7.11 transforms the polar coordinates in a 2 dimensional plane to Cartesian coordinates in 3 dimensions using the M_{rotate} matrix. This matrix can be derived using 3 unit axis rotations which result in the matrix given by equation 7.12.

$$M_{rotation} = \begin{bmatrix} \cos\Omega\cos\omega - sin\Omega\sin\omega\cos i & -\cos\Omega\sin\omega - sin\Omega\cos\omega\cos i & \sin\Omega\sin i \\ \sin\Omega\cos\omega + \cos\Omega\sin\omega\cos i & -\sin\Omega\sin\omega + \cos\Omega\cos\omega\cos i & -\cos\Omega\sin i \\ \sin\omega\sin i & \cos\omega\sin i & \cos i \end{bmatrix} \tag{7.12}$$

For every moment of interest the steps of equations 7.8 to 7.12 have to be repeated in which the longitude of the ascending node and the argument of perigee are updated using simple Euler integration.

7.7.3 Determination of lighting conditions

If the positions of the satellite with respect to the Earth Centered Inertial frame and the position of the Earth with respect to the Helio Centered Inertial frame are known in Cartesian coordinates, the lighting conditions of the instrument can be estimated. The instrument can possibly pass through three stages of lighting during its orbit, depending on the orbit characteristics. Assuming the instrument passes through all three (valid for the vast majority of used orbits), the sketch as depicted in figure 7.2 can be made. In this drawing the three stages are depicted as umbra, penumbra and direct sunlight. When the instrument is in direct sunlight, the instrument receives solar radiation directly. When the instrument is in penumbra (dusk), the amount of direct sunlight steadily reduces to zero percent until the instrument enters umbra (full eclipse) in which it receives no direct sunlight.

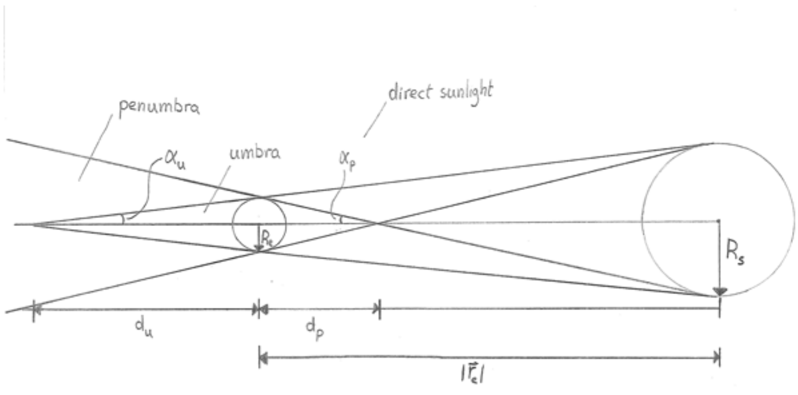

Figure 7.2: Schematic drawing of eclipse-geometry

From figure 7.2 it is easy to deduce the characteristic lengths and angles corresponding to penumbra and umbra. The characteristic length *dp* and angle *p* for the penumbra can be calculated using equations 7.13 and 7.14:

$$d_p = \frac{R_E\,|\vec{r}_e|}{R_S + R_E} \tag{7.13}$$

$$\alpha_p = \sin^{-1}\frac{R_E}{d_p} \tag{7.14}$$

The same can be done for the umbra. This is shown in equations 7.15 and 7.16:

$$d_u = \frac{R_E\,|\vec{r}_e|}{R_S + R_E} \tag{7.15}$$

$$\alpha_u = \sin^{-1}\frac{R_E}{d_u} \tag{7.16}$$

In these equations *RE* is the Earth's radius, *RS* is the radius of the Sun and

$$\vec{r}_e$$

is the vector representing the position of the Earth with respect to the sun.

From these characteristic numbers the dimensions of the penumbral and umbral cone can be deduced. These however are not directly of interest. To determine the lighting conditions the terminators are needed. To find the distance from the instrument to the terminators figure 7.3 is used.

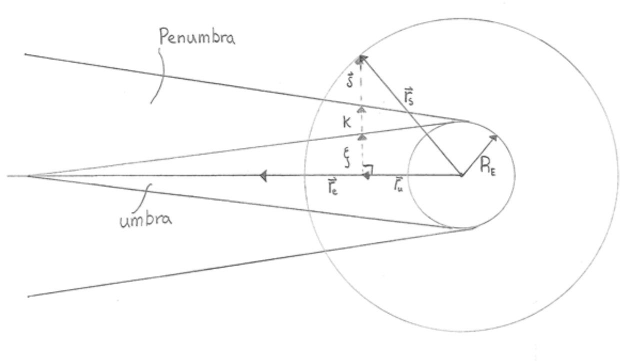

Figure 7.3: Determination of the distance between the instrument and the terminators

In figure 7.3 $\vec{r}_e$ is the vector from the Sun to the Earth which has been translated to the origin of the ECI frame, $\vec{r}_s$ is the vector describing the position of the instrument in the same frame. $\vec{r}_u$ is the orthogonal projection of $\vec{r}_s$ onto $\vec{r}_e$ and can be calculated using equation 7.17.

$$\vec{r}_u = \frac{\vec{r}_s \cdot \vec{r}_e}{|\vec{r}_e|^2}\vec{r}_e \tag{7.17}$$

Using the same figure and vector algebra and geometric relations, the following relations in equations 7.18, 7.19 can also be deduced.

The instantaneous width of the umbra seen from the point in orbit is given by:

$$\xi = (d_u - |\vec{r}_u|) \tan \alpha_u \tag{7.18}$$

Analogously the instantaneous width of the penumbra is given by

$$\kappa = (d_p + |\vec{r}_u|) \tan \alpha_p \tag{7.19}$$

To now determine in what lighting stage the instrument is at a given instant, the following conditions have to be checked:

1. If $\left|\vec{\delta}\right| < \kappa$ and $\vec{r}_s \cdot \vec{r}_e > 0$ the instrument is in penumbra.
2. If $\left|\vec{\delta}\right| < \xi$ and $\vec{r}_s \cdot \vec{r}_e > 0$ the instrument is in umbra.

If not one of these conditions is met, the instrument is in direct sunlight.

7.7.4 Determination of the heat exchange with the environment

If the position of the Earth with respect to the Sun and the position of the instrument with respect to the Earth is known, the position of the instrument with respect to the Sun can be derived using vector algebra.

Attitude control

Before the heat exchange with the environment can be calculated, not only the position with respect to the environment, but also the attitude with respect to the environment needs to be determined. Because the instrument will be observing the Earth, the attitude will be such that the instrument points to nadir. To obtain this attitude, Rodrigues Rotation Matrix [102], shown in equation 7.20 is used to rotate the instrument from its original body fixed reference frame such that its Z-axis is aligned with vector from the Earth to the instrument. The rotation angle θ and the rotation axis ω are found by using the dot and cross product between the position vector and the Z-axis of the body fixed reference frame.

$$R_\omega(\theta) = \begin{bmatrix} \cos\theta + \omega_x^2(1-\cos\theta) & \omega_x\omega_y(1-\cos\theta) - \omega_z\sin\theta & \omega_y\sin\theta + \omega_x\omega_z(1-\cos\theta) \\ \omega_z\sin\theta + \omega_x\omega_y(1-\cos\theta) & \cos\theta + \omega_y^2(1-\cos\theta) & -\omega_x\sin\theta + \omega_y\omega_z(1-\cos\theta) \\ -\omega_y\sin\theta + \omega_x\omega_z(1-\cos\theta) & \omega_x\sin\theta + \omega_y\omega_z(1-\cos\theta) & \cos\theta + \omega_z^2(1-\cos\theta) \end{bmatrix} \tag{7.20}$$

In this equation ω_x, ω_y and ω_z represent the Cartesian components of the rotation axis vector and θ is the rotation angle in [rad].

After rotation the angle between the outward normal vectors of the nodes and the position vectors can be determined. This situation is sketched in figure 7.4. As can be seen from this figure, every node only 'sees' a part of the emitter. This effect is taken into account in the view factor.

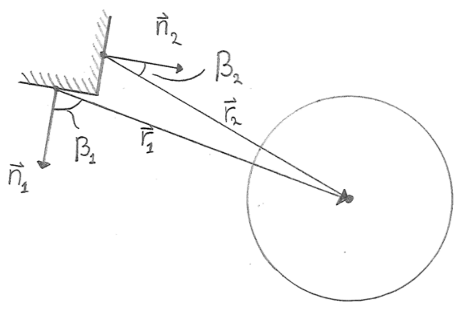

Figure 7.4: Nodal normal vectors and the position vectors

View factors

The amount of radiation intercepted by an arbitrary absorber from an arbitrary emitter can be described by the view factor. The view factor is the fraction of the diffuse energy leaving surface A_i directly and is intercepted by area A_j and the total diffuse energy leaving surface A_i. It can be mathematically expressed as a double surface integral as in equation 7.21 [103] [104].

$$F_{i-j} = \frac{1}{A_i}\int\limits_{A_i}\int\limits_{A_j}\frac{\cos\theta_i\cos\theta_j}{\pi S_{ij}^2}dA_j dA_i \tag{7.21}$$

These integrals can be solved analytically, although this is generally not straight forward. For simple geometries these view factors can be found in large databases described the exact solutions. These can for example be found in [103] [104] [105]. A more detailed discussion of view factors and view factor algebra can be found in [103] [104]

Heat flux received from the environment

The heat exchange with the environment is partially reduced to only receiving heat for most heat sources, including solar radiation, albedo radiation and planetary radiation. This is a valid simplification because the mass and thermal capacity of the Sun and the Earth are much larger than that of the instrument. Therefore the effect of the radiation emitted by the instrument is negligible.

The amount of radiation emitted by a node can be given by Stefan Boltzman's law, as given in equation 7.22. In this equation Q is the heat flux [W/m^2], σ is the Stefan-Boltzmann constant [W/(m$^2K^4$)], ϵ is the emissivity and T is the blackbody temperature of the radiator in [K].

$$\dot{Q}_{emitted} = \epsilon\sigma T^4 \tag{7.22}$$

The heat flux received by another body is given by equation 7.23.

$$\dot{Q}_{received} = \alpha_a A_a F_{e-a}\dot{Q}_{emitted} = \alpha_a A_a F_{e-a}\epsilon_e\sigma {T_e}^4 \tag{7.23}$$

In equation 7.23 α_a is the absorptance of the absorber, A_a is the absorbing area [m2] and ϵ_e is the emittance of the emitter.

For the solar radiation equation 7.23 can be used assuming that the Sun is black body ($\epsilon = 1$) radiating at 5785 [K] [104]. For the planetary radiation the same equation can be used, assuming that the Earth and the upper atmosphere together can be modeled as a gray body radiating at 288 [K] with an emissivity ϵ_e of 0.6. Because the Earth's planetary radiation is mostly infrared radiation the absorptance of the body is equal to its (IR) emittance (Kirchoffs law).

The last source of radiation that is received by the instrument is the albedo radiation. It is assumed that 39% of the solar radiation is diffusely reflected by the Earth. This means that the same view factor can be used as for the planetary radiation. The absorptance however, is not equal to the emissivity of the receiver.

Heat loss to the environment

By assuming that the temperature of the instrument is much higher than the temperature of deep space (T = 2.7 [K]), deep space can be considered a heat sink. The heat loss due to radiation to deep space can be calculated using equation 7.24.

$$\dot{Q}_{heatloss} = A_e\sigma\left(T_i^4 - 2.7^4\right) \tag{7.24}$$

7.7.5 Heat exchange between nodes

Heat exchange does not only occur between the nodes and the environment. It also takes place between the nodes. For heat transfer three mechanisms are possible: convection, conduction and radiation. Assuming that the density of the atmosphere in orbit is too low for convection to have any noticeable effect, the list can be reduced to conduction and radiation.

Conduction

Conduction can be modeled using Fourier's law for heat flow. This law is given by equation 7.25.

$$\vec{q} = -k\nabla T \tag{7.25}$$

In equation 7.25 q is the local heat flux in [W/m^2], k is the material conductivity [W/(mK)] and ∇T the temperature gradient in [K/m]. This can be reduced to equation 7.26 for semi-one dimensional flow with two materials in series. In this equation C_{i-j} is the conductive coupling [W/K], T_i and T_j are the temperatures of node i and j respectively in [K], L_i and L_j are the respective conductive path lengths [m], k_i and k_j are the respective conductivities and A_i and A_j are the respective contact areas.

$$\dot{Q}_{conductive} = C_{i-j}\left(T_j - T_i\right); C_{i-j} = \frac{1}{\frac{L_i}{k_i A_i} + \frac{L_j}{k_j A_j}} \tag{7.26}$$

Radiation

Heat exchange between nodes can also occur via radiation. This radiative coupling can be expressed using equation 7.27. In this equation R_{i-j} is the radiative coupling between the nodes i and j.

$$Q = \sum_{j=1}^{N} \sigma R_{i-j}\left(T_j^4 - T_i^4\right) \tag{7.27}$$

For black bodies the radiative couplings are simple. In that case the radiative couplings are given as $R_{i-j} = A_j F_{i-j}$ [104]. For real surfaces the radiative couplings however are much more complex. If gray, diffuse surfaces are assumed, a algebraic set of equations can be derived. These equations are generalized and given by equation 7.28.

$$\frac{1}{\epsilon_i A_i}\dot{Q}_i - \sum_{j=1}^{N}\left(\frac{1}{\epsilon_j} - 1\right)\frac{F_{i-j}}{A_j}\dot{Q}_j = \sigma T_i^4 - \sum_{j=1}^{N} F_{i-j}\sigma T_j^4 \tag{7.28}$$

This set of equations can be solved for the heat fluxes Q as a function of the view factors, opto-thermal properties and the nodal temperatures.

Calculation of new temperature: The heat balance

If the heat flux to a node is known the heat balance can be used to solve for the new temperature. The heat balance is a simplified form of the energy balance given by equation 7.29.

$$\frac{dE}{dt} = \dot{W}_{net} + \dot{Q}_{net} = \frac{dE_{ele}}{dt} + C\frac{dT}{dt} = \dot{W} + \dot{Q}_{cond_{net}} + \dot{Q}_{conv_{net}} + \dot{Q}_{rad_{net}} \tag{7.29}$$

In this equation E is the total energy in [J], W is the work done to the object [J], Q is the heat added to the object [J] and C is the thermal capacity. By assuming no work is done to the system and no electrical energy is stored, the equation can be reduced to equation 7.30:

$$C\frac{dT}{dt} = \dot{Q}_{net} = mc\frac{dT}{dt} \tag{7.30}$$

in which m is the mass [kg] and c is the specific heat capacity [J/(kg K)]. When using finite difference methods and discretization this can be rewritten as an expression for the new temperature:

$$T_{new} = T_{old} + \frac{Q\Delta t}{mc} \tag{7.31}$$

Using equation 7.31 for every node in the Lumped Network Model, the temperature distribution over the instrument can be estimated.

7.7.6 Verification and validation

As already mentioned in section 7.7.1 the simulation has been split up in three separate modules. These modules have been verified independently. In this section only the verification and validation method will be discussed per module. For the full verification one can access the MATLAB®code as enclosed on the DVD.

Orbital Analysis orbitAnalysis.m

Step 1 of the calculation sequence, as described in section 7.7.1, is put into the orbitAnalysis.m code module. The results of this calculation were checked during development using visual inspection. This entailed the use of typical orbit parameters as input of which the results were checked against common sense and example graphs in [20], [30] and [19]. The 3 dimensional plots of these orbits were checked for number of orbits a day, the separation of orbital planes, the size of the polar gap and the direction of precession of the nodes.

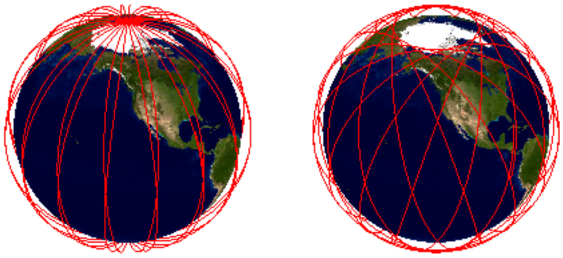

Figure 7.5: Left: Orbit at 540 [km] altitude, 90° inclination ; right: Orbit at 540 [km] altitude, 70° inclination.

Lighting Analysis - lightingAnalysis.m

Steps 2 and 3 of the calculation process, which are the determination of the position of the Earth with respect to the sun and the determination of lighting conditions, are performed in lightingAnalysis.m. This module was verified using visual inspection. For this the number of eclipses per day, the eclipse duration and the presence of (short) penumbral phases was checked and compared to data given in [19]. The eclipse periods were compared for three orbit types: ≈72 minutes of eclipse in geostationary orbit, ≈35 minutes of eclipse in LEO [106] and no eclipse in sun synchronous orbit.

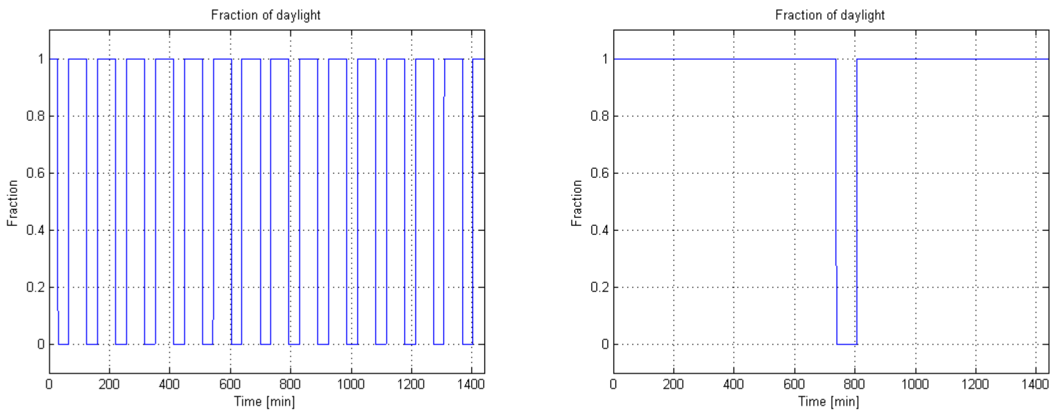

Figure 7.6: Left: Orbit at 540 km altitude, 90° inclination ; right: Geostationary orbit. On the left image clearly 15 orbits can be distinguished. The eclipses last for approximately 35 minutes. On the right image only one eclipse of approximately 72 minutes can be found.

Lumped network model - nodalAnalysis.m

The remaining four out of seven steps, as listed in section 7.7, are included in this module. These steps entail the determination of heat exchange with the environment, internal conductive and radiative couplings and the calculation of the new temperature. To verify the module the following steps were taken:

- The magnitude of the heat fluxes was compared to heat fluxes given in [19] and [30].
- The magnitude of the heat exchanges dependent on external node orientation is checked.
- The dependency of surface materials on the average temperature is checked with examples in [30].
- The fluctuations of nodal temperatures are compared with examples in [30] and [104].
- The effect of initial conditions on the average temperature is considered. It was found that the initial condition damps out in three to four orbits.

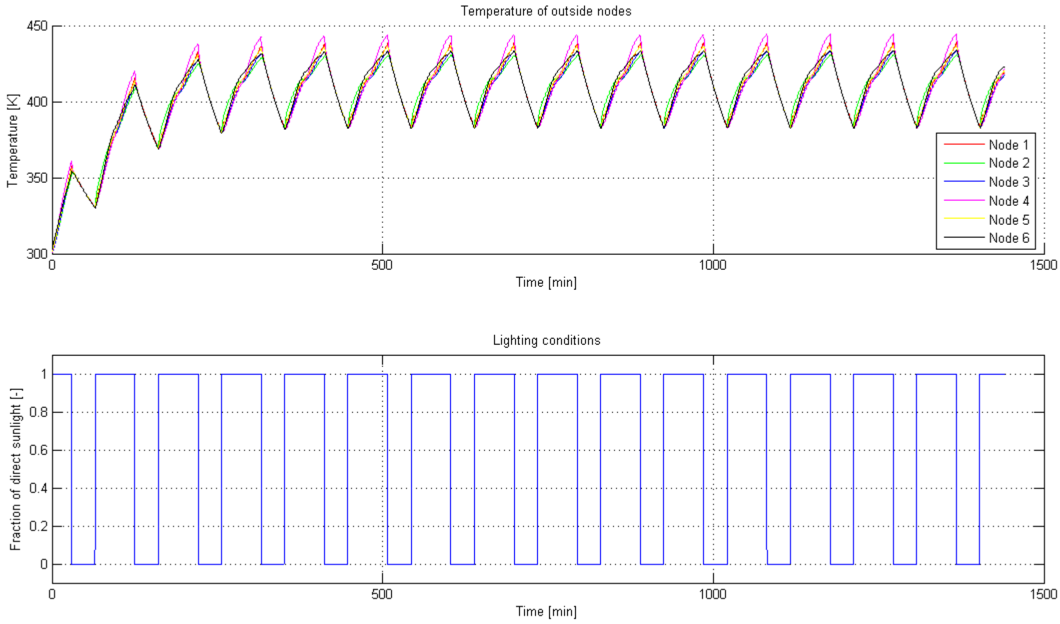

Figure 7.7: Top: Temperatures of nodes. Bottom: Lighting conditions. As can be seen from the top image the effect of initial conditions damps out in three to four orbits. The instrument cools down in period of eclipse.

7.7.7 Representation by six nodes

To study the effects of the orbital parameters and the spin rate on the temperature distribution over the instrument, a six node model is used. This simplified model is also used to determine the possibilities of a passive Thermal Control System that could be used for the integration of the instrument in a satellite.

The model is composed of six nodes as drawn in figure 7.8 Each node is exposed to the space environment and made of Aluminum 7075-T6. To study the effects of orbit parameters and spin rate the absorptivity α was set to 0.21 and the emissivity to ϵ to 0.04. The inside of this aluminum box is painted black and the absorptivity and emissivity are both set to equal to 1. The specific heat capacity c equals 1047 [J/(kg K)] and the thermal conductivity k is equal to 130 [W/(m K)]. In table 7.4 the properties of the nodes are listed. The conductive couplings and radiative couplings can be found in appendix D on the digital supplement.

Table 7.4: Description of nodes

Node ID	Exposed area [m2]	Mass [kg]	Specific heat capacity [J/(kg K)]	Heat Capacity [J/K]
1	$10.0 \cdot 10^{-3}$	$2.70 \cdot 10^{-2}$	1047	$2.8269 \cdot 10^{1}$
2	$15.0 \cdot 10^{-3}$	$4.05 \cdot 10^{-2}$	1047	$4.2404 \cdot 10^{1}$
3	$15.0 \cdot 10^{-3}$	$4.05 \cdot 10^{-2}$	1047	$4.2404 \cdot 10^{1}$
4	$15.0 \cdot 10^{-3}$	$4.05 \cdot 10^{-2}$	1047	$4.2404 \cdot 10^{1}$
5	$15.0 \cdot 10^{-3}$	$4.05 \cdot 10^{-2}$	1047	$4.2404 \cdot 10^{1}$
6	$10.0 \cdot 10^{-3}$	$2.70 \cdot 10^{-2}$	1047	$2.8269 \cdot 10^{1}$
Total	$80.0 \cdot 10^{-3}$	$2.16 \cdot 10^{1}$	-	$2.2615 \cdot 10^{2}$

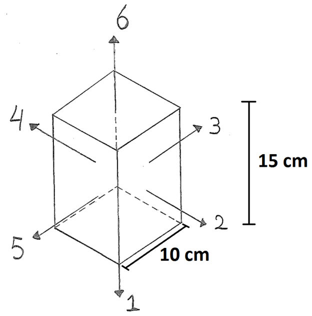

Figure 7.8: Sketch of six node model

Correspondence to the physical instrument

In chapter 5 the layout of the instrument is given. The outer aluminum panels are close to the Invar panels of the instrument. Therefore it can be assumed that all radiation from the outer plates is received by the inner panels. The instrument is made of a bad conductor (Super INVAR®) and because the panels are so close, it can be assumed that the panels of the instrument have approximately the same temperature as the outer shell. For a first order approximation this is sufficient. For a better approximation more advanced simulation programs as ESATAN-TMS, SINDA-TRASYS or THERMICA suite can be used.

In the current mechanical design, the sensor and supporting electronics are fitted into the instrument. These electronics together consume about 800 mW of energy. Even if all this energy is converted into heat, the contribution can be neglected in this analysis. Put into perspective, the heat received from the solar radiation on a 10x10 cm panel equals 13.76 W. This is already 17.2 times more than the 800 mW generated on board.

The thermal model assumes a closed box in which no radiation can penetrate. In the mechanical design however, lenses allow light and radiation to enter the box. The larger part of the IR radiation is blocked by the optical glass and can thus be neglected when considering IR entering the closed box. This radiation is however now absorbed by the bottom plate facing the Earth.

The effect of orbital altitude

To study the effects of orbital altitude the two limiting altitudes of 540 and 1440 km, found in section 3.1 ,are used. To isolate the effect of altitude, the other orbital parameters were kept fixed.

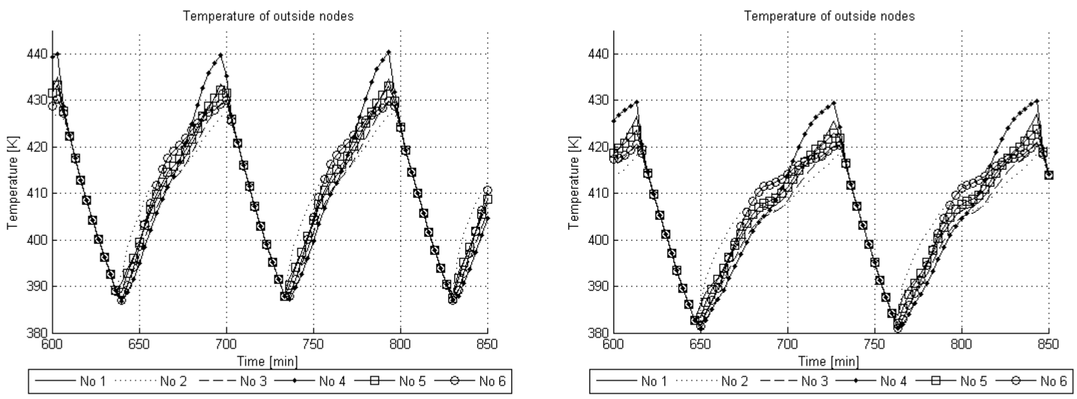

Figure 7.9: Left: Altitude of 540 km and 90° inclination; right: Altitude of 1440 km and 90° inclination.

In figure 7.9 an excerpt of the temperature progression for both altitudes are shown. For 540 km altitude the temperature ranges between 387 K and 440.4 K (temperature range of 53.4 K). As can be seen in the right image the temperatures range between 381.4 K and 429.8 K (temperature range of 48.4 K) at 1440 km altitude. It can be seen that the absolute temperatures encountered are lower. The higher altitude has a bigger effect on the maximum temperature because the contribution of albedo radiation and planetary radiation is greatly reduced due to the larger distance with respect to the Earth.

The effect of spin

Adding spin about the longitudinal axis to the satellite carrying the instrument leads to a reduction in temperature differences between the nodes.

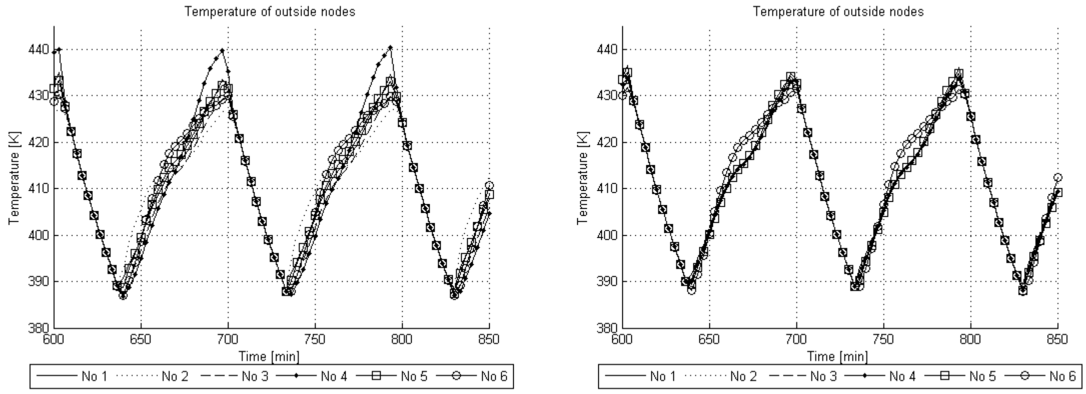

Figure 7.10: 540 km altitude, 90° inclination. Left: No spin. Right: spin-rate 1/10 rev/min.

As can be seen in figure 7.10 the small spin rate of 1/10 rev/min renders the temperature distribution to be more homogeneous. Also the peaks are damped out due to the spin. However, the temperature differences between the nodes are too small to deliberately add spin to the satellite. For a sun-synchronous dawn dusk orbit however, the effects are much more pronounced as depicted in figure 7.11.

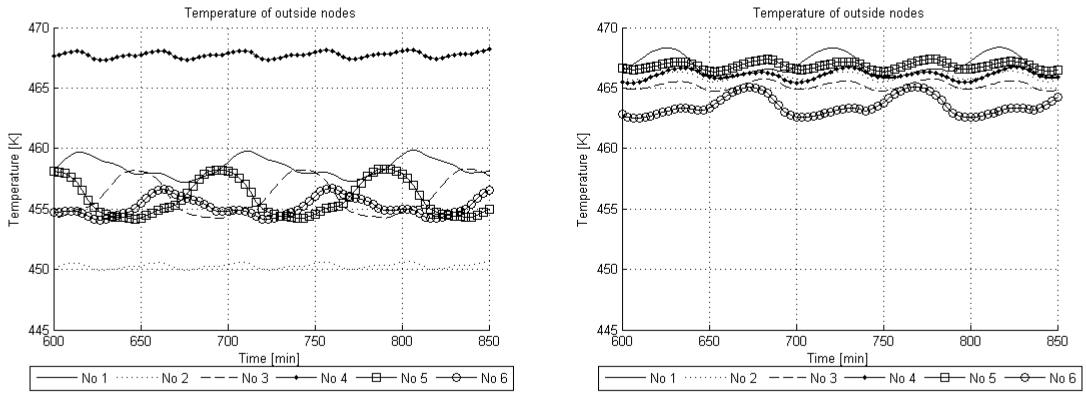

Figure 7.11: 540 km altitude, 90° inclination. Left: No spin. Right: spin-rate 1/10 rev/min.

From figure 7.11 it can be seen that if spin is added in a dawn-dusk orbit, the nodal temperatures converge to a more isothermal state. However, this isothermal temperature is higher than the temperature without spin for the larger part of the nodes. This does not have to be a problem. With a different covering material this isothermal temperature can be shifted up or down to fit the requirements of the instrument.

The effect of inclination

The effect of inclination originates from the orbit of the Earth with respect to the sun. Using the current simulation the effect yields minor differences that are safe to neglect. However, in the current simulation the obliquity is not taken into account. Therefore, further studies will have to show if the effect can truly be neglected. For the rest of the discussion in this chapter, the effect is neglected.

7.7.8 Design of the thermal control system

The Thermal Control System is specific to the selected orbit. For the design of the TCS a polar orbit at 540 km altitude is chosen. Two extremities have to be considered that give the most severe conditions the instrument will have to perform under during its two year lifetime.

These cases are called the hot and the cold scenario. In the hot scenario the instrument is in an orbit for which the Earth is in its perigee with respect to the Sun and for which the orbital plane is under a right angle with the Sun-Earth vector. This case is similar to the near-polar dawn-dusk orbit, the difference being that the instrument is not fixed to this orientation with respect to the sun.

The cold scenario is obtained when the Earth is in its apogee with respect to the sun and has the maximum amount of eclipse that allows it to cool down. This situation occurs when the orbital plane of the satellite is aligned with the Earth-Sun vector.

The two scenarios described above are illustrated in figure 7.12.

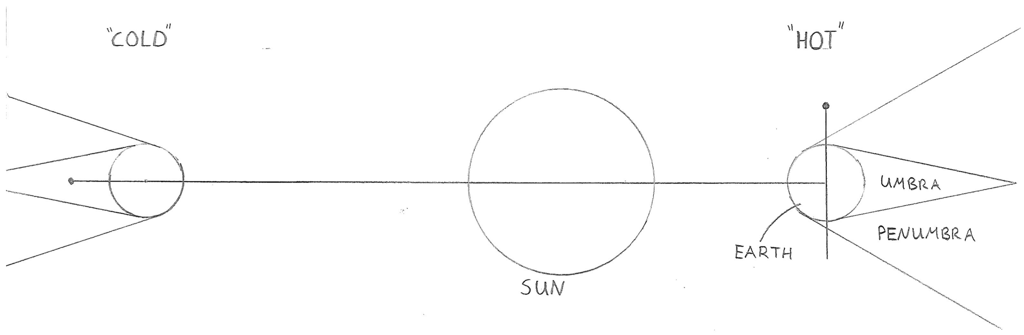

Figure 7.12: Hot and cold scenarios. On the left the orbital plane is aligned with the Sun-Earth vector and the Earth is in its apogee. On the right side the orbital plane is on a right angle with Sun-Earth vector and the Earth is in its perigee.

The reference situation

Before a preliminary TCS can be given, the reference situation has to be considered first. In figure 7.13 the temperature distribution over the nodes is given for both the hot and cold scenario. In this case the nodes are still defined as in section 7.7.7 with the default Aluminum 7075-T6 outer panels [107].

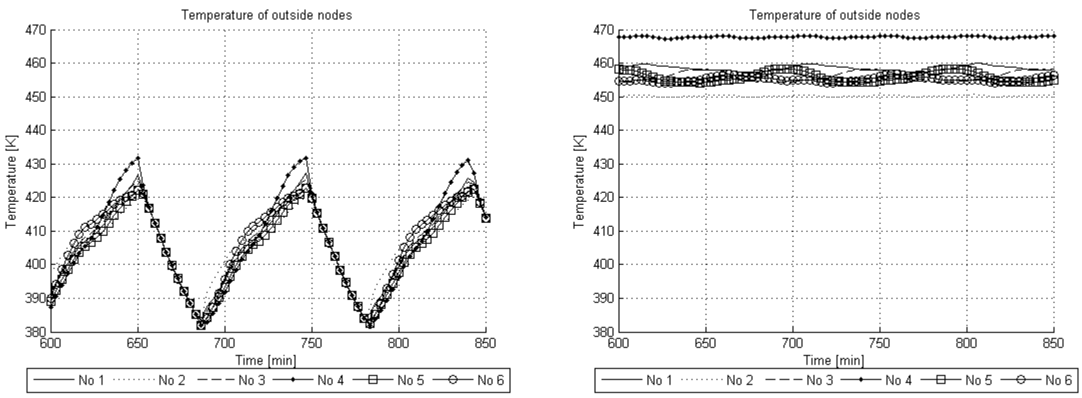

Figure 7.13: Left: Cold scenario ; right: Hot scenario. Both cases use a polar orbit at 540 km altitude.

As can be seen the instrument will encounter temperatures between approximately 380 and 470 K. From section 7.1 this will have to be reduced to a temperature range between 243 K (-30°C) and 313 K (+40°C). The upperbound is determined by the operational temperature (the highest temperatures are encountered in direct sunlight when the instrument can take pictures) and the lower bound is chosen for survival when the instrument is in umbra and cannot take pictures.

Based on the thermo-optical properties found in [30] several cover materials were tried. It was found that silver paint ($\alpha = 0.37$, $\epsilon = 0.44$) added to the Aluminum panels gives an acceptable temperature range. This range is plotted in figure 7.14. As can be seen the temperature range is from 230 to 300 K. On the low side this is 10 K short for operational temperatures. In the cold scenario the temperature difference on short timespans is equal to 70 K in the hot scenario it is reduced to ≈15 K although the average temperature is much higher. These different temperature ranges introduce different problems for both electronics and structures. While for the cold case the problems arise in repetitive loading with large temperature difference, the problems for the hot scenario are in the sustained high temperatures.

If a heat source of 800 mW is added to node 6, the temperature range is lifted to 236 − 313 K. The heat dissipated in the instrument is therefore advantageous in the cold scenario. In the hot scenario it brings the temperatures close to the upper boundary of 313 K (40°C).

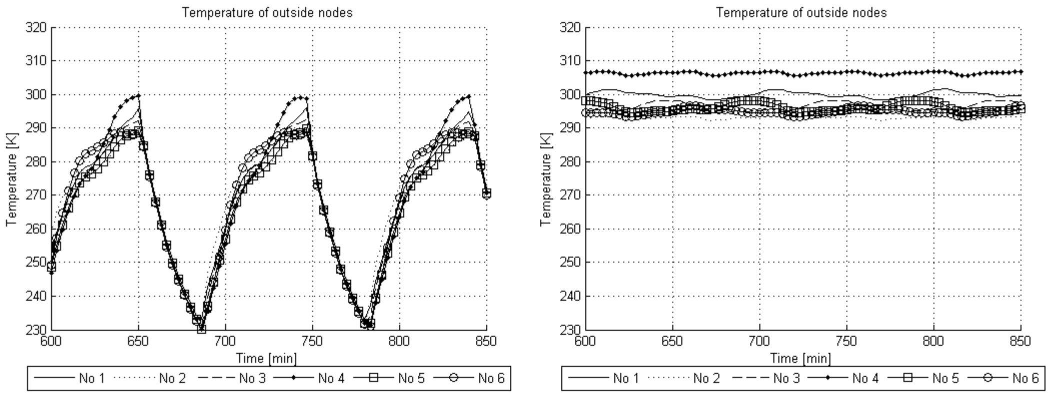

Figure 7.14: Temperature ranges for silver painted Aluminum plates.

Although the temperature range is not exactly met, it can be assumed plausible to only use silver paint to obtain the right temperature range. First of all because in the real case node 6 will not exist and will be replaced by an interface to the satellite bus. This reduces the amount of heat lost to the environment. Secondly because a small amount of heat enters the system through the lenses that is not taken into account now. If silver paint turns out not to suffice on its own several parts of the supporting structure can be painted differently (e.g. black or white to either absorb or repel more heat) or Multi-Layer Insulation (MLI) can be applied locally.

In LEO however, the atomic oxygen that is still present at those altitudes, causes the silver to oxidize which degrades its opto-thermal properties rapidly [108]. Therefore protection against the atomic oxygen will be needed. This protection might be found in transparent layers like lacquer that are added onto the silver paint or paints that renew itself under the influence of radiation or chemical reactions.

7.7.9 Conclusions and recommendations for the thermal control system

From the thermal analysis given in the previous sections it can be concluded that it is possible to limit the temperature range of the instrument to approximately -30 to +40°C. For this a silver painted surface can be used. The use of this paint, however, can be troublesome in Low Earth Orbit and will therefore need an additional protection against the environment.

During orbit the two extreme scenarios introduce problems for the systems lifetime. This is either in the form of thermal fatigue due to repetitive loading over large temperature differences or due to sustained high temperatures.

It is advised that a more accurate thermal analysis is performed using (commercial) packages such as ESATAN-TMS, SINDA-TRASYS or THERMICA. These packages can give insight in the temperature gradients inside the instrument in greater detail and also indicate problems that are not visible now.

Also, as indicated before, this Thermal Control System is designed for a polar orbit at 540 km altitude. Every other altitude or orbit type might require a different solution. If the solutions are limited to a passive control system, the solutions can be found in slow spin rates or specific combinations of surface materials. Also, Multi-layer insulation can be used to isolate specific parts. With this, specific parts can be given their own temperature range. This allows better performance of both the electrical and optical subsystems.

Chapter 8

Environmental protection

Space is a hostile environment, the instrument not only has to survive large mechanical loads and extreme thermal cycles, it is also bombarded with electromagnetic radiation, and all kinds of particles. How the instrument is protected against this is described in this chapter.

8.1 Sector shielding analysis of the Earth observation instrument

The particle radiation as explained in section 3.3.1 is capable of penetrating and damaging vital components of the system, such as the optical sensor and supporting electronics. In order to withstand such radiation, shielding is applied to the satellite itself, and potentially to the support structure of the instrument. In order to save weight and to make the design as efficient as possible, an initial analysis of so-called "shielding" has to be performed. This type of shielding is composed by the support structure itself; already encapsulating the vulnerable components as is suggested in [109].

In order to evaluate the shielding distribution around the system, a sector shielding analysis has to be performed, since the structure cannot be represented by a simple flat plate. The system including the enclosure of the satellite's bus is far too complex for such a simplification. The sector shielding method is a method which evaluates the isotropic shielding distribution of a single predefined reference point, i.e. the shielding distribution over a 4π solid angle is determined in [(% of 4π solid angle)/g/cm^2].

The design as produced using CAD software is too complex to perform such an analysis, so a simplified though representative model has to be used. This model consists of an outer shell of pure aluminum which in essence represents the bus enclosure (also assuming that one end is impenetrable, because of the interface with the remaining satellite's payload), whereas an inner shell should be a simplification of the instruments supporting structure. The supporting structure is not a fully closed box as is suggested here, but it can be assumed that because of all the inner mounting panels this is a valid assumption. The shielding distribution using the sensor as a reference point is shown in figure 8.1, whereas a more detailed summary is given in table 8.1. Figure 8.1 shows the mean position of a binning value, which is equivalent to the amount of material that is present between the sensor and the environment (given in a fraction of the 4π solid angle around the sensor itself).

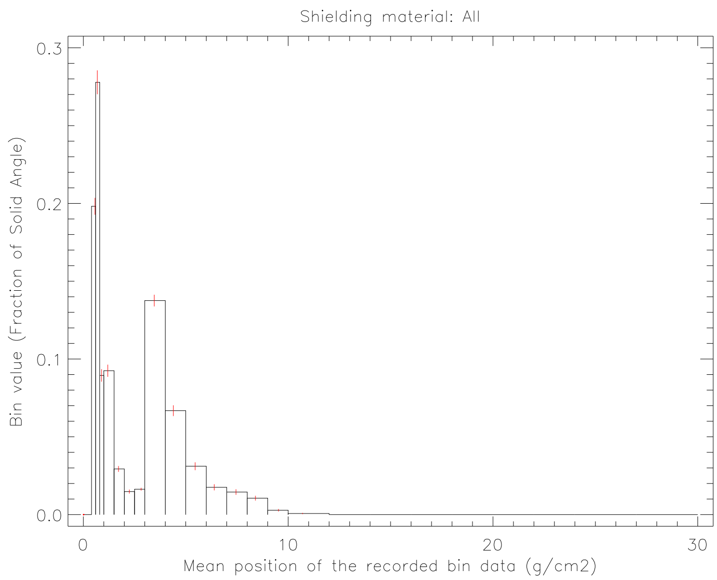

Figure 8.1: Sector shielding analysis of the proposed design

Table 8.1: Detailed summary of the sector shielding analysis adopted from figure 8.1

Sector shielding analysis				
Lower edge of the bin in g/cm^2	Upper edge of the bin in g/cm^2	Mean position of the recorded bin data in g/cm^2	Bin value in % of the 4π solid angle	Error in % of the 4π solid angle
0.400000	0.600000	0.566764	0.198157	0.005403
0.600000	0.800000	0.680502	0.277853	0.007668
0.800000	1.000000	0.889264	0.089450	0.004016
1.000000	1.500000	1.194962	0.092475	0.003911
1.500000	2.000000	1.716503	0.029356	0.001857
2.000000	2.500000	2.247408	0.014799	0.001283
2.500000	3.000000	2.819453	0.016307	0.000907
3.000000	4.000000	3.459691	0.137562	0.003769
4.000000	5.000000	4.394793	0.066802	0.003468
5.000000	6.000000	5.458162	0.031100	0.002523
6.000000	7.000000	6.388803	0.017550	0.001975
7.000000	8.000000	7.453222	0.014507	0.001799
8.000000	9.000000	8.401889	0.010572	0.001542
9.000000	10.000000	9.528322	0.002806	0.000810
10.000000	12.000000	10.702819	0.000702	0.000405

8.2 Dose-depth analysis using the SHIELDOSE-2 model

The SHIELDOSE-2 [110] model is a widely accepted and used model within the industry and it offers the means to compute the dose-depth curves following from the radiations sources as described earlier for a range of shielding depths in g/cm^2. The model is only capable of providing the data with respect to pure aluminum shielding, however if the thickness of pure aluminum (2.7 g/cm^3) that is necessary to reduce to total ionization dose to a certain level is known with respect to its density, than it is certain that for denser materials like Al-7075 (2.81 g/cm^3) and Super Invar® (8.150 g/cm^3) a lesser value for the total ionization dose is encountered.

The sector shielding analysis provided a 4π solid angle shielding distribution with respect to a reference point, which in this particular case will be the sensor. The shielding depth, given in terms of pure aluminum, can be compared to the depths obtained from the dose-depth curves. This comparison should emphasize if the sensor (and potentially other components using a similar analysis) are well protected seen from every direction within a sphere.

The shielding depths that are being evaluated are shown in table 8.2:

Table 8.2: Input shielding depths of the SHIELDOSE-2 model with respect to pure aluminum (2.7 g/cm^3)

Shielding depth values	
mm	g/cm^2
0.5	0.135
0.75	0.2025
1.0	0.27
1.25	0.3375
1.5	0.405
1.75	0.4725
2.0	0.54

The results of the SHIELDOSE-2 model, assuming finite aluminum slabs and a silicon detector, are given in figure 8.2 and 8.3 for the 540 km and the 1440 km heliosynchronous orbits respectively.

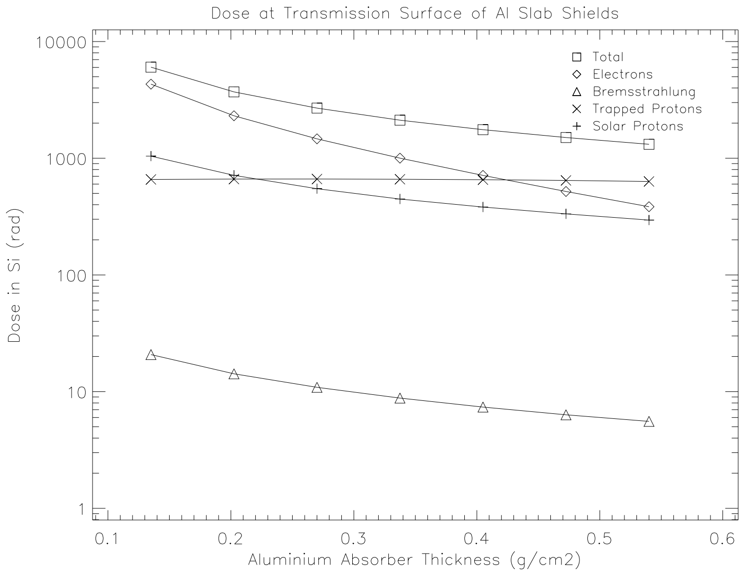

Figure 8.2: Dose-depth curve for a 540 km heliosynchronous orbit, generated using SPENVIS [111] software suite

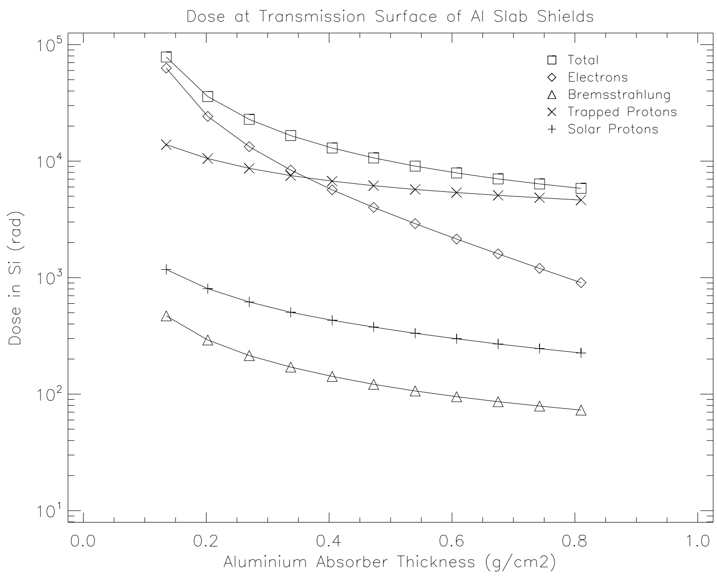

Figure 8.3: Dose-depth curve for a 1440 km heliosynchronous orbit, generated using SPENVIS [111] software suite

8.3 Solar cycle

From the description of the space environment it becomes apparent that the hostility compared to on Earth environment requires specific protection. The protection necessary for a space vehicle is dependent on its location in space as well as its motions. As mentioned in the previous section 7.7.7 the motion of spinning strongly influences the temperature distribution over the vehicle, imposing different shielding requirements than if only one side of the vehicle was constantly heated. To discuss the protection mechanisms in an organized fashion the section has been divided into subsections each addressing a specific environmental influence and the options of protection.

A crucial factor determining environmental factors such as radiation and density is the sun. The sun does not constantly emit the same dose of radiation over time, but varies strongly. The term solar cycle refers to large differences in solar flux over time. The instrument designed will need to withstand the various types of radiation it encounters, especially proton, electron and x-ray radiation. Knowledge about the solar cycle allows a better insight on the space environment to be encountered and through this enables more dedicated design of the orbit and the consequently necessary shielding. On average a solar cycle has a period of eleven years, as can also be seen in figure 8.4 showing the monthly solar flux from 1990 to 2011.

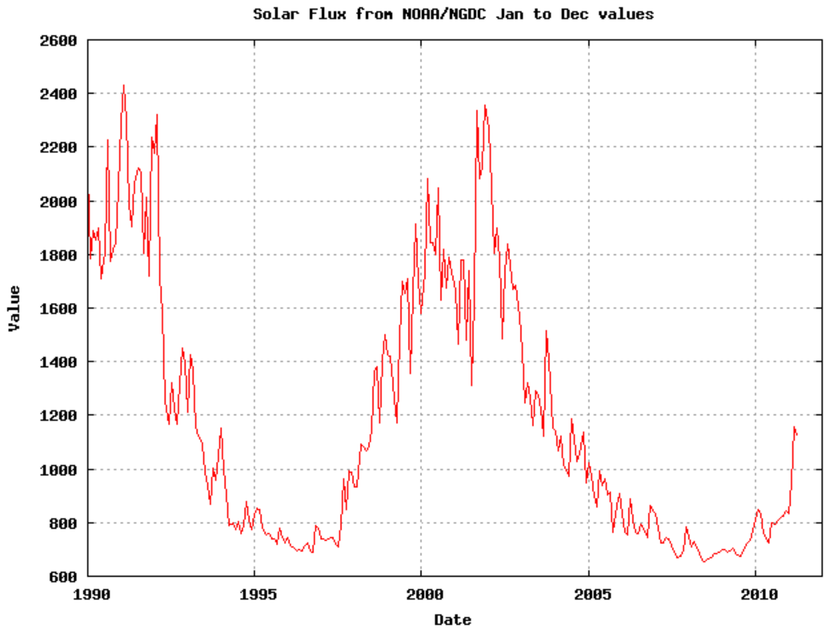

Figure 8.4: Monthly solar flux from 1990 to 2011 provided by NOAA Physical Sciences Division [112]

The main protection mechanisms against radiation is the outer skin of the satellite. During the SPENVIS analysis a box, resembling the satellite housing the optical system, is modeled to precisely evaluate the environmental characteristics of the instrument. The box with Al-7075 walls of 1 mm thickness was able to protect against most of the radiation encountered in the orbital range applicable. However it became apparent from the analysis that increasing the wall thickness further will only have a minor protective effect. This is especially critical when looking at high altitudes where radiation protection is more crucial than at lower altitudes.

For the different orbits under consideration the radiation dosage has been evaluated using ESA's SPENVIS program. In section 8.2 the theory is explained and the data produced can be found in the same section. As can be seen from the graphs in digital supplement B the radiation dose in the reference orbit of 540 km is negligibly small compared to the very large radiation dose in 1440 km. This effect is mainly caused by the Van Allen belts, but in general it is true that the higher the altitude the higher the radiation dose. The most sensitive component of the design is by far the CMOS sensor, CMV4000. From tests performed by the Jet Propulsion Laboratory [113] on similar CMOS sensors and from correspondence with researchers at the EEMC of Delft University of Technology currently investigating the properties of the CMV4000, the sensor chosen in chapter 4 is expected to endure a radiation dose of about 10 krad before severely malfunctioning. In order to reduce the dose encountered by the sensor at 540 km altitude an aluminum wall with a thickness of 1 mm is required, reducing the dose to an acceptable value. For high orbits the shielding of 1 mm does not fully suffice and therefore the expected lifetime of the sensor might not be reached. Also other electric components like the transceiver are considerably affected by radiation and often designed for LEO within a range of 400 to 800 km however not up to 1440 km. In order to withstand the radiation in such altitudes additional shielding is required.

Due to the nature of radiation allowing it to penetrate even thick walls of aluminum alternative protection mechanisms are scarce. Most interesting option is prevention by careful orbit design considering the solar cycle. Furthermore the usage of space grade materials and components during the design process promises a longer lifetime and reliability. In case of this design the most sensitive materials are the lenses used and the electrical components. Due to the design objective to use COTS components and aim to keep the overall costs of the system low, special space grade components are often not an option. Learning from prior missions, such as the Delfi C3, it becomes apparent that some electrical components perform well without being specifically designed for usage in the space environment, as explained in chapter 6. Such insight significantly help, taking decisions on components and material usage during the design phase.

8.4 Atmosphere protection

Although space is generally considered a void, some atmosphere is still present, especially at low Earth orbits. In this section the way the instrument has to be protected against the atmosphere is described. The atmosphere present is described in section 3. First there will be a quick overview what effects the atmosphere has on the satellite. Then will be investigated which parts of the instrument are exposed to the atmosphere and what kind of influence this has on. Finally the protection against these effects will be examined.

8.4.1 Effects of the atmosphere on satellites

In low Earth orbit there is still a noticeable atmospheric density. This means the satellite will experience atmospheric drag, an effect which is especially important for orbits below 600 km. The drag slows the satellite down which results in a decrease in orbital altitude. After some time the orbit will be so low that the satellite will burn up due to aerodynamic drag. Below 600 km altitude the atmospheric drag is one of the main parameters determining lifetime. The lifetime depends on the ballistic coefficient, the starting orbit, and the stage in the solar cycle. Cubesats have a ballistic coefficient of about 20 kg/m^2. This means that when launching into 540 km orbit at solar maximum the satellite will deorbit in 2 years if no active orbit correction is applied. When launched in solar minimum and the same orbit it takes nearly 6 year. In view of a sustainable use of space around the Earth this can be considered an advantage, because in this way the satellite does not add to the amount of space debris. CubeSats are not large, and carrying enough fuel for deorbiting will generally not be considered. By flying low orbits and deorbiting at end of life the satellite due to drag will not clutter the orbits around Earth and can be replaced by new satellites. [114][19]

Satellites move with about 7 km/s through the atmosphere when in LEO. This means particles will impact the satellite with approximately the same velocity, therefore the effects of these collisions are important because this may effect the satellite surface. This effect is even worse when the particles are reactive, such as Atomic oxygen. Atomic oxygen can severely affect the operation of the system unless adequately protected. Due to the low atomic mass of atomic oxygen it is one of the main constituents of the atmosphere between 150 and 1000 km. At 1000 km altitude there are 10^{10} particles per cubic meter, exponentially decreasing with altitude. At 700 km the density of atomic oxygen is a 100 times as low as at 400 km (see section 3.2). Below 550 km altitude the amount of particles heavily depends on the the solar cycle.

8.4.2 Exposure to atomic oxygen

Although the atmosphere does not consist only of atomic oxygen this is by far the most damaging to satellites. However also internal components can be degraded when there are openings in the spacecraft. Venting holes will be required because of the pressure differences during launch. It depends on the design of the bus where these can be placed. With respect to the instrument the most advantageous placing of the venting holes is in the bus so that the optical system is not disturbed. There are three components of the instrument that are exposed to the atmosphere. [115]

- The thermal control system consists of coatings of a certain material on the outside of the satellite. These will degrade due to atomic oxygen and their effectiveness will be reduced throughout the life of the satellite.

- If as suggested in the electronics design a patch antenna is put onto the the outside of the satellite it is directly exposed to the environment (see chapter 6).
- The outer optical glass needs to be able to withstand the atmosphere. Also the outer shell of the instrument needs to be corrosion resistant enough to withstand the atmosphere.

To indicate the total amount of atomic oxygen that the instrument will experience use is made of the *fluence* of atomic oxygen particles. *Fluence* is the flux of particles (or radiative flux) integrated over time. There are several factors that determine the *fluence* of atomic oxygen. The fluence of AO is given by equation 8.1 [108].

$$F_0 = \rho_N \cdot V \cdot T \tag{8.1}$$

First of all the density ρ_N, has a large influence. The density is dependent on the altitude. The reference altitude of 540 is not the only one to be considered. If the instrument is inserted in a 540 km orbit without station keeping fuel that means it could still be operational once it's altitude is down to 300 km caused by drag, which will probably happen within a few years. The lower the orbit the higher the atomic oxygen density. Also the solar cycle influences the density of atomic oxygen. T is the time in orbit, the fluence is the integral of the flux hence the longer the mission lasts the larger the fluence. The velocity, V, is given by the circular velocity of the satellite and depends also on the altitude. Therefore when de altitude decreases the AO fluence increase both due to density increase and velocity increase.

Because of the pointing ability of the reference satellite the antenna and lens may be exposed to atomic oxygen but only to a limited amount of time. The AO fluence depends on the cosine of the angle between the normal of the surface and flightpath angle. The lens will in general be nadir pointing so the angle between the the flight path vector and the surface normal is 70 degrees maximum. The antenna can be either nadir or space pointing, the second solution is used when using relay satellites. Either way the same angle applies, see figure 8.5 Even so also surfaces not in ram direction will experience some influx of atomic oxygen. Finally the combined exposure of the satellite to radiation, thermal stress and radiation may degrade the spacecraft surfaces faster than atomic oxygen alone. In this respect especially UV radiation is important. Many coatings degrade a little bit due to UV radiation which then increase the effect of AO. [116][108]

Figure 8.5: Fluence projection

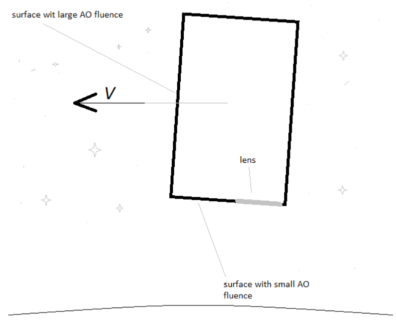

8.4.3 Vulnerability of materials to atomic oxygen

Some components are more vulnerable to AO than others. Most of the data in this section originates from NASA which has launched several dedicated missions to study AO in space.

- The antenna will most likely be a metal component. Most metal components in general have no changes in macroscopic properties, however microscopic changes can occur. It depends on the design of the antenna how sensitive it is to microscopic changes. Some patch antennas use different materials such as meta materials. If the gain of the antenna drops the problem will be that it will be more difficult to attain required data rates. It is unlikely the antenna will become a problem in 2 years lifetime, since they have been designed specifically for space use between 450 and 800 km, and certified for 2 year LEO liftime [117].
- The thermal control system is vulnerable to atomic oxygen. The instrument employs passive thermal control which means surface quality and thus microscopic changes will be important. Besides large parts of the instrument are perpendicular to the flight direction hence the impact is much stronger. In order to mitigate the effects it may be useful to rotate the instrument every once in a while or increase the protection on one side and keep that side in the flow at all times. With respect to thermal coatings there are large differences between coatings. Coatings based on organics are not suitable for use in AO environments, however silicone base paint does not degrade quickly. Paint degradation is influenced by a combination of UV and AO fluence [118]. Another option is to apply a ceramic coating. From space shuttle and LDEF experiments it has become clear that degradation of most paints will slow down over time. The best coating for the satellite is silver paint 7.7.8. This is a problem for the AO protection. Whenever the satellite is in an environment with atomic oxygen metallic silver cannot be used. Silver will oxidize quickly and the oxides will not adhere to the metal and fall off the satellite. In the most adverse conditions a silver plate will degrade with a speed of $3mm$ a year. Silver paint is of course not the same as metallic silver however silver paints will have silver in them. An additional coating is not a durable solution because the coating can easily get damaged, however it may suffice for the duration of the mission. This subject will require further research.
- The optical system is constructed in such a way that it is least vulnerable to the atmosphere. The outside surface will be a flat, thin sheet of optical glass. Optical glass is not very vulnerable to atomic oxygen. However it might be beneficial to have extending baffles that shield the sensor from direct AO impact. The analysis for the reference orbit does not show this as required. However, the surface quality of optical glass is of paramount importance therefore any damage to the surface has to be prevented. To achieve this effect a little bit by careful design the first optical surface is mounted in a hole slightly below the surface of the satellite. This will work as a sort of baffle. [108]

Chapter 9

Production plan

A product may be well designed on paper, however if the production and assembly are not well organized the risk that the product will fail becomes larger. Therefore it is important that during the design phase a production plan is designed, which can be implemented directly after the final design of the product is finished.

In section 5.1.5 the final design was presented, this design is shown in figures 9.1 and 9.2. The upcoming sections will describe how the different parts will be manufactured and assembled into an optical system and ultimately into the satellite. The resources required during the production process will also be described in section 9.1.

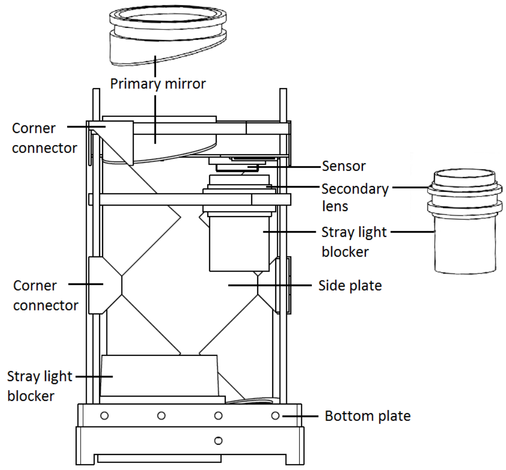

Figure 9.1: Front view of ANT

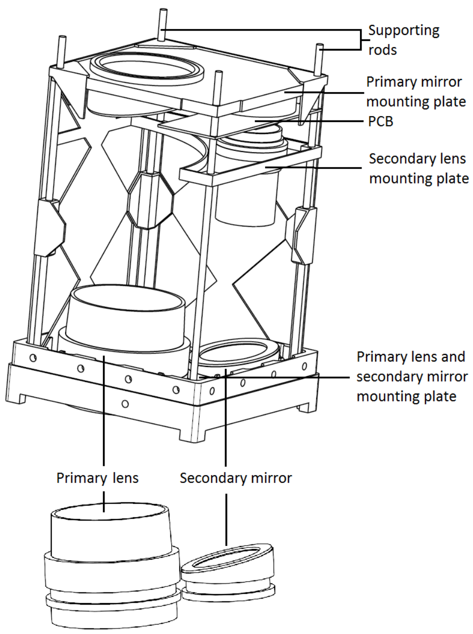

Figure 9.2: Isometric view of ANT

9.1 Required resources

When considering production resources, the first thing that comes to mind are (raw) materials and parts. The resources, however, comprises more than just materials. In this chapter the following kinds of resources are considered: Materials and parts (9.1.1), Facilities (9.1.2) and Equipment (9.1.3).

9.1.1 Materials and parts

As discussed above, materials and parts are the most obvious resources required for the production of any product. When considering the optical system, which is described in this report, the materials and parts used in this system are:

Optical parts

The two doublet lenses and the optical filter can be bought as Commercial Off-The-Shelf (COTS) components at Edmund Optics. The two mirrors need to be custom made, since the dimensions of the COTS mirrors differ from the design.

Sensor

For the final design the CMOSIS CMV4000 sensor was chosen, because of its favorable characteristics. This is a COTS image sensor, which can be bought at CMOSIS in Antwerp, Belgium.

Printed Circuit Board (PCB)

The printing board will have to be custom made, since it has a different form and components than conventional PCB's. There are, however, companies that can produce custom made PCB's for a good price. This PCB will still have a rectangular form, but it can be machined to the desired shape.

Raw material

Some parts of the optical system cannot be purchased as such, so they need to custom produced. Therefore raw material is needed which can be bought from a lot of material suppliers. The optical mountings and mounting plates of the optical system are examples of custom produced parts, which are produced out of Super Invar®.

9.1.2 Facilities

During manufacturing different kinds of facilities are required. First of all there are the production and assembly facilities, where parts can be produced and the final system can be assembled. Since some parts are very vulnerable the optical system needs to be assembled in a clean environment. Usually a clean room is used for this purpose. Clean rooms come in different classes, according to the number and size of particles allowed in the air. For example a Class 10 clean room allows a maximum of 352 particles larger than 0.5 $[\mu/m^3]$ and a Class 100.000 allows 3.520.000 particles of that size in the same volume. Room air usually has 35.200.000 particles larger than 0.5 $[\mu/m^3]$. For the production and assembly of the Delfi-C3 and the Delfi-n3Xt a Class 100.000 clean room was / is used [119]. The parts that do not need to be produced in a clean room, or might even contaminate the clean room will be manufactured in a workshop. After production they will be cleaned and assembled in the clean room.

Secondly testing facilities are required to verify the performance of the system. Different kinds of test can be performed such as vibration testing, thermal vacuum testing, optical performance test etc. Some of these tests require high-tech testing facilities (thermal-vacuum tests), which may be to expensive to build or purchased. There are, however, institutes and companies where these tests can be performed.

9.1.3 Equipment

In order to manufacture the optical system some tools are required. This includes standard equipment like screwdrivers, but also more specific tools like testing equipment. To make the product more viable, relatively easy manufacture methods should be applied, thereby lowering the cost.

For the production of the parts some special machines may be required, like threading machines, milling machines etc. Since these machines can be expensive they may not be present at the production facility and it may be useful to outsource the production of the parts to specialized companies and then assemble them at the own assembly facility.

9.2 Part manufacturing

The optical system designed contains a lot of parts which need to be custom build. In this section the manufacturing for the different parts will be described. To determine which production process would be most suitable the technical drawings of the ANT were presented to the floor manager of the workshop at the faculty of Aerospace Engineering of Delft University of Technology.

9.2.1 Supporting structure

The supporting structure consists of a box to which all the optical parts can be attached. The box itself incorporates several components:

Bottom plate

This is the part of the supporting structure which is also part of the primary satellite structure. The bottom plate is part of a standard CubeSat kit (CubeSat Kit MSP430) by Pumpkin [120], however a circular hole needs to be drilled for the aperture and connections with the rods that will be attached to the plate. After the drilling, the edges of the hole should be polished to achieve a smooth surface.

Mounting plates

On the mounting plates the lenses and mirrors will be attached, therefore these parts need to be thermally stable. For this purpose Super Invar® is chosen, because of its excellent thermal properties described in section 5.2. In these plates holes need to be made for the optical mountings. The mounting plates will be produced using a milling machine, since the parts have some level of detail (holes, round corners, pockets, stringers) as can be seen in figure 9.3. Milling of Super Invar® is somewhat difficult because the machined chips are gummy and stringy , however not impossible especially when using the typical milling speeds for Super Invar®[75]. Since the optical elements will be mounted on these plates, they have low tolerances. Therefore there will be a coarse milling to begin with, followed by very precise milling to finalize the product.

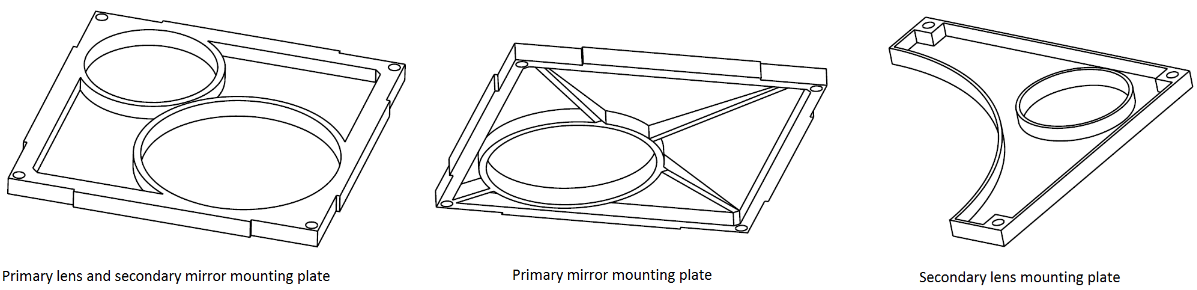

Figure 9.3: The lens and mirror mounting plates

Side plates

The side plates ensure that the box will not deform and provide the structural backbone for all elements within the optical system. It will be produced out of a sheet of Super Invar® by electrical discharge machining, this is a very easy technique which causes almost no stresses in the material.

Corner connector

In order to fix the side plates together, corner connectors are produced. Two types of connectors are used: one for the upper and lower corners, the other for connecting the plates in the middle. The upper/ lower connectors are simple Super Invar® parts which can be produced by a press brake after which holes will drilled to allow the rods to pass through them. The middle connectors are to be milled since they have a solid part where the rod will have to pass through. Both the connectors can be seen in figure 9.4.

9.2.2 Optical parts

Lens mountings

The lens mountings will be incorporated in the holes of the mounting plates. Since these mountings need to support the lenses, they need to be very stable and therefore Super Invar® was chosen once again. The part

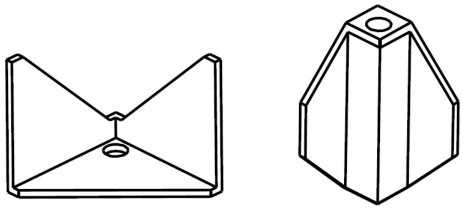

Figure 9.4: Upper and lower connector (left) and the middle connector (right)

will be turned to get the desired shape. After the general shape is finished the bottom part will be threaded to allow fastening onto the mounting plates.

Mirror mountings

For the mirrors separate mountings will have to be produced, since the mirrors need to be placed under an angle. Like the lens mountings, the mirror mountings will be turned after which a thread will be applied at the bottom.

Stray light blocker

To prevent stray light, a tube is attached to the primary and secondary lens mounting. To prevent stresses between the mounting and the stray light blocker, the tube is also made out of Super Invar®. The tube can be manufactured by turning. On the outside of the tube a thread will be applied to fasten the tube to the optical mounting.

9.3 Assembly

In the previous section the manufacturing of the different parts has been described. In this section the assembly of all these parts and the of the shelf components are described, creating the complete optical assembly. After the assembly the optical system needs to be tested. Since the entire system is only 15 cm working space is limited, therefore the smaller parts will first be assembled and then combined with the other parts. The outline of the process is described hereafter.

First the lenses and mirrors will be placed within their optical mountings. The lenses will be fitted in a ring of an elastomer to make sure that if the lens expands, the stress in the lens remains at a maintainable level. The lens needs to be placed with great precision to ensure a good image quality in the end and therefore it needs to be checked if the lens is placed right. This can be done by pointing a laser through the center of the lens onto a crosshair and then rotate the mounting. If the lens is placed properly the projected image will not move, nor defocus. The procedure for the placing and testing of the mirror is similar to the one of the lens, however also the surface angle needs to be checked.

Next the tubes that block the stray light will be connected to the optical mountings. Inside the lens mountings a thread is present as is on the outside of the stray light blocker. Therefore the stray light blockers can be easily installed on these mountings. At this point all the optical elements can be attached to their corresponding mounting plates. The optical mountings can be placed into the holes of their plates after which a closing bracket will be fastened at the other end of the plate to keep the elements in place. If necessary thin washers can be used to position the mounting in its required location.

Now the entire optical system can be assembled. First the upper / lower connectors are screwed to the mounting plates after which these plates can be attached to the side plates. Next the middle connectors are screwed to the side plates, finishing the entire box. To reduce reflecting light inside the box an anti-reflecting coating, like black paint, may be applied. To check whether the optical system satisfies the requirements considering the image quality, the camera needs to be tested. For this purpose laser ray tracing can be used. If the system is not properly aligned the lenses can be shifted in the normal direction by placing washers between the part and the mounting plate. Once the camera is finished and tested, it can be easily integrated in a CubeSat by placing it over the supporting rods of the satellite and fasten it to the bottom plate with screws.

Chapter 10

Design assessment

The assesment of the design of the Advanced Nano Telescope will be discussed in this chapter. An evaluation of the design will be performed to determine whether the current design meets all the requirements set forth during the initial stages of this phase-A study.

First of all the resource budget breakdown will be presented in section 10.1, followed by a cost estimation for the ANT in section 10.2. Thirdly the risk analysis for the system will be performed in section 10.3, to indicate all the possible risks the camera may encounter during its lifetime. Finally it is checked whether the ANT meets all of its requirements by means of a compliance matrix in section 10.4.

10.1 Resource budget breakdown

To keep track of the important technical parameters and make sure these do not exceed the resource availability a technique called technical parameter measurement (TPM) is employed during the detailed design. Four categories of values are used for each performance parameter: The *specified* value is taken from the requirements and determine the absolute limit of the amount of resources to spend. The *target* value is the *specified* value minus a contingency that has previously been defined in the baseline reports *resource allocation and budget breakdown* section and these contingencies are shown in table 10.1. The *actual* value is the amount of resource that is actually being used at the moment. The *current* value is the actual value including a contingency that reflects the status of the actual design. Note that the restrictions concerning the volume and power budgets are dependent on the selected reference satellite and might not be applicable for other satellite busses in which the camera system could be installed.

Table 10.1: Contingencies of technical resource parameters per project phase

	Contingency (%)			
	Mass (m)	Volume (V)	Power (P)	Cost
Straw-man phase	20	15	10	20
Conceptual phase	20	10	10	20
End of phase-A	10	5	5	10

The graphs show the following technical resource parameters at several points in time: the mass, volume, power and cost. The mass and volume trend graphs are shown in figure 10.1.

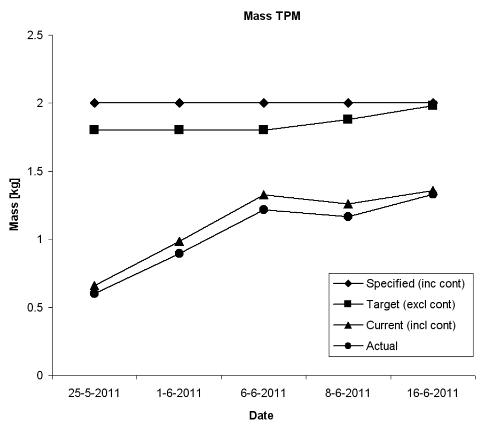

(a) TPM trend graph of the mass.

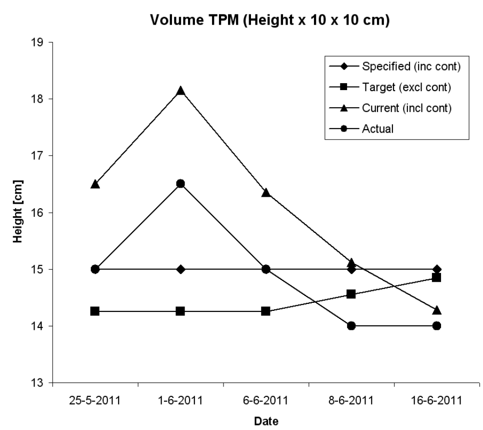

(b) TPM trend graph of the volume.

Figure 10.1: Mass and volume technical performance measurement graphs.

The mass of the system steadily increases because after each iteration mass was added and several parts switched to heavier materials. At the third iteration several components were milled and mass was removed which can be seen from the drop in the graph. In the later stages of the design process some mass emerged that was not incorporated in the budget increasing the design mass slightly. During the design of the camera the mass budget never became problematic and no remediating actions had to be taken to remain within mass budget.

The volume started off exactly sized on the projected available payload space of the Delfi-n3Xt satellite. Once the first iteration was completed it was found that the volume exceeded the target value, since more space between the optical elements was needed due to needed margins that had not been considered in the conceptual design. The layout of the optical system was subsequently altered in such a way as to compress the system into a smaller volume. This lowered the volume back to within the designated boundary. With the movement of the electronics from the back side into the vacant spaces next to the sensor more space was freed such that the total system volume reduced to well within the allowable volume boundary.

The power and cost trend graphs are shown in figure 10.2.

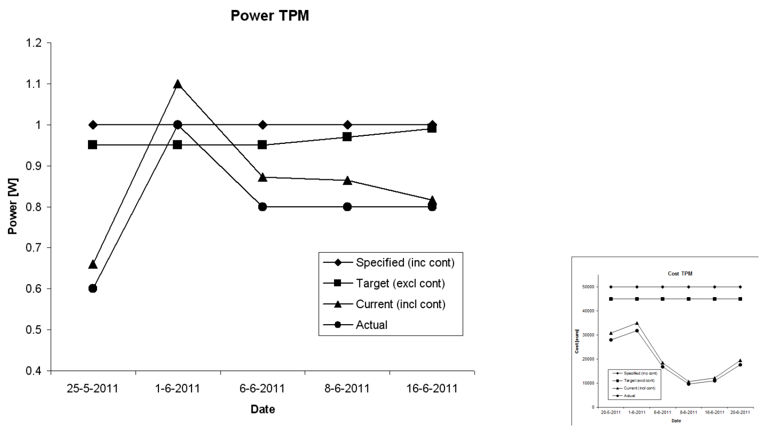

(a) TPM trend graph of the power.

(b) TPM trend graph of the cost.

Figure 10.2: Power and cost technical performance measurement graphs.

The actual value of the power used by the system started off as only the value for the sensor at maximum power consumption rate. Next some estimates of the power usage of on board processing were added which brought up the power usage to beyond the 1 watt boundary. After some more in depth research some of the components could be throttled such that power usage was reduced while only slightly decreasing processing power. Also it was found that due to the downlink data rate being the bottleneck, the sensor would not be able to operate at peak performance. This meant the sensor imaging rate and thus power usage could be reduced.

Regarding the costs, the COTS components coupled with the low amount of material needed allowed the system itself to remain very low cost compared to the available hardware budget. Part creation is the main factor driving up the cost of the system. Due to the current detail of the design the contingencies have not been relaxed as more detailed design could still have a large influence on the cost aspect. For current results the costs have remained well within budget. It should be noted that the costs depicted here show the hardware costs only, the total costs will be presented in section 10.2.

10.2 Cost estimation

A very important factor to produce a successful product is a competitive price. This is also the case for ANT, especially if it would be implemented in a constellation of satellites. This section provides a realistic cost estimation based on experience gained by the Delft University of Technology Space department during similar projects.

To determine the cost of the camera system, first all the relevant contributors to the price need to be determined. These costs can be divided in two different categories: recurring costs and non-recurring costs. In figure 10.3 the Cost Breakdown Structure (CBS) for the ANT is presented.

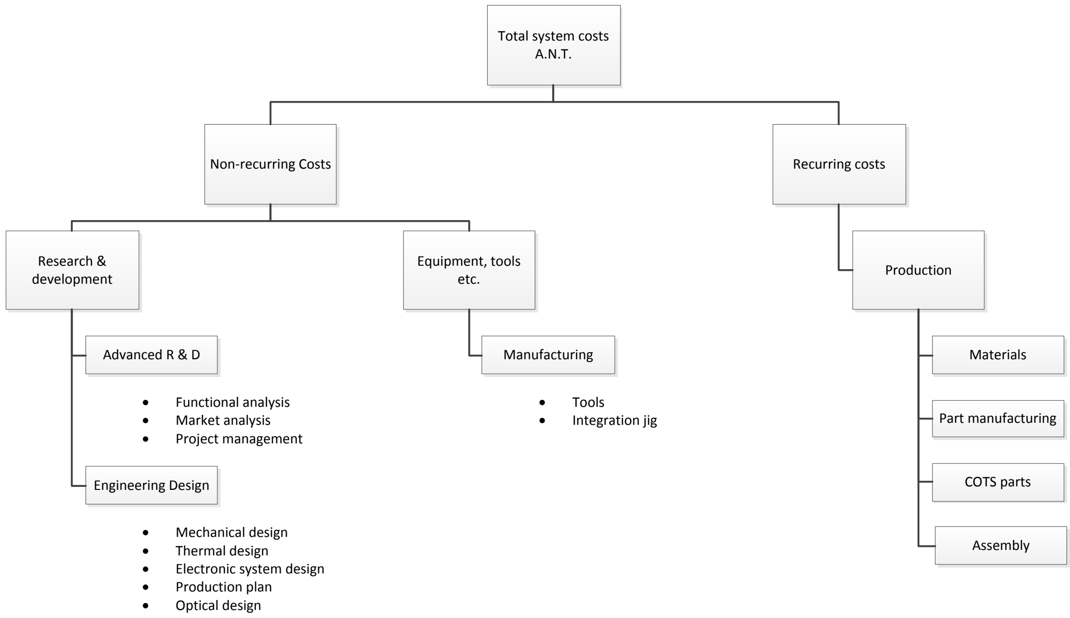

Figure 10.3: Cost Breakdown Structure for the ANT

10.2.1 Recurring costs

The recurring costs represent the costs required for each product, like the material cost. In this section all the recurring costs as depicted in the CBS, figure 10.3, will be treated.

Production

The production of the ANT consists of several components: Materials, Part manufacturing, Commercial Off-The-Shelf (COTS) parts and Assembly. Each of these topics will now be discussed and a cost estimation is given.

Materials Since the optical system designed is very small, a small amount of material is required. For example, the most used material is Super Invar® but for every instrument less than 1 kg of this material is applied. The up-to-date price of Super Invar® could not be found, so the price was estimated to be 150 % of standard Invar. With a price of 8 €/kg for standard Invar the price of Super Invar® becomes 12 €/kg. Assuming 2 kg of Super Invar® is required, the cost becomes €24. The costs for the other materials (aluminum 7075-T6, Stainless Steel, Elastomer) are even lower than the Invar cost. In the end it is estimated that the total material cost for every ANT is about €30.

Part manufacturing The raw materials that will be purchased have to be processed in order to achieve the desired shape, as described in the production plan in chapter 9. To estimate the costs for the processing, the technical drawings of the ANT were evaluated by the floormanager of the workshop at the faculty of Aerospace Engineering of the Delft University of Technology. During this consult the estimated production time of the parts that have to manufactured were discussed. The production times can be found in table 10.2 and considering an hourly wage of €50 a cost estimation can be made. As can be deducted from table 10.2 the total production time is estimated to be 39 days and a corresponding cost of €15,600.

Table 10.2: Part manufacturing times

Part	Process	Time [days]
Mounting plates	Milling	10
Side plates	Electrical discharge machining	1
Corner connectors	Milling	5
Lens and mirror mountings	Turning	20
Stray light blockers	Milling	3

Commercial Off-The-Shelf parts Not all parts have to be manufactured for the ANT, some parts can simply be bought. These are the so-called Commercial Off-The-Shelf (COTS) parts.

The optical components, i.e. the lenses, mirrors and filters that have been used in the ANT can be bought at Edmund Optics [65]. The cost for the primary and secondary lens are €105 and €74 respectively. The optical filters that need to be applied cost €261. The primary and secondary mirror cannot be bought of the shelf, but they can be custom made by Edmund Optics for about €300 and €200 respectively.

Another COTS part is the image sensor used, the CMOSIS CMV4000, which can be bought at CMOSIS in Antwerp for €600. The PCB on which this sensor will be fixed has to be custom made. There are, however, a lot of companies who can produce a custom PCB's for prices of about €50.

The last COTS component used for the ANT is the bottom plate. This bottom plate is part of the MSP430 CubeSat Kit that was also used for the Delfi-n3Xt. The kit, with flight components included, can be purchased at Pumpkin [120] for $ 8750, however only the bottom plates are required, so a price of €500 is assumed.

Adding all the costs discussed in this section together, the total cost for COTS parts is €2090.

Assembly, Integration and Testing (AIT) When all the parts and components are finished, they need to be assembled to produce the end product. Thereafter the system needs to be tested. It is assumed that 320 hours (1 month) are required to assembly the system, which includes the exact aligning of the optical system. Another 320 hours are estimated to test the ANT. Considering an hourly wage of €60. The total assembly cost then becomes €38,400.

10.2.2 Non-recurring costs

The non-recurring costs are the costs that only need to be made once and can therefore be divided over all the produced endproducts. For this calculation it is assumed that a total of 50 ANT's will be produced. This value represents one constellation of 24 ANT's, since with that amount of ANT's full color images can be provided with a temporal resolution of about a month, as was found in section 6.5.4. Another 26 ANT's are estimated to be sold separately.

Research & development

This entire report has described the research and development of an optical system for a nanosatellite. A very promising design was the result of this process, however more research is required before the ANT can enter the production phase. It is assumed that 10% of the entire project is now finished, being ten full-time weeks with nine people which equals 3600 hours. Thus to finish the project approximately 36,000 hours are required. Considering a wage of €60 the costs of research and development becomes €2,160,000.

Equipment and tools

For the manufacturing of the ANT several tools and sorts of equipment are required. For example screwdrivers and drills are required, but also more expensive equipment like an integration jig or testing equipment need to be purchased. The equipment cost is therefore estimated to be €10,000.

10.2.3 Total cost

Now that all the different elements of the CBS in figure 10.3 have been discussed the total estimated cost can be calculated. The result is shown in table 10.3. It can be seen that the total cost per ANT will be around €100,000. The hardware cost can be calculated by subtracting the AIT cost of the recurring costs, which is €17,720.

Table 10.3: Cost estimation for the ANT

Element	Cost [€]
Recurring costs	
Materials	30
Part manufacturing	15,600
COTS parts	2090
AIT	38,400
Total recurring costs	**56,120**
Non-recurring costs	
Research & development	2,160,000
Equipment and tools	10,000
Total non-recurring costs	**2,170,000**
Total non-recurring cost per ANT (50 produced)	**43,400**
Total cost per ANT	**99,520**

10.3 Technical risk assessment

As the system attains its form, it will be possible to determine the primary risk drivers. These risk drivers will employ a range of failure modes that have to be taken into account when the system is operated. The technical risk assessment will be performed by evaluating the risk per independent subsystem and finally a risk map per respective subsystem will be created. The risk map will indicate what potential high risk failure, if present, needs to be mitigated by employing risk mitigation techniques.

10.3.1 Failure modes corresponding to the optical subsystem

As the optical subsystem is considered to be the primary subsystem of the instrument, a failure within this subsystem will most likely lead to a mission failure or at least pose severe limitations to the further continuation of the mission. To this extent the optical system itself and the mounting brackets used (both considered to be part of the optical subsystem) have been designed to limit the risks as it was being designed.

The failure modes under consideration for the optical subsystem have been presented in table 10.4, giving the corresponding failure mode, probability of occurrence and severity of failure.

Table 10.4: Optical subsystem failure modes

#	Failure mode	Probability of occurrence	Severity of failure mode	Remarks
1	Optical surface production errors	Probable	Marginal	The system can be realigned to cope with these errors.
2	De-lamination of the optical surfaces	Improbable	Critical	The cement between the optical surfaces may degrade by large heat fluxes.
3	Induced aberration by an inhomogeneous temperature distribution	Improbable	Marginal	
4	Fracturing of the optical surfaces	Impossible	Catastrophic	Most likely to be caused by large stress gradients within the system.
5	Degradation of the optical surfaces	Improbable	Marginal	Mostly induced by environmental causes, a multitude of radiation sources.
6	Sensor failure by environmental causes	Impossible	Critical	Most likely to be caused by proton and electron radiation.

10.3.2 Structural failure modes

The structural subsystem of the instrument is designed as such that it is able to cope with the launch conditions as experienced, but also to withstand the harsh conditions imposed by the space environment. As it is only designed to handle the loads, failures can still be induced by infrequent events that can't be modeled for. The risk assessment for the structural subsystem is given in table 10.5.

Table 10.5: Structural subsystem failure modes

#	Failure mode	Probability of occurrence	Severity of failure mode	Remarks
7	Eigenmotion excitation during launch	Improbable	Catastrophic	Probably be caused by random acoustic vibrations
8	Plastic deformation during launch	Probable	Critical	Induced by high shock load factors, caused by the high eigenvalues
9	Structural degradation by environmental causes	Probable	Marginal	Most likely to be caused by atomic oxygen
10	Environmental shielding failure	Improbable	Catastrophic	Most likely to be caused by atomic oxygen

10.3.3 Risks corresponding to the electronic subsystem

The electrical subsystem can be seen as an independent system capable of converting the analog signal into a digital one and processing the data such that it can be stored or send back to Earth. Since the electrical subsystem mostly depends on the interface between electrons it is highly susceptible to radiation, which is present abundantly within the space environment. The corresponding risk factors are shown in table 10.6.

Table 10.6: Electrical subsystem failure modes

#	Failure mode	Probability of occurrence	Severity of failure mode	Remarks
11	The occurrence of bit flips	Frequent	Marginal	Double memory is used in order to cope with the bit flips
12	Electrostatic discharge	Probable	Critical	There will be an accumulation of electrons of the surface normal to the flight direction. This could discharge onto the inner structure.
13	Processing failure	Negligible	Critical	A second processor would be over-designing the system
14	Long term storage failure	Probable	Marginal	If failed, a single image is allowed to be stored within the (RAM) memory.
15	Short term storage failure	Improbable	Catastrophic	Both a short-term and long-term memory are incorporated

10.3.4 Thermally induced failure modes

The thermal subsystem on a particular satellite in order for this instrument to operate correctly can be passive. In order to keep the optical system within its predefined temperature range a silver metallic paint has to be applied to the outside of the satellite as well as a protective coating to shield from atomic oxygen deterioration.

Table 10.7: Thermal subsystem failure modes

#	Failure mode	Probability of occurrence	Severity of failure mode	Remarks
16	Oxidation of the thermal paint	Improbable	Critical	It is improbable that the paint degrades within 2 years.

10.3.5 The technical risk map

From the risks that were recognized by evaluating the corresponding risks per independent subsystem, a risk map can be created. This risk map will visualize the probability of occurrence of a respective risk against the severity of the failure mode occurring. Zones will indicate whether a certain risk is acceptable or not, ranging from acceptable (green) up until unacceptable (red). The intermediate zones contain risks that are too expensive or too difficult to design for and attain a level which remains at a relative level of acceptability. The risk map as defined from the risks as noted in the previous section is shown in figure 10.4.

Catastrophic	Green **4**	Yellow **7,10,15**	Orange	Red
Critical	Green **13**	Yellow **2,6,16**	Orange **8,12**	Orange
Marginal	Green	Yellow **3,5**	Yellow **1,9,14**	Yellow **11**
Negligible	Green	Green	Green	Green
	Impossible	**Improbable**	**Probable**	**Frequent**

Figure 10.4: Technical risk assessment for the proposed design

Two particular failure modes stand out from the rest, namely the plastic deformation during launch and the discharge of built-up of an electrostatic charges on the outside of the satellite. The former follows from a single-event shock, which requires a very extensive (and thus expensive) analysis if one wants to model for it. The latter is primarily ignored, since it is assumed that the built-up in two years is not that significant, thus also limiting the discharge.

10.4 Compliance finding

Now that all the elements for the design have been discussed, it has to be checked whether the ANT meets all its requirements which were stated in section 2.1.10. This is done by means of a compliance matrix which is shown in table 10.8. The column *Compliant* can have three values: Yes, No. Specified in the last column is the section in which the validation of the compliance can be found.

Table 10.8: Compliance matrix

ID Level 0	ID Level 1	ID Level 2	ID Level 3	ID Level 4	Description	Compliant	Section
1.0					Perform mission technically	Yes	
	1.1				Provide sufficient image quality	Yes	
		1.1.1			Ground resolution of 7.5 m at 540 km altitude	Yes	4.7
		1.1.2			Field-of-view of 10 x 10 km	Yes	4.2
		1.1.3			Provide sufficient optical image quality	Yes	4
			1.1.3.1		Mirror surface reflection >90%	Yes	4
			1.1.3.2		Lens transmissivity >95%	Yes	4
			1.1.3.3		Provide opto-mechanical-thermal stability	Yes	4.11
			1.1.3.4		Provide a maximum focal ratio of 1/10	Yes	4.7
			1.1.3.5		Provide a low aberration optical track	Yes	4
		1.1.4			Sense the relevant wavelength (VIS 0.3-0.7 μm)	Yes	4.7
	1.2				Provide sufficient image quantity	Yes	
		1.2.1			Link budget	Yes	
			1.2.1.1		Bitrate >9600 bit/s	Yes	6.5
			1.2.1.2		Time between pictures < 2 seconds	Yes	6.2.2
	1.3				Required power <1 Watt	Yes	10.1
2.0					Perform mission with constraints	Yes	
	2.1				Reliability	Yes	2.3
		2.1.1			Provide no single point of failure	Yes	11.4
	2.2				Operational lifetime of 2 years	Yes	6.3.2
	2.3				Sustainability > 80%	Yes	
	2.4				Integrate-able in the CubeSat standard	Yes	9.3
	2.5				Design within available resources and budgets	Yes	10.1
		2.5.1			Mass budget of 2 kg	Yes	10.1
		2.5.2			Volume budget of 10 x 10 x 15 cm	Yes	10.1
		2.5.3			Cost < 50.000 €	Yes	10.2
	2.6				System tolerances	Yes	
		2.6.1			Launch constraints	Yes	
			2.6.1.1		Acoustic loads of max. 2000 Hz with SF=1.41	Yes	5.3.2
			2.6.1.2		Vibration levels of 31 Hz with SF=1.25	Yes	5.3.2

Continued on next page

ID Level 0	ID Level 1	ID Level 2	ID Level 3	ID Level 4	Description	Compliant	Section
			2.6.1.3		Quasi-static loads of max. 6.0 g	Yes	5.3.1
				2.6.1.3.1	Static load factors of max. 4.55 g with SF=1.25	Yes	5.3.1
				2.6.1.3.2	Dynamic load factors of max. 1.45 g with SF=1.25	Yes	5.3.1
			2.6.1.4		Shock loads of max. 2000 g	Yes	5.3.3
		2.6.2			Space environment constraints	Yes	
			2.6.2.1		Withstand radiation levels	Yes	8.1
			2.6.2.2		Provide low outgassing values for all materials	Yes	5.2

As can be seen all the requirements in the compliance matrix are met, so the ANT is expected to comply with all the requirements stated above.

Chapter 11

Satellite constellation advantages

Now that the design of the Advanced Nano Telescope (ANT) has been explained up to the point of production it might be beneficial to illustrate its most outstanding strength: the option to deploy a constellation of multiple satellites each housing the ANT. This option becomes a reality once the ongoing research into formation flying comes to fruition by enabling formation flying satellites. Already during the optical design in chapter 4 it has been mentioned that the single system produces monochromatic or single color images. However, when multiple satellites are used, each imaging a certain wavelength, a full color image could be obtained. Furthermore the use of additional satellites could solve the problems encountered regarding the down-link as well as the revisit time as mentioned in chapter 6. It was discussed that one option would be to make use of a relay satellite in order to cope with large amounts of data. Summarizing this chapter shows the ultimate strength of this system to operate in a constellation of several small and low cost satellites once formation flying has been realized.

11.1 Multiple orbital planes

From chapter 6 it becomes apparent that a specific orbital design is needed in order to image a certain area. When using only one satellite in an orbit of 540 km altitude, 70 deg inclination and a repeat time of 175 days a major problem concerning coverage evolves. Even if the area of interest is imaged during a few orbits the next time the imaged area is revisiting is after 175 days. This means that any application requiring regular satellite image updates will be impeded. Due to the low costs for small satellites, the option of using multiple satellites can help to overcome this problem. By having satellite constellations operating in more than one orbital plane, the revisit time can be reduced dramatically. Assuming six constellations of four satellites each, one for each color and one relay satellite, the revisit time can be reduced to a little more than a month. Choosing the inclination is one method of reducing the revisit time, however it is limited to a certain degree. The usage of multiple orbital planes divides the revisit time by the amount of orbital planes present.

11.2 Color images

The visualization of multi color images in chapter 4 shows the enormous improvements in image quality still possible. However, it was pointed out in the same chapter that it is not possible to design an optical instrument that could capture color images of sufficient quality, only single spectral bands can be imaged at a time by one instrument. The solution lies within the usage of multiple satellites, each of which are optimized to capture a different spectral band. Such a constellation of satellites could then deliver color images and achieve great improvements of overall image quality. Another upside is the fact that specific applications can use just as many satellites as they need spectral bands imaged. In case of monitoring the marine environment, two colors, blue and green would suffice in order to image the change in color of the light emitted to the surface of the water observed. In some cases a single color can be enough, for example in urban development, where only contrast matters, but not the color of the rooftop imaged. Such examples show the potential of the optical instrument and the advantage that can be obtained with a constellation. There are however limitations to the capabilities regarding the wavelength. To capture a wavelength near the infrared spectrum would require drastic changes in the entire satellite design due to the thermal influences resulting from the incoming radiation.

11.3 Relay satellite

The optical system gathers data which eventually has to be down-linked to Earth. This can be done by a direct link with the Earth or by using a data relay satellite. The latter option will be discussed in this section. In order to achieve a large bandwidth connection using a direct down-link to Earth, a lot of power is needed. In chapter 6 is was found that about 5 Watts are needed to have a down-link rate of 1 Mbps. The amount of power was mainly needed to overcome the free space loss. Another disadvantage of a direct link is that the pointing accuracy of the ground station needs to be high. To overcome these problems it is possible to use data relay satellites in low Earth orbit, such that the free space loss of the connection becomes much less (and as such also the power that is needed). The data relay satellite can be part of a constellation of imaging CubeSats, in which the relay satellite is dedicated for the down-link. Another option is to use an existing constellation such as Iridium. In the case of a dedicated CubeSat the amount of power needed for this satellite is less, since it does not need power for payloads other than the transmitter. This means that the transmitter can be one with a higher power output than what could be achieved on an imaging CubeSat. The imaging CubeSats in turn are able to use a less powerful transmitter, because they only transmit to the relay satellite which is closer by than the Earth.

11.4 Redundancy

One of the most apparent advantages of a constellation of satellites is the availability of multiple instruments at all times. In case of malfunctioning or failure of one system, others can continue the mission. Additionally the piggyback option available to small satellites allows easy and fast replacement. With reference to chapter 4 it is clear that loosing one of the three satellites necessary to create a color image, would result in a reduction in image quality. The severity of the quality reduction is dependent on which colors remain operating, as the green image contributes most to the quality of the whole image compared to the blue image. Overall the redundancy provides more freedom to the mission designer due to reduced risks. The redundancy is of special importance as the reliability of small satellites is by far not as high as expected [121]. From all the CubeSat missions launched only 60 percent actually activated and started operating. However finally only 40 percent of the missions were able to announce a successful execution of the mission objectives, often due to failures that are still unexplained. One dramatic example is the CP4 mission (see [121]) where after a month of perfect operational status the satellite stopped responding. After 400 restarts of the onboard electronics and several attempts to solve the unexplainable problem, the satellite came back to life fully charged and perfectly operating after three months. Crazy enough after another month, it went dark again and has since then not responded any more. In order to cope with such situations the advantage of having several similar satellite systems orbiting in a group allows to reduce the risk associated with a complete failure of one of the systems.

11.5 Summary

A constellation of CubeSats with the optical system on-board has several advantages. With a constellation it is possible to obtain a higher temporal resolution, which makes it possible to observe phenomena with a frequency higher than the revisit time of a single satellite. Another possibility is the use of multiple satellites to make multi-spectral images. It was shown that this is advantageous in for example marine environment observation. A constellation also makes it possible to obtain a higher down-link rate through the use of dedicated communication satellites. Finally there is also the advantage of redundancy, which mitigates the mission risk.

Chapter 12

Conclusion & recommendations

The goal of this project was to develop a multiple synthetic aperture solution for Earth observation. A camera payload was designed as a cornerstone for a future distributed Earth observation satellite system applying miniaturization through the use nanosatellites. The satellite camera system should deliver low cost, mid-resolution satellite imagery to meet the increasing demand in market segments such as environmental protection, disaster response and maritime industry. To outperform currently existing systems the upcoming trend in satellite industry of using nanosatellites offer interesting opportunities. From this the idea was born to outperform single large scale satellites with groups of small nanosatellites. During the project different concepts for possible optical designs, able to achieve mid-resolution images from LEO satellites were compared. After a considerable trade-off the outperforming concept using an intelligent lens-mirror combination was then designed in detail within the preliminary design phase. Analyzing orbital configurations, the present space environment and the resulting thermal requirements were going hand in hand with an iterative development of a thermo-mechanically stable structure. The optimization of the optical design and the development of the electronic subsystem completed the design of the Advanced Nano Telescope (ANT).

The conclusion of this project is the proof of the advantages of this system compared to current Earth observation systems. Given the very low development time and estimated single unit costs of less than €100,000 (using realistic cost estimation based on experience gained by the Delft University of Technology Space department during similar projects) the system meets all the requirements. A resolution of 7.5 m with a field of view of 15 km is achieved at an orbital altitude of 540 km. The system is compatible with current CubeSat standards and requiring a volume of less than 10 x 10 x 15 cm, equal to only half a 3U CubeSat such as the Delfi-n3Xt, developed by Delft University of Technology. In the future a satellite constellation of 24 satellites carrying the ANT as a payload could deliver low cost, mid-resolution satellite images at considerably lower prices than current single unit Earth observation systems.

From the results of this project it becomes apparent that there is still a lot to be investigated with respect to small sized multiple aperture systems. Especially the method of using multiple small satellites instead of one single large satellite has shown great potential for further studies and projects. We especially hope that the ANT can one day become a payload of one of the future Delft University of Technology satellites to be sent to space.

Bibliography

[1] European Space Agency, "About ESA - Funding." http://www.esa.int/esaMI/About{_}ESA/SEMNQ4FVL2F{_}0.htm, jan 2011.

[2] Satellite Industry Association, "2010 State of the Satellite Industry Report." http://www.sia.org/IndustryReport.htm, 2010.

[3] Eurimage S.p.A., "Applications." http://www.eurimage.com/applications.html, 2011.

[4] Satellite Imaging Corporation, "Archaeology." http://www.satimagingcorp.com/svc/archaeology.html, 2011.

[5] K. N. Wilkinson, et al., "Satellite imagery as a resource in the prospection for archaeological sites in central Syria," *Geoarchaeology*, vol. 21(7), pp. 735–750, 2006.

[6] Satellite Imaging Corporation, "Environmental Monitoring." http://www.satimagingcorp.com/svc/environmental{_}impact{_}studies.html, 2011.

[7] Satellite Imaging Corporation, "Mining." http://www.satimagingcorp.com/svc/mining.html, 2011.

[8] Satellite Sentinel Project, "About the Satellite Sentinel Project." http://www.satsentinel.org/about, 2011.

[9] Digital Globe, Inc., "Defense and Intelligence." http://www.digitalglobe.com/index.php/47/Industry+Applications?industry{_}id=16, 2011.

[10] M. J. A. Butler, M. C. Mouchot, V. Barale, C. LeBlanc, "The application of remote sensing technology to marine fisheries: an introductory manual," tech. rep., Food and Agriculture Organisation of the United Nations, Rome, 1988.

[11] Northern Sky Research, "Satellite-Based Earth Observation Market Entering Phase of Impressive Growth." http://www.spaceref.com/news/viewpr.html?pid=29665, nov 2009.

[12] M. E. Porter, "How competitive forces shape strategy," *Harvard Business Review*, 1979.

[13] Michael E. Porter, "Competitive Strategy: Techniques for Analysing Industries and Competitors," 1980.

[14] W. J. Smith, *Modern Optical Engineering*. McGraw-Hill, 2008.

[15] D. J. Schroeder, *Astronomical Optics*. Academic Press, 2000.

[16] Lee, S, Hutputanasin, A, Toorian, A, Lan, W, Munakata, R, "CubeSat Design Specification," tech. rep., California Polytechnic State University, 2009.

[17] Perez, E, "Ariane V User Manual Issue 5," tech. rep., Arianespace, 2008.

[18] Van Dale, "Van dale definition of logistics," May 2011.

[19] J.R. Wertz et al, *Space Mission Analysis And Design*. Space Technology Library, 2007.

[20] W.G. Rees, *Physical Principles of Remote Sensing*. Cambridge University Press, 2009.

[21] Klokočník, J., J. Kostelecký, and R.H. Goodin, "On fine orbit selection for particular geodetic and oceanographic missions involving passage through resonances," *Journal of Geodesy, 77, pp 30-40, DOI: 10.1007/s00190-002-0276-3*, 2003.

[22] E.N. Doornbos, *Thermospheric Density and Wind Determination from Satellite Dynamics*. Ipskamp Drukker, 2011.

[23] A.E. Hedin et al, "A global thermospheric model based on mass spectrometer and incoherent scatter data msis. i - n2 density and temperature," *Journal of Geophysical Research*, 1977.

[24] A.E. Hedin, "A revised thermospheric model based on mass spectrometer and incoherent scatter data - msis-83," *Journal of Geophysical Research*, 1983.

[25] A.E. Hedin et al, "The atmospheric model in the region 90 to 2000 km," *Advances in Space Research*, 1988.

[26] A.E. Hedin et al, "Extension of the msis thermospheric model into the middle and lower atmosphere," *Journal of Geophysical Research*, 1991.

[27] J.M. Picone et al, "Thermospheric densities derived from spacecraft orbits - i. accurate processing of two-line element sets," *Journal of Geophysical Research*, 2005.

[28] F.A. Marcos et al, "Neutral density models for aerospace applications," *Journal of Geophysical Research*, 1994.

[29] T. Ersmark, *Geant4 Monte Carlo Simulation of the International Space Station Radiation Environment.* PhD thesis, AlbaNova Universitetscentrum, Kungl Tekniska, 2006.

[30] P. Fortescue et al, *Spacecraft Systems Engineering.* Wiley, 2003.

[31] E.J. Daly et al, "Problems in radiation environment models at low altitudes," *Elsevier Science*, 1996.

[32] R. Noomen and Q.P. Chu and A.Kamp, *Space Engineering and Technology III.* Faculty of Aerospace Engineering, 2007.

[33] G. Valsecchi, A. Rossi, and P. Farinella, "Visualizing impact probabilities of space debris," *Space Debris*, vol. 1, pp. 143–158, 1999.

[34] NASA Langley Research Center, "Long Duration Exposure Facility." `http://setas-www.larc.nasa.gov/LDEF/MET{\_}DEB/mdenviro.html`, 2011.

[35] Eric L. Christiansen, " Design and Performance Equations," *Int. J. Impace Engng*, 1993.

[36] ASM Aerospace Specification Metals Inc., "Aluminum 7075-T6; 7075-T651." `http://asm.matweb.com/search/SpecificMaterial.asp?bassnum=MA7075T6`, 2011.

[37] Dave Litwiller, "CCD vs. CMOS: Facts and Fiction," 2005.

[38] Teledyne Dalsa, "CCD vs CMOS." `http://www.dalsa.com/sensors/Products/ccd~vs~cmos.aspx`, 2010.

[39] X. Wang, "Noise in sub-micron CMOS image sensors," nov 2008.

[40] T. P. Ma, Paul V. Dressendorfer, "Ionizing radiation effects in MOS devices and circuits," pp. 1–4, 1989.

[41] Andrew Gordon Holmes-Siedle, Len Adams, "Handbook of radiation effects, second edition," pp. 142–143, 2002.

[42] Hui Tian, Xinqiao Liu, SukHwan Lim, Stuart Kleinfelder, and Abbas El Gamal, "Active Pixel Sensors Fabricated in a Standard 0.18 um CMOS Technology," 2001.

[43] Heidi N. Becker and Dennis O. Thorbourn and James W. Alexander and Allan R. Eisenman, "Commercial Sensor Survey, Fiscal Year 2010, Radiation Test Report," 2010.

[44] Jan Bogaerts, Bart Dierickx, Guy Meynants, and Dirk Uwaerts, "Total Dose and Displacement Damage Effects in a Radiation-Hardened CMOS APS," 2003.

[45] J. Tan, "Radiation hardness cmosis sensor." email, 6 2011.

[46] Fairchild Imaging, "Fairchild Imaging Delivers Two New CMOS Image Sensor Papers at SPIE Annual Meeting." `http://www.prweb.com/releases/2010/08/prweb4337524.htm`, aug 2010.

[47] Cypress Semiconductor Corporation, "Cypress's High Fill Factor N-Well Pixel," nov 2005.

[48] Mortimer Abramowitz, Michael W. Davidson, "Optical Aberrations." `http://www.olympusmicro.com/primer/anatomy/aberrations.html`, 2010.

[49] Warren J. Smith, *Modern Optical Engineering.* 2008.

[50] Sean McHugh, "Lens Diffraction and Photography." `http://www.cambridgeincolour.com/tutorials/diffraction-photography.htm`, 2010.

[51] Imatest, "Image Sharpness." `http://www.imatest.com/docs/sharpness.html`, 2011.

[52] George Joseph, "How well do we understand Earth observation electro-optical sensor parameters?," 2004.

[53] GeoEye, "IKONOS Instrument/Product Description," 2009.

[54] Fokker Space & System B.V., "Signal to noise basics." Technical document, December 1993.

[55] W. Verhoef et al, "Simulation of hyperspectral and directional radiance images using coupled biophysical and atmospheric radiative transfer models," *Elsevier Science*, 2003.

[56] Jia-Ming Liu, *Photonic devices.* Cambridge University Press, 2005.

[57] Kenneth R. Spring et at, "Concepts in digital imaging technology: Dynamic range." `http://learn.hamamatsu.com/articles/dynamicrange.html`.

[58] CVI Melles-Griot, "Achromats." `https://www.cvimellesgriot.com/Products/Documents/Catalog/LAO.pdf`, 2011.

[59] FOS&S, "Adhesive NOA 61." `http://www.fos-s.be/website/foss/assets/files/productdownloads/adhesive~noa~61.pdf`, 2010.

[60] H. A. Macleod, *Thin-Film Optical Filters.* CRC Press, 4th ed., 2010.

[61] J.M. Kusterer, "What Wavelength Goes With a Color." `http://eosweb.larc.nasa.gov/EDDOCS/Wavelengths\_for\_Colors.html`, Sept. 2007.

[62] Omega Optical, "Astronomy filters." `https://www.omegafilters.com/pdfs/Professional{\_}Astronomy{\_}Filters.pdf`.

[63] *4.2 Megapixel machine vision CMOS image sensor Datasheet*, v2.9 ed.

[64] J. Fischbach, "Standard bandpass filters."

[65] Edmund Optics, "Edmund Optics webshop." `http://www.edmundoptics.com`.

[66] Robert R. Shannon, *Handbook of Optics: Tolerancing Techniques.* 2010.

[67] J. Burge, "Practical optics." `http://www.optics.arizona.edu/opti696/2005/Lecture\%2004,\%20Specifying\%20optical\%20components.pdf`.

[68] Promolding, "Polyamide 11." `http://www.promolding.nl/materiaal-munt.php?lan=nl\&c=108`, 2011.

[69] NASA, "Outgassing Data for Selecting Spacecraft Materials System." `http://outgassing.nasa.gov`, 2011.

[70] P. R. Yoder, *Mounting optics in optical instruments.* 2008.

[71] R. E. Fischer, B. Tadic-Galeb, and P. R. Yoder, *Optical System Design.* McGraw-Hill, 2008.

[72] Engineers edge, "Young's Modulus." `http://www.engineersedge.com/materialscience/youngsmodulus.htm`.

[73] M. Ashby and D. Cebon, "Materials selection in mechanical design." `http://www-mech.eng.cam.ac.uk/cms/publ/papers/gen1.pdf`, June 1993.

[74] E. Argonne Nationa Laboratory, "Beryllium toxicity." `http://www.ead.anl.gov/pub/doc/beryllium.pdf`, August 2005.

[75] Carpenter, "Carpenter super invar 32-5." `http://cartech.ides.com/datasheet.aspx?i=103\&e=179\&c=TechArt`, March 2004.

[76] Matweb, "Matweb material properties." `http://www.matweb.com`.

[77] Granta Design Limited, "Ces edupack." Software suite, 2011.

[78] N. Michael J. Viens, "Outgassing data for selecting spacecraft materials." `http://www-mech.eng.cam.ac.uk/cms/publ/papers/gen1.pdf`, February 2011.

[79] European Cooperation for Space Standardization, *Handbook of structural materials.* March 2011.

[80] Arianespace, "Ariane 5 User's Manual Issue 5 Revision 0," jul 2008.

[81] G. S. Aglietti, "Launch environment," 2010.

[82] M. Wu, "Wiener filtering for image restoration & basics on image compression." `www-ee.uta.edu/dip/courses/ee5356/631pub04sec8compressBasic.ppt`, 2009.

[83] Markus Flierl, “Image and video processing.” http://www.stanford.edu/class/ee368b/Handouts/16-hws3soln.pdf.

[84] P. Willems, “Regarding power consumption of cmv4000.” email, 5 2011.

[85] G. Yu et al., “Image compression systems on board satellites,” *Acta Astronautica 64*, 2009.

[86] Delft University of Technology Space Department. meeting, 5 2011.

[87] Delfi C3, “Command & data handling subsystem.” www.delfic3.nl, 6 2011.

[88] Microchip, “Pic18f2525 2620 4525 4620 data sheet.” www.microchip.com, 6 2011.

[89] Fong et al., “Constrained error propagation for efficient image transmission over noisy channels,” *IEEE Transactions on Consumer Electronics*, 2002.

[90] E. Martinec, “The consequences of noise.” http://theory.uchicago.edu/~ejm/pix/20d/tests/noise/noise-p3\#pixelsize, 1 2010.

[91] Texas Instruments, “Tms320dm6446 digital media system-on-chip.” www.ti.com, 9 2010.

[92] Actel Power Resource Center, “Total System Power in FPGAs,” tech. rep., Actel, 2006.

[93] W. Larson and J. Wertz, *Space Mission Analysis and Design.* Microcosm Press and Springer, 2006.

[94] J. Bouwmeester, G.F. Brouwer, E.K.A. Gill, G.L.E. Monna, J. Rotteveel in *Proceedings of the 61th International Astronautical Congress*, 2010.

[95] Akito Enokuchi, Masaki Nagai, Ryu Funase, Yuya Nakamura and Shinichi Nakasuka, “Remote sensing by university of tokyo’s pico-satellite project ’prism’,” tech. rep., 5th IAA Symposium on small satellites for Earth Observation IAA-B5-0605, Berlin, Germany, April 2005.

[96] M. Noca, G. Roethlisberger, F. Jordan, N. Scheidegger, T. Choueiri, B. Cosandier, F. George, R. Krpoun, “Swisscube mission and system overview,” tech. rep., UNINE / HES-SO / EPFL, 2008.

[97] Yasuhisa Oda, Tatsuhiro Sato, Nobuaki Kinoshita, and Yuya Nakamura, “A report on student Ground Station Network Project in Japan,” in *In proceedings of the 1st International Ground Station Network*, 2006.

[98] GENSO. www.genso.org, 6 2011.

[99] Iridium, “The satellite constellation.” www.iridium.com, 2011.

[100] I. wireless GmbH, “Technical specification of hispico satellite communication system.” www.iq-wireless.com, 2011.

[101] ISIS. www.cubesatshop.com, 6 2011.

[102] Wolfram, “Rodrigues’ rotation formula.” http://mathworld.wolfram.com/RodriguesRotationFormula.html, 2011.

[103] A. Bejan and A.D. Kraus, *Heat Transfer Handbook.* John Wiley and Sons, 2003.

[104] I. Martinez, “Spacecraft thermal control,” 1995 - 2011.

[105] J. R. Howell, “A catalog of radiation heat transfer configuration factors.” http://www.engr.uky.edu/rtl/Catalog/tablecon.html, 2011.

[106] Delfi team, “Delfi space specifications,” 2011.

[107] Cubesat, “The cubesat standard.” http://www.cubesat.org, 2011.

[108] D. Dooling M.M. Finckenor, “Material Selection Guidelines to Limit atomic Oxygen Effects on Spacecraft Surfaces,” 2003.

[109] G.B. Palmerini et al, “Design of the radiation shielding for a microsatellite,” *Acta Astronautica*, 2002.

[110] European Space Agency, “The space environment information system.” http://www.spenvis.oma.be/, 2011.

[111] European Space Agency, “The space environment information system.” http://www.spenvis.oma.be/, 2011.

[112] U.S. Department of Commerce and NOAA and ESRL and Physical Sciences Division, “Monthly solar flux 1990 to 2011.” http://www.esrl.noaa.gov/psd/data/gridded/timeseries.html, 2011.

[113] Becker et al., “Commercial sensor survey fiscal year 2010 radiation test report,” *JPL Publication*, 2010.

[114] J. C. Liou and N. L. Johnson, “PLANETARY SCIENCE: Risks in space from orbiting debris,” *Science*, vol. 311, pp. 340–341, Jan. 2006.

[115] Sharon K. Miller. http://www.grc.nasa.gov/WWW/epbranch/space/AOAbs.htm.

[116] A de Rooij, “Corrosion in Space,” *European Space Technology and Research Center*.

[117] IQ Wireless GmbH, “HISPICO - Hghly Integrated S-Band Transmitter for PICO and NANO Satellites.” http://www.iq-wireless.com/content/view/66/82/lang,english/.

[118] P. L. Conley, *Space Vehicle Mechanisms*. 1998.

[119] G.F. Brouwer, W.J. Ubbels, A.A.Vaartjes, F te Hennepe, “ASSEMBLY, INTEGRATION AND TESTING OF THE DELFI-C3 NANOSATELLITE,” 2008.

[120] Pumpkin Inc., “Pumpkin price list.” http://www.pumpkininc.com/content/doc/forms/pricelist.pdf.

[121] B. Klofas, J. Anderson, K. Leveque, “A Survey of CubeSat Communication Systems,” tech. rep., California Polytechnic State University, 2008.